Deutsche Geophysikalische Gesellschaft e. V.

Protokoll über das 25. Schmucker-Weidelt-Kolloquium für Elektromagnetische Tiefenforschung

Kirchhundem-Rahrbach

23.-27. September 2013

ISSN 0946-7467

herausgegeben von

Ralph-Uwe Börner
Institut für Geophysik und Geoinformatik
TU Bergakademie Freiberg
Gustav-Zeuner-Straße 12
09599 Freiberg

Katrin Schwalenberg
Bundesanstalt für
Geowissenschaften und Rohstoffe
Stilleweg 2
30655 Hannover

Vorwort

Das 25. Schmucker-Weidelt-Kolloquium für Elektromagnetische Tiefenforschung fand vom 23. bis 27. September 2013 im Josef-Gockeln-Haus in Kirchhundem-Rahrbach im südlichen Sauerland statt. Das Kolloquium wurde von Bülent Tezkan und seiner Gruppe von der Universität zu Köln organisiert. Ein großes DANKE dafür geht an die Kölner für all die geleistete Arbeit und die hervorragende Vorbereitung. Die Räumlichkeiten waren gut ausgesucht. Sie verfügten über einfache und bequeme Zimmer sowie modern ausgestattete Tagungsräume. Für Kollegen, die mit ihrem jungen Nachwuchs angereist sind, gab es sogar geräumige Familienzimmer. Mahlzeiten gab es vom Buffet, der Speisesaal bot einen Blick über das oft vom Nebel verhangene Rahrbachtal. Abends traf man sich in lockerer Atmosphäre in der hauseigenen Gaststube oder an der Kegelbahn, auf der manche Kugel auf die schiefe Bahn kam. Ein kleines Hallenbad begeisterte insbesondere den mitgebrachten Nachwuchs.

Die traditionelle Wanderung am Mittwochnachmittag führte durch das hügelig waldige Sauerland zur Molkerei Kruberg, wo Kaffee und Kuchen schon bereitstanden. Im Kaffeeraum waren die Urkunden der vielfach ausgezeichneten Milchkühe zu bestaunen. Es bot sich auch die Gelegenheit, die Stallungen des Milchwirtschaftsbetriebs bei entsprechender Geräusch- und Geruchskulisse zu besichtigen.

Zum 25. Schmucker-Weidelt-Kolloquium haben 85 Teilnehmer aus 6 Ländern (Deutschland, Schweden, Schweiz, Polen, Tschechien, Türkei) und 16 Institutionen beigetragen. Die Universität zu Köln war mit 16 Teilnehmern am stärksten vertreten und wurde gefolgt vom GFZ Potsdam mit 13 und der TU Bergakademie Freiberg mit 10 Teilnehmern. Mit 30 Doktoranden und 17 Studenten bildete der wissenschaftliche Nachwuchs etwa die Hälfte der Teilnehmerzahl.

Das Tagungsprogramm umfasste 24 Vorträge und 50 Poster, die auf Deutsch oder Englisch präsentiert wurden. Bewährt hat sich die vor den Postersessions stattfindende ein- bis zweiminütige mündliche Kurzvorstellung der Posterbeiträge durch ihre Autoren, was technisch ausgezeichnet vorbereitet war und „wie am Schnürchen“ ablief.

Der vorliegende Kolloquiumsband umfasst 17 Beiträge. Das sind bedeutend weniger als in den vergangenen Jahren (38 in 2011, 32 in 2009, 38 in 2007, 41 in 2005, 36 in 2003). Ursache hierfür ist vermutlich eine im Vorfeld des Kolloquiums begonnene kontroverse Diskussion um die Ablehnung eines beim *Geophysical Journal International* zur Publikation eingereichten Artikels, der zuvor in ähnlicher Form im letzten Kolloquiumsband erschien. Wir hoffen, dass dies ein Einzelfall bleibt.

Unsere „Blauen Bände“ können auf eine lange Tradition zurückblicken. Sie haben auch ohne *peer review* international hohes Ansehen erlangt. Insbesondere für den wissenschaftlichen Nachwuchs bieten sie eine gute Gelegenheit, nicht nur abgeschlossene Projekte, sondern auch laufende Arbeiten schriftlich zusammenzufassen. Sie stellen eine hervorragende Möglichkeit dar, das breite Spektrum der aktuellen Schwerpunkte deutscher EM-Forschung festzuhalten, wertvolle Ergebnisse zu dokumentieren oder eine Veröffentlichung in einer referierten Zeitschrift vorzubereiten.

Wir danken allen Teilnehmern, die sich trotz aller in den Diskussionen vorgebrachten Bedenken die Mühe gemacht haben, dennoch einen Beitrag zu liefern. Bei allen, die sich diesmal zurückgehalten haben, hoffen wir, dass sie nächstes Mal wieder dabei sein werden.

Wir sind sehr optimistisch, dass die „Blauen Bände“ ihren Status als gern genutztes und vielbeachtetes Instrument des wissenschaftlichen Austauschs zurückerobern werden.

Schließlich möchten wir den Firmen Metronix Braunschweig und KMS Technologies für ihre finanzielle Unterstützung herzlich danken, sowie der Universität zu Köln für die hervorragende Organisation. Alle haben in hohem Maße zum Gelingen des Kolloquiums beigetragen. Bei Herrn Bertelmann von der Bibliothek des GFZ Potsdam bedanken wir uns für die professionelle Unterstützung und die Gewährleistung der Online-Verfügbarkeit unseres Kolloquiumsbandes.

Die Blicke sind nun auf den 22. Internationalen „Electromagnetic Induction Workshop“ gerichtet, welcher vom 24.-30. August 2014 in Weimar stattfinden wird.

Katrin Schwalenberg und Ralph-Uwe Börner
Hannover und Freiberg, im Juni 2014

Inhaltsverzeichnis

3D MT inversion - reduced Hessian method with Gauss Newton approximation using the all-at-once approach

Wenke Wilhelms[1], Ralph-Uwe Börner[1], and Klaus Spitzer[1]

[1] *TU Bergakademie Freiberg*

1 Summary

In this article the reduced Hessian method is used to restate the so-called Karush-Kuhn-Tucker (KKT) system. This is a huge system of equations containing first and second derivatives of the objective function. Applying a Gauss Newton approximation second order information is ignored and the system becomes easier to handle. 3D magnetotelluric inversion results for the reduced Hessian method together with a Gauss Newton approximation are presented.

2 Introduction

As a first step in the process of developing a 3D all-at-once inversion code, we have investigated the 1D problem (Figure 1). The resulting models are comparable with those of a traditional Gauss Newton (GN) inversion. The first part of this article deals with the formulation of the inverse problem using the all-at-once approach. There we show how to build up the KKT matrix. The second part of the article explains the reduced Hessian method with Gauss Newton approximation. Both were applied to the KKT system and led to first 3D inversion results.

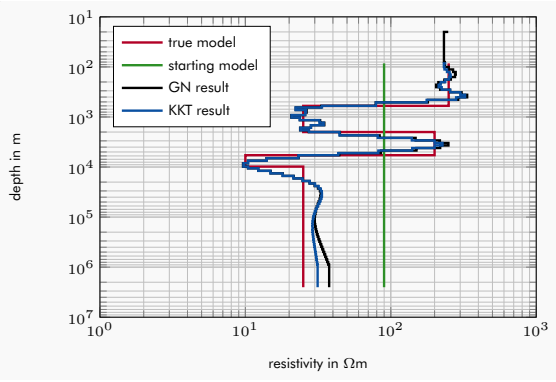

Figure 1: Inversion results for 1D magnetotellurics.

3 Inverse problem

As described by Haber, Ascher, and Oldenburg (2000) for the 1D magnetotelluric problem the Lagrangian $\mathcal{L}$ is formed by setting up the optimization problem in a constrained form. In doing so, the forward problem $\bar{\mathbf{A}}$ is incorporated using Lagrange multipliers $\boldsymbol{\lambda}$ in the objective function:

$$\mathcal{L}(\boldsymbol{u}, \boldsymbol{m}, \boldsymbol{\lambda}) \quad = \quad f(\boldsymbol{u}) + \tfrac{\beta}{2}||\mathbf{W}(\boldsymbol{m} - \boldsymbol{m}_{\text{ref}})||^2 \boldsymbol{\lambda}^\top [\bar{\mathbf{A}}(\boldsymbol{m})\boldsymbol{u} - \boldsymbol{b}(\boldsymbol{m})] \tag{1}$$

where the first term on the right-hand side is the data resi-dual. The second term of eq. (1) is a regularisation term. For minimizing the Lagrangian via Newton's method, the gradient $\nabla\mathcal{L}$ and the Hessian $\nabla^2\mathcal{L}$ need to be calculated. The gradient is a vector containing the partial derivatives of $\mathcal{L}$ with respect to all three parameters $\boldsymbol{u}$, $\boldsymbol{m}$, and $\boldsymbol{\lambda}$:

$$\begin{aligned} \nabla\mathcal{L} \quad &= \quad \begin{pmatrix} \mathcal{L}_{\boldsymbol{u}} \\ \mathcal{L}_{\boldsymbol{m}} \\ \mathcal{L}_{\boldsymbol{\lambda}} \end{pmatrix} \\ &= \quad \begin{pmatrix} \bar{\mathbf{Q}}^\top \bar{\mathbf{Q}}(\boldsymbol{u} + \boldsymbol{u}_p) + \bar{\mathbf{A}}^\top \boldsymbol{\lambda} \\ \beta \mathbf{W}^\top \mathbf{W}(\boldsymbol{m} - \boldsymbol{m}_{\text{ref}}) + (\bar{\mathbf{G}} - \bar{\mathbf{B}})^\top \boldsymbol{\lambda} \\ \bar{\mathbf{A}}\boldsymbol{u} - \boldsymbol{b} \end{pmatrix}. \end{aligned} \tag{2}$$

Matrices $\bar{\mathbf{G}}$ and $\bar{\mathbf{B}}$ contain first derivatives as explained by Haber et al. (2000).
The Hessian $\nabla^2\mathcal{L}$ (or KKT matrix $\mathcal{H}_{kkt}$) contains the second derivatives of the objective function with respect to all three parameters:

$$\begin{aligned} \mathcal{H}_{kkt} \quad &= \quad \begin{pmatrix} \mathcal{L}_{\boldsymbol{u},\boldsymbol{u}} & \mathcal{L}_{\boldsymbol{u},\boldsymbol{m}} & \mathcal{L}_{\boldsymbol{u},\boldsymbol{\lambda}} \\ \mathcal{L}_{\boldsymbol{m},\boldsymbol{u}} & \mathcal{L}_{\boldsymbol{m},\boldsymbol{m}} & \mathcal{L}_{\boldsymbol{m},\boldsymbol{\lambda}} \\ \mathcal{L}_{\boldsymbol{\lambda},\boldsymbol{u}} & \mathcal{L}_{\boldsymbol{\lambda},\boldsymbol{m}} & \mathcal{L}_{\boldsymbol{\lambda},\boldsymbol{\lambda}} \end{pmatrix} \\ &= \quad \begin{pmatrix} \bar{\mathbf{Q}}^\top \bar{\mathbf{Q}} & \bar{\mathbf{K}} & \bar{\mathbf{A}}^\top \\ \bar{\mathbf{K}}^\top & \beta \mathbf{W}^\top \mathbf{W} + \mathbf{R} - \mathbf{D} & (\bar{\mathbf{G}} - \bar{\mathbf{B}})^\top \\ \bar{\mathbf{A}} & \bar{\mathbf{G}} - \bar{\mathbf{B}} & \mathbf{0} \end{pmatrix}. \end{aligned} \tag{3}$$

Matrices $\bar{\mathbf{K}}$, $\mathbf{R}$, and $\mathbf{D}$ contain first and second derivatives (Haber et al., 2000).
The Newton method then reads

$$\mathcal{H}_{kkt} \cdot \begin{pmatrix} \boldsymbol{\delta u} \\ \boldsymbol{\delta m} \\ \boldsymbol{\delta \lambda} \end{pmatrix} = - \begin{pmatrix} \mathcal{L}_{\boldsymbol{u}} \\ \mathcal{L}_{\boldsymbol{m}} \\ \mathcal{L}_{\boldsymbol{\lambda}} \end{pmatrix}, \tag{4}$$

with $\delta\mathbf{u}$, $\delta\mathbf{m}$, and $\delta\boldsymbol{\lambda}$ as parameter updates. After each Newton iteration the inversion produces updates for all three different types of parameters:

$$\begin{pmatrix} \boldsymbol{u}^{n+1} \\ \boldsymbol{m}^{n+1} \\ \boldsymbol{\lambda}^{n+1} \end{pmatrix} \quad = \quad \begin{pmatrix} \boldsymbol{u}^{n} \\ \boldsymbol{m}^{n} \\ \boldsymbol{\lambda}^{n} \end{pmatrix} + \begin{pmatrix} \boldsymbol{\delta u} \\ \boldsymbol{\delta m} \\ \boldsymbol{\delta \lambda} \end{pmatrix}. \tag{5}$$

Thus, explicit forward modelling after each iteration is not necessary.

4 Reduced Hessian method

As described by Haber and Ascher (2001) $\boldsymbol{\delta u}$ and $\boldsymbol{\delta \lambda}$ are eliminated and the system of equations (4) can be written in the following way:

$$\boldsymbol{\delta m} = \mathbf{H}_{\text{red}}^{-1}\boldsymbol{p}, \tag{6}$$

with

$$\begin{aligned}\mathbf{H}_{\text{red}} = {} & \mathbf{J}^\top\mathbf{J} + \mathbf{J}_b^\top\mathbf{J}_b - \mathbf{J}^\top\mathbf{J}_b - \mathbf{J}_b^\top\mathbf{J} + \beta\mathbf{W}^\top\mathbf{W} \\ & + \mathbf{R} - \mathbf{D} - \mathbf{S} + \mathbf{S}_b - \mathbf{S}^\top + \mathbf{S}_b^\top,\end{aligned} \tag{7}$$

and

$$\begin{aligned}\boldsymbol{p} = {} & \beta\mathbf{W}^\top\mathbf{W}(\boldsymbol{m} - \boldsymbol{m}_{\text{ref}}) - \mathbf{J}^\top\bar{\mathbf{Q}}\bar{\mathbf{A}}^{-1}\boldsymbol{b} \\ & + \mathbf{J}_b^\top\bar{\mathbf{Q}}\bar{\mathbf{A}}^{-1}\boldsymbol{b} + \bar{\mathbf{K}}^\top(\boldsymbol{u} - \bar{\mathbf{A}}^{-1}\boldsymbol{b}).\end{aligned} \tag{8}$$

The Jacobians $\mathbf{J}$ and $\mathbf{J}_b$ are dense matrices. They can be written as products of three sparse matrices which is easier to handle:

$$\mathbf{J} = -\bar{\mathbf{Q}}\bar{\mathbf{A}}^{-1}\bar{\mathbf{G}}, \tag{9}$$

$$\mathbf{J}_b = -\bar{\mathbf{Q}}\bar{\mathbf{A}}^{-1}\bar{\mathbf{B}}. \tag{10}$$

$\mathbf{S}$ and $\mathbf{S}_b$ are dense matrices also factorable in three sparse matrices each:

$$\mathbf{S} = \bar{\mathbf{K}}^\top\bar{\mathbf{A}}^{-1}\bar{\mathbf{G}}, \tag{11}$$

$$\mathbf{S}_b = \bar{\mathbf{K}}^\top\bar{\mathbf{A}}^{-1}\bar{\mathbf{B}}. \tag{12}$$

The plots of the Jacobian $\mathbf{J}$ in Figure 2 show sensitivities of the different model cells of a zy-slice at $x = 0\,\text{km}$ with respect to a data aquisition site at $(x, y) = (0, -8)\,\text{km}$ at the Earth's surface. This is right above the good conductive anomaly with a conductivity of $\sigma = 1\,{}^{S}/_{\text{m}}$ (see 3D-2 COMMEMI model (Zhdanov & Weaver, 1997)) that shows highest sensitivies.

5 Inversion Results for Gauss Newton approximation

Using the Gauss Newton approximation second derivative information is ignored. That is why $\mathbf{H}_{\text{red}}$ and $\boldsymbol{p}$ in eq. (6) reduce to

$$\mathbf{H}_{\text{red}} = \mathbf{J}^\top\mathbf{J} + \mathbf{J}_b^\top\mathbf{J}_b - \mathbf{J}^\top\mathbf{J}_b - \mathbf{J}_b^\top\mathbf{J} + \beta\mathbf{W}^\top\mathbf{W}, \tag{13}$$

and

$$\boldsymbol{p} = \beta\mathbf{W}^\top\mathbf{W}(\boldsymbol{m} - \boldsymbol{m}_{\text{ref}}) - \mathbf{J}^\top\bar{\mathbf{Q}}\bar{\mathbf{A}}^{-1}\boldsymbol{b} + \mathbf{J}_b^\top\bar{\mathbf{Q}}\bar{\mathbf{A}}^{-1}\boldsymbol{b}. \tag{14}$$

The matrix $\mathbf{H}_{\text{red}}$ is now symmetric and positive definite.
The inversion results for the 3D-2 COMMEMI model are gained for 64 data points at the surface at frequencies of 0.1 Hz and 0.01 Hz. The grid we used was $49 \times 48 \times 44$ cells and had about 100,000 cells in total. We had about 300,000 degrees of freedom. The starting model was a homogenous halfspace with a conductivity σ of $10^{-3}\,{}^{S}/_{\text{m}}$.
Results of the inversion will not be shown here since not all effects that occur can be explained yet. Further work will be done to better understand the behaviour of the inversion together with e.g. regularisation.

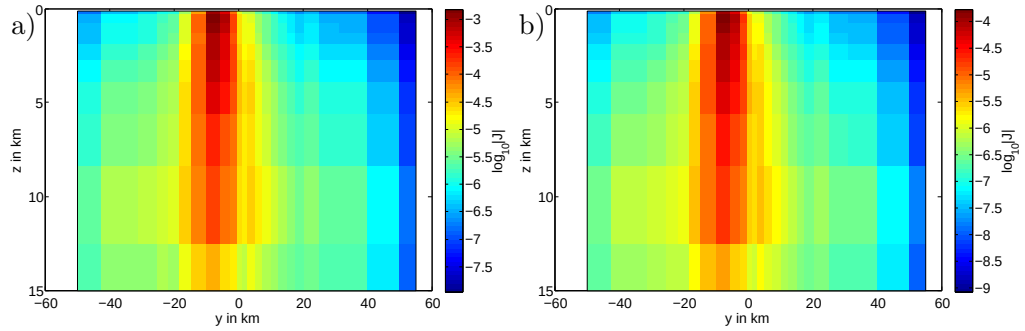

Figure 2: Sensitivity plots for a slice through the 3D-2 COMMEMI model at $x = 0\,\text{km}$ for frequencies of 0.1 Hz in a) and 0.01 Hz in b). The measuring site is at the Earth's surface at $(x, y) = (0, -8)\,\text{km}$.

6 Outlook

The next step will be the implementation of the full all-at-once inversion scheme. Then a system of equations with a symmetric and indefinite matrix needs to be solved. Therefore preconditioning is indispensable.

7 Acknowledgments

Thanks to all colleagues for their support and to Eldad Haber for his personal advice.

References

Haber, E., & Ascher, U. M. (2001). Preconditioned all-at-once methods for large, sparse parameter estimation problems. *Inverse Problems*, *17*, 1847 - 1864.

Haber, E., Ascher, U. M., & Oldenburg, D. (2000). On optimization techniques for solving nonlinear inverse problems. *Inverse Problems*, *16*, 1263 - 1280.

Zhdanov, M. S., & Weaver, J. T. (1997). Methods for modelling electromagnetic fields. *Journal of Applied Geophysics*, *37*, 133 - 271.

EM fields of a VMD calculated at arbitrary points within a layered half-space

Mathias Scheunert[1,2], Ralph-Uwe Börner[1], and Bernhard Siemon[3]

[1] *TU Bergakademie Freiberg*
[2] *Helmholtz-Zentrum Dresden-Rossendorf*
[3] *BGR Hannover*

1 Problem statement

In this paper, we derive expressions for all electromagnetic (EM) field components which can be observed, when a vertical magnetic dipole (VMD) is located at $z = -h$, $h > 0$ over a stratified earth, i.e., when the electrical conductivity is a piecewise constant function of depth z. We further allow a non-vanishing but small electrical conductivity in the air layer, and let the electrical permittivity vary from its vacuum value. Apart from traditional approaches, we use a non-vanishing air conductivity to be consistent with our 3-D discretizations which would otherwise yield singular mass matrices.
The basic ideas of the derivation within the following paragraphs emanate from Ward and Hohmann (1988) and Zhdanov (2009). While the first sections of this paper concern the two-layer (i.e., the nearly non-conductive air and the conductive homogeneous half-space) case we expand the concept to the general N-layer case in the last section.
This work has been motivated by the one-dimensional forward and inverse problem of helicopter electromagnetics (HEM). To evaluate the observed total fields by a numerical discretization scheme, the secondary field approach requires the calculation of the analytical solution of the EM fields at the receiver positions within the air half-space. Furthermore, in order to calculate the Jacobian matrix, these fields are required at arbitrary points within the conductive layered half-space.

1.1 General expressions

We aim at finding expressions for the EM fields with a time dependence of $\mathrm{e}^{i\omega t}$ corresponding to the Fourier transform pair

$$\boldsymbol{F}(\omega) = \int_{-\infty}^{\infty} \boldsymbol{f}(t)\, \mathrm{e}^{-\mathrm{i}\omega t}\, \mathrm{d}t, \tag{1}$$

$$\boldsymbol{f}(t) = \frac{1}{2\pi} \int_{-\infty}^{\infty} \boldsymbol{F}(\omega)\, \mathrm{e}^{\mathrm{i}\omega t}\, \mathrm{d}\omega. \tag{2}$$

A vertical magnetic dipole with dipole moment $\boldsymbol{m}$ is located at $z = -h, h > 0$ over a homogeneous half-space. Without loss of generality, let the interface between air and the conductive half-space be at $z = 0$.

As an additional simplification the magnetic permeability for both media is set to its vacuum value $\mu^0 = \mu^1 = \mu_0$.
It is convenient to describe the behavior of the fields with a vector potential which is consistent with Maxwell's equations.
The choice of the source type (VMD) requires the use of the magnetic vector potential $\boldsymbol{F}$, such that there holds after application of the Lorenz gauge condition

$$\boldsymbol{E} = -\nabla\times\boldsymbol{F} \qquad\qquad \boldsymbol{H} = -(\sigma + \mathrm{i}\epsilon\omega)\boldsymbol{F} + \frac{1}{\mathrm{i}\omega\mu_0}\nabla(\nabla\cdot\boldsymbol{F}), \tag{3}$$

where $\boldsymbol{E} = \boldsymbol{E}(\boldsymbol{x},\omega)$ and $\boldsymbol{H} = \boldsymbol{H}(\boldsymbol{x},\omega)$ denote the electrical and magnetic field, resp., ω the angular frequency, $\sigma = \sigma(z)$ the electrical conductivity, and $\epsilon = \epsilon(z)$ the electrical permittivity. The vector potential $\boldsymbol{F}(\boldsymbol{x},\omega)$ is solution of the inhomogeneous Helmholtz equation

$$\begin{aligned}\nabla^2\boldsymbol{F} + k^2\boldsymbol{F} &= -\boldsymbol{J}_\mathrm{s} = -\mathrm{i}\omega\mu_0\boldsymbol{m}\,\delta(x,y,z+h)\,,\\ k^2 &= -\mathrm{i}\omega\mu_0\sigma + \omega^2\mu_0\epsilon,\end{aligned} \tag{4}$$

where $\boldsymbol{J}_\mathrm{s} = \boldsymbol{J}_\mathrm{s}(\boldsymbol{x},\omega)$ is a source current density or source magnetization. When the source dipole moment $\boldsymbol{m}$ is aligned, e.g., with the z-axis, i.e., $\boldsymbol{m} = [0,0,m]^\top$, then we have

$$\boldsymbol{F} = [0,0,F_z]\,, \tag{5}$$

and (3) reads component-wise as

$$\begin{aligned} E_x &= -\frac{\partial F_z}{\partial y} & H_x &= \frac{1}{\mathrm{i}\omega\mu_0}\frac{\partial^2 F_z}{\partial x\partial y},\\ E_y &= -\frac{\partial F_z}{\partial x} & H_y &= \frac{1}{\mathrm{i}\omega\mu_0}\frac{\partial^2 F_z}{\partial y\partial z},\\ E_z &= 0 & H_z &= \frac{1}{\mathrm{i}\omega\mu_0}\left(\frac{\partial^2 F_z}{\partial z^2} + k^2 F_z\right). \end{aligned} \tag{6}$$

Due to the symmetry of the problem (cf. Fig. 1), the choice of cylindrical coordinates with

$$\begin{aligned} x &= r\cos\phi,\\ y &= r\sin\phi, \end{aligned} \tag{7}$$

is appropriate, which yields

$$\begin{aligned} E_\phi &= \frac{\partial F_z}{\partial r} & H_r &= \frac{1}{\mathrm{i}\omega\mu_0}\frac{\partial^2 F_z}{\partial r\partial z},\\ & & H_z &= -\frac{1}{\mathrm{i}\omega\mu_0}\frac{1}{r}\frac{\partial}{\partial r}\left(r\frac{\partial F_z}{\partial r}\right), \end{aligned} \tag{8}$$

or, equivalently,

$$\begin{aligned} E_x &= -E_\phi\frac{y}{r} & H_x &= H_r\frac{x}{r},\\ E_y &= E_\phi\frac{x}{r} & H_y &= H_r\frac{y}{r}. \end{aligned} \tag{9}$$

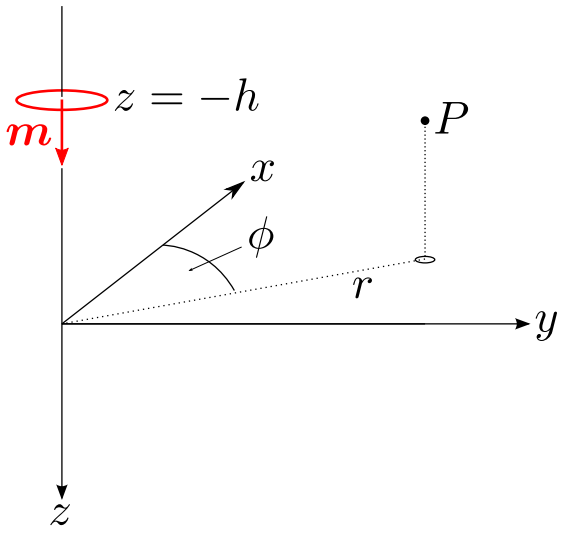

Figure 1: Sketch of the cylindrical coordinate system with position of the VMD at height $z = -h$, $h > 0$, and dipole moment m indicated by a red circle. At the point P the components of the EM fields shall be calculated.

1.2 Continuity conditions

To completely describe the behavior of the EM fields, two conditions regarding the potential F_z have to be enforced. First, it is convenient to set the potential at infinite distance to zero, i.e.,

$$\lim_{R\to\infty} \boldsymbol{F} \to 0 \quad \text{for} \quad R = \sqrt{r^2 + (z+h)^2}. \tag{10}$$

By virtue of the continuity of the tangential electrical field $\boldsymbol{E}^{\tan} = [E_\phi, 0, 0]$ and magnetic field $\boldsymbol{H}^{\tan} = [0, H_r, 0]$ at the interface between media 0 and 1, the continuity conditions are

$$F_z^0 = F_z^1 \qquad\qquad \frac{\partial F_z^0}{\partial z} = \frac{\partial F_z^1}{\partial z}, \tag{11}$$

respectively. We note that the continuity of the potential and its vertical derivative is a direct consequence of the continuity of the tangential components of E_ϕ and H_r, which can be obtained by integrating the associated expressions in (8) with respect to r and exploiting condition (10).

1.3 Solution approach - half-space problem

We decompose the total field in air by separating the (primary) singular potential in the full-space F_z^* and the (secondary) potential originating from induced currents in the lower conducting half-space F_z^0. The expression of the full-space potential F_z^* has a closed analytical form. The secondary potential in the upper half-space and the remaining potential

in the lower half-space F_z^1 have independent solutions but can be matched by use of (11) (Zhdanov 2009).
With $F = F_z$, we obtain

$$\begin{aligned} F^0_{\text{tot}} &= F^* + F^0 && \text{for } z < 0, \\ F^1_{\text{tot}} &= F^1 && \text{for } z > 0, \end{aligned} \tag{12}$$

and with $\nabla^2 \to \frac{\partial^2}{\partial z^2}$ we arrive at the homogeneous Helmholtz equations for the secondary potentials

$$\begin{aligned} &\frac{\partial^2 F^0}{\partial z^2} + k^2 F^0 = 0, \\ &k_0^2 = -\mathrm{i}\omega\mu_0\sigma_0 + \omega^2\mu_0\epsilon_0, \\ &\frac{\partial^2 F^1}{\partial z^2} + k^2 F^1 = 0, \\ &k_1^2 = -\mathrm{i}\omega\mu_0\sigma_1 + \omega^2\mu_0\epsilon_1. \end{aligned} \tag{13}$$

2 Derivation of the primary full-space potential F^*

The full-space expression of F^* can be obtained by applying the 3-D spatial Fourier transform on (4) with $\boldsymbol{F}^* = F^*\boldsymbol{e}_\mathrm{z}$ (Ward and Hohmann 1988). The Fourier representation is

$$\tilde{F}^*(k_x, k_y, k_z) = \int_{-\infty}^{\infty}\int_{-\infty}^{\infty}\int_{-\infty}^{\infty} F^*(x, y, z)\, \mathrm{e}^{-i(k_x x + k_y y + k_z z)}\, \mathrm{d}x\, \mathrm{d}y\, \mathrm{d}z, \tag{14}$$

and

$$F^*(x, y, z) = \frac{1}{8\pi^3}\int_{-\infty}^{\infty}\int_{-\infty}^{\infty}\int_{-\infty}^{\infty} \tilde{F}^*(k_x, k_y, k_z)\, \mathrm{e}^{i(k_x x + k_y y + k_z z)}\, \mathrm{d}k_x\, \mathrm{d}k_y\, \mathrm{d}k_z. \tag{15}$$

After transformation of (4) we obtain a simple algebraic expression, which has a representation as a convolution integral in space domain,

$$F^*(x, y, z) = \int_{-\infty}^{\infty}\int_{-\infty}^{\infty}\int_{-\infty}^{\infty} G\big(x - x', y - y', z - z'\big)\, J_\mathrm{s}\big(x', y', z'\big)\, \mathrm{d}x'\, \mathrm{d}y'\, \mathrm{d}z', \tag{16}$$

where the Green's function G is the impulse response of the conductive full-space, and by virtue of the Sommerfeld identity, has an integral representation

$$\frac{\mathrm{e}^{-\mathrm{i}kR}}{4\pi R} = G(x, y, z) = G(r, z) = \frac{1}{4\pi}\int_0^{\infty} \frac{\lambda}{u}\, \mathrm{e}^{-u|z+h|}\, J_0(\lambda r)\, \mathrm{d}\lambda. \tag{17}$$

The Fourier transform of G with respect to the horizontal coordinates is

$$\tilde{G}(k_x, k_y, z) = \frac{\mathrm{e}^{-u|z+h|}}{2u}, \tag{18}$$

where

$$u = \sqrt{\lambda^2 - k^2}, \qquad \lambda^2 = k_x^2 + k_y^2. \tag{19}$$

Finally $F^*(r,z)$ can be written as a weighted Green's function in the space domain and cylindrical coordinates

$$F^*(r,z) = \frac{\mathrm{i}\omega\mu_0 m}{4\pi R}\,\mathrm{e}^{-\mathrm{i}kR}, \qquad R = \sqrt{r^2+z^2}. \tag{20}$$

For completeness, the respective field components can be obtained by (8) and the chain rule:

$$\begin{aligned}
E_\phi^* &= -\frac{\mathrm{i}\omega\mu_0 m}{4\pi}\frac{r}{R^3}\,(\mathrm{i}kR+1)\,\mathrm{e}^{-\mathrm{i}kR},\\
H_r^* &= -\frac{m}{4\pi}\frac{r(z+h)}{R^5}\left(k^2R^2 - 3\mathrm{i}kR - 3\right)\mathrm{e}^{-\mathrm{i}kR},\\
H_z^* &= \frac{m}{4\pi}\frac{1}{R^5}\left[2\mathrm{i}kR^3 + \left(k^2r^2+2\right)R^2 - 3\mathrm{i}kr^2R - 3r^2\right]\mathrm{e}^{-\mathrm{i}kR}.
\end{aligned} \tag{21}$$

3 Derivation of the secondary potentials F^0 and F^1

As stated out by Zhdanov (2009) the solution of the problem by applying the spatial Fourier transform in analogy to (15) can be understood as a superposition of plane wave solutions in the spatial domain. Hence the observed secondary potentials in each half-space can also be considered as potentials associated with incident, reflected, and transmitted waves, respectively. In analogy to Section 2 we depart from the 2-D spatial Fourier transform of the homogeneous Helmholtz equations for both media

$$\tilde{F}(k_x,k_y,z) = \int_{-\infty}^{\infty}\int_{-\infty}^{\infty} F(x,y,z)\,\mathrm{e}^{-i(k_x x + k_y y)}\,\mathrm{d}x\,\mathrm{d}y, \tag{22}$$

and

$$F(x,y,z) = \frac{1}{4\pi^2}\int_{-\infty}^{\infty}\int_{-\infty}^{\infty} \tilde{F}(k_x,k_y,z)\,\mathrm{e}^{i(k_x x + k_y y)}\,\mathrm{d}k_x\,\mathrm{d}k_y, \tag{23}$$

such that the Helmholtz equations in both half-spaces read

$$\frac{\partial^2 \tilde{F}^j}{\partial z^2} + u_j^2 \tilde{F}^j = 0 \quad \text{for} \quad j = 0, 1. \tag{24}$$

The solutions of these equations are given by

$$\begin{aligned}
\tilde{F}^0 &= \tilde{F}_+^0(k_x,k_y)\,\mathrm{e}^{-u_0 z} + \tilde{F}_-^0(k_x,k_y)\,\mathrm{e}^{u_0 z},\\
\tilde{F}^1 &= \tilde{F}_+^1(k_x,k_y)\,\mathrm{e}^{-u_1 z} + \tilde{F}_-^1(k_x,k_y)\,\mathrm{e}^{u_1 z},
\end{aligned} \tag{25}$$

a superposition of plane waves traveling in positive ($\tilde{F}_+^j$) and negative ($\tilde{F}_-^j$) $z-$direction.

Since we don't observe upward-travelling waves in $z > 0$ nor downward-travelling waves in $z < 0$, we set

$$\tilde{F}^0_+ = \tilde{F}^1_- \stackrel{!}{=} 0, \tag{26}$$

which ensures that (10) is valid.
We now apply the continuity conditions (11), and obtain two equations for the unknown amplitudes $\tilde{F}^0_-$ and $\tilde{F}^1_+$ which satisfies (12) for $z = 0$,

$$\begin{aligned} \frac{\mathrm{i}\omega\mu_0 m}{2}\frac{\mathrm{e}^{-u_0 h}}{u_0} + \tilde{F}^0_- &= \tilde{F}^1_+, \\ -\frac{\mathrm{i}\omega\mu_0 m}{2}\,\mathrm{e}^{-u_0 h} + u_0\tilde{F}^0_- &= -u_1\tilde{F}^1_+. \end{aligned} \tag{27}$$

Note that the solution of the full-space field $\tilde{F}^*$ is given by the Green's function in the domain of the horizontal wave numbers ((18)) scaled by the source J_s

$$\tilde{F}^*(k_x, k_y, z) = \frac{\mathrm{i}\omega\mu_0 m}{2}\frac{\mathrm{e}^{-u_0|z+h|}}{u_0}. \tag{28}$$

Solving the resulting linear system of equations

$$\underbrace{\begin{bmatrix} 1 & -1 \\ u_0 & u_1 \end{bmatrix}}_{\boldsymbol{S}} \begin{bmatrix} \tilde{F}^0_- \\ \tilde{F}^1_+ \end{bmatrix} = \begin{bmatrix} -\dfrac{1}{u_0} \\ 1 \end{bmatrix} \frac{\mathrm{i}\omega\mu_0 m}{2}\,\mathrm{e}^{-u_0 h}, \tag{29}$$

with

$$\boldsymbol{S}^{-1} = \frac{1}{\det(S)}\mathrm{adj}\,(S) = \frac{1}{u_0 + u_1}\begin{bmatrix} u_1 & 1 \\ -u_0 & 1 \end{bmatrix}, \tag{30}$$

the respective fields are

$$\tilde{F}^0(k_x, k_y, z) = \underbrace{\frac{\mathrm{i}\omega\mu_0 m}{2}\left(\left[1 - \frac{u_1}{u_0}\right]\left[\frac{1}{u_0 + u_1}\right]\right)\mathrm{e}^{-u_0 h}}_{\tilde{F}^0_-}\,\mathrm{e}^{u_0 z}, \qquad z \le 0 \tag{31}$$

$$\tilde{F}^1(k_x, k_y, z) = \underbrace{\frac{\mathrm{i}\omega\mu_0 m}{2}\left(\frac{2}{u_0 + u_1}\right)\mathrm{e}^{-u_0 h}}_{\tilde{F}^1_+}\,\mathrm{e}^{-u_1 z}, \qquad z \ge 0. \tag{32}$$

In our case, the integrand is an axi-symmetric function. We can express the two-dimensional Fourier transformation by the Hankel transformation (Ward and Hohmann 1988)

$$\frac{1}{4\pi^2}\int_{-\infty}^{\infty}\int_{-\infty}^{\infty}\tilde{F}^j(k_x, k_y, z)\,\mathrm{e}^{i(k_x x + k_y y)}\,\mathrm{d}k_x\,\mathrm{d}k_y = \frac{1}{2\pi}\int_{-\infty}^{\infty}F^j(\lambda)\,\lambda J_0(\lambda r)\,\mathrm{d}\lambda, \tag{33}$$

leading to the desired total potentials for the air and earth layer expressed in cylindrical coordinates

$$F^0_{\mathrm{tot}} = \frac{\mathrm{i}\omega\mu_0 m}{4\pi} \int_0^\infty \frac{\lambda}{u_0} \left[\mathrm{e}^{-u_0|z+h|} + \left(\frac{u_0 - u_1}{u_0 + u_1} \right) \mathrm{e}^{u_0(z-h)} \right] J_0(\lambda r)\, \mathrm{d}\lambda, \tag{34}$$

$$F^1_{\mathrm{tot}} = \frac{\mathrm{i}\omega\mu_0 m}{4\pi} \int_0^\infty \frac{2\lambda}{u_0 + u_1} \mathrm{e}^{-u_0 h}\, \mathrm{e}^{-u_1 z}\, J_0(\lambda r)\, \mathrm{d}\lambda. \tag{35}$$

To calculate the electromagnetic fields from the vector potential, the following Bessel function identities are helpful (Abramowitz and Stegun 1972):

$$\begin{aligned} \partial_r J_0(\lambda r) &= -\lambda J_1(\lambda r)\,, \\ \partial_\lambda J_0(\lambda r) &= -r J_1(\lambda r)\,, \\ \partial_r J_1(\lambda r) &= \lambda \left[J_0(\lambda r) - \frac{1}{\lambda r} J_1(\lambda r) \right], \\ \partial_r \left(r J_1(\lambda r) \right) &= \cancel{J_1(\lambda r)} + \lambda r J_0(\lambda r) - \cancel{J_1(\lambda r)}. \end{aligned} \tag{36}$$

The fields in $z \leq 0$ resulting from (34) are

$$E^0_{\phi,\mathrm{tot}} = \frac{-\mathrm{i}\omega\mu_0 m}{4\pi} \int_0^\infty \frac{\lambda^2}{u_0} \left[\mathrm{e}^{-u_0|z+h|} + \left(\frac{u_0 - u_1}{u_0 + u_1} \right) \mathrm{e}^{u_0(z-h)} \right] J_1(\lambda r)\, \mathrm{d}\lambda, \tag{37}$$

$$H^0_{r,\mathrm{tot}} = \frac{m}{4\pi} \int_0^\infty \lambda^2 \left[\mathrm{e}^{-u_0|z+h|} + \left(\frac{u_0 - u_1}{u_0 + u_1} \right) \mathrm{e}^{u_0(z-h)} \right] J_1(\lambda r)\, \mathrm{d}\lambda, \tag{38}$$

$$H^0_{z,\mathrm{tot}} = \frac{m}{4\pi} \int_0^\infty \frac{\lambda^3}{u_0} \left[\mathrm{e}^{-u_0|z+h|} + \left(\frac{u_0 - u_1}{u_0 + u_1} \right) \mathrm{e}^{u_0(z-h)} \right] J_0(\lambda r)\, \mathrm{d}\lambda. \tag{39}$$

In $z \geq 0$, the field expressions are

$$E^1_{\phi,\mathrm{tot}} = \frac{-\mathrm{i}\omega\mu_0 m}{4\pi} \int_0^\infty \frac{2\lambda^2}{u_0 + u_1} \mathrm{e}^{-u_0 h}\, \mathrm{e}^{-u_1 z}\, J_1(\lambda r)\, \mathrm{d}\lambda, \tag{40}$$

$$H^1_{r,\mathrm{tot}} = \frac{m}{4\pi} \int_0^\infty \frac{2\lambda^2 u_1}{u_0 + u_1} \mathrm{e}^{-u_0 h}\, \mathrm{e}^{-u_1 z}\, J_1(\lambda r)\, \mathrm{d}\lambda, \tag{41}$$

$$H^1_{z,\mathrm{tot}} = \frac{m}{4\pi} \int_0^\infty \frac{2\lambda^3}{u_0 + u_1} \mathrm{e}^{-u_0 h}\, \mathrm{e}^{-u_1 z}\, J_0(\lambda r)\, \mathrm{d}\lambda. \tag{42}$$

4 The N-layer case

We now consider the more general case where we have N conducting layers and an additional air layer, and N layer boundaries at $z = z_j$, $j = 0, 1, \ldots, N-1$ (Fig. 2). The solution for the secondary potential in layer $1 \leq j < N$ has the general form

$$\tilde{F}^j = \tilde{F}^j_+ \mathrm{e}^{-u_j(z - z_{j-1})} + \tilde{F}^j_- \mathrm{e}^{u_j(z - z_j)}\,. \tag{43}$$

Conceiving the upward traveling wave as reflected from the bottom layer boundary, the downward traveling originates as transmitted wave from the top layer boundary, respectively. In the layers $j = 0$ and $j = N$ we only observe emanating waves, hence, the solutions are

$$\tilde{F}^0 = \tilde{F}^0_- \, \mathrm{e}^{u_0 z}, \tag{44}$$

$$\tilde{F}^N = \tilde{F}^N_+ \, \mathrm{e}^{-u_N (z - z_{N-1})}. \tag{45}$$

For the total potential, the primary potential $\tilde{F}^*$ has to be added in layer $j = 0$. It acts like the potential of an incident wave with amplitude $\tilde{F}^0_+$

$$\tilde{F}^0_+ := \frac{\mathrm{i}\omega\mu_0 m}{2} \frac{1}{u_0}. \tag{46}$$

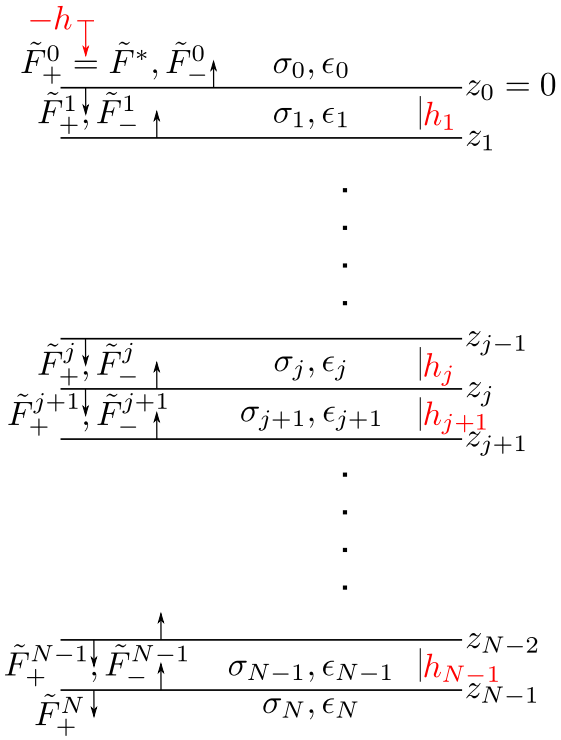

Figure 2: Sketch of the layered half-space model.

Application of the continuity conditions at the interfaces $z = z_j, j = 0, 1, \ldots, N-1$ leads to a system of $2N$ boundary conditions for $2(N-1)+2$ unknown coefficients. Hence it holds at $z = z_0 = 0$:

$$\tilde{F}^0_+ \, \mathrm{e}^{-u_0 h} + \tilde{F}^0_- = \tilde{F}^1_+ + \tilde{F}^1_- \, \mathrm{e}^{-u_1 h_1}, \tag{47}$$

$$-u_0 \tilde{F}^0_+ \, \mathrm{e}^{-u_0 h} + u_0 \tilde{F}^0_- = -u_1 \tilde{F}^1_+ + u_1 \tilde{F}^1_- \, \mathrm{e}^{-u_1 h_1}, \tag{48}$$

at $z = z_j$:

$$\tilde{F}_+^j \, \mathrm{e}^{-u_j(z_j - z_{j-1})} + \tilde{F}_-^j = \tilde{F}_+^{j+1} + \tilde{F}_-^{j+1} \, \mathrm{e}^{-u_{j+1} h_{j+1}}, \tag{49}$$

$$-u_j \tilde{F}_+^j \, \mathrm{e}^{-u_j h_j} + u_j \tilde{F}_-^j = -u_{j+1} \tilde{F}_+^{j+1} + u_{j+1} \tilde{F}_-^{j+1} \, \mathrm{e}^{-u_{j+1} h_{j+1}}, \tag{50}$$

and at $z = z_{N-1}$:

$$\tilde{F}_+^{N-1} \, \mathrm{e}^{-u_{N-1} h_{N-1}} + \tilde{F}_-^{N-1} = \tilde{F}_+^N, \tag{51}$$

$$-u_{N-1} \tilde{F}_+^{N-1} \, \mathrm{e}^{-u_{N-1} h_{N-1}} + u_{N-1} \tilde{F}_-^{N-1} = -u_N \tilde{F}_+^N, \tag{52}$$

with

$$h_j = z_j - z_{j-1}, \quad \text{and } h_{j+1} = z_{j+1} - z_j. \tag{53}$$

The resulting system of equations for the determination of the $2N$ coefficients $\tilde{F}_+^j$, $j = 1, 2, \ldots, N$, and $\tilde{F}_-^k$, $k = 0, 1, \ldots, N-1$ can be solved explicitly. In fact, the recursion formulae given in the literature are equivalent to the application of a straightforward Gauss elimination scheme.

4.1 Calculation of the secondary potential $\tilde{F}^0$ in the wavenumber domain

To obtain the potentials in $z \leq 0$ we need to transfer the amplitudes across the layer boundaries up to the surface. This can be accomplished by introducing the amplitude ratio

$$R := \frac{\tilde{F}_-}{\tilde{F}_+} \qquad z < z_N, \tag{54}$$

$$R = 0 \qquad z \geq z_N. \tag{55}$$

The first equation also holds for $z \leq 0$ due to the presence of a wave travelling downward from the source. The continuity conditions (49) and (50) for an arbitrary layer boundary $z = z_j$, $j = 0, 1, \ldots, N-1$ therefore are

$$\tilde{F}_+^j \left(\mathrm{e}^{-u_j h_j} + R_j \right) = \tilde{F}_+^{j+1} \left(1 + R_{j+1} \, \mathrm{e}^{-u_{j+1} h_{j+1}} \right), \tag{56}$$

$$u_j \tilde{F}_+^j \left(-\mathrm{e}^{-u_j h_j} + R_j \right) = u_{j+1} \tilde{F}_+^{j+1} \left(-1 + R_{j+1} \, \mathrm{e}^{-u_{j+1} h_{j+1}} \right). \tag{57}$$

Now we divide (56) by (57) and rearrange the expressions

$$u_j \frac{\left(-\mathrm{e}^{-u_j h_j} + R_j\right)}{\left(\mathrm{e}^{-u_j h_j} + R_j\right)} = u_{j+1} \frac{\left(-1 + R_{j+1}\,\mathrm{e}^{-u_{j+1} h_{j+1}}\right)}{\left(1 + R_{j+1}\,\mathrm{e}^{-u_{j+1} h_{j+1}}\right)},$$

$$u_j \left(-\mathrm{e}^{-u_j h_j} + R_j\right)\left(1 + R_{j+1}\,\mathrm{e}^{-u_{j+1} h_{j+1}}\right) = u_{j+1}\left(\mathrm{e}^{-u_j h_j} + R_j\right)\left(-1 + R_{j+1}\,\mathrm{e}^{-u_{j+1} h_{j+1}}\right),$$

$$u_j R_j \left(1 + R_{j+1}\,\mathrm{e}^{-u_{j+1} h_{j+1}}\right) - u_{j+1} R_j \left(-1 + R_{j+1}\,\mathrm{e}^{-u_{j+1} h_{j+1}}\right) = u_j\,\mathrm{e}^{-u_j h_j}\left(1 + R_{j+1}\,\mathrm{e}^{-u_{j+1} h_{j+1}}\right) + u_{j+1}\,\mathrm{e}^{-u_j h_j}\left(-1 + R_{j+1}\,\mathrm{e}^{-u_{j+1} h_{j+1}}\right), \tag{58}$$

separate R_j

$$R_j = \frac{u_j\left(1 + R_{j+1}\,\mathrm{e}^{-u_{j+1} h_{j+1}}\right) + u_{j+1}\left(-1 + R_{j+1}\,\mathrm{e}^{-u_{j+1} h_{j+1}}\right)}{u_j\left(1 + R_{j+1}\,\mathrm{e}^{-u_{j+1} h_{j+1}}\right) - u_{j+1}\left(-1 + R_{j+1}\,\mathrm{e}^{-u_{j+1} h_{j+1}}\right)}\,\mathrm{e}^{-u_j h_j}, \tag{59}$$

$$R_j = \frac{u_j R_{j+1}\,\mathrm{e}^{-u_{j+1} h_{j+1}} + u_j - u_{j+1} + u_{j+1} R_{j+1}\,\mathrm{e}^{-u_{j+1} h_{j+1}}}{u_j R_{j+1}\,\mathrm{e}^{-u_{j+1} h_{j+1}} + u_j + u_{j+1} - u_{j+1} R_{j+1}\,\mathrm{e}^{-u_{j+1} h_{j+1}}}\,\mathrm{e}^{-u_j h_j},$$

$$R_j = \frac{(u_j - u_{j+1}) + (u_j + u_{j+1})\,R_{j+1}\,\mathrm{e}^{-u_{j+1} h_{j+1}}}{(u_j + u_{j+1}) + (u_j - u_{j+1})\,R_{j+1}\,\mathrm{e}^{-u_{j+1} h_{j+1}}}\,\mathrm{e}^{-u_j h_j}, \tag{60}$$

and finally expand by the term $\frac{1}{u_j + u_{j+1}}$

$$R_j = \frac{\dfrac{u_j - u_{j+1}}{u_j + u_{j+1}} + R_{j+1}\,\mathrm{e}^{-u_{j+1} h_{j+1}}}{1 + \dfrac{u_j - u_{j+1}}{u_j + u_{j+1}} R_{j+1}\,\mathrm{e}^{-u_{j+1} h_{j+1}}}\,\mathrm{e}^{-u_j h_j}, \tag{61}$$

an upward-directed recursion for the amplitude ratio $R_j(R_{j+1})$ can be obtained

$$R_j = \frac{r_j + R_{j+1}\,\mathrm{e}^{-u_{j+1} h_{j+1}}}{1 + r_j R_{j+1}\,\mathrm{e}^{-u_{j+1} h_{j+1}}}\,\mathrm{e}^{-u_j h_j}, \tag{62}$$

where

$$r_j = \frac{u_j - u_{j+1}}{u_j + u_{j+1}}, \tag{63}$$

and

$$R_{N-1} = \frac{u_{N-1} - u_N}{u_{N-1} + u_N}\,\mathrm{e}^{-u_{N-1} h_{N-1}}\,. \tag{64}$$

Alternatively, (59) can be substituted into

$$R_j = \frac{u_j a_{j+1} - u_{j+1} b_{j+1}}{u_j a_{j+1} + u_{j+1} b_{j+1}} \, \mathrm{e}^{-u_j h_j}, \tag{65}$$

with

$$a_{j+1} = 1 + R_{j+1} \, \mathrm{e}^{-u_{j+1} h_{j+1}}, \quad \text{and} \quad b_{j+1} = 1 - R_{j+1} \, \mathrm{e}^{-u_{j+1} h_{j+1}} \, . \tag{66}$$

We are now able to write down the resulting wavenumber-domain potentials for $z < 0$ by including (65) and (46) into (43)

$$\begin{aligned} \tilde{F}^0 &= \tilde{F}^0_+ \left[\mathrm{e}^{-u_0 |z+h|} + R_0 \, \mathrm{e}^{u_0 z} \right], \\ &= \frac{\mathrm{i}\omega\mu_0 m}{2} \frac{1}{u_0} \left[\mathrm{e}^{-u_0 |z+h|} + \frac{u_0 a_1 - u_1 b_1}{u_0 a_1 + u_1 b_1} \, \mathrm{e}^{u_0 (z-h)} \right]. \end{aligned} \tag{67}$$

The potential F^0_{tot} can be obtained by the Hankel transformation

$$F^0_{\mathrm{tot}} = \frac{\mathrm{i}\omega\mu_0 m}{4\pi} \int_0^\infty \frac{\lambda}{u_0} \left[\mathrm{e}^{-u_0 |z+h|} + \left(\frac{u_0 a_1 - u_1 b_1}{u_0 a_1 + u_1 b_1} \right) \mathrm{e}^{u_0 (z-h)} \right] J_0(\lambda r) \, \mathrm{d}\lambda, \tag{68}$$

where the coefficients $a_1 = a_1(R_{N-1}, \ldots, R_1)$ and $b_1 = b_1(R_{N-1}, \ldots, R_1)$ have to be evaluated by the recursion introduced in this section.

4.2 Stabilization of the solution F^0 in $z \leq 0$

When the field components $E^0_{\phi,\mathrm{tot}}$ and $H^0_{z,\mathrm{tot}}$ have to be evaluated in $z \leq 0$, the appearance of the coefficient $\frac{\lambda}{u_0}$ in (34) and (68) leads to difficulties in the numerical evaluation of the associated Hankel integrals. These difficulties arise from complex zeros in $u_0 = \sqrt{\lambda^2 - k^2}$. For certain combinations of λ^2 and $k^2 = \omega^2 \mu_0 \epsilon - i\omega\mu_0\sigma$ the real part of u_0 vanishes. To perceptibly reduce that undesired effect, an integration by parts can be applied. Because the primary potential F^* can be expressed analytically by (20) only the secondary part

$$F^0 = \frac{\mathrm{i}\omega\mu_0 m}{4\pi} \int_0^\infty \frac{\lambda}{u_0} \left(\frac{u_0 - u_1 \dfrac{b_1}{a_1}}{u_0 + u_1 \dfrac{b_1}{a_1}} \right) \mathrm{e}^{u_0 (z-h)} \, J_0(\lambda r) \, \mathrm{d}\lambda, \tag{69}$$

has to be considered. At first the term

$$\frac{\lambda}{u_0} \left(\frac{u_0 a_1 - u_1 b_1}{u_0 a_1 + u_1 b_1} \right) = \frac{-\lambda}{u_0} \left(\frac{u_0 a_1 + u_1 b_1 - 2 u_0 a_1}{u_0 a_1 + u_1 b_1} \right) = \underbrace{\frac{2\lambda a_1}{u_0 a_1 + u_1 b_1}}_{\mathbf{A}} - \underbrace{\frac{\lambda}{u_0}}_{\mathbf{B}}, \tag{70}$$

is split into a sum. Because the media 0 and 1 are always expected to be different, the singularity problem is now attached to part **B** only. Hence by making use of

$$-\int_0^\infty x(\lambda) \, \partial_\lambda y(\lambda) \, \mathrm{d}\lambda = -x(\lambda) \, y(\lambda) \Big|_0^\infty + \int_0^\infty \partial_\lambda x(\lambda) \, y(\lambda) \, \mathrm{d}\lambda, \tag{71}$$

with (19), (36), and

$$\begin{aligned} y &\coloneqq \mathrm{e}^{u_0(z-h)} & \partial_\lambda y &= \frac{\lambda(z-h)}{u_0}\,\mathrm{e}^{u_0(z-h)}, \\ x &= \frac{1}{(z-h)}J_0(\lambda r) & \partial_\lambda x &= -\frac{r}{(z-h)}J_1(\lambda r)\,, \end{aligned} \tag{72}$$

(69) can be expressed by

$$\begin{aligned} F^0 = \frac{\mathrm{i}\omega\mu_0 m}{4\pi}\Bigg[&\int_0^\infty \frac{2\lambda a_1}{u_0 a_1 + u_1 b_1}\,\mathrm{e}^{u_0(z-h)}\,J_0(\lambda r)\;\mathrm{d}\lambda \\ &- \int_0^\infty \frac{r}{(z-h)}\,\mathrm{e}^{u_0(z-h)}\,J_1(\lambda r)\;\mathrm{d}\lambda \\ &- \frac{1}{(z-h)}J_0(\lambda r)\,\mathrm{e}^{u_0(z-h)}\Big|_0^\infty\Bigg]. \end{aligned} \tag{73}$$

Here

$$-\frac{1}{(z-h)}J_0(\lambda r)\,\mathrm{e}^{u_0(z-h)}\Big|_0^\infty = -\frac{1}{(z-h)}\,\mathrm{e}^{-k_0(z-h)}, \tag{74}$$

since

$$\begin{aligned} J_0(\lambda) &\to 0 \quad \text{for} \quad \lambda \to \infty, \\ J_0(\lambda) &\to 1 \quad \text{for} \quad \lambda \to 0. \end{aligned} \tag{75}$$

Since the evaluation of (74) is independent of r, it doesn't contribute to the respective field components E_ϕ^0 and H_z^0. The total field components in $z \le 0$ therefore read

$$\begin{aligned} E^0_{\phi,\mathrm{tot}}(r,z) = \frac{-\mathrm{i}\omega\mu_0 m}{4\pi}\Bigg[&\frac{r}{R^3}\left(\mathrm{i}kR+1\right)\mathrm{e}^{-\mathrm{i}kR} \\ &+ \int_0^\infty \frac{2\lambda^2 a_1}{u_0 a_1 + u_1 b_1}\,\mathrm{e}^{u_0(z-h)}\,J_1(\lambda r)\;\mathrm{d}\lambda \\ &+ \int_0^\infty \frac{\lambda r}{(z-h)}\,\mathrm{e}^{u_0(z-h)}\,J_0(\lambda r)\;\mathrm{d}\lambda\Bigg], \end{aligned} \tag{76}$$

$$\begin{aligned} H^0_{z,\mathrm{tot}}(r,z) = \frac{m}{4\pi}\Bigg[&\frac{1}{R^5}\left(2\mathrm{i}kR^3 + \left(k^2r^2+2\right)R^2 - 3\mathrm{i}kr^2R - 3r^2\right)\mathrm{e}^{-\mathrm{i}kR} \\ &+ \int_0^\infty \left(\frac{2\lambda^3 a_1}{u_0 a_1 + u_1 b_1} + \frac{2\lambda}{z-h}\right)\mathrm{e}^{u_0(z-h)}\,J_0(\lambda r)\;\mathrm{d}\lambda \\ &- \int_0^\infty \frac{\lambda^2 r}{(z-h)}\,\mathrm{e}^{u_0(z-h)}\,J_1(\lambda r)\;\mathrm{d}\lambda\Bigg]. \end{aligned} \tag{77}$$

4.3 Evaluation of the potential $\tilde{F}^j$ in the wavenumber domain

Once the recursion (62) for the calculation of the amplitude ratio $R_j(R_{j+1})$ has been carried out, we are able to back propagate the surface amplitude into the ground $z \geq 0$. We arrive at a downward-directed recursion algorithm for the unknown amplitudes $\tilde{F}_+^{j+1}\left(\tilde{F}_+^j\right)$ by solving (56) for $\tilde{F}_+^{j+1}$

$$\tilde{F}_+^{j+1} = \frac{\tilde{F}_+^j\left(\mathrm{e}^{-u_j h_j} + R_j\right)}{\left(1 + R_{j+1}\,\mathrm{e}^{-u_{j+1}h_{j+1}}\right)}, \tag{78}$$

which gives, after exploiting (65),

$$\begin{aligned}
&= \frac{\tilde{F}_+^j\left(1 + \dfrac{u_j a_{j+1} - u_{j+1} b_{j+1}}{u_j a_{j+1} + u_{j+1} b_{j+1}}\right)\mathrm{e}^{-u_j h_j}}{a_{j+1}}, \\
&= \frac{\tilde{F}_+^j\left(\dfrac{2u_j a_{j+1}}{u_j a_{j+1} + u_{j+1} b_{j+1}}\right)\mathrm{e}^{-u_j h_j}}{a_{j+1}}, \\
&= \tilde{F}_+^j \frac{2u_j}{u_j a_{j+1} + u_{j+1} b_{j+1}}\,\mathrm{e}^{-u_j h_j},
\end{aligned} \tag{79}$$

The coefficient $\tilde{F}_-^{j+1}$ can be obtained using the relation (54):

$$\tilde{F}_-^{j+1} = R_{j+1}\tilde{F}_+^{j+1}. \tag{80}$$

To arrive at a compact formulation for the potentials within an arbitrary layer j, i.e., for $z_j < z < z_{j-1}$, we express the recursion (79) for the amplitudes $\tilde{F}_+^j$ as a function of $\tilde{F}_+^1$ and the amplitude decay over each layer, which yields

$$\begin{aligned}
\tilde{F}_+^j &= \frac{\mathrm{i}\omega\mu_0 m}{2u_0}\left(\frac{2u_0\,\mathrm{e}^{-u_0 h}}{u_0 a_1 + u_1 b_1}\right)\cdot\left(\frac{2u_1\,\mathrm{e}^{-u_1 h_1}}{u_1 a_2 + u_2 b_2}\right)\cdot\ldots\cdot\left(\frac{2u_{j-1}\,\mathrm{e}^{-u_{j-1}h_{j-1}}}{u_{j-1}a_j + u_j b_j}\right), \\
&= \tilde{F}_+^0 \cdot \frac{\tilde{F}_+^1}{\tilde{F}_+^0}\cdot\underbrace{\frac{\tilde{F}_+^2}{\tilde{F}_+^1}\cdot\ldots\cdot\frac{\tilde{F}_+^j}{\tilde{F}_+^{j-1}}}_{Q_j},
\end{aligned} \tag{81}$$

introducing the amplitude decay function Q_j

$$Q_j = \prod_{k=2}^{j}\frac{\tilde{F}_+^k}{\tilde{F}_+^{k-1}}, \quad j \geq 2. \tag{82}$$

which finally yields the wavenumber potential at an arbitrary depth $z_{j-1} < z < z_j$ expressing (43) including (54) gives

$$\begin{aligned}
\tilde{F}^j(z) &= \tilde{F}_+^1 Q_j\left[\mathrm{e}^{-u_j(z-z_{j-1})} + R_j\,\mathrm{e}^{u_j(z-z_j)}\right], \\
&= \frac{\mathrm{i}\omega\mu_0 m}{2}\left(\frac{2Q_j}{u_0 a_1 + u_1 b_1}\right)\mathrm{e}^{-u_0 h}\left[\mathrm{e}^{-u_j(z-z_{j-1})} + R_j\,\mathrm{e}^{u_j(z-z_j)}\right].
\end{aligned} \tag{83}$$

4.4 Derivation of $\tilde{F}^j$ from $\tilde{F}^0$

As an alternative way to describe the fields within an arbitrary depth z we can propagate the potential downward. To this end, we do not use the amplitudes $\tilde{F}^j_+$ and $\tilde{F}^j_-$, but rather the expressions for the potentials $\tilde{F}^j$. The basic idea can be described as follows: First, express the potential at depth $z_{j-1} < z < z_j$ by the potential of the layer j at its top boundary $z = z_{j-1}$. Then, starting with the potential at $z = 0$, the potentials at the bottom of each overlying layer can be represented by the potential at the top of this layer. The ratio of the potential $\tilde{F}^{j-1}$ taken at the top and bottom boundary is given by

$$\begin{aligned}\frac{\tilde{F}^{j-1}(z_{j-1})}{\tilde{F}^{j-1}(z_{j-2})} &= \frac{\tilde{F}^{j-1}_+ \,\mathrm{e}^{-u_{j-1}(z_{j-1}-z_{j-2})} + \tilde{F}^{j-1}_- \,\mathrm{e}^{u_{j-1}(z_{j-1}-z_{j-1})}}{\tilde{F}^{j-1}_+ \,\mathrm{e}^{-u_{j-1}(z_{j-2}-z_{j-2})} + \tilde{F}^{j-1}_- \,\mathrm{e}^{u_{j-1}(z_{j-2}-z_{j-1})}} \\ &= \frac{\mathrm{e}^{-u_{j-1}h_{j-1}} + R_{j-1}}{1 + R_{j-1}\,\mathrm{e}^{-u_{j-1}h_{j-1}}}. \end{aligned} \tag{84}$$

The decay within the layer j can be expressed in terms of the potential at the top boundary $z = z_{j-1}$ by

$$\frac{\tilde{F}^j(z)}{\tilde{F}^j(z_{j-1})} = \frac{\tilde{F}^j_+ \,\mathrm{e}^{-u_j(z-z_{j-1})} + \tilde{F}^j_- \,\mathrm{e}^{u_j(z-z_j)}}{\tilde{F}^j_+ \,\mathrm{e}^{-u_j(z_{j-1}-z_{j-1})} + \tilde{F}^j_- \,\mathrm{e}^{u_j(z_{j-1}-z_j)}} = \frac{\mathrm{e}^{-u_j(z-z_{j-1})} + R_j \,\mathrm{e}^{u_j(z-z_j)}}{1 + R_j \,\mathrm{e}^{-u_j h_j}}. \tag{85}$$

Rearranging terms and applying the continuity conditions yields an expression which relates the potential within layer j to the potential at the bottom of the overlying layer

$$\begin{aligned}\tilde{F}^j(z) &= \tilde{F}^{j-1}(z_{j-2})\,\frac{\mathrm{e}^{-u_{j-1}h_{j-1}} + R_{j-1}}{1 + R_{j-1}\,\mathrm{e}^{-u_{j-1}h_{j-1}}} \cdot \frac{\mathrm{e}^{-u_j(z-z_{j-1})} + R_j\,\mathrm{e}^{u_j(z-z_j)}}{1 + R_j\,\mathrm{e}^{-u_j h_j}}, \\ &= \tilde{F}(0) \cdot \underbrace{\frac{\tilde{F}(z_1)}{\tilde{F}(z_0)} \cdot \ldots \cdot \frac{\tilde{F}(z_{j-1})}{\tilde{F}(z_{j-2})}\,\frac{\tilde{F}(z)}{\tilde{F}(z_{j-1})}}_{Z_j(z) \coloneqq \dfrac{\tilde{F}(z)}{\tilde{F}(z_0)}}, \end{aligned} \tag{86}$$

With the abbreviation

$$Z_j(z) = \prod_{k=1}^{j-1} \frac{\tilde{F}(z_k)}{\tilde{F}(z_{k-1})}\,\frac{\tilde{F}(z)}{\tilde{F}(z_{j-1})}, \quad j \geq 2. \tag{87}$$

we are able to relate $\tilde{F}^j(z)$ to its surface value $\tilde{F}(0)$ at $z = 0$:

$$\begin{aligned}\tilde{F}^j(z) &= \frac{\mathrm{i}\omega\mu_0 m}{2}\frac{1}{u_0}\left[1 + \frac{u_0 a_1 - u_1 b_1}{u_0 a_1 + u_1 b_1}\right]\mathrm{e}^{-u_0 h}\, Z_j(z)\,, \\ &= \frac{\mathrm{i}\omega\mu_0 m}{2}\left(\frac{2Z_j(z)}{u_0 + u_1\frac{b_1}{a_1}}\right)\mathrm{e}^{-u_0 h}\,. \end{aligned} \tag{88}$$

Finally, we obtain the potential in the spatial domain by a Hankel transform. For an arbitrary depth $z \geq 0$ it reads

$$F^j_{\mathrm{tot}}(r,z) = \frac{\mathrm{i}\omega\mu_0 m}{4\pi}\int_0^\infty \left(\frac{2\lambda Z_j}{u_0 + u_1\dfrac{b_1}{a_1}}\right)\mathrm{e}^{u_0(z-h)}\, J_0(\lambda r)\,\mathrm{d}\lambda. \tag{89}$$

Note that $Z_j = Z_j(z)$ which has to be taken into account when deriving the H_r field component from (8).

4.5 Consistency checks

In this section we show that the results derived in the preceding two sections are consistent. We will restrict ourselves to the case $N = 2$, i.e., a two-layer case with one boundary separating two infinitely thick layers at $z = 0$. As introduced above, the VMD is located at $z = -h$, $h > 0$. In this case $R_1 = 0$ and

$$R_0 = r_0 \, \mathrm{e}^{-u_0 h} \, . \tag{90}$$

Solving (54) for the unknown coefficient $\tilde{F}_-^0$ yields for $z = 0$

$$\tilde{F}_-^0 = r_0 \, \mathrm{e}^{-u_0 h} \, \tilde{F}_+^0 = \frac{\mathrm{i}\omega\mu_0 m}{2} \frac{1}{u_0} \frac{u_0 - u_1}{u_0 + u_1} \, \mathrm{e}^{-u_0 h}, \tag{91}$$

which agrees with (31). Similarly, from (51), we obtain for $z = 0$

$$\tilde{F}_+^1 = \tilde{F}_+^0 \, \mathrm{e}^{-u_0 h_0} + \tilde{F}_-^0 = \frac{\mathrm{i}\omega\mu_0 m}{2} \frac{1}{u_0} \left[\frac{u_0 - u_1}{u_0 + u_1} + 1 \right] \mathrm{e}^{-u_0 h} = \frac{\mathrm{i}\omega\mu_0 m}{2} \frac{2}{u_0 + u_1} \, \mathrm{e}^{-u_0 h}, \tag{92}$$

which is consistent with the result given in (32).
We now turn to the results given in Section 4.3 and Section 4.4.
With

$$\frac{\tilde{F}_+^j}{\tilde{F}_+^{j-1}} = \frac{2u_{j-1} \, \mathrm{e}^{-u_{j-1} h_{j-1}}}{u_{j-1} a_j + u_j b_j} = \frac{2u_{j-1} \, \mathrm{e}^{-u_{j-1} h_{j-1}}}{u_{j-1} + u_j \dfrac{b_j}{a_j}} \frac{1}{a_j} = \frac{\mathrm{e}^{-u_{j-1} h_{j-1}} + R_{j-1}}{a_j}, \tag{93}$$

The amplitude decay function defined in (82) can be modified such that

$$Q_j^* = \prod_{k=2}^{j} \frac{1}{a_{k-1}} \frac{\tilde{F}_+^k}{\tilde{F}_+^{k-1}} \frac{a_k}{1}, \tag{94}$$

which, inserted in (83), leads to

$$\tilde{F}^j(z) = \frac{\mathrm{i}\omega\mu_0 m}{2} \left(\frac{2Q_j^*}{u_0 + u_1 \dfrac{b_1}{a_1}} \right) \mathrm{e}^{-u_0 h} \, \frac{\left[\mathrm{e}^{-u_j (z - z_{j-1})} + R_j \, \mathrm{e}^{u_j (z - z_j)} \right]}{a_j}. \tag{95}$$

It holds for the ratio of the potentials at two adjacent boundaries z and z_{j-1}, that, according to (84),

$$\frac{\tilde{F}^j(z_j)}{\tilde{F}^j(z_{j-1})} = \frac{\mathrm{e}^{-u_j h_j} + R_j}{1 + R_j \, \mathrm{e}^{-u_j h_j}} = \frac{\mathrm{e}^{-u_j h_j} + R_j}{a_j}, \tag{96}$$

We define a decay function similar to Z_j which resembles Q_j^*

$$Z_j^* = \prod_{k=1}^{j-1} \frac{\tilde{F}(z_k)}{\tilde{F}(z_{k-1})} \stackrel{!}{=} Q_j^* \tag{97}$$

It can be shown that (88) now reads

$$\tilde{F}^j(z) = \frac{\mathrm{i}\omega\mu_0 m}{2} \left(\frac{2Z_j^*}{u_0 + u_1 \dfrac{b_1}{a_1}} \right) \mathrm{e}^{-u_0 h} \, \frac{\left[\mathrm{e}^{-u_j (z - z_{j-1})} + R_j \, \mathrm{e}^{u_j (z - z_j)} \right]}{a_j}. \tag{98}$$

References

Abramowitz, M. and Stegun, I. A. (1972). Handbook of Mathematical Functions with Formulas, Graphs, and Mathematical Tables. 10th edition. Dover Publications.

Ward, S. H. and Hohmann, G. W. (1988). "Electromagnetic Theory for Geophysical Applications". *Electromagnetic Methods in Applied Geophysics*. Edited by M. N. Nabighian. Volume 1. Investigations in Geophysics 3. Society of Exploration Geophysicists, pages 130–311.

Zhdanov, M. S. (2009). Geophysical Electromagnetic Theory and Methods. 1st edition. Elsevier.

Regularization on unstructured grids

Julia Weißflog[1], Felix Eckhofer[2], Ralph-Uwe Börner[1], Michael Eiermann[2], Oliver G. Ernst[2], Klaus Spitzer[1]

[1]Institute of Geophysics and Geoinformatics
[2]Institute of Numerical Mathematics and Optimization
TU Bergakademie Freiberg (Germany)

1 Introduction

The Geotechnologien project Multi-EM addresses the combination of different electromagnetic methods in a joint inversion approach to exploit their individual advantages. In Freiberg, we focus on the combination of the transient electromagnetic (TEM) and the DC resistivity method.
We have implemented a new DC resistivity forward operator in MATLAB using finite elements on unstructured tetrahedral grids that can easily be combined with our already existing TEM software (Afanasjew et al., 2010). This code enables us to deal with even complex topography and to extract the derivatives, which are crucial for the inversion while retaining full control over the assembly process of the system matrix (Weißflog et al., 2012).
For simplicity, we apply a regularized Gauss-Newton method in view of a combination of different electromagnetic methods in one inversion algorithm. We focus on an appropriate regularization technique that has been outlined in (Schwarzbach & Haber, 2013).

2 3D DC resistivity modeling

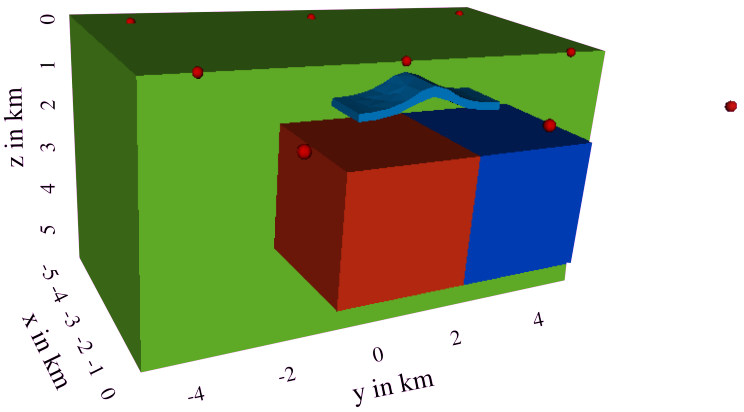

Figure 1: Synthetic model: $\sigma_1 = 0.1\,\frac{\mathrm{S}}{\mathrm{m}}$ (green), $\sigma_2 = 0.01\,\frac{\mathrm{S}}{\mathrm{m}}$ (top blue), $\sigma_3 = 1\,\frac{\mathrm{S}}{\mathrm{m}}$ (red) and $\sigma_4 = 0.002\,\frac{\mathrm{S}}{\mathrm{m}}$ (bottom blue).

DC resistivity modeling requires the discretization of the equation of continuity:

$$-\nabla \cdot (\sigma \nabla \phi) = I\delta(\boldsymbol{x} - \boldsymbol{x}_0), \tag{1}$$

with ϕ as the electric potential, a given distribution of conductivity $\sigma(\boldsymbol{x})$ and a point source of strength I located at $\boldsymbol{x}_0 \in \mathbb{R}^3$.
Figure 1 shows a conductivity model for the Multi-EM project, currently used in Freiberg for DC inversion. The red dots mark source positions, see "Numerical Experiments".

3 Smoothness regularization

We use $\boldsymbol{m} = \ln(\boldsymbol{\sigma})$ to avoid problems with negative parameter values. For the inversion process, a minimization problem which combines the residual norm and a regularization operator $R(\boldsymbol{m})$ has to be solved:

$$\Phi(\boldsymbol{m}) = \|Q\boldsymbol{u} - \boldsymbol{b}\|_2^2 + \beta R(\boldsymbol{m} - \boldsymbol{m}_{\text{ref}}) \rightarrow \min_{\boldsymbol{m}} \tag{2}$$

subject to $A(\boldsymbol{m})\boldsymbol{u} = \boldsymbol{f}$. Here, $\boldsymbol{b}$ is the measured data, $\boldsymbol{u} = A(\boldsymbol{m})^{-1}\boldsymbol{f}$ the modeled data, $\boldsymbol{m}$ are the model parameters, Q is some measurement operator ($Q\boldsymbol{u} \approx \boldsymbol{b}$), $\boldsymbol{m}_{\text{ref}}$ is the reference model and β represents the regularization parameter.
To stabilize the inversion procedure and provide additional information to avoid ambiguities, a suitable regularization strategy is necessary. As our inversion approach is based on a finite element discretization of the potential equation (1) using a piecewise constant representation of the conductivity model, this requires a regularization operator $R(\boldsymbol{m})$ applicable to piecewise constant model parameters on unstructured grids and weak formulations. We have implemented a smoothness regularization in which the penalty function measures the norm of a weak gradient of the conductivity field:

$$R(\boldsymbol{m}) = \int_\Omega \nabla \boldsymbol{m} \cdot \nabla \boldsymbol{m} \, dV. \tag{3}$$

As laid out in (Brezzi & Fortin, 1991) we derive the mixed formulation of (2) incorporating (3):

$$\Phi(\boldsymbol{m}, \boldsymbol{u}) = \; F(\boldsymbol{m}) - \beta \int_\Omega |\boldsymbol{u}|^2 \, dV + 2\beta \int_\Omega (\boldsymbol{m} - \boldsymbol{m}_{\text{ref}}) \nabla \cdot \boldsymbol{u} \, dV, \tag{4}$$

with $F(\boldsymbol{m}) = \|Q\boldsymbol{u} - \boldsymbol{b}\|_2^2$ being the residual norm, $\boldsymbol{m} \in L^2(\Omega)$ and $\boldsymbol{u} \in H_0(\text{div}; \Omega) = \{\boldsymbol{u} \in L^2(\Omega)^3; \nabla \cdot \boldsymbol{u} \in L^2(\Omega); \boldsymbol{n} \cdot \boldsymbol{u}|_{\partial\Omega}\}$. To achieve a conformal discretization we use Raviart-Thomas elements of lowest order (RT_0). This ensures continuity of normal components between elements. A discrete representation of (4) then reads:

$$\Phi(\boldsymbol{m}, \boldsymbol{u}) = \; F(\boldsymbol{m}) - \beta \boldsymbol{u}^T M \boldsymbol{u} \; + 2\beta (\boldsymbol{m} - \boldsymbol{m}_{\text{ref}})^T D \boldsymbol{u}. \tag{5}$$

M is the RT_0 mass matrix and D is the discrete divergence operator. The RT_0 basis functions are vector-valued. Figure 2 shows the three functions for the reference triangle, each belonging to one edge of the triangle. The basis functions have a normal component of one on the associated edge and on the other two edges, the normal component is zero and there are only tangential components.
In order to minimize (5) the gradient of $\Phi(\boldsymbol{m}, \boldsymbol{u})$ with respect to $\boldsymbol{u}$ must vanish:

$$-2\beta M \boldsymbol{u} + 2\beta D^T (\boldsymbol{m} - \boldsymbol{m}_{\text{ref}}) = \boldsymbol{0} \Rightarrow \boldsymbol{u} = M^{-1} D^T (\boldsymbol{m} - \boldsymbol{m}_{\text{ref}}). \tag{6}$$

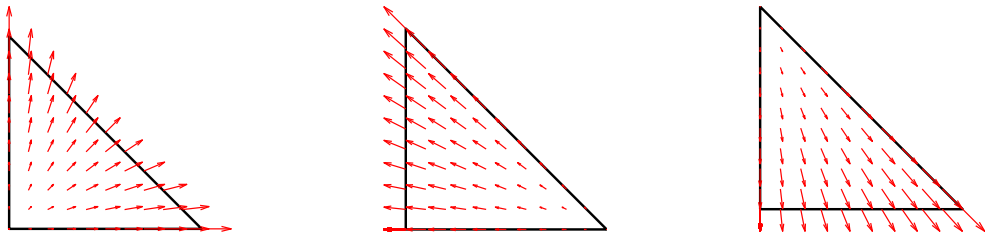

Figure 2: RT_0 basis functions in 2D

Using condition (6) we eliminate the dual variable and arrive at the final objective function:

$$\Phi(\boldsymbol{m}) = F(\boldsymbol{m}) + \beta(\boldsymbol{m} - \boldsymbol{m}_{\text{ref}})^T D M^{-1} D^T (\boldsymbol{m} - \boldsymbol{m}_{\text{ref}}) \to \min_{\boldsymbol{m}}. \tag{7}$$

Applying a Gauss-Newton scheme to solve this non-linear least squares problem enables us to linearize $\Phi(\boldsymbol{m})$. The resulting linear problem can then be solved, e.g. by an iterative Krylov subspace method, to find a better approximation to the model parameters $\boldsymbol{m}$ in each Gauss-Newton step.

4 Algebraic multigrid

To solve the forward problems $\boldsymbol{u} = A(\boldsymbol{m})^{-1}\boldsymbol{f}$ we chose to use an algebraic multigrid (AMG) solver to take advantage of the good scaling properties of this method. We integrated HSL-MI20 (Boyle, Mihajlović, & Scott, 2007) from the HSL Mathematical Software Library into our code and observed the expected $\mathcal{O}(N)$ behavior.
The following figure compares the running time of MATLAB's backslash operator with the AMG code. The first AMG variant uses a simple V-cycle iteration $\boldsymbol{u}_{k+1} = \boldsymbol{u}_k + P^{-1}(\boldsymbol{f} - A\boldsymbol{u}_k)$, while the second variant uses the matrix of a single V-cycle P^{-1} as preconditioner for CG.

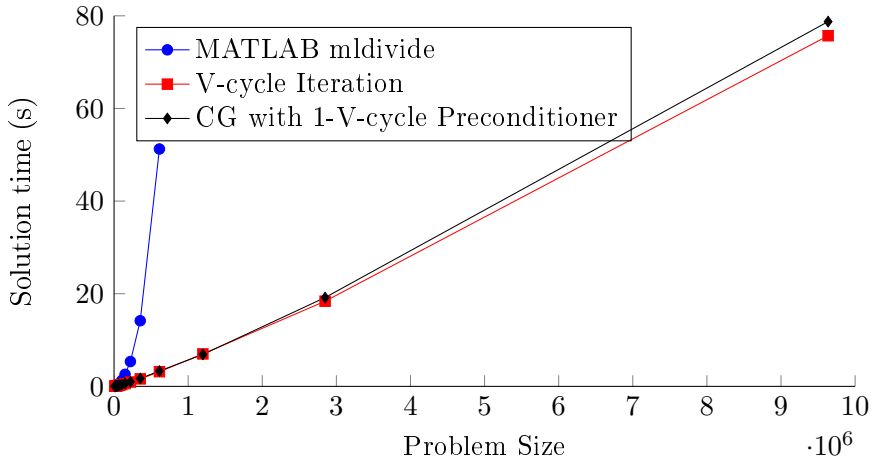

Figure 3: Solution times for the discretized problem from Figure 1 on an Intel Xeon CPU E5-4620 2.20GHz

5 Numerical experiments

To judge the effectiveness of our regularization approach, we tried to reconstruct the model shown in Figure 1 from synthetic data.
As reference model $\boldsymbol{m}_{\text{ref}}$ we chose a homogeneous conductivity of $\sigma = 0.1\,\frac{\text{S}}{\text{m}}$, which is equal to the conductivity at the sources. This is also what we used as our starting model $\boldsymbol{m}_0$. The model was coarsely discretized into about 13 000 elements and allowed the parameter $\boldsymbol{m}$ to vary on each tetrahedron. We present one inversion result for nine sources located on the earth's surface. Each source generates about 250 data points.
The regularization parameter β was chosen to be $\beta = 10^{-14}$ and the iteration terminated once we reached a residual norm of 10^{-7}.

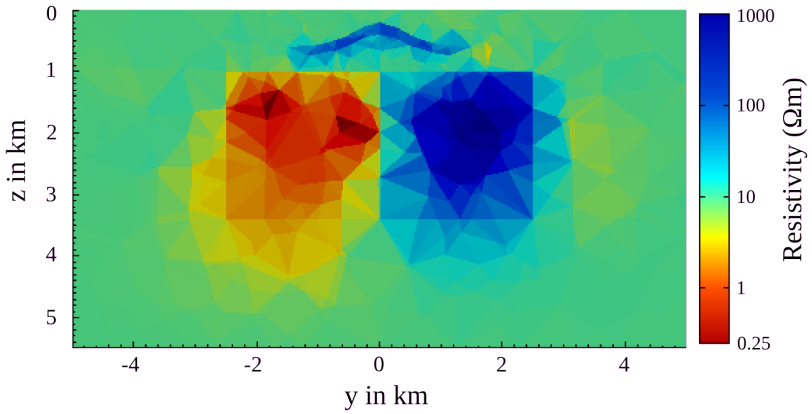

Figure 4: Inversion result for the nine sources shown in Figure 1

Figure 4 shows a frontal slice of the inversion result at $x = 0\,\text{m}$. Even with a small value of β the regularization operator stabilized the iteration and guaranteed the convergence of the Gauss-Newton scheme.
As the number of sources is increased, the reconstruction of embedded conductive or resistive bodies becomes progressively more accurate.

6 Conclusion

With the regularization based on weak gradients and the AMG solver we have completed the last two building blocks for our state-of-the-art 3D DC resistivity inversion code based on finite elements. We will now proceed to combine this software with the other methods from the Multi-EM project in an effort to create a joint inversion scheme.

7 Acknowledgements

This project is funded by the German Ministry of Education and Research (BMBF) and the German Research Foundation (DFG) under the Geotechnologien Programme, grant 03G0746A,B.

References

Afanasjew, M., Börner, R.-U., Eiermann, M., Ernst, O. G., Güttel, S., & Spitzer, K. (2010, Sep 18 – 24, 2010, Giza, Egypt). 2D Time Domain TEM Simulation Using Finite Elements, an Exact Boundary Condition, and Krylov Subspace Methods, Extended Abstract. *Proceedings:* 20^{th} *International Workshop on Electromagnetic Induction in the Earth*.

Boyle, J., Mihajlović, M. D., & Scott, J. A. (2007). *Hsl mi20: an efficient amg preconditioner*.

Brezzi, F., & Fortin, M. (1991). *Mixed and hybrid finite elements methods*. Springer-Verlag.

Schwarzbach, C., & Haber, E. (2013). Finite element based inversion for time-harmonic electromagnetic problems. *Geophysical Journal International*, *193*(2), 615-634.

Weißflog, J., Eckhofer, F., Börner, R.-U., Eiermann, M., Ernst, O. G., & Spitzer, K. (2012, Aug 25 – 31, 2012, Darwin, Australia). 3D DC resistivity FE modelling and inversion in view of a parallelised Multi-EM inversion approach, Extended Abstract. *Proceedings:* 21^{st} *Electromagnetic Induction Workshop*.

Elektromagnetische Explorations- und Überwachungsmethoden in der Geothermie

Jana Börner[1], Matthias Bär[1] und Klaus Spitzer[1]

[1]*Institut für Geophysik und Geoinformatik*
Technische Universität Bergakademie Freiberg

1 Zusammenfassung

Geophysikalische Verfahren liefern einen unverzichtbaren Beitrag zur Erkundung und Überwachung von Geotechnologien wie der Tiefengeothermie, da sie nicht-invasiv große Bereiche des Erdinneren strukturell und stofflich charakterisieren können. Elektromagnetische Methoden sind dabei von großer Bedeutung, da sie sensitiv auf die Porenraumfüllung der Gesteine reagieren. Wir stellen eine Methodik vor, wie mit Hilfe virtueller Experimente elektromagnetische Messungen für das Monitoring eines stimulierten geothermischen Kluftsystems konfiguriert werden können. Dazu werden bestehende 3D-Modelle des Untergrundes als Geometrie eingebunden und für Finite-Elemente-Simulationen verwendet. Exemplarisch stellen wir Berechnungen transientelektromagnetischer Felder für den geplanten Tiefengeothermiestandort am Roten Kamm bei Schneeberg (Sachsen) vor. Wir zeigen, dass mit einer Quelle an der Erdoberfläche und einem Empfänger im Bohrloch Änderungen im Messsignal, hervorgerufen durch das stimulierte Kluftsystem in mehr als 5000 m Tiefe, von etwa 25% erwartet werden können.

2 Einführung

Bei der Geothermie bestehen neben der strukturellen Abbildung der geologischen Einheiten im Untergrund, wofür seismische Verfahren besonders geeignet sind, zusätzliche Fragestellungen z.B. hinsichtlich Porosität und Klüftigkeit des Gesteins, Wassergehalt und -zusammensetzung in potentiellen Reservoiren. Unter diesen Gesichtspunkten stellen elektromagnetische Methoden eine entscheidende Ergänzung zu seismischen Verfahren dar, vor allem da sie hochsensitiv auf Änderungen in der Porenfüllung der Gesteine reagieren. Der spezifische elektrische Widerstand eines Gesteines wird durch das Archie-Gesetz beschrieben (Archie, 1942). Es sagt aus, dass der Gesteinswiderstand direkt proportional zum spezifischen elektrischen Widerstand der Porenfüllung und der Wassersättigung ist. So können elektromagnetische Methoden einen entscheidenden Beitrag zur Überwachung von Geotechnologien wie der Tiefengeothermie oder der CO_2-Verpressung liefern (Börner et al., 2013). Entscheidend für ein robustes und sensitives Monitoring von Reservoiren in großer Tiefe ist jedoch die optimale Konfiguration des Messaufbaus. Diese ist methodenabhängig und standortspezifisch.
Virtuelle Experimente ermöglichen, das Verhalten und die Sensitivität einer geophysikalischen Methode im Vorfeld zu studieren und den Messaufbau zu optimieren. Um belastbare und realitätsnahe Ergebnisse zu erhalten müssen neben angepassten numerischen

Simulationsmethoden vor allem die petrophysikalischen Gesteinsparameter wirklichkeitsnah gewählt werden und die reale Geologie muss hinreichend korrekt abbildet werden. Wir stellen daher exemplarisch das Vorgehen und die Ergebnisse eines virtuellen transientelektromagnetischen Experimentes am zukünftigen Geothermiestandort am Roten Kamm bei Schneeberg vor.

3 Einbindung und Vernetzung von geologischen 3D-Modellen

Im vergangenen Jahrzehnt sind zahlreiche 3D-Modelle des geologischen Untergrundes von Deutschland erarbeitet worden. Diese Modelle beschreiben sowohl den geologischen Aufbau als auch hydrogeologische und geothermische Ressourcen und liegen gewöhnlich im Format der Paradigm® Programme Gocad® oder Skua® vor. Dabei werden die vorhandenen geologischen Informationen zusammengeführt und die Grenzen zwischen geologischen Einheiten in Form von triangulierten Flächen im dreidimensionalen Raum beschrieben.
Mit Hilfe eines Plugins (Zehner, 2011) werden diese Flächen an eine Softwareumgebung zur Geometriebearbeitung und Vernetzung exportiert – hier Ansys Workbench®. Dort werden die Triangulationen in Freiformflächen (z.B. non-uniform rational B-splines – NURBS) umgewandelt und mittels Geometrieoperationen Körper der geologischen Einheiten erstellt, die den mathematischen Anforderungen der nachfolgenden Vernetzung genügen. Die fertige Geometrie wird mit einem unstrukturierten Tetraedergitter vernetzt, dessen lokale Feinheit an die geologischen Charakteristika des Modells, die Materialeigenschaften und die geophysikalische Methode angepasst wird.

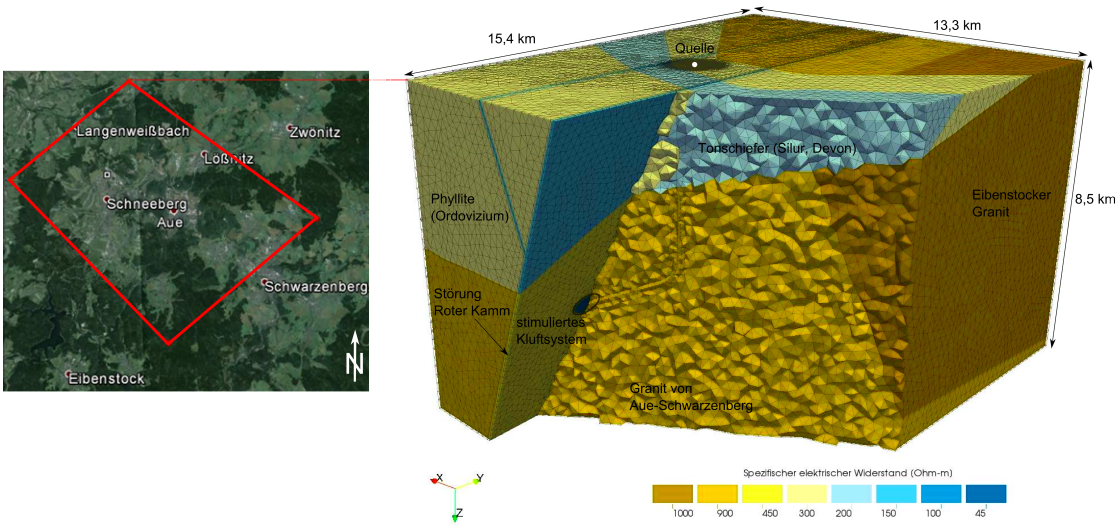

Abb. 1: Lageplan und dreidimensionale Darstellung des vernetzten Modells. Lokale Netzverfeinerungen wurden an der Quelle und um das Kluftsystem angebracht. Die Farben der geologischen Einheiten bezeichnen den spez. el. Widerstand.

4 Geologie und Modell

Als Beispiel für die Planung und Optimierung eines transientelektromagnetischen Monitorings mit Hilfe virtueller Experimente dient der potentielle Standort für die Tiefengeothermie in Sachsen nahe Schneeberg (siehe Abb. 1, links; Reich, 2013). Von der Region Schneeberg wurde vom Landesamt für Umwelt, Landwirtschaft und Geologie (LfULG) des Landes Sachsen ein geologisches 3D-Modell zur Verfügung gestellt. Dieses 3D-Modell wurde wie oben beschrieben in eine vernetzbare Geometrie überführt (Abb. 1 rechts). Die Flächen der Störungen Roter Kamm und Schwerin wurden zu 100 m mächtigen Zonen erweitert (angelehnt an Kuschka, 1989). Die elektromagnetische Quelle (VMD) befindet sich an der Erdoberfläche und wird fein vernetzt. Symmetrisch um den Landepunkt der Erkundungsbohrung in ca. 5300 m Tiefe wurde zur Simulation eines stimulierten Kluftsystems ein ellipsenförmiger Teil des Roten Kammes von 1,2 x 0,5 km Größe abgetrennt (Landesamt für Umwelt, Landwirtschaft und Geologie, 2010). Das resultierende Tetraedergitter beinhaltet 1,33 Millionen Freiheitsgrade für die Simulation.
Die spezifischen elektrischen Gesteinswiderstände wurden mit Hilfe von Literaturwerten (Schön, 1996) und dem Archie-Gesetz abgeschätzt (Archie, 1942). Die mechanisch beanspruchten Störungszonen zeichnen sich durch eine erhöhte Porosität aus. Für ein hydraulisch gut permeables stimuliertes Kluftsystem gehen wir von einer Porositätserhöhung auf etwa 12% aus. Der stimulierte Bereich des Roten Kammes hebt sich so durch einen etwa um Faktor 10 geringeren Widerstand von der umgebenen Störungszone ab.

5 Virtuelles TEM-Experiment

Für das so vorbereitete Modell wurden die transientelektromagnetischen Felder für zwei Fälle berechnet:

- Keine Stimulierung des Kluftsystems hat stattgefunden. Dazu wird der gesamte tiefe Rote Kamm mit einem einheitlichen spez. el. Widerstand belegt. Diese Berechnung liefert die Hintergrundantwort.
- Eine Stimulierung hat stattgefunden und das Kluftsystem weist den beschriebenen verringerten Widerstand auf. In Relation zur Hintergrundantwort zeigt diese Berechnung, ob ein stimuliertes Kluftsystem einen Einfluss auf die transientelektromagnetischen Felder hat und wenn ja, ob dieser Einfluss messbar wäre.

Für die Berechnungen wurde der Finite-Elemente-Simulationscode von Martin Afnanasjew (Afanasjew et al., 2013) verwendet. Als Berechnungsergebnis erhält man den Vektor des elektrischen Feldes $\mathbf{e}$ im gesamten Simulationsgebiet. Durch Anwendung des Rotationsoperators auf $\mathbf{e}$ ergibt sich auch der Vektor der Zeitableitung der magnetischen Flussdichte $\dot{\mathbf{b}}$, der direkt proportional zur Messspannung ist. Alle Größen werden für mehrere Zeitpunkte bis zu einer Sekunde nach dem Abschalten des VMDs berechnet.
Die Betrachtung von $\dot{\mathbf{b}}$ erlaubt Rückschlüsse darauf, wie groß das Messsignal an einem beliebigen Punkt im Simulationsgebiet ist und ob durch das stimulierte Kluftsystem ein lokal hinreichend hoher Unterschied in der Messspannung entsteht, sodass ein Empfänger an dieser Stelle zur Überwachung beitragen könnte.

6 Ergebnisse und Diskussion

Das berechnete Stromsystem weist eine charakteristische Ringform auf und propagiert mit der Zeit in die Tiefe, wobei es sich lateral ausbreitet und an Magnitude verliert. Die Ausbreitung des Stromsystems hängt wesentlich vom spez. el. Widerstand des Gesteins ab. Die in dem hier berechneten Modell überwiegenden hohen Widerstände bewirken eine schnelle und effektive Ausbreitung des Stromsystems in die Tiefe mit verhältnismäßig geringer Dissipation.
Entscheidend für die Messung ist die erreichte Messspannung an einem potentiellen Empfänger. Abbildung 2 zeigt daher, welche prozentuale Änderung das stimulierte Kluftsystem gegenüber dem ungestörten Hintergrundmodell bewirkt. Die Änderung ist 2 ms nach dem Abschalten des VMDs dargestellt. Zu etwa diesem Zeitpunkt passiert das Stromsystem den Bereich um das Kluftsystem. Informationen über das Kluftsystem sind daher auch nur in diesem Zeitfenster zu erwarten. Deutlich früher bzw. deutlich später ist kein Einfluss des Kluftsystems mehr sichtbar.

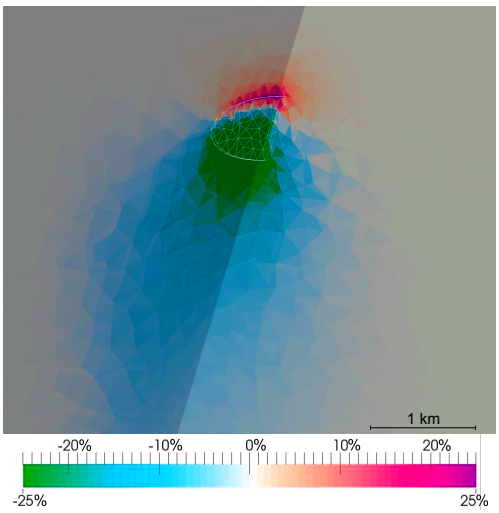

Abb. 2: Prozentuale Änderung von $\dot{\mathbf{b}}$ (entspricht der prozentualen Änderung der Messspannung) hervorgerufen durch das stimulierte Kluftsystem 2 ms nach dem Ausschalten des Stromes in der Sendespule.

Zu dem dargestellten sensitiven Zeitpunkt sieht man einen deutlich den Einfluss des Kluftsystem, der über die geometrische Begrenzung des stimulierten Gebietes weit hinausgeht. Oberhalb des stimulierten Bereiches zeigt sich eine Zone mit um bis zu 25% erhöhtem Messsignal. Kontraste in dieser Größenordnung wären zuverlässig messbar. Unterhalb bildet sich eine deutlich größere Zone mit bis zu 30% verringerten Messwerten. Dies ist dadurch zu erklären, dass das gut leitfähige stimulierte Kluftsystem das Stromsystem stärker hält und dämpft. Als logische Konsequenz entsteht unterhalb des Kluftsystems ein verarmter Bereich. Für die hier exemplarisch gewählte Quellposition wäre also ein unterhalb des Kluftsystems im Roten Kamm platzierter Empfänger besonders sensitiv. Entlang des Erkundungsbohrloches prognostiziert die Simulation Veränderungen von nur $\pm 10\%$. Hier zeigt sich, dass die Position des VMDs nicht optimal gewählt ist, wenn ein Bohrlochempfänger (vergl. Abb. 1) an das Erkundungsbohrloch gebunden wäre. Mit Hilfe weiterer Berechnungen kann die Quellposition optimiert werden. Es wäre dem Messsignal zuträglich, wenn sich das stimulierte Kluftsystem etwa zwischen Quelle und Empfänger befinden würde.

7 Fazit

Unsere Untersuchungen zeigen, dass elektromagnetische Methoden einen Beitrag zur Überwachung von stimulierten Kluftsystemen für die Tiefengeothermie leisten können. Die präsentierten Berechnungen auf Basis des realitätsnahen geologischen Modells prognostizieren einen deutlichen Einflussbereich für transientelektromagnetische Messungen um das stimulierte Kluftsystem mit deutlichen Kontrasten von etwa 25%. Es wird ebenfalls deutlich, dass ein so tiefes Erkundungsziel nur mittels eines Empfängers im Bohrloch aufgelöst werden kann.
Zum anderen erweisen sich realitätsnahe virtuelle Experimente als kostengünstiges und aussagekräftiges Instrument für die Planung und Optimierung von Erkundungs- und Überwachungsvorhaben. Für das hier vorgestellte Szenario könnte so eine optimale Quellposition gefunden werden. Die hier vorgestellte Methodik ist auf die meisten Fragestellungen, Standorte und geophysikalischen Verfahren anwendbar und bietet daher großes Potenzial.

8 Danksagung

Die Autoren bedanken sich beim Sächsischen Landesamt für Umwelt, Landwirtschaft und Geologie (LfULG), speziell Sascha Görne, für die Zusammenarbeit und das zur Verfügung gestellte 3D-Modell. Weiterhin danken wir Martin Afanasjew für die Bereitstellung des TEM-Simulationscodes, sowie Dr. Björn Zehner für das Gocad® und Skua® Plugin.

Referenzen

Afanasjew, M., Börner, R.-U., Eiermann, M., Ernst, O., & Spitzer, K. (2013, Oct 10 - 12). *Efficient three-dimensional time domain TEM simulation using finite elements, a nonlocal boundary condition, multigrid, and rational krylov subspace methods.*

Archie, G. E. (1942). The electrical resistivity log as an aid in determining some reservoir characteristics. *Trans. Americ. Inst. Mineral. Met.*, *146*(146), 54–62.

Börner, J. H., Herdegen, V., Repke, J.-U., & Spitzer, K. (2013). The impact of CO_2 on the electrical properties of water bearing porous media - laboratory experiments with respect to carbon capture and storage. *Geophysical Prospecting*, *61*, 446 - 460.

Kuschka, E. (1989). Zur Tektonik der Spatgänge führenden Bruchstrukturen im paläogeographieozoischen Grundgebirge Südwest- und Mittelsachsens / Versuch einer Klassifikation tektonischer Bruchzonen und Störungssysteme mit Bewertung ihrer Perspektivität auf Fluorit- und Barytlagerstätten. *Z. Geol. Wiss.*, *17*(5), 445-462.

Landesamt für Umwelt, Landwirtschaft und Geologie. (2010). *Forschungsbericht Tiefengeothermie Sachsen, 1. Arbeitsetappe 09/2009 - 07/2010* (Tech. Rep.).

Reich, M. (2013). *Tiefengeothermie in Deutschland, Bohrtechnische Erschließung regenerativer Lagerstätten.* Berg- und Hüttenmännischer Tag, 12.06.2013 Freiberg, Deutschland.

Schön, J. (1996). *Physical properties of rocks - fundamentals and principles of petrophysics* (1 ed., Vol. 18). Pergamon.

Zehner, B. (2011). *Constructing geometric models of the subsurface for finite element simulation.* Conference of the International Association of Mathematical Geosciences (IAMG 2011), Salzburg, Austria, 5th-9th September 2011.

RMS – Rather Meaningless Simplification?

Grayver, A.V., Tietze, K and Ritter, O.
Helmholtz-Centre Potsdam - GFZ German Research Centre for Geosciences
{agrayver | ktietze | oritter}@gfz-potsdam.de

Abstract

For a long time the root mean square (RMS) error has been used in the EM community:

- to characterize data fit for a particular model;
- as a criterion to compare several models obtained from inversion.

The RMS error appears to be a natural choice since we usually tackle inverse problems in a least-squares sense. Over the years, RMS became a customary criterion and gained ultimate significance. However, on the hunt for low RMS values, one often needs to introduce subjectivity by arbitrarily adjusting error floors or masking "bad" data without referring to the assumptions behind RMS. In this contribution, we revisit basic assumptions behind RMS, demonstrate its deficiency and propose alternative ways, which may provide more insight into our data and allow a more comprehensive assessment of the quality of the modelling result/resistivity model.

Definition of RMS

Let ϕ_d denote the data misfit calculated as

$$\phi_d = \sum_i^N r_i^2, \tag{1}$$

where normalized residuals *r* are:

$$r_i = \frac{d_i^{pred} - d_i^{obs}}{e_i}; \quad i = 1 \dots N. \tag{2}$$

Vectors $\boldsymbol{d}^{pred}, \boldsymbol{d}^{obs} \in \mathbb{R}^N$ represent predicted and observed data, respectively, and $\boldsymbol{e}$ is the vector of the estimated data errors (e.g., standard deviations). Assuming that the residuals in equation (2) are zero-mean normal independent random variables, ϕ_d is an asymptotically χ2-distributed random variable with expected value $E[\phi_d]$ = N. This immediately brings us to the well-known expression

$$\text{RMS} = \sqrt{\frac{\phi_d}{N}}. \tag{3}$$

If the majority of the predicted data are within the data error bounds, RMS ≈ 1.

Deficiency of RMS

The RMS error is based on several assumptions which can be violated in real-world problems: we assume that (i) our error estimations in (2) are correct and (ii) the residuals are zero-mean Gaussian independent random variables.

Ideally, one should be able to obtain good estimates for the standard deviations from data processing. In practice, however, standard deviations obtained from data processing have other shortcomings. For instance, a large number of observations are usually available for

high frequency data, but very few for low frequency measurements. Thus, data variances usually increase with period length. Data points can be strongly biased but with very small uncertainty. Normally noise affects all input- and output channels thereby violating underlying assumptions for our data processing. More uniform data quality can be achieved with artificial or arbitrary error floors, which are often used in real data inversion. Often, the choice of error floors is driven by the desire to achieve an RMS of ~ 1 for the recovered model.

The second point, namely an assumed Gaussian distribution of the residuals, is trickier. If the residuals originate mainly from noise in observed data, this noise has to be normally distributed with zero mean in order to make the RMS measure optimal. Obviously, in reality residuals do not contain idealized cultural noise and measurement error. In addition the modelling results contain numerical errors e.g. related to a particular discretization and modelling.

Furthermore, being non-robust RMS is sensitive to outliers. Few outliers may result in a violation of the normal distribution assumption.

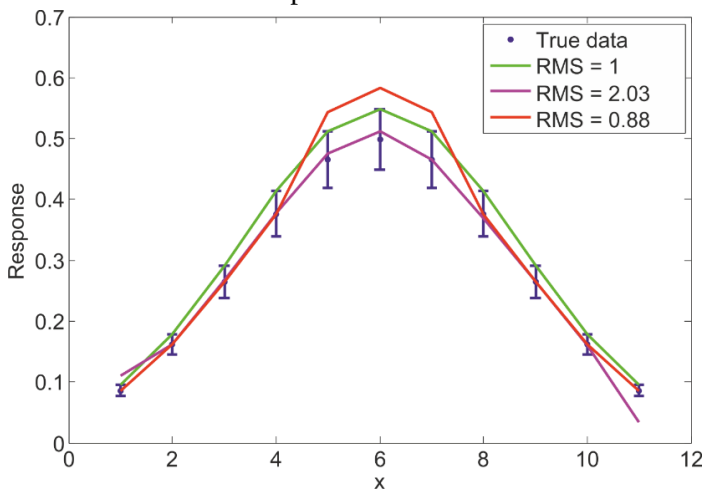

Figure 1: A number of artificial cases to demonstrate that RMS values can be misleading. Blue dots are the true response of a model with error bars corresponding to 10% of the original data amplitudes. The green line is a "true" response systematically shifted to fit the upper limit of the error bars, resulting in an RMS of one. The magenta line shows the ``true'' data perturbed with 1% normal noise and two outliers added at the ends of the curve, which results in an RMS of 2.03. The red line shows ``true'' data with three data points outside the error bars with a total RMS of 0.88.

Comparing models (MT example)

The RMS is often used as a criterion to rank a series of inversion models (when dealing with real data). However, being a single number the RMS cannot reliably describe a complicated model nor does it give any insight into structural differences between models. Figure 2 shows results for three MT 3D inversions runs for the same synthetic data set, but using different starting/prior models. Visual inspection suggests that the first inversion using a 10 Ωm starting model recovers the underlying resistivity structure best (upper panel). If we judge the results only by RMS the model obtained with a starting model of 20 Ωm should be preferred since it results in the lowest RMS; second would be the result using a 50 Ωm half-space. However, in both results the prominent conductive anomaly is missing. This mystery is

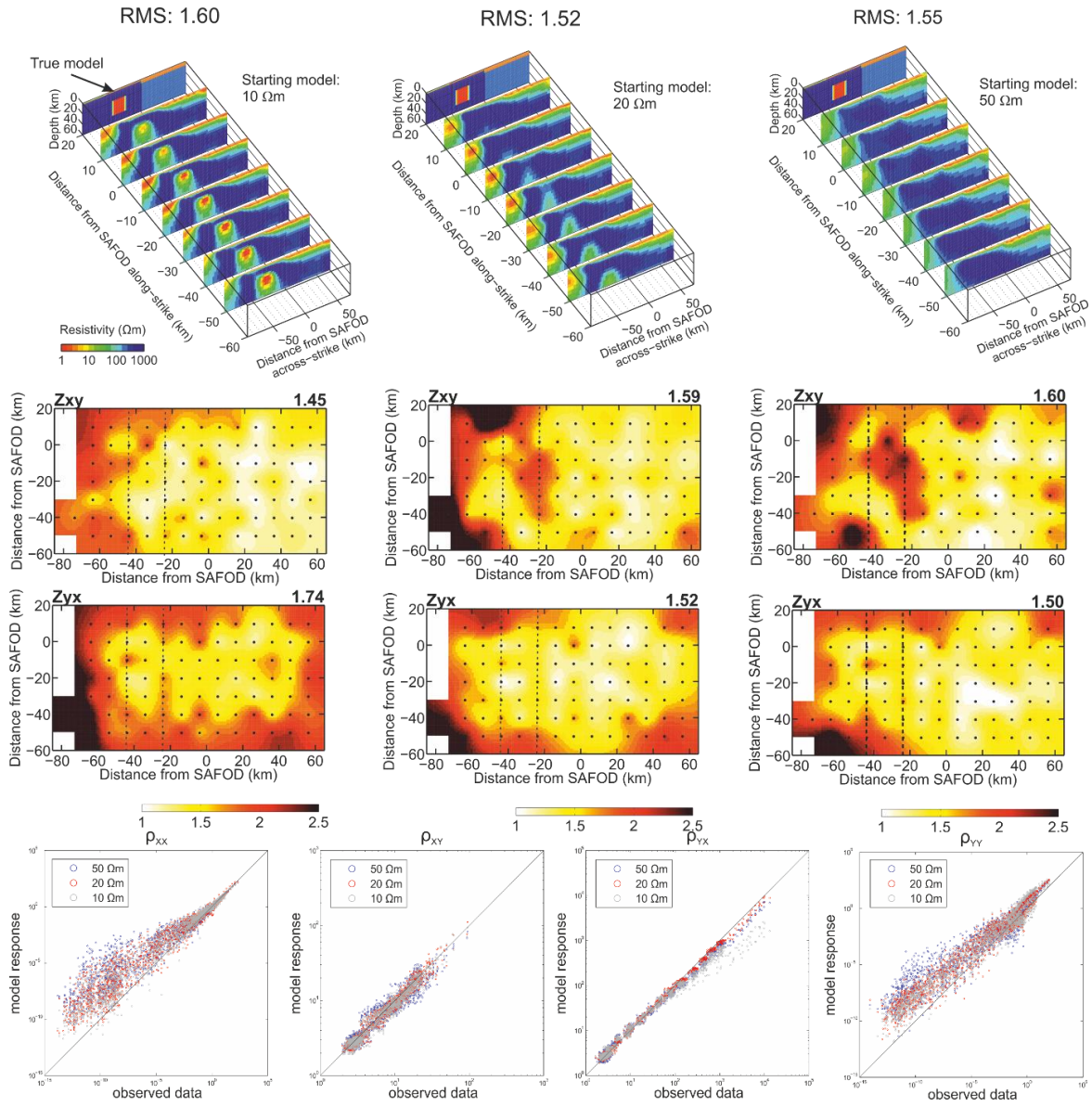

Figure 2: ***Top panel****: Comparison of 3D MT inversion results for three different starting model resistivities (10, 20, 50 Ω*m*); data were generated for a synthetic model shown as slice in the back. Note, the resistivity structure is predominantly 2D with the coarse 3D bathymetry of the Pacific Ocean added; the coastline is located at the left edge of the profiles. The conductive anomaly at depth disappears only for starting resistivities above 10 Ω*m*.*
Middle panel*: Systematic analysis of data misfits in the frequency-space domain of the inversion results reveals large-scale structural deviations of 3D inversion results, which are not reflected in the overall RMS.*
Bottom panel*: Cross-plot of observed and modelled apparent resistivities for all four impedance components. In the ideal case, points would lie on the black line. Scattering around the black line is lowest for model responses obtained with 10 Ω*m* starting model, in particular for the xy-component. The plots also show that the very high apparent resistivities (> 1000 Ω*m*) of the yx-component are difficult to recover for all shown inversions.*

solved when the RMS distribution over the array is assessed in more detail (middle panel of Figgure 2) . For starting models of 20 and 50 Ωm we observe systematically higher RMS values for the Zxy component – the component which is most sensitive to the conductive anomaly – at stations above the conductive anomaly; in return high resistivities of the Zyx component close to the ocean (left edge of the profiles) are better fit. For both components RMS values of the 10 Ωm inversion result show a more uniform distribution of the data misfit. The choice of the model obtained with a starting model of 10 Ωm can also be justified when comparing scatter plots of apparent resistivities for all impedance tensor components. They reveal that the 10 Ωm model (shown in grey) follows the observed data better and has smallest variance.

Estimating data fit (CSEM example)

Usually, we argue that a high RMS value means poor data fit and we infer that the inversion result is not reliable. Given the possibility to choose error floors arbitrarily in (2) one can artificially reduce RMS values by taking/applying larger error floors. Figure 3 shows a section along a profile from 3D inversion models of real CSEM data, and histograms of initial and final normalized residuals for a number of inversion runs with increasing error floors. All inversions were stopped after 30 iterations. All models are very similar. The final RMS shown above each model indicates that increasing the error floor results in lower RMS values. The histograms show that the distribution of residuals is not normal. Increasing error floors shrinks the starting residuals, but has little to do with actual data fit. In addition, red numbers in brackets indicate RMS values calculated with 10% of the most poorly fit data dropped. Without these data values, the RMS values are reduced by more than 40% which indicates the non-robust nature of the root mean square.

Conclusions

The aspects discussed in the previous sections suggest the following conclusions:

- If residuals do not obey a standard normal distribution, RMS is not an optimal measure. It can still be used, but does not need to approach a value of 1 even for geologically justified models.
- The choice of error floors and manual selection of “good” data are subjective and we should try to avoid such assumptions.
- We recommend using more elaborate tools instead of a single RMS number such as investigation of the RMS distribution in the frequency-space domain; analysis of histograms of normalized residuals or scatter plots of modeled vs. observed data.

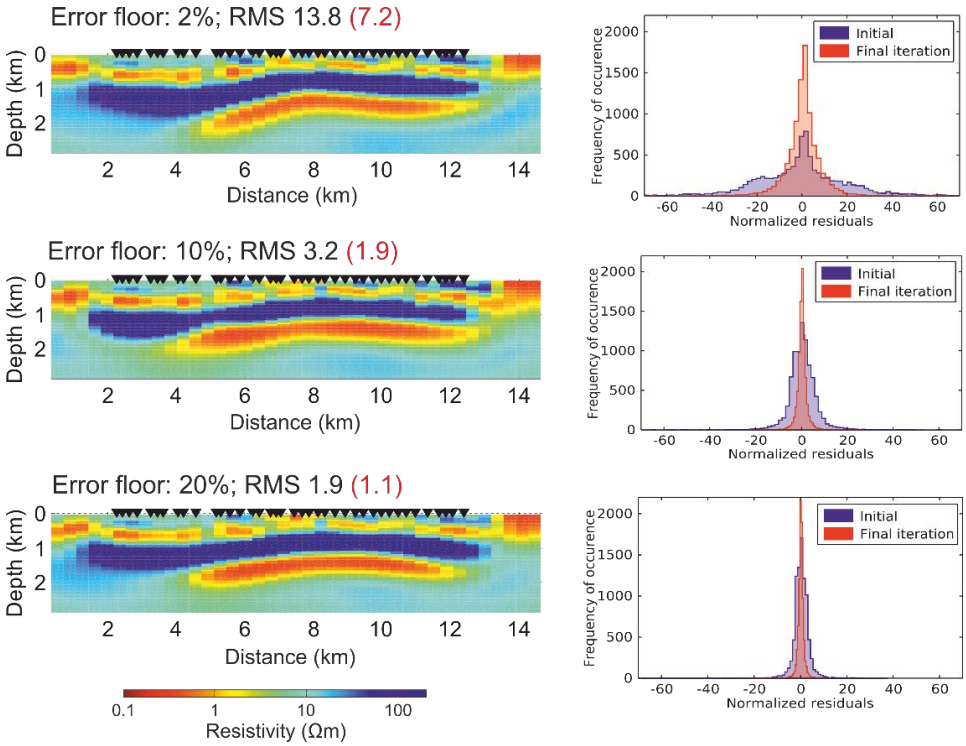

Figure 3. Conductivity sections along the profile line (left) and histograms of initial and final normalized residuals (right) for predefined error floors of (a) 2, (b) 10 and (c) 20\%. The final RMS is given in the title of each plot. Red numbers in brackets indicate RMS values calculated with 10\% of the most poorly fit data values dropped. All three inversions were stopped after 30 iterations.

References

Grayver, A. V., 2013, Three-dimensional controlled-source electromagnetic inversion using modern computational concepts, PhD Thesis, FU Berlin.

Tietze, K., 2012, Investigating the electrical conductivity structure of the San Andreas fault system in the Parkfield-Cholame region, central California, with 3D magnetotelluric inversion, PhD Thesis, FU Berlin.

Multiple-station data processing

Anna Platz[1, 2] (aplatz@gfz-potsdam.de), Ute Weckmann[1, 2]
[1] Helmholtz Centre Potsdam - German Research Centre for Geosciences GFZ, Potsdam, Germany
[2] University of Potsdam, Institute of Geosciences, Potsdam, Germany

SUMMARY

Magnetotellurics (MT) relies on natural electromagnetic field variations to investigate the electrical conductivity structure of the subsurface. Modern MT data are often multivariate due to simultaneous recordings of multiple-channel time series of two (horizontal) electric and three magnetic field components at multiple stations. Single site and remote reference processing only use a small portion of data to estimate the impedance tensor. The multiple-station approach, initially presented by Egbert (1997), uses all data information to improve the signal-to-noise ratios, which results in better estimations of the transfer functions.
This is particularly import in industrialized regions, where the influence of man-made noise signals often exceeds the natural EM fields and hampers the estimation of MT impedance tensors. We have included the multiple-station data approach in our processing scheme EMERALD and tested it with different data sets. A non-robust calculation of the impedance tensor based on the multiple-station approach shows already slightly improved results compared to robust single site or even remote reference estimators. However, in case of high level man-made noise advances of the multiple-station algorithm are not observed. Tests with existing robust routines within EM, which are based on bivariate assumptions, do not reveal a significant improvement.

Keywords: Magnetotellurics, multiple-station data processing

INTRODUCTION

The magnetotelluric method (MT) utilizes natural electromagnetic (EM) field variations, which penetrate into the subsurface and induce secondary fields depending on the electrical conductivity structure of the Earth. In industrialized regions these natural signals are (severely) disturbed by man-made noise sources, which often exceed the natural EM fields and hamper the estimation of MT impedance tensor. To obtain high quality MT results advanced processing approaches have to be applied. The multiple-station approach, initially presented by Egbert (1997), uses all data information to improve the signal-to-noise ratios and provides indications for the existence of coherent noise. Furthermore the approach works in the frequency domain with Fourier coefficients derived from a series of short overlapping time segments and uses a robust MEV (multivariate errors-in-variables) estimation scheme. This multiple-station approach has been included in our processing routines; however, having an interface based on auto and cross spectra averaged to specific centre frequencies, it has to be modified and tested with parts of our robust algorithm in EMERALD, being different from Egbert's robust algorithm.
Six stations, measured in Namibia in 2011, are used to test the new data processing approach within

EMERALD. We assigned three stations to a network, marked with red and blue stars in Figure 1. All of these stations have high data quality and can be regarded as a reference data set for testing the approach. We will show results of the common single site processing compared with multiple-station processing results and discuss the influence of the applied robust statistics scheme within EMERALD.

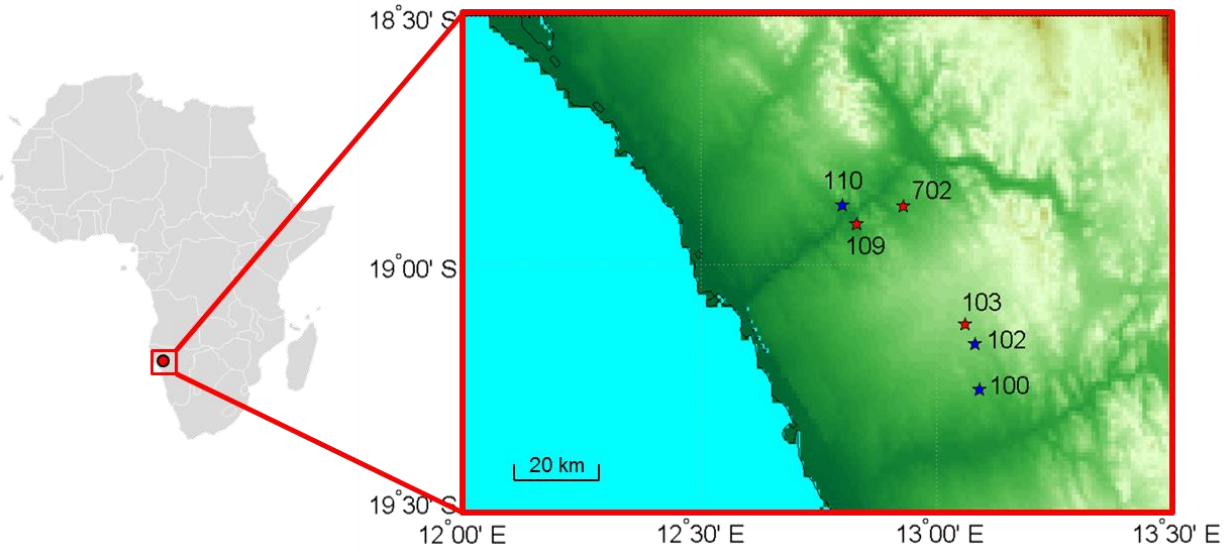

Figure 1: Locations of six exemplary stations from measurements in Namibia: The first network is composed of stations 103, 109 and 702 (red stars) and is characterized by almost noise-free MT data. The second network consists of stations 100, 102 and 110 (blue stars) and contains more EM noise.

NORMAL DATA PROCESSING METHODS

In frequency domain, a linear relationship between the horizontal electric and horizontal magnetic components exists given by the MT impedance tensor $\underline{Z}$

$$\begin{pmatrix} E_x \\ E_y \end{pmatrix} = \begin{pmatrix} Z_{xx} & Z_{xy} \\ Z_{yx} & Z_{yy} \end{pmatrix} \cdot \begin{pmatrix} B_x \\ B_y \end{pmatrix} \tag{1}$$

with $\boldsymbol{E}$ being the electric field in $mVkm^{-1}$ and the magnetic field $\boldsymbol{B}$ in nT. The components Z_{ij} $(i,j = x,y)$ of the impedance tensor are in units of ms^{-1}.

For presentation purposes and to convert the complex numbered impedance tensor elements into physically more meaningful quantities apparent resistivity $\rho_{a,ij}$ in Ωm and phase values ϕ_{ij} in deg are computed.

$$\rho_{a,ij}(\omega) = 0{,}2\, T \left| Z_{ij}(\omega) \right|^2 \tag{2}$$

$$\phi_{ij}(\omega) = \tan^{-1}\left(\frac{Im\{Z_{ij}(\omega)\}}{Re\{Z_{ij}(\omega)\}} \right) \tag{3}$$

The period length T is given in units of s and the angular frequency ω is expressed in units of Hz. The complex impedance tensor contains information on the conductivity structure of the subsurface and is a final result of data processing. A flow chart of the main steps of the applied data processing EMERALD is shown in Figure 2. The original time series are band-pass filtered into narrow frequency bands and divided into short,

subsequent segments of a fixed length of typically 128 samples. These short segments are cosine tapered prior to Fourier transformation. After which they are called ‘events’. These events are corrected for instrument response functions and then averaged at center frequencies, which are equally distributed on a logarithmic scale (Weckmann et al., 2005). For each sub-band and each of the five measured components smoothed auto and cross spectra are calculated. The estimations of impedance tensor are derived by stacking single event spectra from all frequency bands using a robust algorithm described in Ritter et al. (1998). The results are influenced by coherent and incoherent noise similarly. The magnetic channels are assumed to be noise-free and systematic underestimation of noise in these channels leads to a bias of the apparent resistivity curves since noise does not cancel out in auto spectra. For the remote reference (RR) method, auto spectra in the denominators are substituted by cross spectra of the magnetic channels of the local and the reference site. Therefore the existence of a remote station is mandatory, which has to be located far away from the local station to guarantee that EM noise at both stations is incoherent. Finding and maintaining such a reference site during a field campaign is usually expensive and time consuming.

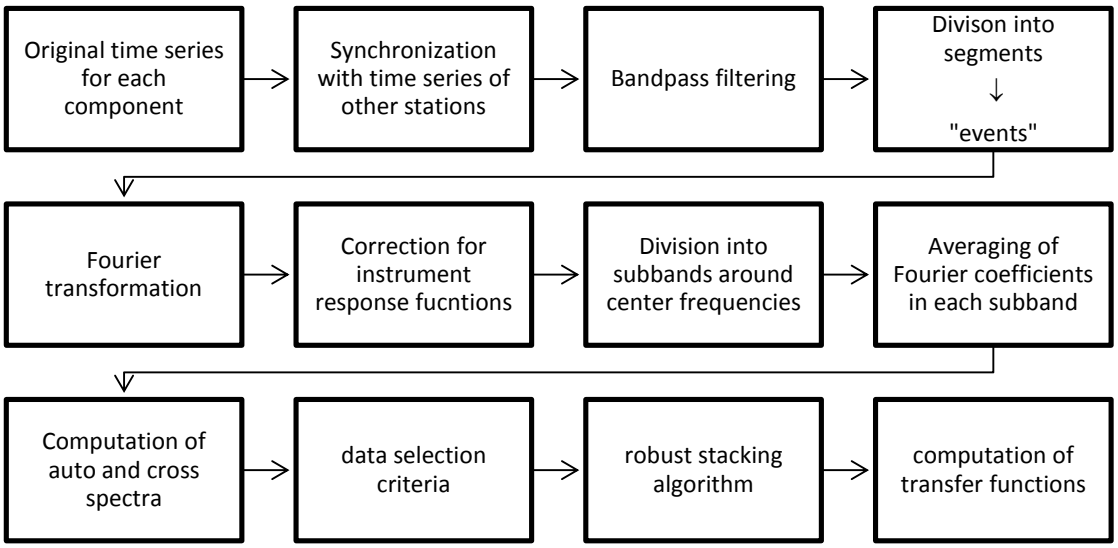

Figure 2: Flow chart of magnetotelluric data processing. All steps displayed in the first row take place in time domain, while the rest already applies to frequency domain.

In Figure 3 results of single site processing for station 109 are shown. The coherency criterion within the robust algorithm is used with a threshold of 0.9. In Figure 3b single site results are overlaid with RR results of station 109 with station 103. The diagonal component Z_{xx} of the impedance tensor shows a typical bias in the period range $1 - 10s$, which can be eliminated using the remote reference method (see orange curves in Figure 3b, which overlay the red curves for most frequencies except the frequency range around the dead band between $1s$ and $10s$).

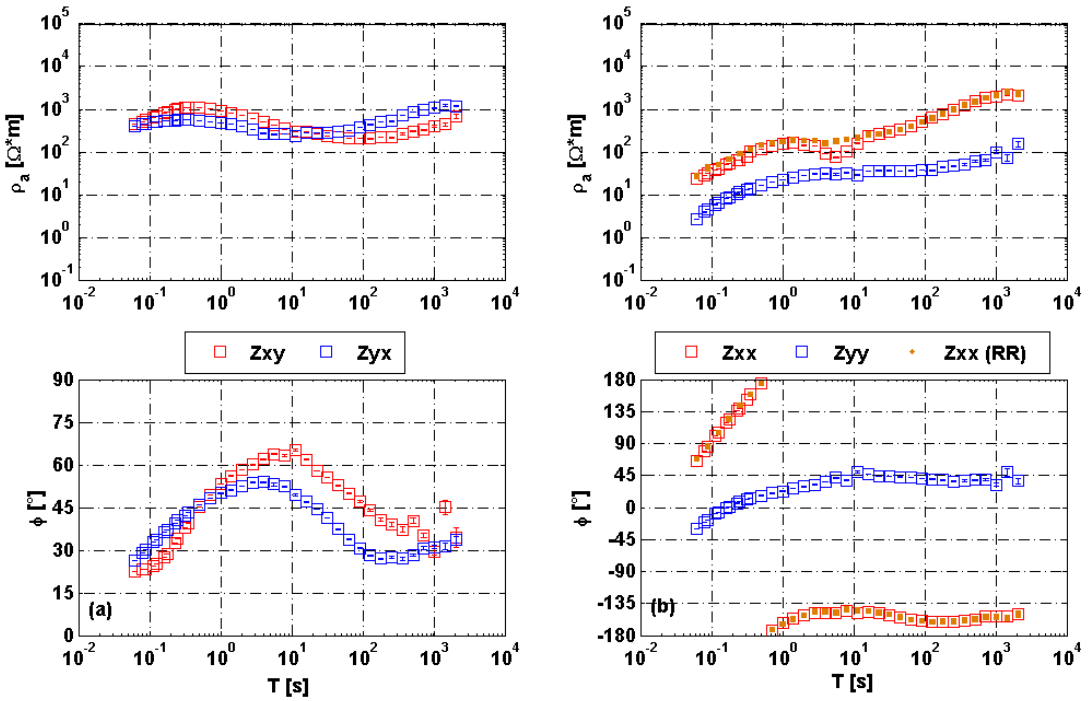

Figure 3: Single site results of station 109. The curves of the off-diagonal components are smooth (a). (b) The apparent resistivity of the Z_{xx} component shows a bias between 1s and 10s, which is eliminated by the remote reference method (see orange curve). Single site as well as remote reference results are obtained by using the robust algorithm within EMERALD with a threshold of 0.9 for the coherency criterion and without phase criterion.

Both methods, single site and remote reference, are based on univariate and bivariate statistics and only use a small portion of the available data. The spectral density matrix (SDM) contains all possible auto and cross spectra, exemplary shown for a single station in (4).

$$\underline{SDM} = \begin{bmatrix} \langle B_x B_x^* \rangle & \langle B_x B_y^* \rangle & \langle B_x B_z^* \rangle & \langle B_x E_x^* \rangle & \langle B_x E_y^* \rangle \\ \langle B_y B_x^* \rangle & \langle B_y B_y^* \rangle & \langle B_y B_z^* \rangle & \langle B_y E_x^* \rangle & \langle B_y E_y^* \rangle \\ \langle B_z B_x^* \rangle & \langle B_z B_y^* \rangle & \langle B_z B_z^* \rangle & \langle B_z E_x^* \rangle & \langle B_z E_y^* \rangle \\ \langle E_x B_x^* \rangle & \langle E_x B_y^* \rangle & \langle E_x B_z^* \rangle & \langle E_x E_x^* \rangle & \langle E_x E_y^* \rangle \\ \langle E_y B_x^* \rangle & \langle E_y B_y^* \rangle & \langle E_y B_z^* \rangle & \langle E_y E_x^* \rangle & \langle E_y E_y^* \rangle \end{bmatrix} \quad (4)$$

The SDM is a hermitian matrix, wherefore in our example 10 of the 25 components are dependent coloured in gray. For the estimation of the full impedance tensor only the seven components in blue are used. Most of the calculated spectra therefore are not used for the estimation of the impedance tensor.

Although modern MT data are often multivariate due to simultaneous recordings of multiple-channel time series of two (horizontal) electrical and three magnetic field components at multiple stations, data of each station is processed separately. Unfortunately, in industrialized regions the influence of man-made noise signals often exceeds the natural EM fields and hampers the estimation of MT impedance tensors. This coherent noise can be eliminated neither by remote reference nor by single site processing using robust statistics to obtain a mean impedance tensor. To obtain high quality MT results different processing approaches have to be applied, which utilize available information about signal and noise in all recording

channels. The multiple-station approach, initially presented by Egbert (1997), uses all data information to improve the signal-to-noise ratios by separating different field components and thus hoping to separate and identify EM noise within. Therefore the multiple-station approach works with networks of stations instead of single stations.

MULTIPLE-STATION DATA PROCESSING

The multiple-station approach was presented by Egbert (1997) and works with Fourier coefficients derived from time series. We have included a non-robust multiple-station data processing in our processing routines within EMERALD. The approach is still based on the ideas of Egbert, but we have to adopt it to work with auto and cross spectra. This multiple-station approach is based on a multivariate linear model, which describes the formation of the data vector $\overrightarrow{X_i}$ by the electric and magnetic Fourier coefficients h_{ji}, e_{ji} for the ith time segment at the site j of the station network.

$$\overrightarrow{X_i} = \begin{pmatrix} h_{1i} \\ e_{1i} \\ \vdots \\ h_{Ji} \\ e_{Ji} \end{pmatrix} = \begin{pmatrix} \eta_{11} \\ \zeta_{11} \\ \vdots \\ \eta_{J1} \\ \zeta_{J1} \end{pmatrix} \beta_{1i} + \begin{pmatrix} \eta_{12} \\ \zeta_{12} \\ \vdots \\ \eta_{J2} \\ \zeta_{J2} \end{pmatrix} \beta_{2i} + \varepsilon_i = \underline{U}\overrightarrow{\beta_i} + \overrightarrow{\varepsilon_i} \tag{5}$$

For MT data each station typically consists of two electrical and three magnetic channels, so that in total $K = 5J$ channels exist within a network. The data vector can be sub-divided into three vectors, in which two of them contain the Fourier coefficients η_{ji}, ζ_{ji} corresponding to the two orthogonal plane-wave MT sources. The parameters $\beta_{li}, l = 1, 2$ define the polarization of these source fields and the additional vector $\vec{\varepsilon}_i$ represents all sources of coherent and incoherent noise, which we assume to be statistically independent of our MT signals. The first two vectors can be summarized to the matrix U, which ideally contains the electrical and magnetic fields that would be observed at all sites within a network for idealized quasi-uniform magnetic sources, which are linearly polarized in north-south and east-west direction. All channels of all stations within a network can contain noise, wherefore bias, which is observed in single site processing, is avoided. Coherent noise in the data within a station network can be clearly detected. The impedance tensor for each station can be determined from the elements of U, which correspond to the x and y components of the electrical and magnetic fields observed at the jth station. Estimates of the matrix U can be obtained by the solution of following generalized eigenvalue problem:

$$Su = \lambda \Sigma_N u \tag{6}$$

The matrix S is the spectral density matrix containing in our case all possible auto and cross spectra within a station network and the matrix Σ_N is the covariance matrix of all noise sources. The eigenvectors of the two largest eigenvalues build the matrix U. Unfortunately, in most cases the coherent noise structure within a network is unknown and without a priori knowledge of noise geometry, development of a parametric model for Σ_N is impossible. The simplest model for Σ_N is a diagonal matrix, which assumes that noise is incoherent between stations as well as between channels of a single site.

$$\Sigma_N = diag(\sigma_1^2 \dots \sigma_k^2) \tag{7}$$

The parameters σ_k^2 represent the variances of incoherent noise and can be calculated from the auto and

cross spectra by using a multiple linear regression to fit data for channel k to the remaining $K-1$ channels. By definition the incoherent part of the data in each channel is independent from data in the remaining channels, so that the magnitude of the residuals of the multiple linear regression provides an estimation of the variances.

A modified model of (5) introduces the matrix V, which represents coherent noise sources. In this case $\vec{\varepsilon_i}$ contains only signals from incoherent noise guaranteeing that Σ_N can be expressed in form of (7).

$$\overrightarrow{X_i} = \underline{U}\vec{\beta_i} + \underline{V}\overrightarrow{\gamma_i} + \overrightarrow{\varepsilon_i} = [\underline{U} \quad \underline{V}] \begin{bmatrix} \overrightarrow{\beta_i} \\ \overrightarrow{\gamma_i} \end{bmatrix} + \overrightarrow{\varepsilon_i} = \underline{W}\overrightarrow{\alpha_i} + \overrightarrow{\varepsilon_i} \tag{8}$$

Then the eigenvectors of all dominant eigenvalues build the matrix W, which can be an arbitrary mixture of signal matrix U and coherent noise matrix V. In absence of coherent noise, two dominant eigenvalues exist representing the two natural source polarizations. In this case, the matrix W is equal to the matrix U and impedance tensor for each station can be derived. Existence of more than two dominant eigenvalues indicates that the MT data contain coherent noise and successful estimation of impedance tensor is only possible by separating coherent noise from the signal, which is not possible in every case.

With this knowledge we can implement a non-robust multiple-station approach in two steps. In the first step we calculate the incoherent noise variances for each channel to estimate the matrix Σ_N, while in the second step the eigenvalue problem is solved. The eigenvectors associated with the two largest eigenvalues build the matrix U. The impedance tensor Z_j for each station is derived by elements of U corresponding to the x and y components of electric and magnetic fields observed at station j.

$$Z_j = \begin{bmatrix} \zeta_{xj1} & \zeta_{xj2} \\ \zeta_{yj1} & \zeta_{yj2} \end{bmatrix} \begin{bmatrix} \eta_{xj1} & \eta_{xj2} \\ \eta_{yj1} & \eta_{yj2} \end{bmatrix}^{-1} \tag{9}$$

Application to MT data from Namibia

For the station network 103-109-702 two dominant eigenvalues exist almost over the entire frequency range (Figure 4). Therefore the two eigenvectors of these two eigenvalues are used to build the matrix U and the impedance tensor for each station. In Figure 5, robust single site results of station 109 are compared with results of the non-robust multiple-station approach. For most frequencies the results match very well. As expected the bias for the Z_{xx} component in the single site result is eliminated by the non-robust approach. The implemented approach works properly and in case of almost noise-free data the results are as good as or better than the robust single site results. Contain the data more noise than the non-robust approach does not suffice to resolve the impedance tensor over the entire frequency range. For some frequency of the second network, 100-102-110, more than two dominant eigenvalues exist. Using the eigenvectors associated with the two largest eigenvalues for estimation of impedance in such a case does not guarantee good results, because the matrix W is an arbitrary mixture of coherent noise signal and MT signal and the two largest eigenvalues do not need to represent the MT signal.

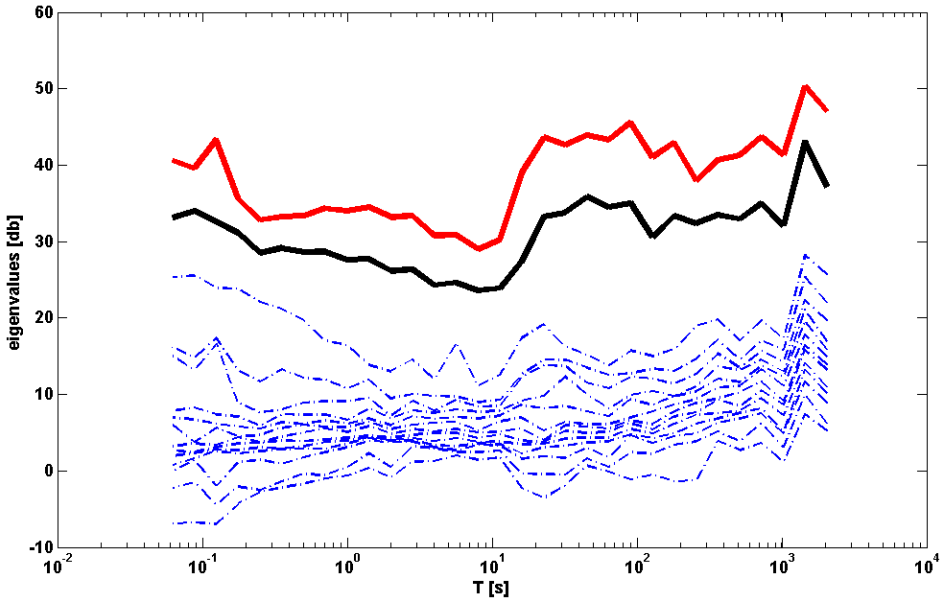

Figure 4: Eigenvalues for the non-robust multiple-station approach for station network 103-109-702. The two largest eigenvalues are marked in red and black and they are for almost all frequencies clearly larger than the other 13 eigenvalues. The eigenvectors associated with these two are used for estimation of impedance tensor. Magnitude of all eigenvalues is comparable with the eigenvalues shown by Egbert (1997).

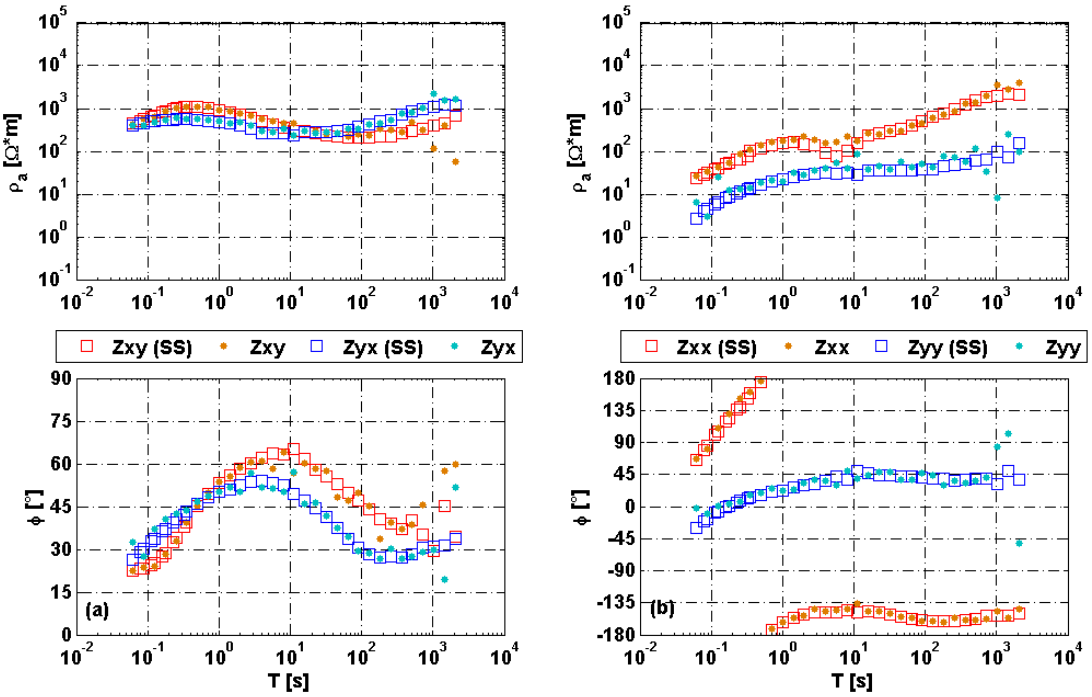

Figure 5: Comparison between robust single site results (red and blue squares) and non-robust multiple-station results (orange and cyan dots) for station 109. For most frequencies the non-robust multiple-station approach can resolve the curves in the same quality as robust single site processing. Only for long periods, where naturally less events exist and where we resolve more than two dominant eigenvalues, values scatter. The bias of component Z_{xx} is automatically eliminated by multiple-station approach (b).

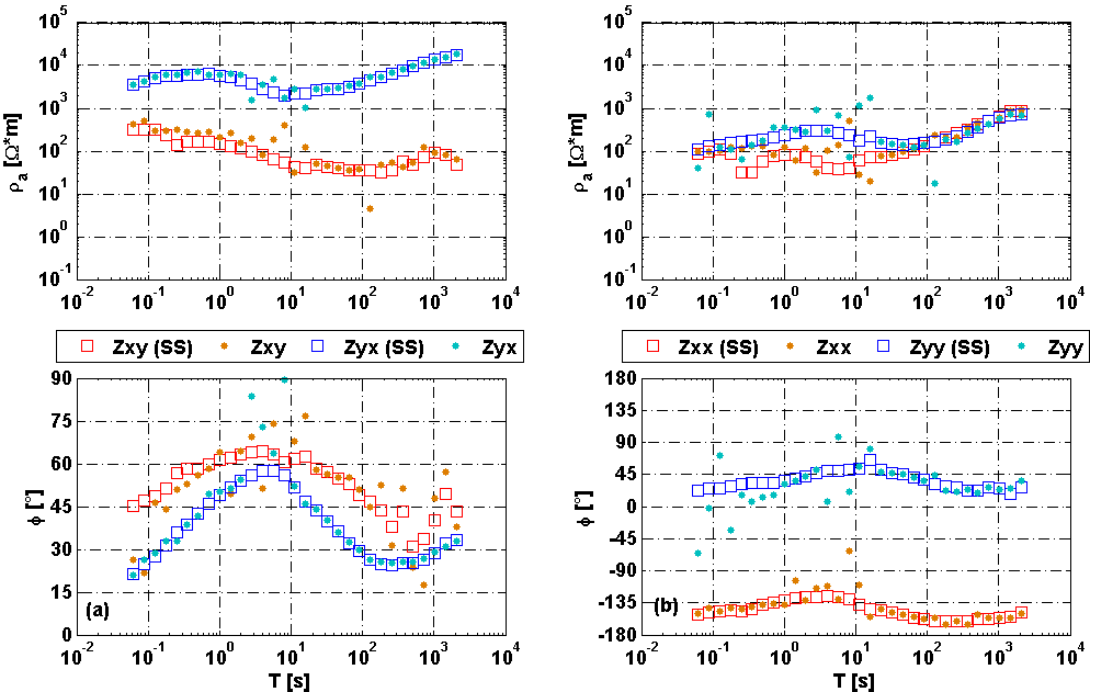

Figure 6: Comparison between robust single site results (red and blue squares) and non-robust multiple-station results (orange and cyan dots) for station 100. Single site results are obtained by using the robust algorithm with a threshold of 0.9 for the coherency criterion and without using phase criterion. For periods shorter than 10*s* more than two dominant eigenvalues exist and phase values for both off-diagonal (a) and diagonal components (b) scatter in this frequency range for the non-robust multiple-station approach. Although the general curve shapes are resolved for all four impedance tensor components, a robust algorithm is necessary to improve results of multiple-station approach.

Figure 6 shows an exemplary result for this network: Although for many frequencies the robust single site results and the non-robust multiple-station result match, a lot of frequencies exist with significant differences in the results. This particularly applies to the high frequencies for which four dominant eigenvalues are observed although data quality is good. Therefore the next step is an extension of the non-robust approach by robust statistics, which eliminate the influence of outliers.

COMBINATION WITH EXISTING ROBUST STATISTICS

The non-robust multiple-station approach is combined with parts of robust statistics which is already implemented in the processing scheme “EMERALD”. The robust algorithm consists of data selection criteria and a robust stacking algorithm described in more detail by e.g. Weckmann et al. (2005), Ritter et al. (1998) and Krings (2007). Normally it is used for standard single site and RR processing and therefore it is based on univariate and bivariate statistics e.g. by calculating bivariate coherences and using the bivariate equations in (1). Figure 7 shows results of the robust and non-robust multiple-station approach for station 109. Both results seem to coincide and illustrate that in this case the robust algorithm has no influence of the estimation of the impedance tensor. The main reason for this is the high data quality with almost no outliers within this station network.

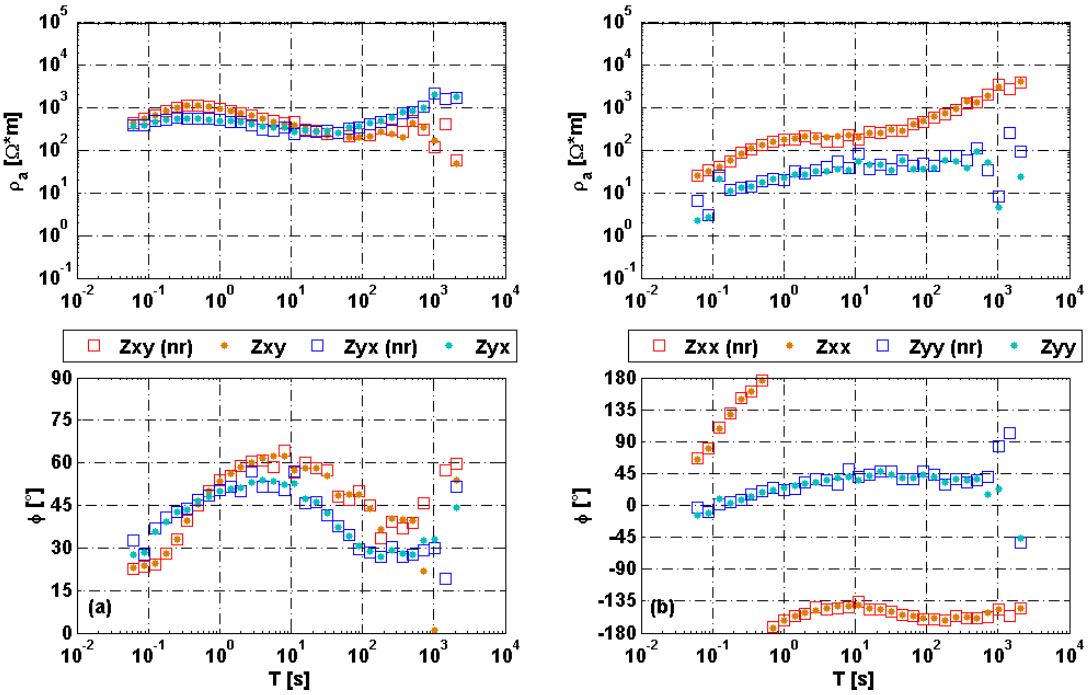

Figure 7: Comparison between non-robust multiple-station results (red and blue squares) and robust multiple-station results (orange and cyan dots) for station 109. For the robust processing coherency criterion with a threshold of 0.92 is used and the first part of the robust stacking algorithm using Huber and Tukey weights. Both results match well and in this case the robust algorithm seems to have hardly an influence of processing results.

The data of the second network contain more outliers, which normally should be sorted out by the robust algorithm. Unfortunately, this does not seem to be the case (Figure 8). The processing results of both approaches match well and a significant improvement of apparent resistivity and phase curves cannot be observed. The robust algorithm uses bivariate equations and statistics, which can not sufficiently characterize the multivariate structure of the dataset. Therefore a useful characterization of outliers is not possible by using bivariate statistics in combination with a multiple-station approach. Furthermore neither the non-robust nor the robust multiple-station approach separate coherent noise from desired MT signal. Processing of data, which contain coherent noise shown by a high number of dominant eigenvalues leads to unwanted results.

To illustrate advances of the multiple-station approach a comparison of non-robust single site and non-robust multiple-station processing of station 100 is shown in Figure 9. Single site processing without any robust algorithm and data selection criteria cannot resolve apparent resistivity and phase curves over the entire frequency range. On the other hand non-robust multiple-station processing can resolve the shape of the curves and the quality of the results is much higher.

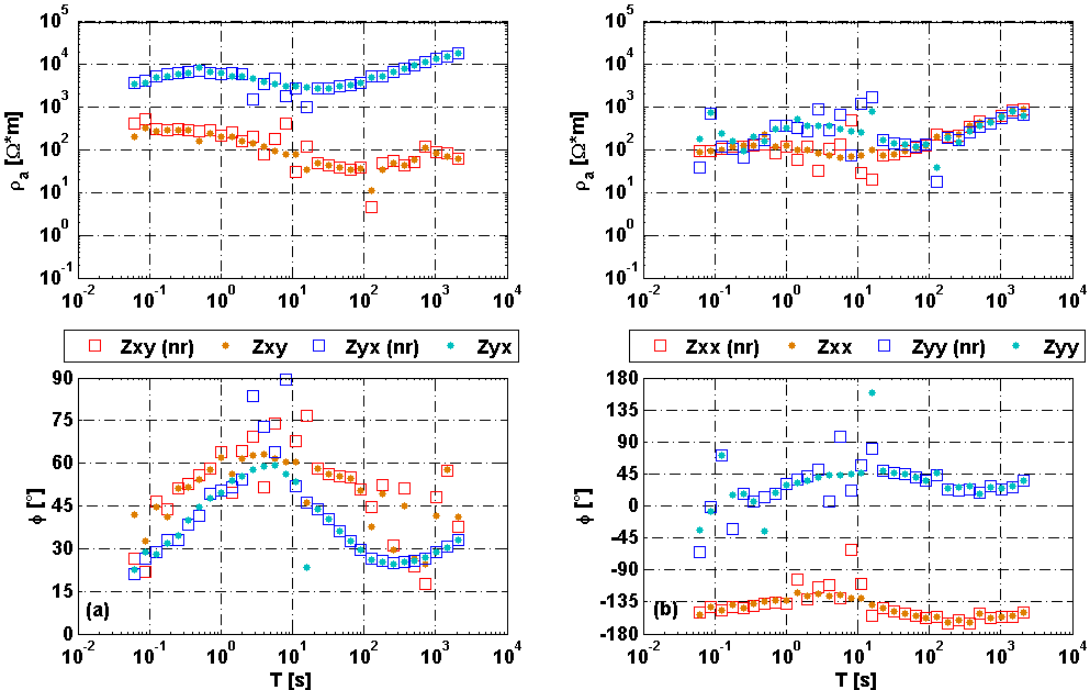

Figure 8: Comparison between non-robust multiple-station results (red and blue squares) and robust multiple-station results (orange and cyan dots) for station 100. For the robust processing coherency criterion with a threshold of 0.9 is used and the first part of the robust stacking algorithm using Huber and Tukey weights. Both results match for many frequencies. A significant improvement of apparent resistivity and phase curves cannot be observed.

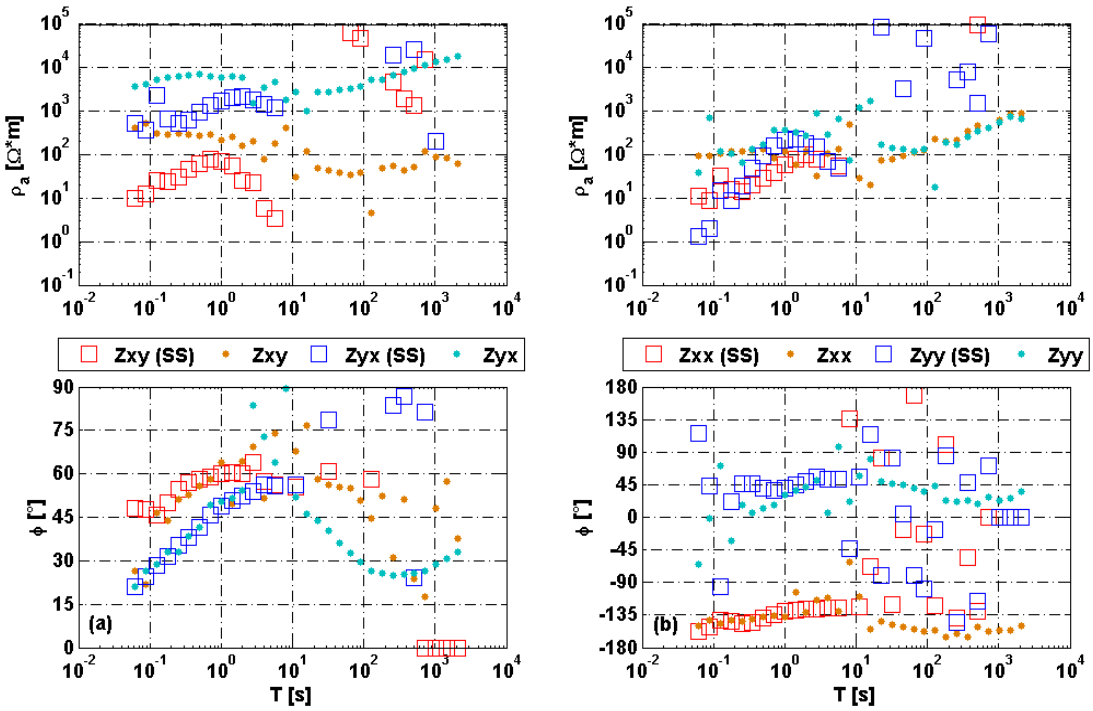

Figure 9: Comparison between non-robust single site results (red and blue squares) and non-robust multiple-station results (orange and cyan dots) for station 100. The non-robust multiple-station processing resolves the results much better than non-robust single site processing. In the period range between $10 - 100s$ some apparent resistivity values for the off-diagonal components (a) are higher than 10,0000 Ωm. These values are in this case unrealistic and are not displayed.

CONCLUSION

A non-robust multiple-station approach is integrated in our processing routines showing already improved results for almost noise-free data compared to robust single site or even remote reference estimators. However, in case of a higher level of man-made noise advances of the non-robust multiple-station approach in comparison with robust single-site results are not observed. But a direct comparison of non-robust single site and non-robust multiple-station processing shows the advances of the novel algorithm. Tests with the existing robust routines, which are based on bivariate assumptions, do not reveal a significant improvement. It seems that the robust algorithm based on bivariate assumptions counteracts the multivariate characteristic of the multiple-station approach. Therefore future steps include development of new data selection criteria and integration of robust multivariate statistics.

REFERENCES

Egbert G (1997) Robust multiple-station magnetotelluric data processing. Geophys. J. Int. 130, 475-496

Krings T (2007) The influence of robust Statistics, Remote Reference, and Horizontal Magnetic Transfer Functions on data processing in Magnetotellurics. Diploma thesis, Westfälische Wilhelms-Universität, Münster

Ritter et al. (1998) New equipment and processing for magnetotelluric remote reference observations. Geophysical Journal International 132, 535-548

Weckmann et al. (2005) Effective noise separation for magnetotelluric single site data processing using a frequency domain selection scheme. Geophysical Journal International 161, 635-652

3-D forward modelling of frequency-domain helicopter-borne electromagnetic data: A comparative study

Marion P. Miensopust[1], Bernhard Siemon[1], Ralph-Uwe Börner[2], and Seyedmasoud Ansari[3]

[1] *Federal Institute for Geosciences and Natural Resources, Hannover, Germany*
[2] *Technische Universität Bergakademie Freiberg, Freiberg, Germany*
[3] *Memorial University of Newfoundland, St. John's, Newfoundland, Canada*

1 Introduction

Frequency-domain helicopter-borne electromagnetic (HEM) data sets are commonly interpreted using one-dimensional (1-D) modelling and inversion tools. In many cases this approach is valid (e.g., horizontally layered targets and groundwater applications) but there are areas of higher dimension that are not recovered correctly applying 1-D methods. In recent years multi-dimensional forward modelling codes became available. As there is no analytic solution to verify (or falsify) the obtained numerical solutions, comparison with 1-D values as well as amongst various two-dimensional (2-D) and three-dimensional (3-D) codes is essential. Values obtained over the background structure and at the centre of a large (a few hundred metres edge length) structure should match 1-D values. At the edges of the structure – i.e., at higher dimensional parts – only a comparison of different codes is possible. The more codes – especially if based on different methods and/or written by different programmers – agree the more reliable is the obtained synthetic data set.

2 Forward Modelling Codes

Multi-dimensional modelling codes vary considerably regarding their advantages but also their restrictions. The latter mainly result from structure related requirements but also from memory usage and computation time. The following codes were available for this study: ArjunAir, MarcoAir, SamAir and LokiAir — all part of the AMIRA package (Raiche, Sugeng, & Wilson, 2007), X3Da (Avdeev, Kuvshinov, Pankratov, & Newman, 1998), fdm_adapt (Börner, Ernst, & Spitzer, 2012) and csem3dfwd (Ansari & Farquharson, 2011, 2013). ArjunAir is a 2.5-D code whereas all others are 3-D codes. MarcoAir and X3Da use an integral equation approach, while ArjunAir, LokiAir and csem3dfwd are finite-element codes and SamAir a compact finite-element code, fdm_adpat is the only finite-difference algorithm. According to these methodical differences also the implementation of background and anomalous structure differ. All codes use the quasi-static solution except for X3Da, where the exact solution is implemented. Furthermore the ability to deal with topography and variable sensor height differs for the various codes. Other limitations are a small resistivity contrast (MarcoAir), a restricted size of anomalous region (SamAir) and artifacts close to structural boundaries at low frequencies (ArjunAir). For

detailed information regarding those codes the interested reader is referred to the specified literature.

3 Model A - small conductive block

This simple model consists of a 50 Ωm block (100 m × 500 m × 20 m) in a 100 Ωm homogeneous halfspace. Its top is at 10 m depth and the profile of interest is crossing at the centre of the block. In-phase and Quadrature values were calculated for five horizontal coplanar transmitter-receiver coil pairs (8 m separation, 387 Hz to 133200 Hz) using a sensor height of 30 m. Figure 1 shows a sketch of the model on the left and the obtained anomalous amplitudes ($I - I_{bg}$, $Q - Q_{bg}$) on the right. Additionally, the listed, colour-coded values stand for the differences between the accurate 1-D solution and the obtained solution above the background.

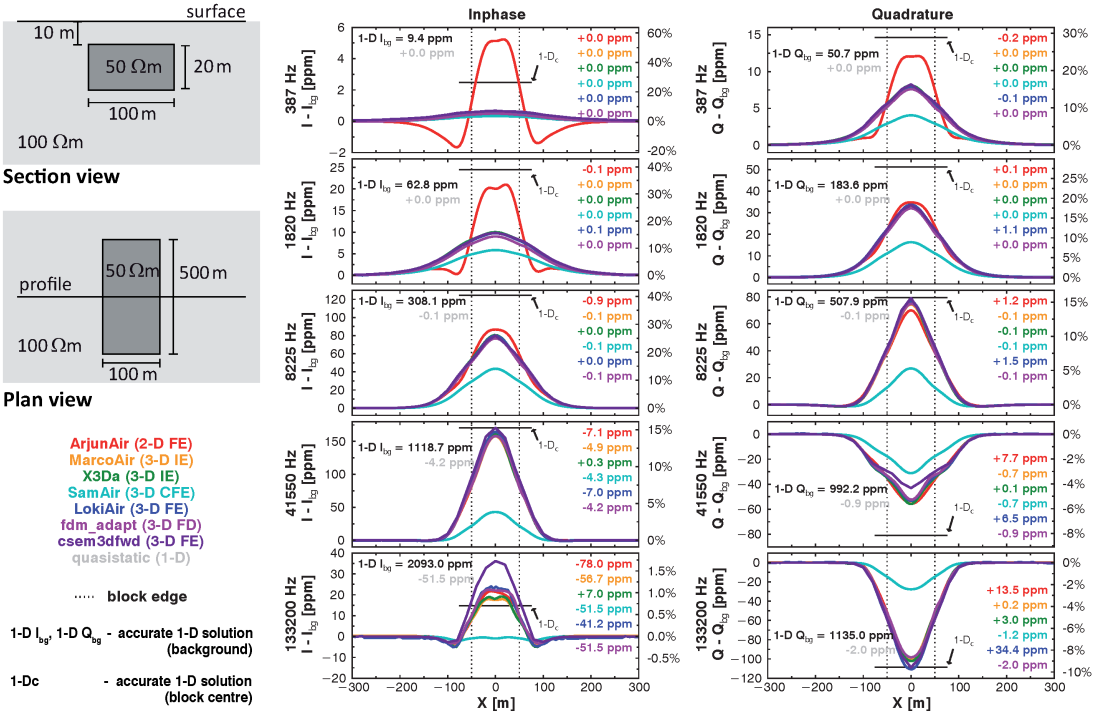

Figure 1: Sketch of the Model A (left) and the obtained anomalous In-phase and Quadrature values (right). The colour-coding is according to the list of codes on the left and respective coloured ppm values in each panel state the differences between the accurate 1-D solution and the obtained solution above the background.

4 Model B - large conductive block

Model B is almost identical to Model A but the lateral extent of the 50 Ωm block is increased (600 m × 600 m × 20 m) to allow to approach 1-D values at the centre of the block. Figure 2 shows absolute In-phase and Quadrature values for all five frequencies and accurate (solid) and quasi-static (dashed) 1-D solutions for reference.

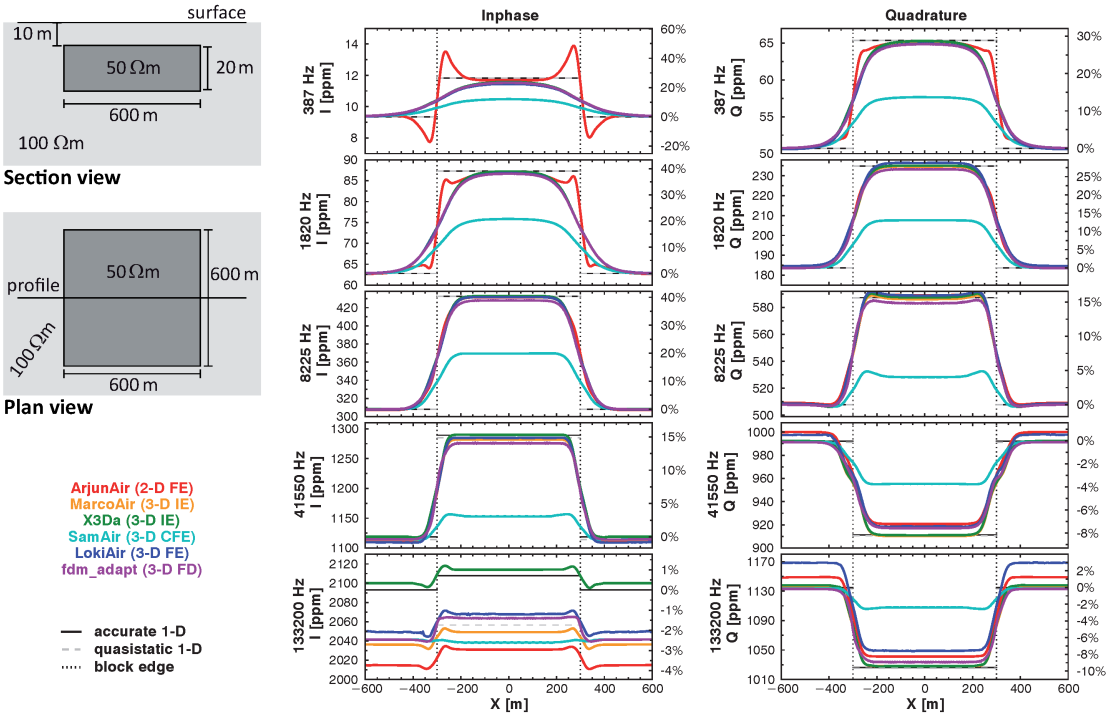

Figure 2: Sketch of the Model B (left) and the obtained absolute In-phase and Quadrature values (right). The colour-coding is according to the list of codes on the left.

5 Conclusion

The comparative study demonstrates that ...

... all codes recover the background values well, difference are only obvious close to the edges of the block and above the structure.

... SamAir fails to calculate values above the anomalous structure.

... ArjunAir fails — due to its limitations regarding the used 2.5-D approximation (David Annetts, CSIRO, pers. comm.) — to model the low frequencies above small structures and values close to the edges of larger blocks correctly.

... X3Da allows to model high frequency data more accurately than all others, which use the quasi-static approximation.

... codes with full-domain discretisation are sensitive to cell size. Oscillation or off-sets can be the result which is also dependent on the sensor height and the resistivity.

... if inversion, topography and/or variable sensor height are required, the choice of applicable codes is limited.

It is important to analyse the model/data set of interest to trade-off the advantages and limitations of the different codes to find the most applicable one for this particular model/data set. One could also apply different codes to investigate different aspects of the model/data set. Differences in memory usage and computation time are not considered in this comparison but might also matter.

6 Outlook

Additional models (e.g., resistive anomaly, layered background) will also be investigated to get a general idea of the status quo. As soon as reliable forward solutions are ensured, the next step is to examine the available inversion algorithms systematically.

7 Acknowledgements

We thank the Commonwealth Scientific and Industrial Research Organisation (CSIRO; www.csiro.au) and AMIRA International (www.amira.com.au) who made their comprehensive modelling and inversion tools package developed under the P223 EM Modeling Projects freely available for scientific use. This work was done in close cooperation with the AIDA project (German Federal Ministry of Education and Research grant 03G0).

References

Ansari, S., & Farquharson, C. G. (2011). *3D finite-element simulation of electromagnetic data for inductive and galvanic components.* SEG Technical Program Expanded Abstracts, 766-770.

Ansari, S., & Farquharson, C. G. (2013). *Numerical modeling of geophysical electromagnetic inductive and galvanic components.* SEG Technical Program Expanded Abstracts, 669-674.

Avdeev, D. B., Kuvshinov, A. V., Pankratov, O. V., & Newman, G. A. (1998). Three-dimensional frequency-domain modelling of airborne electromagnetic responses. *Expl. Geophys.*, *29*.

Börner, R.-U., Ernst, O., & Spitzer, K. (2012). *A 3-D finite difference forward modelling framework for MT and CSEM appliactions.* 24th Schmucker-Weidelt-Kolloquium für Elektromagnetische Tiefenforschung, Extended Abstracts, 16-21.

Raiche, A., Sugeng, F., & Wilson, G. (2007). *Practical 3D EM inversion - the P223F software suite.* 19th ASEG Geophysical Conference and Exhibition, Extended Abstracts,(1),1-5.

Messungen zur 3-D-Positionsbestimmung einer Dipolquelle über dem Forschungs- und Lehrbergwerk "Reiche Zeche"

S.Malecki, R.-U. Börner und K. Spitzer
Institut für Geophysik und Geoinformatik, TU Bergakademie Freiberg

1 Zusammenfassung

Es soll ein Verfahren zur Positionsbestimmung unter Tage entwickelt werden. Die Grundlage bildet die zeitliche Erfassung transienter elektromagnetischer Felder. Dabei werden mehrere magnetische Dipolquellen an der Erdoberfläche ausgelegt. Nach Abschalten des Stromes in einer Sendespule wird das transiente Magnetfeld dieser Quelle unter Tage an einem Punkt aufgezeichnet. Das Verfahren wird für jede weitere Senderposition in gleicher Weise wiederholt. Die Koordinaten des untertägigen Messpunktes werden durch einen Inversionsalgorithmus automatisch bestimmt.
Das Prinzip der Umkehrbarkeit von Sendern und Empfängern (Reziprozitätsprinzip) ermöglicht in der Erprobungsphase eine einfachere Messanordnung, die übertage eine Dipolquelle und unter Tage mehrere Messpunkte vorsieht. Erste Experimente wurden im Freiberger Forschungs- und Lehrbergwerk "Reiche Zeche" durchgeführt.

2 Einleitung

Die dreidimensionale Positionsbestimmung unter Tage, unabhängig von geodätischen Netzen, ist insbesondere bei der Erforschung von Höhlensystemen oder historischen Bergwerken von großer Bedeutung. Herkömmliche geodätische Verfahren bauen meist auf Festpunktfeldern über Tage auf. Für eine schnelle Positionsbestimmung sind sie wenig geeignet.
Es wird ein Verfahren vorgestellt, welches die unabhängige, dreidimensionale Positionsbestimmung mit Hilfe elektromagnetischer Felder unter Tage erlaubt. Für die Berechnung der Position des unbekannten Punktes sind mindestens drei geodätisch bestimmte Punkte erforderlich. Durch eine deutliche Überbestimmung ist eine zuverlässige Fehlerangabe und Konfidenzschätzung möglich.
Die Methode ist im geodätischen Sinn ein absolutes Verfahren. Bei jeder Messung ist entgegen gebräuchlicher Verfahren kein Bezug zu vorherigen Messpunkten notwendig. Somit können sich Fehler nicht summieren.

3 Modellbeschreibung

Abbildung 1 zeigt den verwendeten Messaufbau und gleichzeitig das zu lösende Positionierungsproblem. Die Koordinaten der Messpunkte Rx_i sind geodätisch in x, y, z bestimmt, jedoch ist die 3-D-Position des vertikalen magnetischen Dipols (VMD) unbekannt.
In einer quadratischen, an der Erdoberfläche liegenden, $100\,\mathrm{m} \times 100\,\mathrm{m}$ großen Drahtschleife fließt ein Gleichstrom mit $\mathrm{I} = 25\,\mathrm{A}$. Dieser generiert ein stationäres Magnetfeld. Wird der Gleichstrom unterbrochen, bricht das Magnetfeld zusammen. Dabei wird aufgrund

der zeitlichen Änderung des Stromes I im Untergrund ein Stromsystem induziert. Dieses breitet sich dem Medium entsprechend charakteristisch aus.
An beliebigen Stellen (Rx) kann das Magnetfeld als Funktion der Zeit gemessen werden. In den so aufgezeichnenten Transienten sind Informationen über die elektrische Leitfähigkeit des zwischen dem VMD und den Rx liegenden Mediums enthalten. Sind die Abstände zwischen VMD und Rx bekannt, kann die elektrische Leitfähigkeit bestimmt werden.
Das hier beschriebene Verfahren kehrt diese Sichtweise um. Für ein gegebenes Leitfähigkeitsmodell hängt die Form des Transienten nur noch von der Lage des Zeitfensters und den Koordinaten von VMD und den Rx ab.

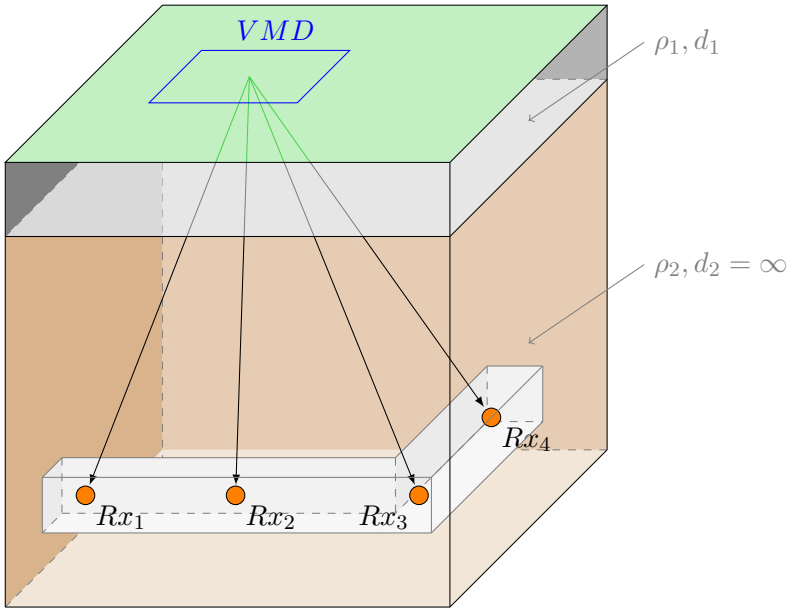

Abbildung 1: Skizze zum verwendeten 2-Schichtfall: Die quadratische Sendespule liegt als Drahtschleife an der Erdoberfläche, die Messpunkte Rx_i befinden sich in einem Stollen unter Tage. Die Pfeile zwischen dem VMD und den Rx_i symbolisieren vereinfacht den Ausbreitungsweg des transienten Magnetfeldes ohne Anspruch an physikalische Genauigkeit.

4 Theorie

Ein am Institut für Geophysik und Geoinformatik der TU Bergakademie Freiberg entwickelter 1D-TEM Vorwärtsoperator (Ward and Hohmann [1988]) berechnet Transienten für einen gegebenen geschichteten Halbraum und die entsprechenden Abstände zwischen VMD und Rx. Dieser Vorwärtsoperator kann bei festgehaltener Leitfähigkeitsverteilung auch als Baustein in einem Inversionsverfahren dienen, welches aus gemessenen Transienten die Abstände zwischen VMD und Rx bestimmt.
Das den Berechnungen zugrunde gelegte Leitfähigkeitsmodell ist durch einen Zweischichtfall unter Verwendung geologischer Informationen angenähert.

4.1 Berechnung der Abstände zwischen dem VMD und den Rx_i

In einem ersten Schritt werden die horizontalen und vertikalen Abstände $(\boldsymbol{r}, \Delta\boldsymbol{z})$ zwischen dem VMD und den Rx_i aus der Minimierung der Residuen $\boldsymbol{r}$ zwischen den Daten $\boldsymbol{d}$ (auf den Rx_i gemessenene Transienten) und den unter Verwendung des Vorwärtsoperators berechneten Transienten berechnet. Der Transient hängt dadurch nur noch von der Geometrie $(\boldsymbol{r}, \Delta\boldsymbol{z})$ ab, die im Modellvektor $\boldsymbol{m}$ zusammengefasst wird.
Die zu minimierende Funktion

$$\phi\left(\boldsymbol{m}\right) = \frac{1}{2}\left\|\boldsymbol{F}\left(\boldsymbol{m}\right) - \boldsymbol{d}\right\|_2^2 + \frac{\lambda}{2}\left\|\boldsymbol{I}(\boldsymbol{m} - \boldsymbol{m}_{\mathrm{ref}})\right\|_2^2 \tag{1}$$

ist nichtlinear. Zur Linearisierung wird eine Taylorreihenentwicklung in der Umgebung von $\boldsymbol{m}_0$ verwendet. Man erhält eine neue Funktion

$$\phi_{\mathrm{lin}}(\boldsymbol{m}) = \frac{1}{2}\left\|\boldsymbol{F}(\boldsymbol{m}_0) + \boldsymbol{J}(\boldsymbol{m}_0)(\boldsymbol{m} - \boldsymbol{m}_0) - \boldsymbol{d}\right\|_2^2 + \frac{\lambda}{2}\left\|\boldsymbol{I}(\boldsymbol{m} - \boldsymbol{m}_{\mathrm{ref}})\right\|_2^2 \tag{2}$$

$$\phi_{\mathrm{lin}}(\boldsymbol{m}) = \frac{1}{2}\left\|\boldsymbol{J}(\boldsymbol{m}_0)(\boldsymbol{m} - \boldsymbol{m}_0) - \Delta\boldsymbol{d}\right\|_2^2 + \frac{\lambda}{2}\left\|\boldsymbol{I}(\boldsymbol{m} - \boldsymbol{m}_{\mathrm{ref}})\right\|_2^2, \tag{3}$$

die zu minimieren ist. Wir setzen $\boldsymbol{m}_{\mathrm{ref}} = \boldsymbol{m}_0$, $\Delta\boldsymbol{m} = \boldsymbol{m} - \boldsymbol{m}_0$ und der besseren Lesbarkeit wegen $\boldsymbol{J}(\boldsymbol{m}_0) = \boldsymbol{J}$. Die Normen aus (3) werden aufgelöst.

$$\phi_{\mathrm{lin}}(\boldsymbol{m}) = \frac{1}{2}\left[\Delta\boldsymbol{m}^\top\boldsymbol{J}^\top\boldsymbol{J}\Delta\boldsymbol{m} - 2\Delta\boldsymbol{m}^\top\boldsymbol{J}^\top\Delta\boldsymbol{d} + \boldsymbol{d}^\top\boldsymbol{d} + \Delta\boldsymbol{m}^\top\boldsymbol{I}^\top\boldsymbol{I}\Delta\boldsymbol{m}\right] \tag{4}$$

Die Minimierung soll bezüglich $\Delta\boldsymbol{m}$ erfolgen. Somit wird (4) nach $\Delta\boldsymbol{m}$ abgeleitet und Null gesetzt.

$$0 = \frac{1}{2}\left[\Delta\boldsymbol{m}^\top\boldsymbol{J}^\top\boldsymbol{J}\Delta\boldsymbol{m} - 2\Delta\boldsymbol{m}^\top\boldsymbol{J}^\top\Delta\boldsymbol{d} + \boldsymbol{d}^\top\boldsymbol{d} + \lambda\Delta\boldsymbol{m}^\top\boldsymbol{I}^\top\boldsymbol{I}\Delta\boldsymbol{m}\right]\frac{\partial}{\partial\Delta\boldsymbol{m}} \tag{5}$$

$$0 = \boldsymbol{J}^\top\boldsymbol{J}\Delta\boldsymbol{m} - \boldsymbol{J}^\top\Delta\boldsymbol{d} + \lambda\boldsymbol{I}\Delta\boldsymbol{m} \tag{6}$$

$$\Delta\boldsymbol{m} = \left(\boldsymbol{J}^\top\boldsymbol{J} + \lambda\boldsymbol{I}\right)^{-1}\boldsymbol{J}^\top\Delta\boldsymbol{d} \stackrel{!}{=} \boldsymbol{p} \tag{7}$$

Jedes Gauß-Newton-Verfahren liefert eine Abstiegsrichtung $\boldsymbol{p}$. Die Einführung einer Schrittweite α begrenzt den Iterationsfortschritt. In jedem Iterationsschritt

$$\boldsymbol{m}_{k+1} = \boldsymbol{m}_k + \alpha\boldsymbol{p} \qquad \alpha \in (0, 1], \tag{8}$$

wird die Schrittweite α mit einem Line-search-Algorithmus bestimmt.

4.2 Line-search-Algorithmus

Der Line-search-Algorithmus passt mit dem Faktor α die über die Linearisierung $\phi_{\mathrm{lin}}(\boldsymbol{m})$ berechnete Suchrichtung $\boldsymbol{p}$ an die ursprüngliche Funktion $\phi(\boldsymbol{m})$ an. Dabei ändert sich nicht die Richtung von $\boldsymbol{p}$, sondern nur seine Länge bzw. sein Betrag. (vgl. (8))
Abbildung 2 illustriert beispielhaft die Wirkungsweise des Faktors α. Gut zu erkennen ist, dass das Minimierungsproblem $\phi_{\mathrm{lin}}(\boldsymbol{m})$ durch das Modellupdate $\Delta\boldsymbol{m}$ exakt gelöst ist $(\alpha = 1)$. Das Minimum von $\phi(\boldsymbol{m})$ für das gleiche Modellupdate $\Delta\boldsymbol{m}$ liegt im Beispiel jedoch bei $\alpha = 0.5$.
Aufgabe des Line-search ist es, ein $\alpha \in (0, 1]$ zu bestimmen, das die Schrittweite in der Abstiegsrichtung $\boldsymbol{p}$ so bestimmt, dass es dem Minimum der nichtlinearen Ausgangsfunktion nahe kommt. Dabei ist es nicht wichtig ein α zu finden, welches das Minimum exakt trifft. Es soll lediglich einen Mindestabstieg sichern. Es gibt verschiedene Methoden für die Berechnung von α. (vgl. Nocedal and Wright [2006])

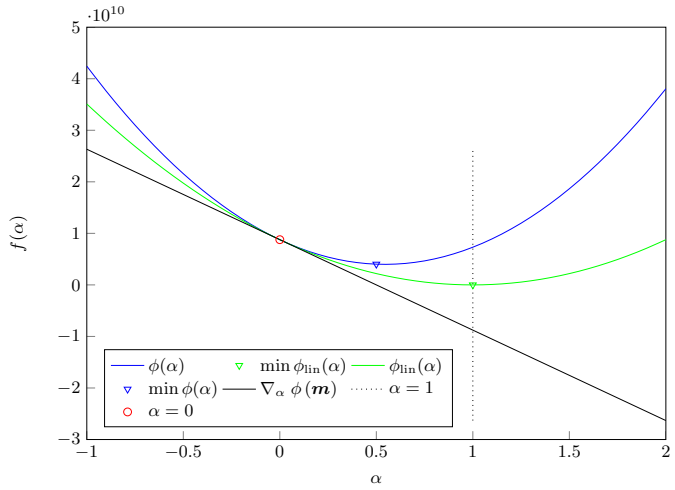

Abbildung 2: Line-search: Beispiel zur Wirkungsweise des Faktors α. Der Wertebereich ist zur besseren Ansicht auf $\alpha \in (-1, 2)$ erweitert dargestellt, da so die Form der Minimierungsfunktionen $\phi(\boldsymbol{m})$ und $\phi_{\text{lin}}(\boldsymbol{m})$ deutlich zu erkennen sind.

4.3 Berechnung der 3-D-Position mittels Least-Squares-Ansatz

Sind für jeden Messpunkt Rx die Abstände $\boldsymbol{r}$ und $\Delta \boldsymbol{z}$ bekannt, wird in einem zweiten Schritt eine Transformation die Position des VMD im gewünschten globalen kartesischen Koordinatensystem (x, y, z) berechnet.
Die 3-D-Positionen der Standorte der Rx_i sind geodätisch bestimmt und ermöglichen damit die Berechnung der Lagekoordinaten des VMD (x, y) allein aus den Radien r_i.
Das geometrische Problem ist in Abbildung 3 beispielhaft dargestellt und kann durch einen geeigneten Inversionsansatz gelöst werden.

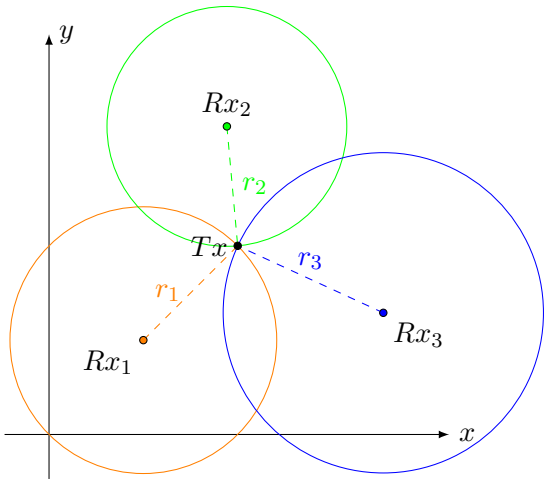

Abbildung 3: Bei einem sog. Bogenschnitt bilden die berechneten Radien ein Optimum an der Stelle, an welcher die Residuen von (10) minimal werden.

Die Bestimmungsgleichung zur Berechnung der Radien r_i ist mit

$$g_i(x, y) = r_i = \sqrt{(x - x_i)^2 + (y - y_i)^2} \tag{9}$$

gegeben, wobei die Koordinaten x und y die Lagekoordinaten des gesuchten VMD und die x_i und y_i die Lagekoordinaten der geodätisch bestimmten Rx_i sind. Mit diesem Vorwärtsoperator $\boldsymbol{g}(x, y)$ kann das Minimierungsproblem in einem Least-Squares-Ansatz formuliert werden. Die zu minimierende Funktion

$$\phi_r\,(x, y) = \frac{1}{2}\,\|\boldsymbol{g}\,(x, y) - \boldsymbol{r}\|_2^2 \qquad \text{mit } \boldsymbol{r} = [r_1, r_2, \ldots, r_n]. \tag{10}$$

ist nichtlinear. Die Linearisierung erfolgt wiederum durch eine Taylorreihenentwicklung in deren Ergebnis mit dem Modellupdate

$$\Delta_{x,y} = \left(\boldsymbol{J}_{xy}^{\top}\boldsymbol{J}_{xy}\right)^{-1}\boldsymbol{J}_{xy}^{\top}\,(\boldsymbol{r} - \boldsymbol{g}(x, y)_k) \tag{11}$$

die Rekursion

$$(x, y)_{k+1} = (x, y)_k + \left(\boldsymbol{J}_{xy}^{\top}\boldsymbol{J}_{xy}\right)^{-1}\boldsymbol{J}_{xy}^{\top}\,(\boldsymbol{r} - \boldsymbol{g}(x, y)_k)\,. \tag{12}$$

angegeben werden kann. Zur Unterscheidung der Jacobimatrix aus (7) von der Jacobimatrix aus (12) trägt diese den Index 'xy'. Diese Matrix $\boldsymbol{J}_{xy}$ enthält die Ableitungen der Funktion (9) nach den beiden Modellparametern x, y für alle bekannten Punkte Rx_i.
Als Startwert für die Iteration nach (12) wird der Mittelwert aller Lagekoordinaten der Rx_i gewählt. Damit findet das Gauß-Newton-Verfahren zuverlässig eine Lösung.
Die zuvor berechneten $\Delta\boldsymbol{z}$ ermöglichen eine direkte Berechnung der z-Koordinate des VMD unter Verwendung der globalen Höhen der Rx_i.

$$z_{\mathrm{VMD}} = \frac{\sum_{i=1}^{n} z_{Rx_i} + \Delta z_i}{n} \qquad \text{mit } i = 1, 2, \ldots, n \tag{13}$$

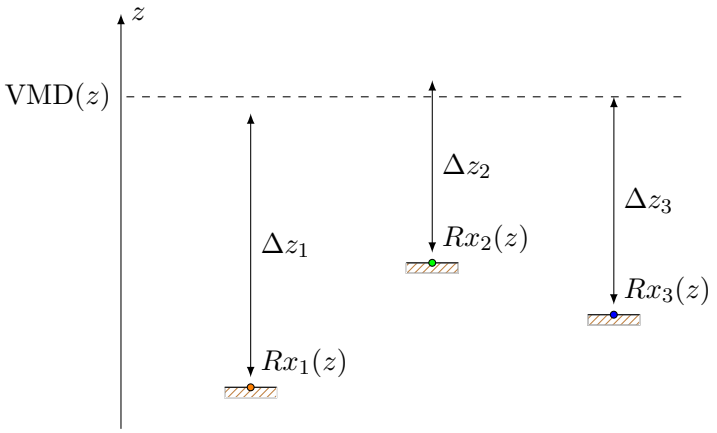

Abbildung 4: Die z-Koordinate des VMD ist auf jedem Rx_i unterschiedlich bestimmt und wird im Ergebnis durch Mittelwertbildung berechnet.

4.4 Fehlerrechnung und Konfidenzschätzung

Eine Fehlerrechung ermöglicht die Qualitätsbewertung der Ergebnisse aus den vorangegangenen Berechnungen. Die Genauigkeitsangabe zur Lageberechnung des VMD ist durch

die aus dem letzten Iterationsschritt von (10) hervorgegangene Jacobmatrix $\boldsymbol{J}_{xy}$ und das Modellupdate $\Delta(x,y) = (x,y)_{k+1} - (x,y,)_k$ möglich. Dabei werden zunächst das Residuum

$$\boldsymbol{v} = \boldsymbol{J}_{xy}\Delta(x,y) + \boldsymbol{g}(x,y) - \boldsymbol{r} \tag{14}$$

und die empirische Varianz

$$s_0^2 = \frac{\boldsymbol{v}^\top \boldsymbol{v}}{n-2} \tag{15}$$

berechnet. Die Eigenwerte der Varianz-Kovarianz-Matrix

$$\boldsymbol{C} = s_0^2 \left(\boldsymbol{J}_{xy}^\top \boldsymbol{J}_{xy}\right)^{-1} \tag{16}$$

$$\boldsymbol{C} = s_0^2 \begin{bmatrix} u_1 & u_2 \\ u_1 & u_2 \end{bmatrix} \begin{bmatrix} \lambda_1 & 0 \\ 0 & \lambda_2 \end{bmatrix} \begin{bmatrix} u_1 & u_1 \\ u_2 & u_2 \end{bmatrix} \qquad \text{mit } \lambda_1 > \lambda_2 \tag{17}$$

kennzeichnen den maximalen und minimalen Fehler

$$mp_{max} = \sqrt{s_0^2 \lambda_1} \quad \text{bzw.} \quad mp_{min} = \sqrt{s_0^2 \lambda_2} \tag{18}$$

der Lageberechnung und bilden die Hauptachsen der Helmertschen Fehlerellipse.
Die Verdrehung gegen die x-Achse ist durch den Winkel

$$\tan 2\gamma = \frac{2C_{1,2}}{C_{1,1} - C_{2,2}} \qquad \text{mit } C_{1,2} = C_{2,1} \tag{19}$$

gegeben. (vgl. Niemeier [2008])
Die empirische Varianz der z-Koordinate des VMD

$$s_z^2 = \frac{1}{n-1} \sum_{i=1}^{n} \left(z_{\text{VMD}} - z_i - \Delta z_i\right)^2 \tag{20}$$

berechnet sich ausschließlich aus den globalen Höhen der Rx_i und den zugehörigen Höhenunterschieden Δz_i zwischen dem VMD und den Rx_i.
In den meisten Fällen sind die Varianzen jedoch zu optimistisch geschätzt. Mit einem Konfidenzintervall ist ein wichtiges Kriterium zur kritischen Beurteilung des Berechnungsergebnisses gegeben. Ein gutes statistisches Werkzeug hierfür ist eine Konfidenzschätzung mit der Student-t-Verteilung. Deren Quantile t_s bilden einen Faktor mit dem $\boldsymbol{C}$ aus (16) multipliziert

$$\boldsymbol{C}_{t_s} = t_s s_0^2 \left(\boldsymbol{J}_{xy}^\top \boldsymbol{J}_{xy}\right)^{-1} \tag{21}$$

und so die Fehler- in eine Konfidenzellipse überführt wird. In gleicher Weise kann auch ein Konfidenzintervall für die Höhenberechnung des VMD angegeben werden.

5 Ergebnisse

Abbildung 5 veranschaulicht die Verhältnisse zwischen gesuchtem und berechnetem Punkt. Der horizontale Abstand zum Sollpunkt beträgt 51,7 m. Die Hauptachsen der Helmertschen Fehlerellipse wurden mit $mp_{max} = 27{,}7\,\text{m}$ und $mp_{min} = 16{,}7\,\text{m}$ bestimmt.
Nach der Konfidenzschätzung mit einer statistischen Sicherheit von 98% ergibt sich aus der Student-t-Verteilung ein Quantil von $t_s = 3.143$. Damit ergibt sich eine Konfidenzellipse, die den gesuchten Punkt mit einschließt.
Abbildung 6 zeigt die Verteilung der berechneten Höhen des VMD für jeden Rx_i. Der Mittelwert dieser Höhen weicht vom Sollwert 54,8 m ab. Das schon zuvor gewählte Konfidenzintervall von 98% schliesst den Sollwert mit ein.

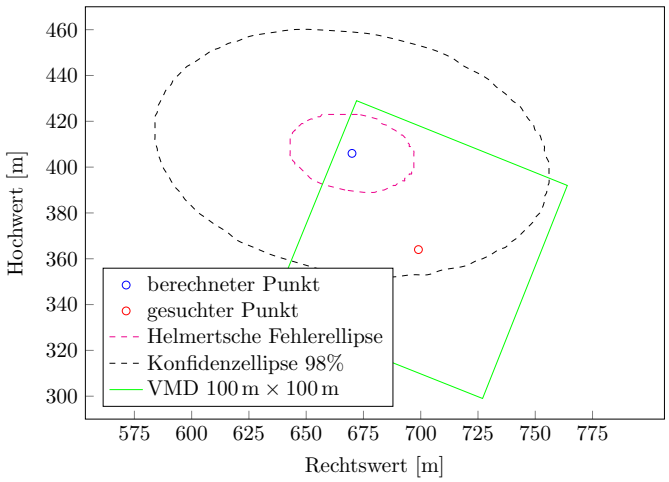

Abbildung 5: In Grün ist der an der Erdoberfläche ausgelegte VMD dargestellt, dessen Zentrum der gesuchte Punkt (Rot) bildet. In Blau ist der berechnete Punkt mit der Helmertsche Fehlerellipse (Magenta) und der Konfidenzellipse (Schwarz) eingezeichnet.

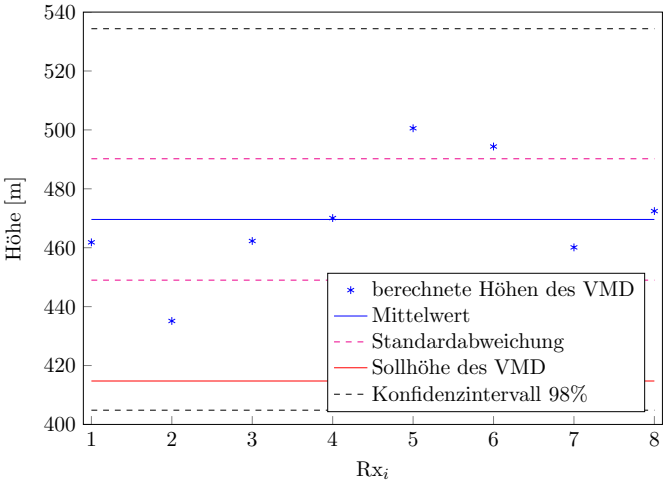

Abbildung 6: Blaue Sterne kennzeichnen die Berechnungsergebnisse der Höhe des VMD für jeden Rx$_i$ und die blaue Linie den Mittelwert aus diesen Einzelergebnissen. In Rot ist die Sollhöhe, in Magenta der mittlere Fehler und in Schwarz das 98%ige Konfidenzintervall eingetragen.

6 Schlussfolgerungen

Es konnte gezeigt werden, dass eine sichere Bestimmung der 3-D-Position eines Punktes mittels elektromagnetischer Verfahren möglich ist. Genauigkeitssteigerungen sind im bewußt einfach gehaltene Leitfähigkeitsmodell (Zweischichtfall) zu vermuten. Komplexere Strukturen die sich stärker an den im Bergwerk vorhandenen Verhältnissen orientieren, könnten dazu einen Beitrag leisten.
Die Größe des VMD läßt vermutlich kaum eine weitere Annäherung an sein Zentrum zu. In weiteren Versuchen soll daher geprüft werden, ob eine Verkleinerung der Fläche und damit eine bessere Fokussierung des VMD Genauigkeitsverbesserungen ermöglichen.
Desweiteren kann geprüft werden, ob die Parameter des aus geologischen Angaben geschätzten Leitfähigkeitsmodells in der Inversion mit bestimmt werden können. Die starke Überbestimmung des Problems könnte diesen Weg eröffnen.
Die hier vorgestellte Regularisierung der Inversion der Abstände $\boldsymbol{r}, \Delta\boldsymbol{z}$ ist noch nicht optimal. In weiteren numerischen Experimenten soll eine verbesserte Berechnung des Regularisierungsparameters λ das Verfahren beschleunigen.
Die Berücksichtigung der Fehler der Lage- und Höhenberechnung in jedem Interationsschritt der Inversion der Abstände könnte ebenfalls eine deutliche Beschleunigung der Berechnung ermöglichen.

Literatur

W. Niemeier. *Ausgleichsrechnung – Eine Einführung für Studierende und Praktiker des Vermessungs-und Geoinformationswesens.* Walter de Gruyter, Berlin-New York, 2nd rev. and ext. edition, 2008.

J. Nocedal and S. Wright. *Numerical Optimazation.* Springer Science+Business Media, LLC, 2 edition, 2006.

S. H. Ward and G. W. Hohmann. Electromagnetic theory for geophysical applications. *Electromagnetic methods in applied geophysics*, 1:131–311, 1988.

Three-dimensional MT modelling for the Pomerania region in NW Poland

Katarzyna Ślęzak[1], Krzysztof Nowożyński[1], Waldemar Jóźwiak[1], David Martens[2], and Heinrich Brasse[2]

[1]Institute of Geophysics, P. A. S., Department of Magnetism, ul. Ks. Janusza 64, 01-452 Warsaw Poland. E-mail: katarzyna.slezak@igf.edu.pl
[2]Freie Universität Berlin, Fachrichtung Geophysik, Malteserstr. 74-100, 12249 Berlin, Germany

1. Introduction

During recent years many magnetotelluric (MT) and magnetovariational (EM) soundings across the Northeast German and the Polish Basin have been realized. Two-dimensional (2-D) models were constructed for most of the obtained data of the study area. However, there are clear indications for three-dimensionality, particularly seen in the behaviour of induction vectors. Therefore 2-D modelling can only be regarded as a first step in interpretation that might even yield a false image of conductivity structures at depth. The primary objective of this work was to obtain a detailed, three-dimensional image of electrical conductivity distribution in the Earth's crust below the Trans-European Suture Zone (TESZ) in the northwest part of Poland (Pomerania). To achieve this purpose we applied a 3-D inversion code (Siripunvaraporn et al. 2005), which allowed us to obtain more realistic model geometries. We got a clearer image of the highly conductive rock complexes, which we tentatively connected to deformation fronts, as well as their position in relation to the margin of the East European Platform (Dadlez, 2000).

2. Geological background

The area covered by the survey is part of the Trans-European Suture Zone. It is the most interesting segment of this geologic structure because of the geotectonic processes which have been taking place there. This large tectonic transition zone extends from the North Sea to the Black Sea. The origin of this zone links to the collision of the Baltica Craton with younger terranes from the south and west, dating to the end of the Ordovician period. Also, more recently very significant tectonic movements occurred within this zone. As the TESZ represents a boundary of lithospheric scale separating the Precambrian East European Craton (EEC) from the Paleozoic Platform (PP), it has a fundamental importance for understanding the geodynamic processes in this part of Europe. Due to the significance of the TESZ it was subject to a number of large-scale, international seismic experiments as well as several international electromagnetic research programs (i.e., the EMTESZ project). These were conducted by the Polish Academy of Sciences in cooperation with Free University of Berlin and the Russian Academy of Sciences.

As a part of the Central European Basin System, the TESZ is covered by a thick layer of Quaternary-Paleozoic sediments along almost its entire length, so only geophysical data can provide valuable information about its deeper structures. Previous 2-D interpretation of MT profile data across the TESZ revealed a poorly conducting and deep-reaching EEC, a less resistive Paleozoic Platform and thick, highly-conducting sediments over the whole study area (Ernst et al. 2008, Habibian et al. 2010).

3. Methodology

During the recent EMTESZ project, all variants of electromagnetic methods, i.e., magnetotelluric and magnetovariational soundings were applied (Brasse et al. 2006, Ernst et al. 2008, Habibian et al. 2010, and Schäfer et al. 2011). Between 2004 and 2013 a large number of long-period soundings (T = 10 – 10 000 s) were carried out in Northwest Poland (Fig. 1). It allowed us to collect a unique, exceptional data set.

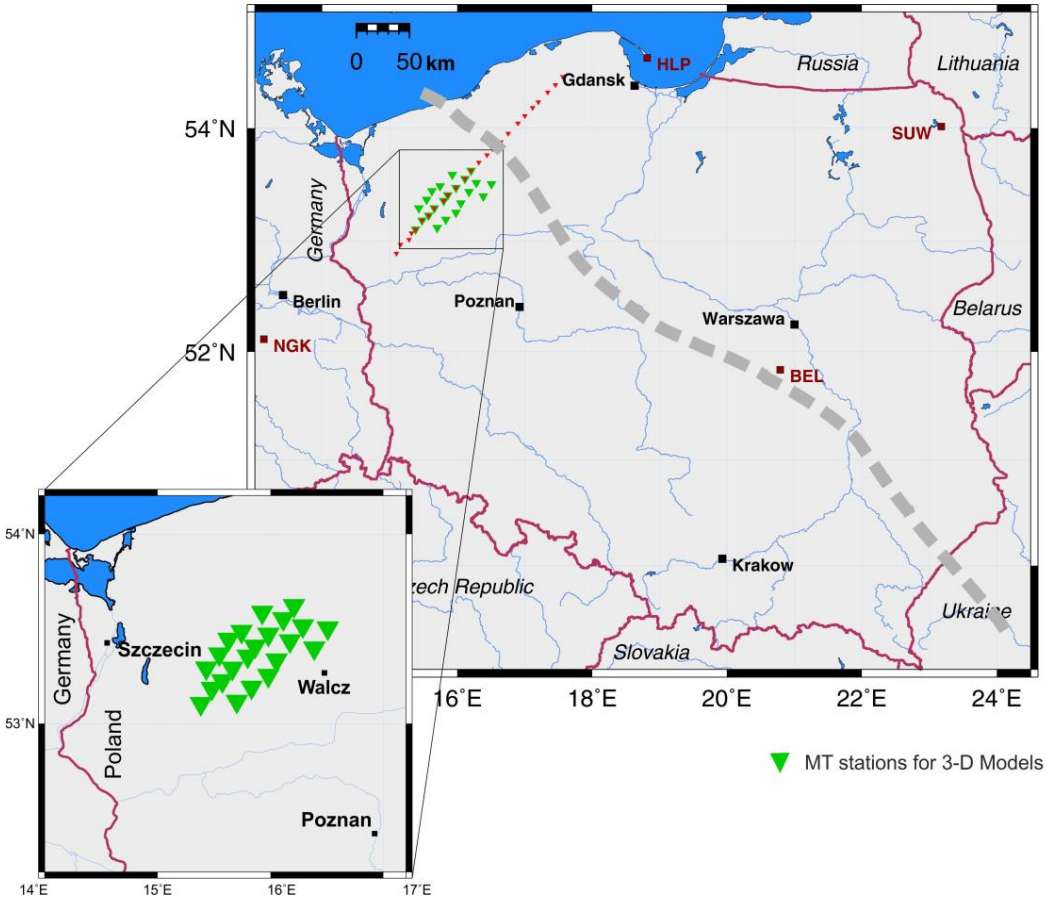

Fig. 1. Location of MT sites (red triangles represent profile LT-7 from the EMTESZ project). HLP, SUW and BEL refer to Hel, Suwalki and Belsk geomagnetic observatories which delivered data for remote reference. Approximate crude course of TESZ is outlined by grey, dashed line.

In addition to several profiles recorded earlier, we obtained 17 new sites over an area of approximately 100 km × 50 km. Data quality was usually excellent with the exception of sites which were built up in the vicinity of DC railways and commuter trains.

Induction vectors in the Polish Trough and easternmost part of the Palaeozoic Platform significantly deviate from simple 2-D behaviour, pointing even perpendicularly to the profiles (Fig. 1 and Fig. 2). The dimensionality and strike analysis employing the phase tensor method of Caldwell et al. (2004) additionally hint at a three-dimensional (3-D) subsurface beneath the TESZ (Fig. 2). 3-D behaviour of induction vectors appears in the centre of our mesh. Such effects are most likely caused by resistive salt domes, diapirs or pillows.

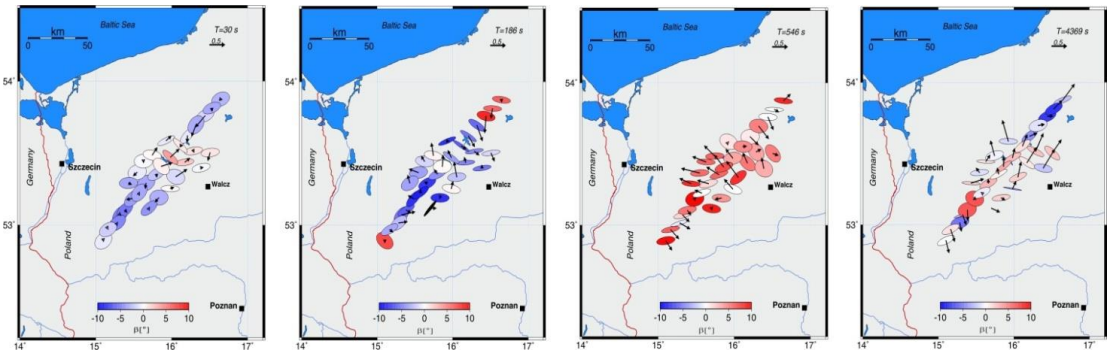

Fig. 2. Phase tensor plot and induction arrows (real parts) for selected periods. The colour code represents the skew angle as a measure of dimensionality β [°].

The WSINV3DMT code (Siripunvaraporn et al. 2005) is a full 3-D inversion program for magnetotelluric data (impedances). The inversion seeks the smoothest minimum structure model subject to an appropriate fit to the data. The 3-D modelling has been carried out for data at periods 10 - 10 000 s for the central profile alone as well as for the complete array. The overall RMS misfit was 2.03 (with 7.5 % error floor) for the full model and 1.35 for the model computed from the central profile (with 5 % error floor). An example of data fit (apparent resistivities and phases for the full impedance tensor) of the model depicted in Fig. 4 is shown in Fig. 3. Fit is very good for the minor diagonal (Zxy, Zyx) and only slightly worse for the main diagonal (Zxx, Zyy).

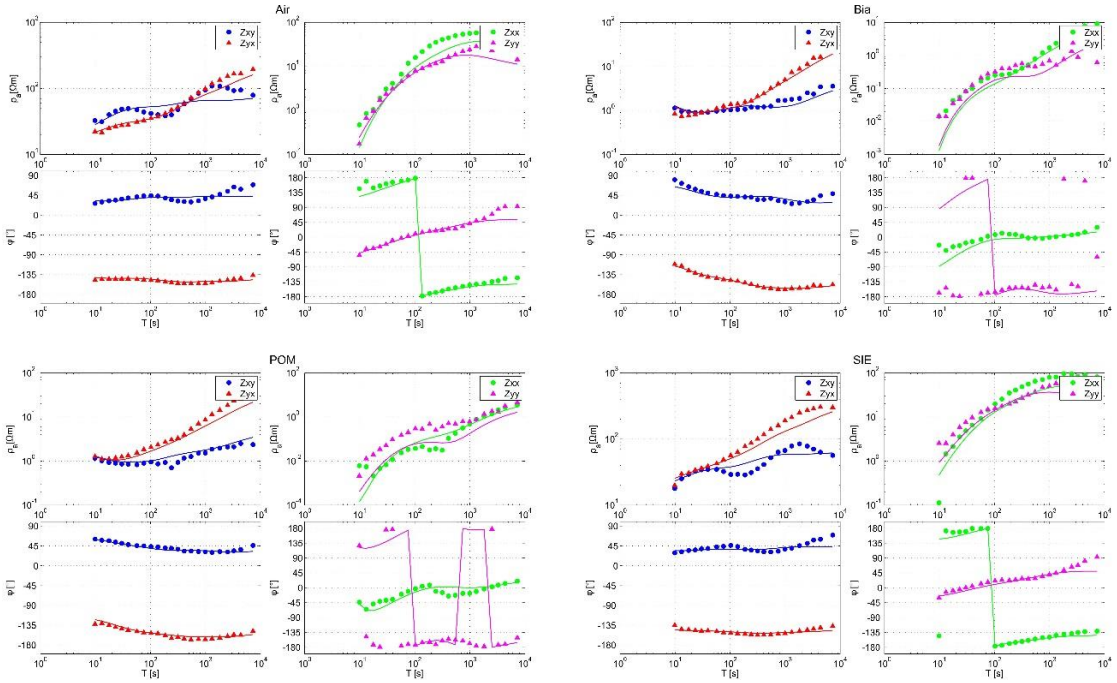

Fig. 3. Examples of data and model responses for selected sites.

The resulting model of electrical resistivity for the central part of our mesh and the full 3-D model are shown in Fig. 4. Both models show similar conductive features

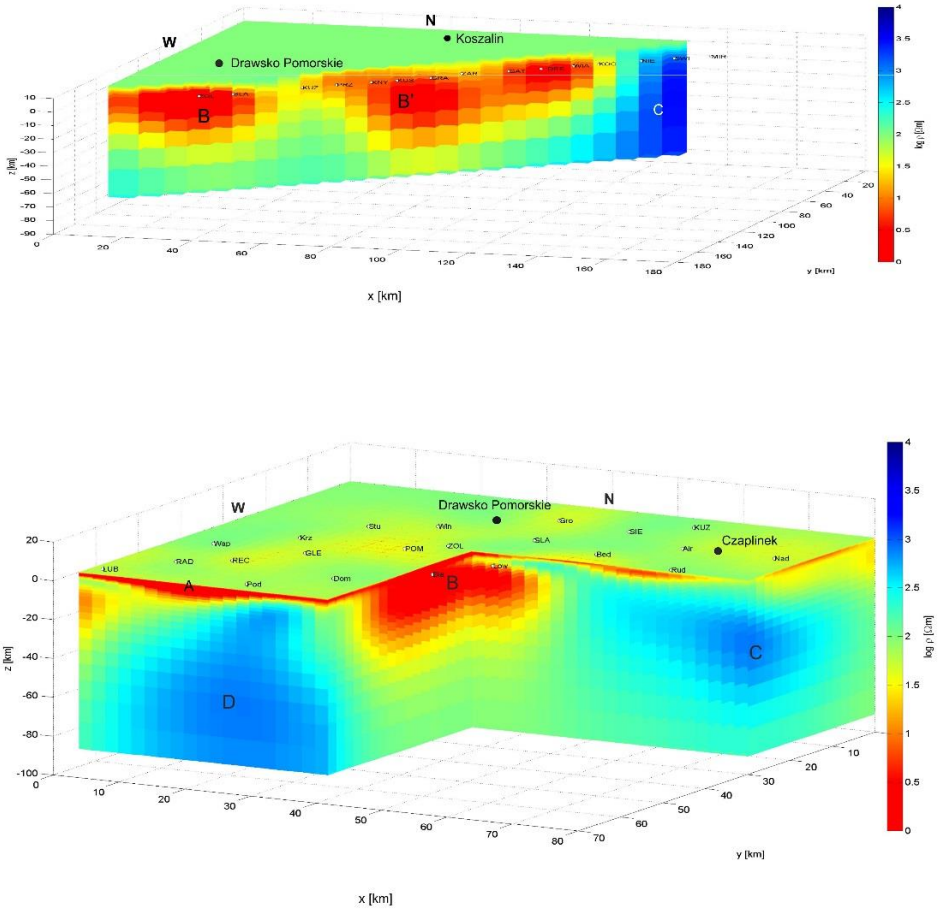

Fig. 4. Top: 3-D resistivity model along the central profile. Bottom: Section of the 3-D model, taking into account the full data set. A represents the highly-conductive sediments, B and B' are conductors associated with the Variscan and Caledonian deformation fronts, respectively. C and D point at the poorly conducting basements of the EEC and PP.

4. Conclusions

A well-conducting Cenozoic-Mesozoic sedimentary cover (A) appears in the full 3-D model (Fig. 4). Rocks in this layer with conductivity around 1-2 S/m are impregnated with saline waters, similar to findings in the NE German Basin (cf. Schäfer et al. 2011). Thickness of this layer varies throughout the model area. The higher resistive East European Craton (C) strongly marks here, and block (D) corresponds presumably to the Paleozoic Platform. Both models shown here include prominent, NW-SE striking, broad conductive lineaments which extend to depths of 10–30 km (B and B'). These structures are located in mid-crustal levels and they are related to the TESZ. The middle structure (B) in Fig. 4 we tentatively connect to the Variscan Deformation Front, the bigger N striking structure (B') may be associated with the Caledonian Deformation Front.

In the near future we plan to enhance and complete our data set of the study area with additional measurements.

Acknowledgements

This work has been funded by the Ministry of Science and Higher Education of the Republic of Poland (grants: NCN 2011/01/B/ST10/07046 and NCN 2011/01/B/ST10/07305) and German Science Foundation (grant: BR1351/9-1).

References:

[1] Brasse, H., and EMTESZ Working Group (2006): Electrical conductivity of the Trans-European Suture Zone, *EOS*, 87 (29), paper 2006ES001383.

[2] Caldwell, T.G., H.M. Bibby, and C. Brown (2004): The magnetotelluric phase tensor, *Geophys. J. Int.*, 158, 457-469.

[3] Dadlez, R. (2000). Pomeranian Caledonides (NW Poland), fifty years of controversies: a review and a new concept. Geol. Quart., 44(3), 221–236.

[4] Ernst, T., H. Brasse, V. Cerv, N. Hoffmann, J. Jankowski, W. Jozwiak, A. Kreutzmann, A. Neska, N. Palshin, L. Pedersen, M. Smirnov, E. Sokolova, and I. M. Varentsov (2008), Electromagnetic images of the deep structure of the Trans-European Suture Zone beneath Polish Pomerania, *Geophys. Res. Lett.*, 35, doi:10.1029/2007GL034610.

[5] Habibian, B.D., Brasse, H., Oskooi, B., Ernst, T., Sokolova, E., Varentsov, I., and EMTESZ Working Group (2010): The conductivity structure across the Trans-European Suture Zone from magnetotelluric and magnetovariational data modeling, *Phys. Earth Planet. Inter.*, 183, doi:10.1016/j.pepi.2010.08.005.

[6] Schäfer, A., Houpt, L., Brasse, H., Hoffmann, N., and EMTESZ Working Group (2011): The North German Conductivity Anomaly revisited, *Geophys. J. Int.*, 187, doi:10.1111/ j.1365-246X.2011.05145.x.

[7] Siripunvaraporn, W., Egbert, G., Lenbury, Y., and Uyeshima, M. (2005): Three-dimensional magnetotelluric inversion: data-space method, *Phys. Earth Planet. Inter.*, 150, 3-14.

Einfluss dreidimensionaler anisotroper Strukturen auf Bipol-Quadrupol Geoelektrik und Audimagnetotellurik Messungen

Annika Rödder[1] and Andreas Junge[1]

[1] *Institut für Geowissenschaften, Goethe-Universität Frankfurt am Main*

1 Einleitung

Modellierungen von geoelektrischen scheinbaren spezifischen Widerstandstensoren und magnetotellurischen Phasentensoren zeigen eine große Sensitivität beider Größen für anisotrope Leitfähigkeitsanomalien. Die scheinb. spez. Widerstandstensoren haben zudem den großen Vorteil, dass in ihnen alle Richtungsinformationen der zur Berechnung verwendeten elektrischen Felder enthalten sind. Bei einfachen „in-line“ Multielektroden Geoelektrik Messungen werden dagegen nur die Felder in Richtung der Elektrodenauslage verwendet. Generell ist das Muster der Stromdichteverteilung $\underline{J}$ stark von der Stromeinspeisedipol-Richtung abhängig. In Abb. 1 ist diese Verteilung beispielhaft für zwei verschiedene Strondipolrichtungen durch die roten Pfeile dargestellt. Der farbige Hintergrund zeigt die Potentialverteilung, der schwarze Pfeil markiert Lage und Orientierung des Stromeinspeisedipols. In beiden Fällen wird der Strom im linken schlecht leitenden $1000\Omega m$ Viertelraum eingespeist, der spezifische Widerstand des rechten Viertelraums beträgt $10\Omega m$.

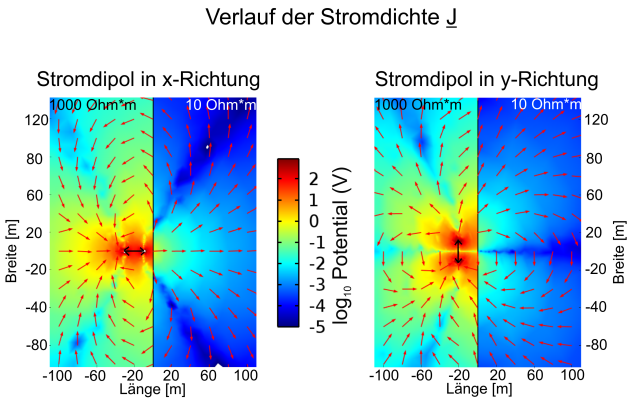

Abbildung 1: Vergleich des Potentials (farbig) und des Verlaufs der Stromdichte $\underline{J}$ für unterschiedliche Stromeinspeiserichtungen in einem schlecht leitenden $1000\Omega m$ Viertelraum. Der schwarze Pfeil zeigt Lage und Orientierung des Dipols. Bei der Stromeinspeisung parallel zum Widerstandskonstrast zum gut leitenden $10\Omega m$ Viertelraum werden die Ströme nur leicht abgelenkt (links), beim Einspeisen senkrecht dazu erfahren die Stromsysteme eine starke Ablenkung an der Grenzfläche (rechts).

Bei Stromeinspeisung senkrecht zum Widerstandskontrast (linkes Bild) werden die Felder an der Grenze der Viertelräume nur leicht abgelenkt, bei paralleler Einspeisung (rechts) werden die Ströme im oberen Teil regelrecht in den guten Leiter hineingezogen und dort

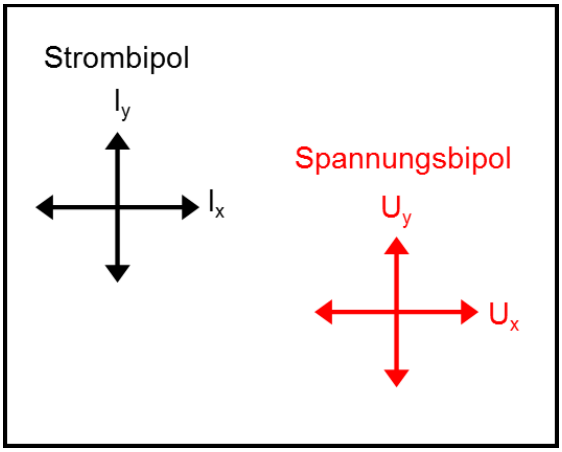

Abbildung 2: Skizze eines Bipol-Quadrupol Aufbaus. Die schwarzen Pfeile stellen die Stromdipole dar, mit denen nacheinander eingespeist wird, in rot ist ein Spannungsbipol eingezeichnet. Hier werden die Spannungen in x- und y-Richtung mit einem Datenlogger aufgezeichnet.

vom Lot weg abgelenkt.
Da bei anisotropen Strukturen die Widerstandsverteilung an sich schon richtungsabhängig ist, ist es umso wichtiger, die Informationen aus verschieden Stromeinspeiserichtungen zu kombinieren. Daher wurde für diese Arbeit die Bipol-Quadrupol Auslage mit den daraus nach Bibby [1986] berechneten scheinb. spez. Widerstandstensoren verwendet. Im folgenden Text wird zwischen zwei Polen mit von Null verschiedenem Abstand (Bipol) und infinitisimalem Abstand (Dipol) unterschieden.

2 Bipol-Quadrupol Geoelektrik

Bei der Bipol-Quadrupol Geoelektrik handelt es sich um eine kombinierte Messung von Strom- und Spannungsmessungen an beliebigen Orten in unterschiedlichen Richtungen. Die Skizze in Abb. 2 soll das Schema einer Messung verdeutlichen. Mit einem Datenlogger werden die Spannungen in x- und in y-Richtung aufgezeichnet (rot). An anderer Stelle wird erst an einem Bipol in x-Richtung und anschließend dazu senkrecht in y-Richtung ein Strom eingespeist (schwarz).
Aus der Spannung U_x lässt sich nun das elektrische Feld E_{xIy} bei einer Stromeinspeisung I_y bestimmen und am Ort der Spannungsmessung die zu dieser Bipolkonfiguration gehörige Stromdichte J_{xIy} für einen homogenen Halbraum berechnen. Man beachte, dass die Stromdichte unabhängig vom Widerstand des Halbraumes ist! Für alle Dipolkombinationen erhält man so vier elektrische Feldstärken und vier Stromdichten. Aus diesen lässt sich nach Bibby [1986] der scheinbare spezifische Widerstandstensor $\underline{\rho}$ berechnen:

$$\underline{\rho} = \begin{pmatrix} E_{xIx}J_{yIy} - E_{xIy}J_{yIx} & E_{xIy}J_{xIx} - E_{xIx}J_{xIy} \\ E_{yIx}J_{yIy} - E_{yIy}J_{yIx} & E_{yIy}J_{xIx} - E_{yIx}J_{xIy} \end{pmatrix} / \left(J_{xIx}J_{yIy} - J_{xIy}J_{yIx}\right) \qquad (1)$$

Alternativ lässt sich der Widerstandstensor über seine Invarianten und zwei Rotationsmatrizen ausdrücken:

$$\underline{\rho} = \Pi_1 \begin{pmatrix} cos2\alpha & sin2\alpha \\ sin2\alpha & -cos2\alpha \end{pmatrix} + \Pi_2 \begin{pmatrix} cos2\beta & sin2\beta \\ -sin2\beta & cos2\beta \end{pmatrix} \qquad (2)$$

Diese Parameter lassen sich als Ellipse darstellen, indem man die Größen ρ_{max}, ρ_{min} als

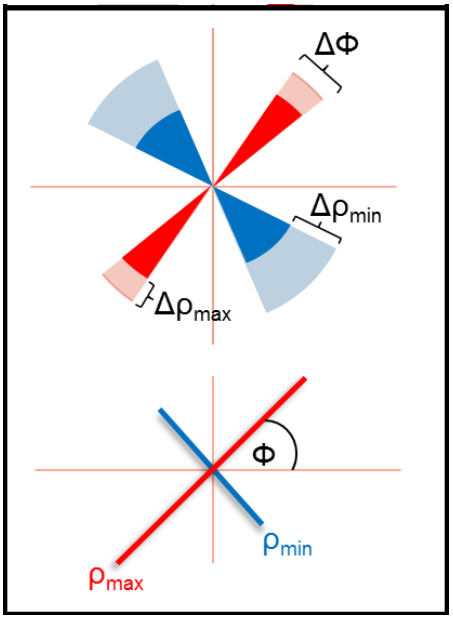

Abbildung 3: Skizze der Darstellung von ρ_{max},ρ_{min} und Φ für gemessene Daten mit Fehlern (oben) und modellierte Daten (unten). Ihr Wert wird über die Farbe dargestellt. Bei den Messdaten ist die Länge der Kreissegmente normiert, die Breite des transparenten Bereichs stellt den Fehler im Widerstand dar, die Breite gibt den Fehler des Winkels wieder. Bei modellierten Daten spiegelt auch die Länge der Balken ihren Wert wieder.

die Länge ihrer Hauptachsen sowie Φ als ihren Rotationswinkel definiert:

$$\rho_{max} = \Pi_1 + \Pi_2 \tag{3}$$
$$\rho_{min} = \Pi_1 - \Pi_2 \tag{4}$$
$$\Phi = \alpha - \beta \tag{5}$$

Zur Darstellung der Messdaten und Modellierungen werden im Folgenden allerdings keine Ellipsen sondern Balken bzw. Kreissegmente, deren Farben die Widerstandswerte angeben, verwendet (s. Abb. 3). Die obere Skizze zeigt ein Beispiel für Messdaten. Ihre Fehler werden hier durch die transparenten Bereiche und die Breite des Segments gezeigt. Die Gesamtlänge aller Kreissegmente ist normiert: desto größer der transparente Bereich erscheint, desto ungenauer ist der Wert bestimmt. Da die modellierten Widerstandstensoren keinen Fehler haben, werden im unteren Teil der Skizze in Abb.3 nur farbige Balken dargestellt. Um das Verhältnis von ρ_{max} zu ρ_{min} besser zu verdeutlichen, sind in diesem Fall auch die Längen der Balken proportional zum Wert des Widerstandes.

3 Modellrechnungen

Zur Untersuchung des Einflusses einer anisotropen Anomalie auf Widerstands- und Phasentensoren wurden einfache Vorwärtsmodellen mittels *COMSOL Multiphysics* berechnet. In einem $100\Omega m$ Halbraum wurde ein $400 \times 400 \times 1000m$ großer Störkörper direkt an der Oberfläche beginnend eingefügt. Im isotropen Modell hat dieser einen spezifischen Widerstand von $316\Omega m$. Im anisotropen Modell beträgt der spezifische Widerstand in x-Richtung $\rho_{xx} = 1000\Omega m$ und in y- und z-Richtung $\rho_{yy} = \rho_{zz} = 316\Omega m$.
In Abb. 4 sind die modellierten scheinbaren spezifischen Widerstandstensoren für das oben beschriebene Modell dargestellt. Bei der oberen Abbildung wurde der Strom bei $150m|150m$, also direkt in den Störkörper, eingespeist, bei der unteren lag der Einspeisepunkt (markiert durch den schwarzen Kreis) außerhalb bei $300m|0m$. Die linken Bilder zeigen jeweils die Ergebnisse mit dem anisotropen Störkörper, im rechten Bild ist die Anomalie isotrop. Bei der Einspeisung im schlecht leitenden Störkörper zeichnet sich dieser

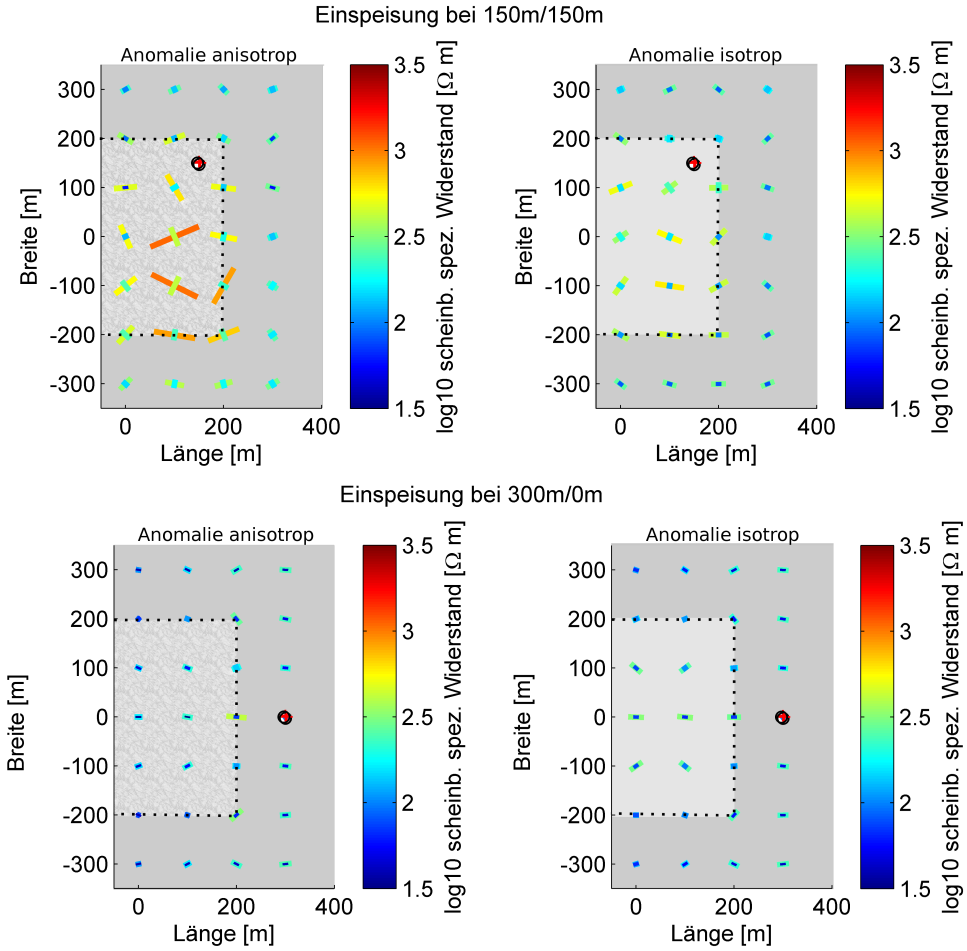

Abbildung 4: Spezifische Widerstandstensoren für zwei Einspeisepunkt (schwarze Kreise) mit isotropem (rechts) und anisotropem (links) Störkörper. Bei der Stromeinspeisung in die schlechter leitende Anomalie zeichnen sich deren Umrisse deutliche ab, wobei die Anisotropie einen starken Einfluss auf die Elliptizität hat. Bei Einspeisung außerhalb des Störkörper (unten) ist kaum ein Unterschied zwischen den beiden Modellen erkennbar.

deutlich ab. Im anisotropen Fall ist ρ_{max} deutlich größer als ρ_{min} und ihre Werte sind stark vom Abstand zur Stromeinspeisung abhängig. Die Werte des Widerstandes außerhalb des Störkörpers werden vor allem im unteren Bereich deutlich überschätzt.
Wird der Strom außerhalb der Anomalie eingespeist, ist der Unterschied zwischen dem isotropen und anisotropen Modell viel geringer. In beiden Fällen liegen die Werte von ρ_{min} und ρ_{max} deutlich unter den Modellwiderständen. Im anisotropen Fall sind sie sogar noch geringer als im isotropen Fall, obwohl der Widerstand in x-Richtung um das dreifache größer gewählt war.
Die Werte des scheinbaren spezifischen Widerstandstensors sind also sehr stark von der Einspeiseposition abhängig. Und obwohl der Tensor sehr sensitiv auf Anisotropie im Untergrund reagiert, kann diese übersehen werden, wenn dort kein Strom eingespeist wird. Für Feldmessungen ist es also wichtig, an vielen unterschiedlichen Orten Strom einzuspeisen, gerade wenn kleinräumige anisotrope Strukturen vermutet werden. Zu beachten ist

weiterhin, dass die unterschiedlichen Widerstandstensoren sehr unterschiedliche Tiefeninformationen enthalten. Auch wenn sie hier in einer Ebene dargestellt werden, ist diese keinesfalls als Tiefenschnitt zu verstehen. Der Mittelpunkt von ρ_{min} und ρ_{max} befindet sich hier über dem Mittelpunkt des zur Berechnung verwendeten Spannungsquadrupols.
Abb. 5 zeigt die modellierten Phasentensoren [Caldwell et al. 2004] in der Balkendarstellung [Häuserer & Junge 2011] an den gleichen Positionen wie die Widerstandstensoren für $32kHz$ (oben) und $512Hz$ (unten). Für beide Frequenzen ist der Einfluss der Anisotropie deutlich durch die gegenüber ϕ_{min} erhöhten ϕ_{max} Werte zu erkennen. Würde es sich hier bei diesem Effekt um den Einfluss der 3D Struktur des Störkörpers handeln, so müsste er sich auch im isotropen Fall zeigen. Beim isotropen Störkörper sind allerdings ϕ_{min} und ϕ_{max} fast gleich groß, auch wenn ihre Werte innerhalb des Störkörpers etwas größer als 45° sind. Für größere Eindringtiefen werden diese Effekte abgeschwächt. Dafür sehen auch Stationen außerhalb der anisotropen Zone ihren Einfluss und auch im isotropen Modell erhöht sich ϕ_{max} außerhalb des Störkörpers etwas.

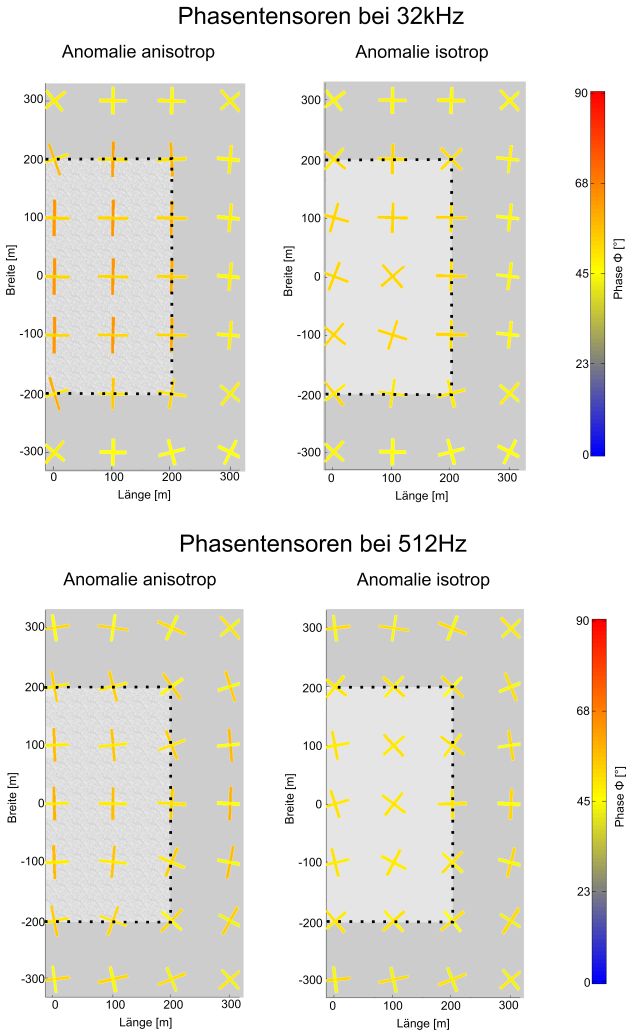

Abbildung 5: Phasentensoren berechnet für zwei Frequenzen mit isotropem (rechts) und anisotropem (links) Störkörper. Bei $32kHz$ zeigen sich deutlich die Umrisse der Anomalie. Im anisotropen Fall sind hierbei allerdings sowohl ϕ_{min} als auch ϕ_{max} deutlich größer als im isotropen Fall, wo sie nur leicht höher als 45° sind. Bei abnehmenden Frequenzen (wie in der unteren Abb. bei $512Hz$) ist der Einfluss der Anomalie, wie erwartet, auch schon bei Stationen in größerer Entfernung zu erkennen, dafür aber schwächer. Auch der Einfluss der Anisotropie ist nun außerhalb des Störkörpers feststellbar.

Abbildung 6: Stationsaufbau der Bipol-Quadrupol Testmessung im Mai 2013. Die einzelnen Markierung *mid_gxy* zeigen die Position der Spannungsbipol-Mittelpunkte. Die Markierungen *I1* bis *I4* zeigen die Lage der Elektroden zur Stromeinspeisung.

4 Messung

Zur Beobachtung einer oberflächennahen anisotropen Leitfähigkeitsverteilung in der Natur haben wir eine Lokation im nördlichen Westerwald im rheinischen Schiefergebirge ausgewählt. Dort finden sich unterschiedlich stark geschieferte Grauwacken, Sandstein- und Tonschiefer. Die Streichrichtung verläuft in NO-SW Richtung parallel zum variszischen Streichen. Das Fallen der Schieferung ist durch die vergangenen Faltungsprozesse lokal sehr unterschiedlich und variiert zwischen horizontaler bis hin zu senkrechten Lagerung [Quiring 1935].
Für die Testmessung im Mai 2013 wurden auf einer Wiese fünf Datenlogger mit Spannungsbipolen aufgestellt. Zwischen den Spannungsbipolen wurde an vier unterschiedlichen Positionen Strom eingespeist (*I1* bis *I4*, s. Abb. 6).
Aus den gemessenen Spannungen wurden für die unterschiedlichen Stromeinspeisungen die scheinbaren spezifischen Widerstandstensoren berechnet und ihre Invarianten wie oben beschrieben als Kreissegmente dargestellt. Abb. 7 zeigt die Tensoren für zwei der vier Stromeinspeisungen. Im oberen Bild sind die Werte für die erste Stromeinspeisung bei $103m|22m$ gezeigt (markiert durch den weißen Punkt). Auffällig ist, dass alle ρ_{max} Werte zwischen $400\Omega m$ und $1000\Omega m$ liegen, die ρ_{min} variieren zwischen $30\Omega m$ und $200\Omega m$. Die Ausrichtung der ρ_{max} Achsen in NO-SW-Richtung entspricht ungefähr der erwarteten Streichrichtung.
Im unteren Teil der Abbildung ist die vierte Stromeinspeisung bei $126m|-32m$ gezeigt. Die Werte der Widerstände sind ähnlich groß wie bei der ersten Einspeisung, allerdings ist bei *mid_g32* unten in der Mitte kaum ein Unterschied zwischen ρ_{min} und ρ_{max} erkennbar, wie man es für den homogenen Fall erwarten würde. Der große Fehlerbereich für den Rotationswinkel deutet zusätzlich auf einen homogenen Bereich hin, da sich dort keine Vorzugsrichtung bestimmen lässt. Die Ausrichtung der anderen Achsen ist hier nicht so gleichförmig wie bei der Stromeinspeisung bei *I1*. Allerdings liegen die relativen Fehler z.T. bei mehr als 50%.
Bei nicht gezeigten Einspeisungen rotieren die Tensoren auch leicht unterschiedlich, die Widerstandswerte bleiben aber ähnlich. Man kann also allein durch diese einfache Darstellung

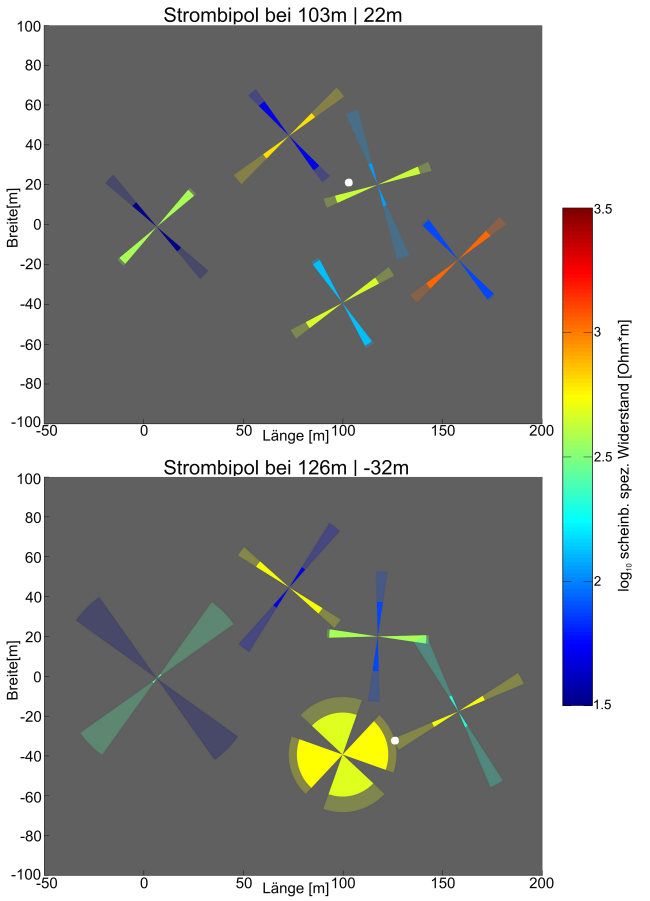

Abbildung 7: Berechnete scheinbare spezifische Widerstandstensoren für Stromeinspeisung *I1* oben und *I4* unten. Die weißen Punkte markieren die Mittelpunkte der Strombipole, die Tensorinvarianten sind wieder an der Position der Spannungsbipolmittelpunkte eingezeichnet. In der oberen Abbildung ist eine einheitliche Ausrichtung zu erkennen, die ρ_{max}-Achsen zeigen in NO-SW-Richtung, die ρ_{min}-Achsen in NW-SO Richtung. Im unteren Bild ist die Ausrichtung nicht mehr so einheitlich: Z.B. bei dem Messpunkt unten in der Mitte sind die Werte der Achsen im Gegensatz zu den restlichen Messungen nahezu gleich groß. Allerdings liegen die relativen Fehler z.T. bei 50%

und mit nur vier Einspeisepunkten schon erkennen, dass sich der Untergrund kleinräumig ändern muss.

Zur Auswertung der Daten wurde zunächst eine isotrope 3D Inversion der einzelenen Messkonfigurationen, also nicht der Widerstandstensoren, gemacht. Dazu wurde das Programm *BERT (Boundless Electrical Resistivity Tomography)* von Günther et al. [2006] verwendet. Aufgrund der verwendeten Elektroden-Anordnungen und den so entstandenen sehr großen Geometriefaktoren wurde nur ca. ein Drittel der gemessen Daten für die Inversion verwendet. Da wir aber alle gemessen Daten mit unserem Modell erklären möchten, werde ich hier nicht genauer auf die Inversionsergbnisse eingehen. Um das Inversionsmodell auch für die nicht verwendeten Daten zu testen, wurde ein daraus entwickteltes, vereinfachtes Vorwärtsmodell mit *COMSOL Multiphysics* berechnet. Im folgenden werden anstatt der scheinb. spez. Widerstandstensoren die elektrischen Felder für die unterschiedlichen Stromeinspeiserichtungen gezeigt.

Abb. 8 zeigt eine Aufsicht auf das berechnete Vorwärtsmodell. Der grüne Bereich im Norden wurde mit $500\Omega m$ angenommen, der orangene, südliche Bereich hat $1000\Omega m$. Die Punkte markieren die Mittelpunkte der verwendeten Spannungsbipole, das Kreuz zeigt den Einspeisebipol, der der ersten Stromeinspeisung *I1* bei der Messung entspricht. Im Verlauf der Modellierung wurden verschiedene Kombinationen von isotropen und anisotropen Widerstandsverteilungen in diesem Modell getestet. Die hier gezeigten Ergebnisse

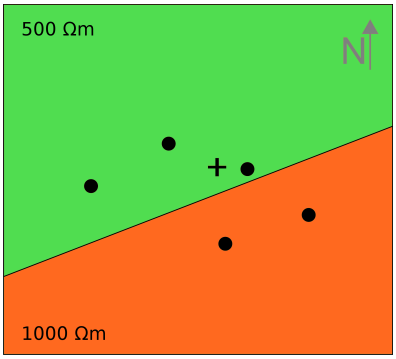

Abbildung 8: Einfaches Vorwärtsmodell nach dem 3D Inversionsmodell. Der südliche Teil ist schlechtleitend mit $1000\Omega m$, der nördliche Bereich ist mit $500\Omega m$ etwas besser leitend. Die Punkte markierten die Positionen der Spannungsbipole, das Kreuz markiert die hier gezeigte Einspeiseposition. Im zweiten Fall wurde der südliche Bereich als anisotrop angenommen: in Streichrichtung der Anisotropie von 50°N und mit einem Fallen von 22° SW $\rho_{xx} = \rho_{zz} = 500\Omega m$, senkrecht dazu $\rho_{yy} = 1000\Omega m$.

des anisotropen Modells in Abb. 9 unten entsprechen einem Modell mit einer anisotropen Widerstandsverteilung im südlichen Bereich. Hierzu wurden die Streichrichtung der Anisotropie mit 50°N und ihr Fallen mit 22°SW angenommen. Der spezifische Widerstand in Streichrichtung beträgt $\rho_{xx} = \rho_{zz} = 500\Omega m$, senkrecht dazu wurde $\rho_{yy} = 1000\Omega m$ festgelegt.
Zur Darstellung der gemessenen elektrischen Felder wurden Kreissegmente gewählt. In einem Bild sind immer die an den fünf Spannungsbipolen gemessenen Felder bezüglich einer Stromeinspeisereichtung gezeigt. In Abb. 9 sind so auf der linken Seite die Felder für die Stromeinspeisung in Nord-Süd-Richtung, rechts die Einspeisung mit dem Ost-West Dipol dargestellt. Die Position der Stromelektroden ist mit schwarzen Kreuzen markiert. Da die Daten fehlerbehaftet sind, wird die Richtung des gemessenen Feldes als Bereich angegeben. Der mittlere Absolutbetrag des Feldes ist über die Farbe angegeben. Die Pfeile zeigen in die Richtung der modellierten elektrischen Felder, auch hier gibt die Farbe ihren Betrag an.
Für das isotrope Modell kann man im oberen Teil der Abbildung erkennen, dass für beide Richtungen einige Punkte gut angepasst werden, bei anderen Stationen zeigt das Feld fast in die entgegen gesetzte Richtung. Durch Hinzufügen der Anisotropie (unten) lassen sich die Daten am östlichsten Punkt bei N-S-Einspeisung und am westlichsten Punkt bei O-W-Einspeisung besser anpassen. Bei den anderen Punkten ist kaum ein Unterschied bemerkbar. Auffällig ist besonders die Verbesserung beim westlichen Punkt mit der O-W Einspeisung, obwohl dieser außerhalb des anisotropen Bereichs liegt.
Die großen Abweichungen, z.B. am südlichen Punkt, lassen sich mit keinem der berechneten einfachen Modelle erklären. Hier wurden aber auch schon in den Widerstandstensoren in Abb. 7 starke Abbhängigkeiten von der Einspeiseposition festgestellt, die auf lokale Variationen der Widerstandsverteilung im Untergrund hindeuten. Um die Daten also mit Modellen erklären zu können, sind kleinräumige Strukturen notwendig.

5 Zusammenfassung und Ausblick

Zur Erfassung der richtungsabhängigen Einflüsse in der Geoelektrik und zur Berechnung des scheinbaren spezifischen Widerstandstensors eignen sich Bipol-Quadrupolmessungen. Die Methode ist einfach und schnell anzuwenden und im Feld praktikabel. Die Auswertung mittels 3D Inversion gestaltet sich aufgrund der großen Geometriefaktoren als schwierig, weshalb vorerst auf Vorwärtsrechnungen zurückgegriffen wird. Die gezeigten Modellrechnungen bestätigen die Vermutung, dass der scheinbare spezifische Widerstandstensor sehr

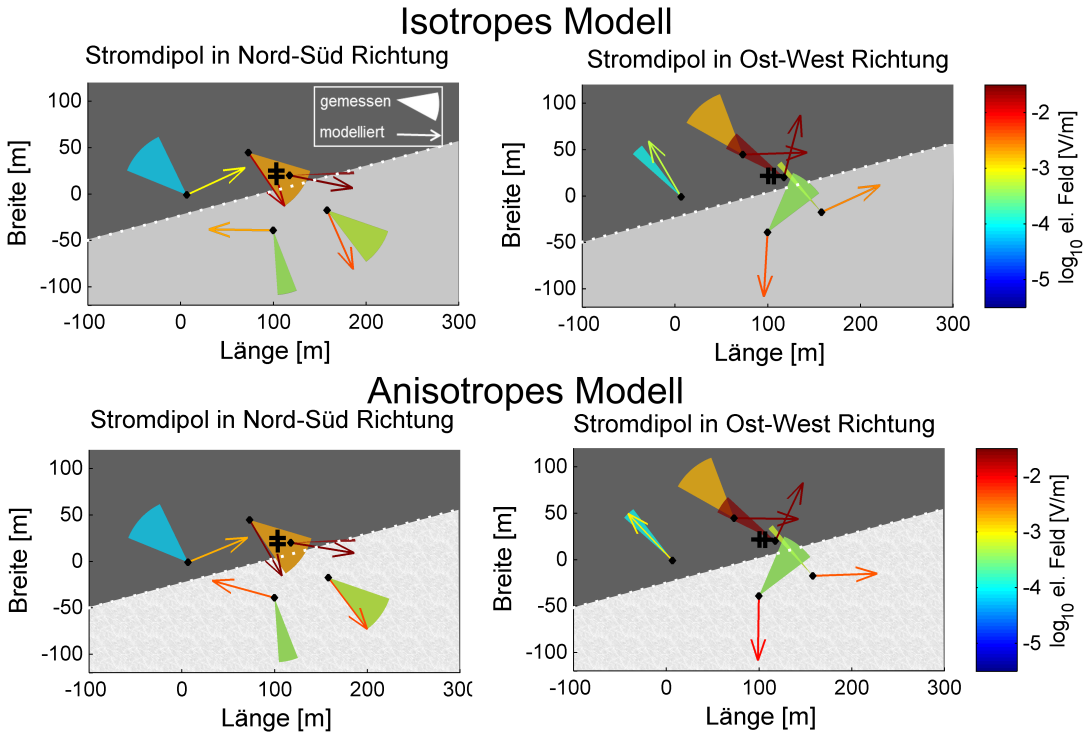

Abbildung 9: Vergleich der gemessenen und modellierten normierten elektrischen Felder für das Modell aus Abb.8. Oben sind die Ergebnisse für das isotrope Modell gezeigt, unten ist der südliche Bereich anisotrop gewählt. Die Kreissegmente zeigen die Richtung des normierten gemessenen elektrischen Feldes, wobei ihre Breite ihren Fehlerbereich überdeckt. Der Betrag des elektrischen Feldes ist über die Farbe wiedergegeben. Die Pfeile zeigen in Richtung des modellierten E-Feldes, auch hier ist der Betrag über die Farbe angegeben. Die schwarzen Kreuze markieren die Lage der verwendeten Stromelektroden. Auf der linken Seite sind somit die elektrischen Felder für eine Stromeinspeisung in Nord-Süd gezeigt, recht wurde der Strom in Ost-West-Richtung eingespeist.

sensitiv für anisotrope Widerstandsverteilungen ist. Auch Phasentensoren reagieren auf anisotrope Anomalien. Die gezeigten Daten werden durch das anisotrope Modell besser angepasst, lassen sich allerdings mit dem hier gezeigten Modell nicht vollständig erklären. Die lokalen Variationen in den scheinbaren spezifischen Widerstandstensoren und elektrischen Feldern deuten auf einen sehr komplexen Untergrund hin, welcher mit weiteren Modellen besser erklärt werden soll.
Desweiteren ist eine Sensitivitätsstudie bzgl. des Einflusses der Anisotropie geplant.
Im Juni 2014 gibt es eine weitere Messkampagne in Kooperation mit dem *LIAG*, bei der großflächiger und mit mehr Datenloggern gearbeitet wird. Zusätzlich werden dann noch Magnetotellurik Messungen durchgeführt.

Literatur

Bibby, H. M. (1986). Analysis of multiple-source bipole-quadripole resistivity surveys using the apparent resistivity tensor. *Geophysics*, *51*, 972-983.

Caldwell, T., Bibby, H. & Brown, C. (2004). The magnetotelluric phase tensor. *Geophys. J. Int.*, *158*, 457-469.

Günther, T., Rücker, C. & Spitzer, K. (2006). 3-d modeling and inversion of DC resestivity data incorporating topography - Part II: Inversion. *Geophys. J. Int.*, *166(2)*, 506-517.

Häuserer, M. & Junge, A. (2011). Electrical mantle anisotropy and crustal conductor: A 3D conductivity model of the Rwenzori region in western Uganda. *Geophys. J. Int.*, *185*, 1235-1242.

Quiring, H. (1935). Erläuterungen Blatt: Wissen Nr. 3039. In *Geologische Karte von Preußen.*

Investigations of submarine gas hydrates and methane seep sites on Opouawe Bank, Hikurangi Margin, New Zealand

Dennis Rippe[1], Martin Engels[1], Katrin Schwalenberg[1], and Carsten Scholl[2]

[1] *Bundesanstalt für Geowissenschaften und Rohstoffe, Stilleweg 2, 30655 Hannover, Germany*
[2] *CGG Electro Magnetics (Germany GmbH), Pettenkofer Str. 16-18, 10247 Berlin, Germany*

Abstract

Previous geophysical measurements found several methane seep sites and wide-spread bottom simulating reflectors along the Hikurangi Margin in New Zealand. To study the variability of methane seepage and the distribution of gas hydrate filled sediments, marine controlled source electromagnetic (CSEM) data were collected over a number of known seep sites on Opouawe Bank as part of the multidisciplinary NEMESYS project. The CSEM data were inverted to give one-dimensional layered and laterally continuous two-dimensional electrical resistivity models, which revealed anomalously high resistivities (3-100 Ωm) coincident with several seep sites, namely North Tower, South Tower, Piwakawaka, Pukeko and Rironiro. The resistivity anomalies are located in the top 200 mbsf with lateral extents of 500-1000 m. These results are also consistent with three-dimensional forward modeling studies. A possible explanation for the high resistivities is the presence of resistive gas hydrates beneath the seep sites, although the presence of free gas and carbonate crust cannot be completely ruled out. To explain the observed resistivity anomalies, gas hydrate fractions of 31-40% are required. In contrast, Takahe seep site is characterized by only a narrow channel (200 m) of moderately elevated resistivities (5 Ωm), which can be explained by gas hydrate fractions of ∼20%.

1 Introduction

The Hikurangi Margin located off the east coast of the North Island of New Zealand is the result of active east-west subduction of the Pacific plate beneath the Australian Plate, which occurs at a slow rate of 40-50 mm/yr at a low angle of 3° (Barnes et al., 2010). Further north, the trench continues along the Tonga-Kermadec subduction zone. The central part of the Hikurangi margin is characterized by accretion of 500-2000 m thick marine sediments of Pliocene to Quaternary age (Davy & Wood, 1994). The sediments lie on top of the 10-15 km thick crust of the Hikurangi Plateau, which was formed by MORB of Pre-Tertiary age. The slope of the accreted sediments is generally less than 4°, suggesting low friction at the plate interface, presumably the result of high water contents in the sedimentary layer (Barnes et al., 2010).

Previous geophysical studies along the Hikurangi Margin found several methane seep sites and wide-spread bottom simulating reflectors (BSR) (e.g. Bialas et al., 2007; Greinert et al., 2010) indicating the presence of submarine gas hydrates. In 2011, marine controlled source electromagnetic (CSEM) measurements were conducted as part of the multidisciplinary NEMESYS project (Bialas, 2011) on Opouawe Bank located on the Southern Central Hikurangi Margin to study the variability of methane seepage and the distribution of gas hydrate filled sediments. During cruise SO214 of RV Sonne, marine CSEM data were collected over a number of known seep sites along three SW-NE profiles in 1000-1100 m water depth (Figure 1). Profile SO214-1 consists of 26 sites along a 9 km long profile, covering Piwakawaka, Pukeko, North Tower and Takahe seep sites. Profile SO214-2 is 8 km long and consists of 22 sites, covering Rironiro, Pukeko, North Tower and Takahe seep sites. It runs north of profile SO214-1, which it intersects near Takahe. The 3.5 km long profile CSEM-SO214-3 consists of 9 sites and extends from seep site Piwakawaka, where it intersects profile SO214-1, to South Tower. All three profiles intersect with two previously measured profiles completed during cruise SO191 of RV Sonne in 2007 (Schwalenberg et al., 2010).

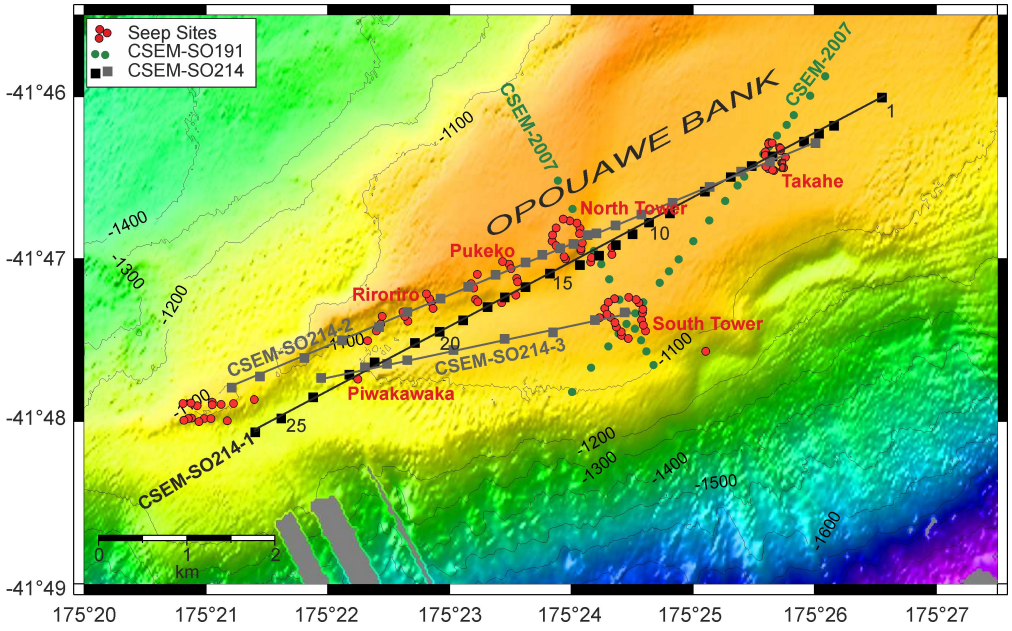

Figure 1: Bathymetry map of Opouawe Bank, showing the location of the three new CSEM profiles (SO214-1: black squares, SO214-2 and SO214-3: grey squares) and the two old CSEM profiles (SO191: green circles). Red circles indicate the outline of various seep sites picked from parasound data.

2 CSEM measurements

The marine CSEM measurements on Opouawe Bank during cruise SO214 were conducted using a modular, bottom-towed time-domain electric dipole-dipole system called Hydra (Figure 2). Hydra was developed at the Federal Institute for Geosciences and Natural Resources (BGR), and consists of four receivers towed in-line behind a horizontal electric

transmitter dipole. This new system is an advancement of a previous CSEM system built at the University of Toronto, which consists of two receivers and was used during cruise SO191 (Schwalenberg et al., 2010). The transmitter is a horizontal, 101 m long electric dipole with two 70 cm long copper pipes as current electrodes and has a dipole moment of 5 A $\times$ 101 m. The receiving dipoles are 10-20 m long with a pair of Ag/AgCl electrodes on either end, which are towed behind the transmitter on the seafloor with offsets increasing from 160 m (RX1) to 750 m (RX4). A heavy weight called pig is attached to the front of the array and hosts the array control unit, a CTD (conductivity, temperature, density) sensor and an acoustic transponder system. The pig also serves to keep the CSEM array on the seafloor. The source signal is a square wave with a period of 6 s and an amplitude of $\pm$5 A, which is generated by a current transmitter on board and sent down to the transmitting dipole via the coaxial deep-tow cable.

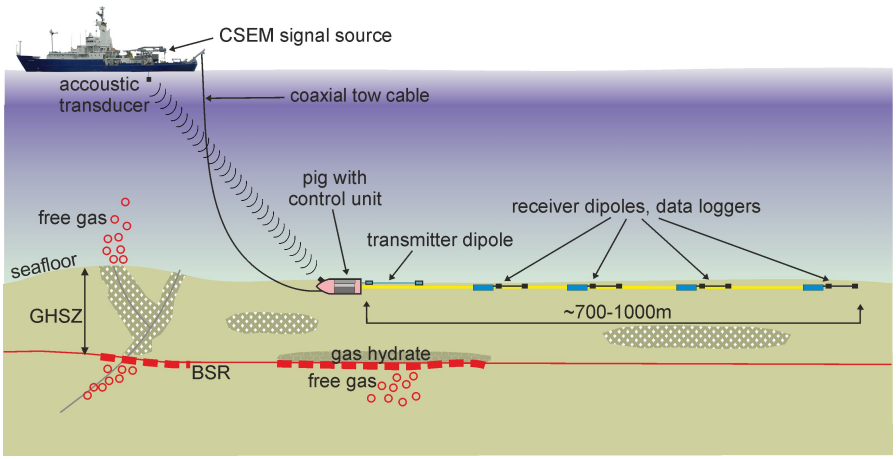

Figure 2: Setup of the bottom-towed time-domain marine CSEM system Hydra. The system consists of four receivers towed in-line behind a horizontal electric dipole transmitter.

3 CSEM data processing

At each site, the horizontal electric field at each receiver was measured for ~10 minutes with a sampling rate of 10 kHz. The recorded time series were decimated from the original sampling rate of 10 kHz to 1.25 kHz. Before decimation, a zero phase Butterworth low-pass filter with a cut-off frequency equal to the Nyquist frequency of the decimated time series was applied to reduce internal high frequency noise from the electronics. In addition, an offset and drift correction was applied to the data. The decimated time series were used to derive a stacked dataset using an iterative stacking scheme. Figure 3 shows an example of the derived stacked half-periods for receiver 4 along profile SO214-2. The stacked data show a clearly pronounced 'double-bump' for measurements above the seep sites, which is indicative of a strong resistivity contrast between the conductive sea-water and highly resistive marine sediments beneath (Edwards & Chave, 1986). The first increase at early times is associated with the electromagnetic signal propagating through the resistive sediments, whereas the second increase at late times is the part of the signal propagating through the more conductive seawater.

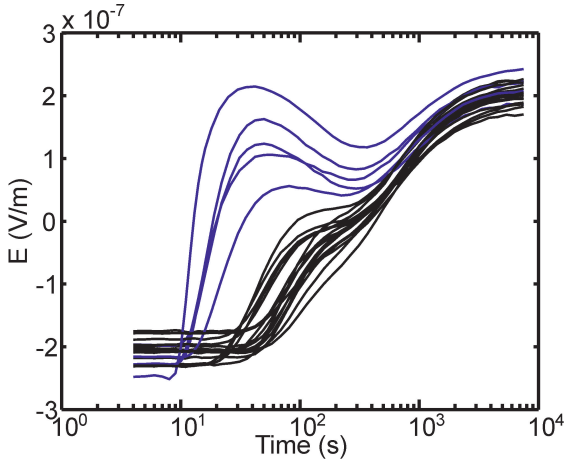

Figure 3: Example of a stacked data set recorded at 26 sites along Profile SO214-2 by the fourth receiver with an offset of 610 m. The stacked data above the seep sites (blue) show a clearly pronounced 'double-bump', which is indicative of a strong resistivity contrast between the conductive sea-water and highly resistive marine sediments.

4 One-dimensional electrical resistivity models

The stacked data sets for each site can be used to calculate a preliminary layered subsurface resistivity model using a one-dimensional inversion. For our analysis, we used a 1D inversion program provided by C. Scholl (University of Toronto, 2007, unpublished software), which uses both Marquardt and Occam type inversions to determine the vertical subsurface resistivity structure from the stacked receiver data sets. Water depth and seawater conductivity measurements taken from the CTD sensor inside the pig were included as a-priori information in the inversion.

In a first step, a Marquardt inversion was conducted to obtain halfspace apparent resistivities for each of the transmitter-receiver pairs. The results of these initial inversions correspond to the average resistivity beneath each transmitter-receiver pair and provide a first indication of the subsurface resistivity distribution. Figure 4 shows an example of the obtained halfspace apparent resistivities along profile SO214-2, which clearly indicates anomalous resistivities beneath the known seep sites, while normal resistivities of of 1-2 Ωm are observed away from the seep sites.

In a second step, multi-layered Occam inversions were conducted to obtain constraints on the vertical electrical resitivity distribution. For this, receivers were sorted into common-mid-point gathers and were inverted jointly. The individual 1D layered resistivity models have been stitched together laterally for a 2D presentation of the subsurface resistivity structure along each profile (Figure 5). For all three profiles, the 1D electrical resistivity models show a relatively homogeneous background resistivity of 1-2 Ωm away from the seep sites. For the majority of these sites, no vertical layering is obvious, which is a direct consequence of the Occam type inversion. In this type of inversion, the data misfit and the model roughness are minimized simultaneously, so that a homogeneous subsurface resistivity model is preferred over a layered model, if it fits the data. Electrical resistivities beneath the individual seep sites are generally elevated (5-50 Ωm) in the top 200 mbsf (meters below seafloor) compared to the background resistivities. At greater depths, anomalously

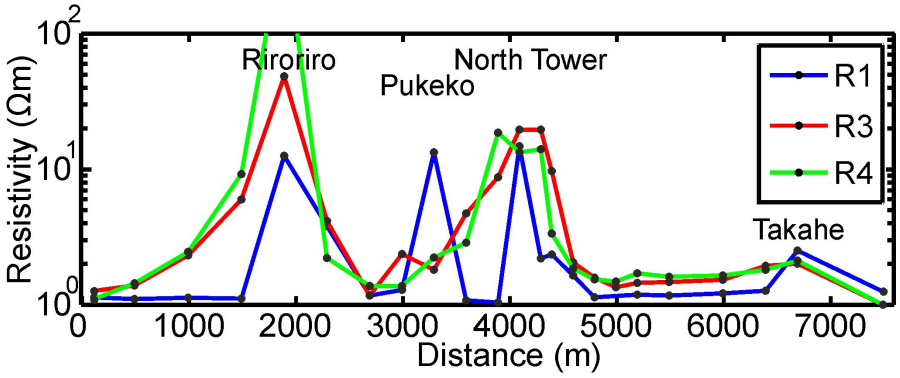

Figure 4: Halfspace electrical resistivities derived from 1D Marquardt inversion of each transmitter-receiver pair along Profile SO214-2. Offsets for the receivers were 160 m (R1), 400 m (R3) and 610 m (R4). No data were available for receiver 2 at 260 m offset.

low resistivities are observed, which are thought to be artifacts of the 1D inversion caused by 2D or 3D effects in the data, and are therefore excluded from the interpretation.

5 Two-dimensional electrical resistivity models

Whereas 1D resistivity models provide a first impression of the subsurface resistivity structure, they do not provide a laterally continuous, smooth image of the subsurface. In addition, r.m.s. misfits > 1 above the seeps suggest that a 1D interpretation is not appropriate for these sites. The unreasonably low resistivities beneath the seep sites also imply that a 1D layered model is not justified. Therefore, a two-dimensional inversion of all three profiles was conducted. For our analysis, we used a 2D finite difference inversion algorithm by C. Scholl (CGG Electro Magnetics, proprietary software), which uses an Occam type inversion to determine a smooth two-dimensional image of the subsurface resistivity structure. It allows taking into account the regional bathymetry along the profiles, with the depth and dip of the transmitter and receivers being adjusted accordingly. For the inversion, it was necessary to convert the measured time-series into frequency domain. The data errors in the frequency domain were estimated using a Fisher distribution (Olsen, 1991).
The 2D electrical resistivity models are shown in Figure 6, and fit the data with r.m.s. misfits of 1.31, 1.18 and 1.12 respectively. Away from the seep sites, all three profiles show a homogeneous background resistivity of 1-2 Ωm, consistent with the results from the 1D inversion. The seep sites are generally associated with anomalously high resistivities (3-100 Ωm) in the top 200 mbsf. Unlike for the 1D inversion, no unrealistically low resistivities are found beneath the seep sites, supporting our assumption that these are artifacts of the 1D inversion. For most seep-sites, namely North Tower, South Tower, Piwakawaka, Pukeko and Ririoriro, the lateral extents of the resistivity anomalies are 500-1000 m. In contrast, Takahe seep site is characterized by only a narrow channel (200 m) of moderately elevated resistivities (5 Ωm). Further three-dimensional forward modeling studies are required to confirm how well the width and resistivity of these resistivity anomalies is constrained.

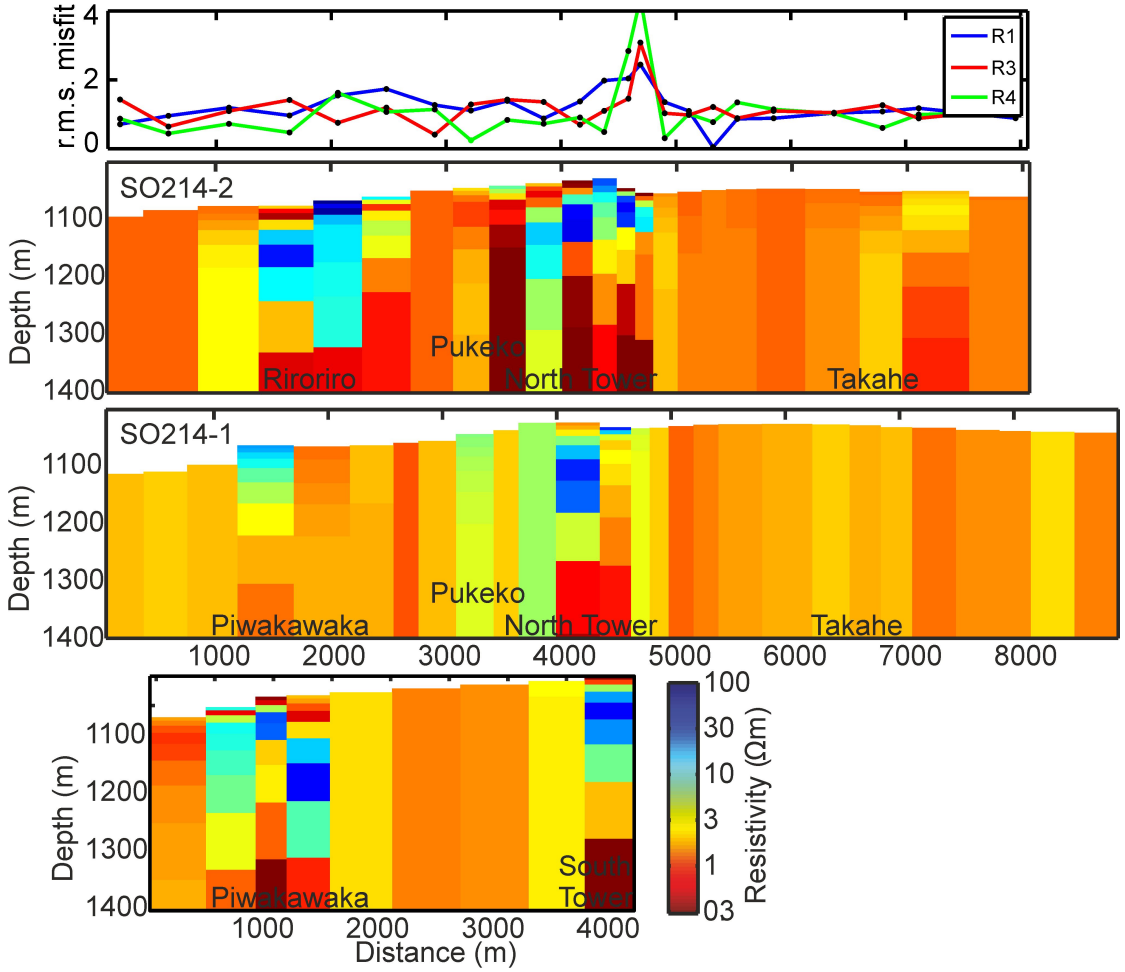

Figure 5: One-dimensional, layered electrical resistivity models for the profiles SO214-2 (top), SO214-1 (middle) and SO214-3 (bottom) derived from a joint 1D Occam style inversion of all receivers. The individual 1D resistivity models for each profile have been stitched together laterally for a 2D presentation of the subsurface resistivity structure. An example of along profile variations of the r.m.s. misfit is shown for profile SO214-2 (top).

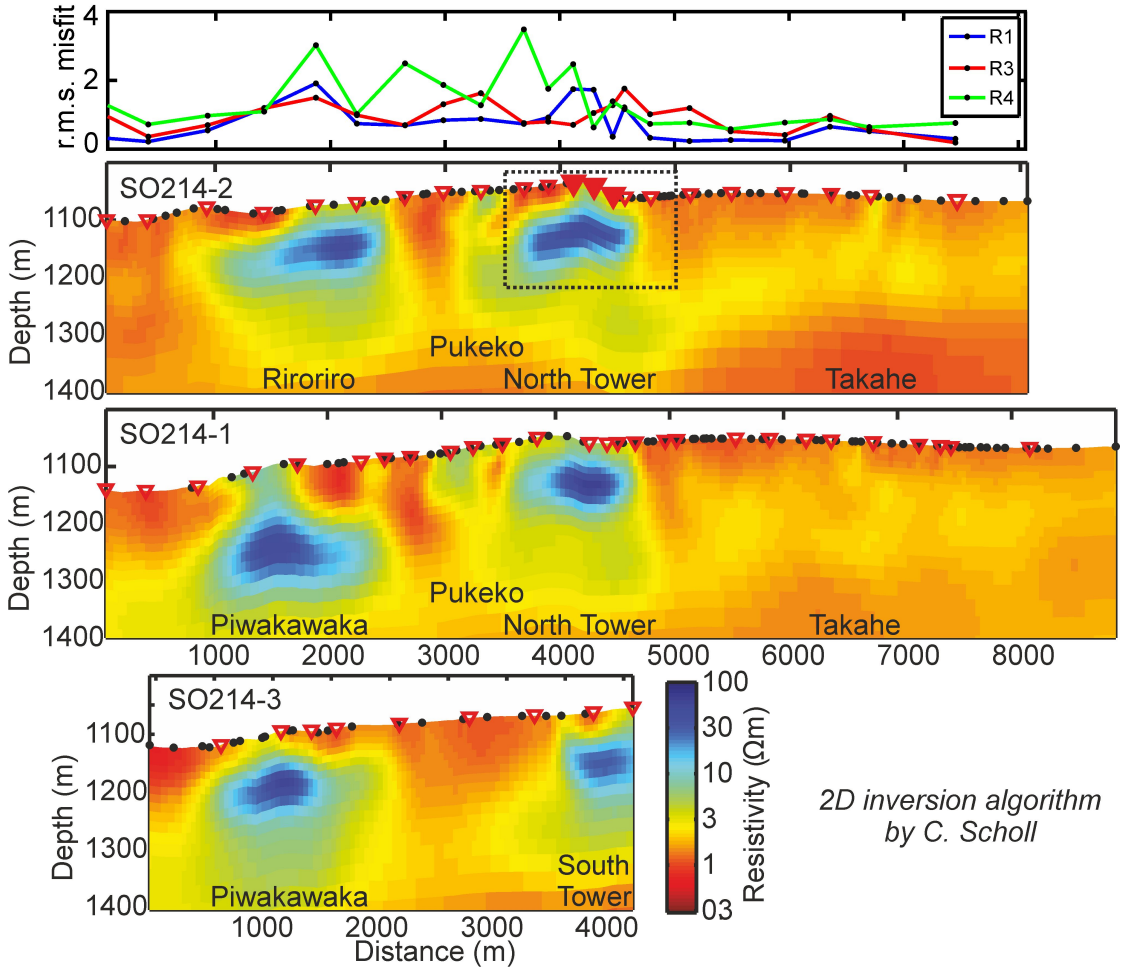

Figure 6: Two-dimensional marine CSEM resistivity models for the profiles SO214-2 (top), SO214-1 (middle) and SO214-3 (bottom) derived from a joint inversion of all receivers. Red triangles indicate transmitter locations, black circles indicate receiver locations. The total r.m.s. misfit for the profiles is 1.18 (SO214-2), 1.31 (SO214-1) and 1.12 (SO214-3). An example of along-profile variations in the r.m.s. misfit is shown for profile SO214-2 (top).

6 Three-dimensional electrical resistivity models

To investigate possible three-dimensional effects of the seep structures on the CSEM data, further three-dimensional forward modeling studies are required. These studies also allow to confirm how well the width and resistivity of the seep structures are constrained, e.g. whereas seismic studies confirm the presence of narrow channel structures beneath the seep sites, it is not clear from the 2D inversion if narrow resistive channel structures are consistent with the CSEM data.
For the three dimensional analysis, we used the commercial finite-element software package Comsol. The calculations were done with the ACDC module using a spherical model setup. An infinite element layer was used at the model boundaries, which maps the coordinates from a local, finite domain to a stretched domain and thus effectively scales the coordinates of the model boundaries towards infinity. Even though the program allows inclusion of bathymetry, we did not include regional bathymetry data to reduce the computational cost of the forward modeling problem. Instead, we used a model setup consisting of three layers, i.e. a resistive air layer, a 1075 m thick conductive seawater layer with a resistivity of 0.3 Ωm and a sedimentary layer with a homogeneous background resistivity of 1.5 Ωm. The regions of elevated resistivities beneath the seep sites were modeled as cylindrical structures.
Initial three-dimensional forward modeling studies of the seep sites included systematic variations of the radii, thicknesses, depths and electrical resistivities of the cylindrical structures as well as their lateral position along the profile. An example of these studies is shown in Figure 7 for three sites above the eastern edge of the North Tower seep site. It can be seen, that in first order North Tower seep site can be approximated by a cylindrical structure of 1000 m width and 250 m height with a resistivity of 50 Ωm and mid-point located ∼4100 m along profile direction. Whereas the data fit for receivers 3 and 4 at offsets of 400 m and 610 m is generally good, systematic fine-tuning of the shallow structure is required to improve the data fit at high frequencies for receiver 1 at 160 m offset.
Based on these systematic forward modeling studies, a three-dimensional resistivity model was derived, which generally confirmed the widths and resistivities of the resistivity anomalies derived from the 2D inversion. A possible explanation for the anomalously high resistivities beneath the seep sites is the presence of resistive gas hydrates, as will be discussed below, although the presence of free gas or carbonate crust cannot be completely ruled out.

7 Constraints on gas hydrate saturation

The physical parameter that can be derived from marine CSEM data is the electrical bulk resistivity of the marine sediments. It is generally controlled by the porosity of the sediments, the kind of fluid present in the pore space, its electrical resistivity and connectivity. In first approximation, the bulk resistivity of the marine sediments can be described by Archie's Law (Archie, 1942)

$$\rho_f = a\rho_w\Phi^{-m}$$

where ρ_f is the formation resistivity of the marine sediments, ρ_w is the electrical resistivity of the pore fluid, Φ is the porosity of the sediments, m is the cementation factor and a is an empirical constant, commonly set to 1. The cementation factor m describes the

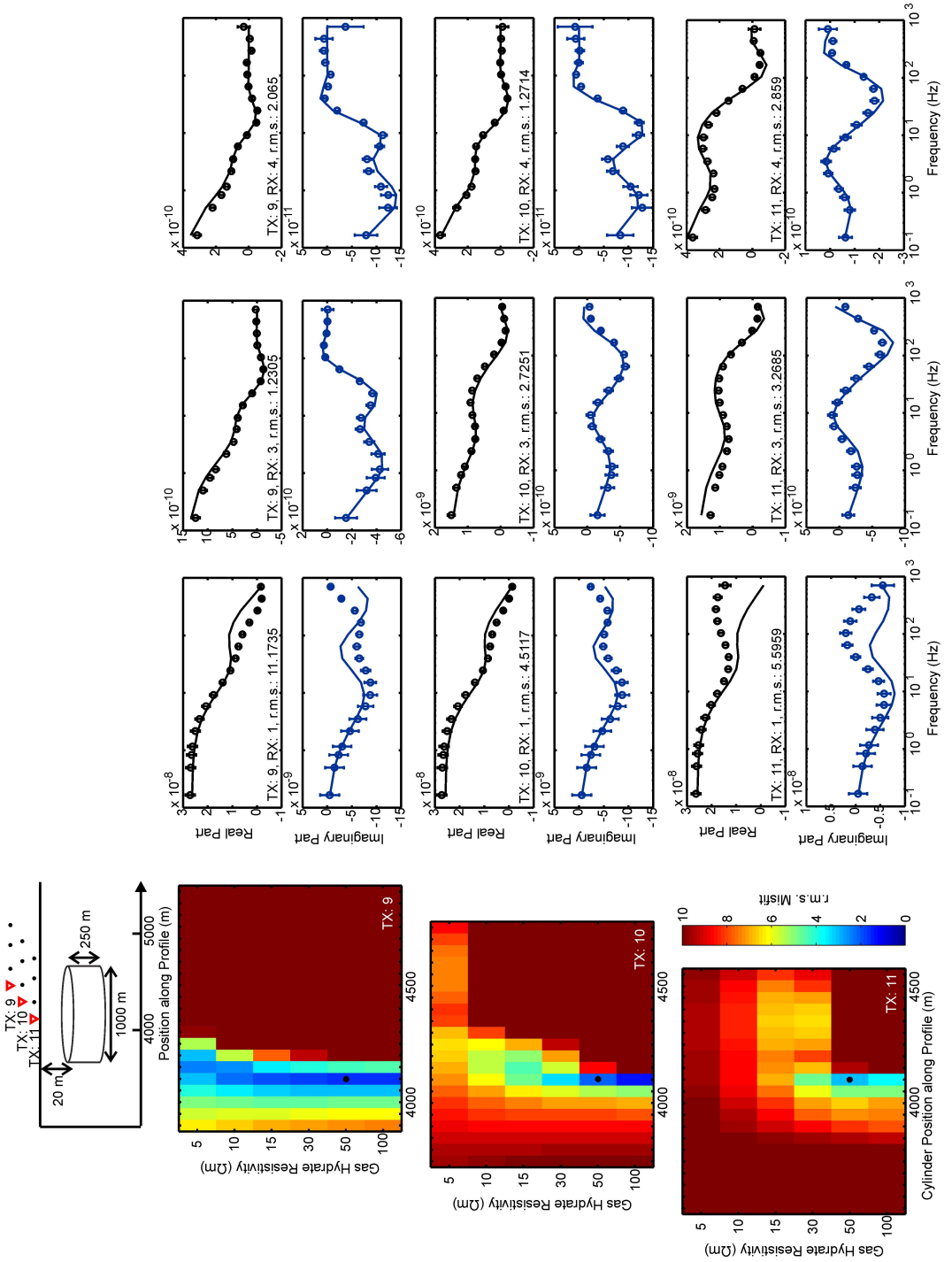

Figure 7: Three-dimensional forward modeling results for a cylindrical structure with a width of 1000 m, height of 250 m and variable electrical resistivity. Pseudo-color plots (left) show the r.m.s. misfit for different parameter combinations. The frequency-domain CSEM data for sites 9, 10, and 11 of Profile SO214-2 (compare dashed box Figure 6) and the corresponding model fit is shown. (right).

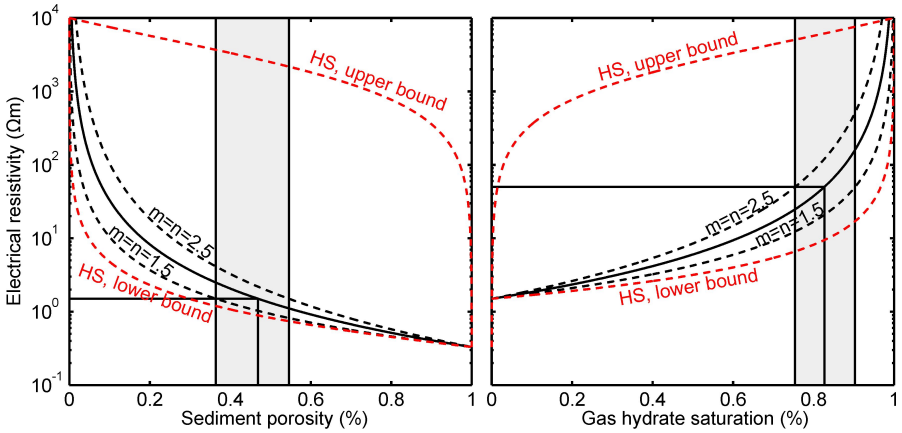

Figure 8: Constraints on the sediment porosity (left) and gas hydrate saturation (right) using Archie's Law (Archie, 1942). A resistivity anomaly of 50 Ωm with a background resistivity of 1.5 Ωm was assumed. Cementation and saturation factor cover the range m=n=1.5-2.5. Red dashed lines correspond to the upper and lower Hashin-Shtrikman bounds (Hashin & Shtrikman, 1963).

connectivity of the pore fluid, with lower values of m corresponding to a higher degree of interconnection.

Studies on various artificial and natural marine sediment samples indicate that the cementation factor typically ranges between 1.4 and 2, with values increasing with depth, as the grains become less spherical (Jackson et al., 1978). In the top few hundred meters of the seafloor, the formation resistivity of marine sediments typically range between 1 and 2 Ωm, consistent with the observed background resistivity of 1-1.5 Ωm away from the seep sites. Assuming an average formation resistivity of ρ_w=1.5 Ωm for the marine sediments and a pore fluid resistivity of ρ_w=0.3 Ωm (i.e. sea water), Archie's Law can be used to estimate the porosity of the sediments. For a cementation factor in the range m=1.5-2.5, porosities can be calculated to be 34-53% (Figure 8). Note that if small amounts of gas hydrates were present in the pore space away from the seep sites, these would effectively replace some of the pore fluid and reduce the inferred porosity.

Resistive gas hydrates can replace some of the pore fluids, thus effectively reducing the volume of the pore space, which cause a higher formation resistivity of the sediments. In this case, Archie's Law can be generalized to

$$\rho_f = a\rho_w \Phi^{-m} S_w^{-n}$$

where S_w is the pore fluid saturation factor and n is the saturation coefficient. The saturation coefficient n describes the connectivity of the pore fluid in the presence of an additional resistive phase, and is often set equal to the cementation factor m. The fractional concentration of the gas hydrates in the pore space can be expressed as $S_h = 1 - S_w$.

If we assume, that porosity does not change along profile, the observed zones of anomalously high resistivities beneath the seep sites can only be explained if part of the conductive pore fluid got replaced by resistive material, such as gas hydrates. In this case, the observed electrical resistivities beneath the seep sites can be used to calculate the fractional gas hydrate volume. For resistivities of 50 Ωm, as observed beneath seep sites Piwakawaka, Rironiro, North Tower and South Tower, and a saturation coefficient in the range of n=1.5-

2.5, a gas hydrate saturation of 75-90% is required to explain the data. This corresponds to a fractional gas hydrate volume of 31-40%. In contrast, Takahe seep site, which is characterized by a very narrow, vertical channel with moderately elevated resistivities of ∼5 Ωm, requires a gas hydrate saturation of 38-55%, corresponding to a volume fraction of ∼20%.

8 Conclusions

Previous geophysical studies found several methane seep sites and wide-spread bottom simulating reflectors along the accretionary Hikurangi Margin in New Zealand, which indicate the presence of gas hydrate filled sediments. To study the variability of methane seepage and the distribution of gas hydrates in the sediments, marine CSEM measurements were conducted on Opouawe Bank on the Hikurangi Margin in 2011 as part of the multidisciplinary Nemesys project. During cruise SO214 of RV Sonne, CSEM data were collected using a new, bottom-towed, multi-receiver system along three profiles over a number of known seep sites.

Initial one-dimensional inversion of the data produced layered models of sub-seafloor resistivity, which revealed anomalously high resistivities coincident with several seep sites. However, the one-dimensional inversion does not well constrain the vertical extent of these resistivity anomalies. In addition, unresolved low resistivity artifacts and r.m.s. misfits > 1 for data at the seep sites suggest that one-dimensional inversion is not justified. Therefore, a two-dimensional Occam inversion of the data was conducted, taking into account regional bathymetry. The inversion confirmed the presence of anomalously high resistivities (3-100 Ωm) in the top 200 mbsf beneath several seep sites, namely North Tower, South Tower, Piwakawaka, Pukeko and Rironiro, with lateral extents of 500-1000 m. These results are also consistent with three-dimensional forward modeling studies.

A possible explanation for the high resistivities is the presence of resistive gas hydrates beneath the seep sites, although the presence of free gas and carbonate crust cannot be completely ruled out. Assuming that the gas hydrates are distributed in the pore space of the sediments, where they replace the conductive pore fluid, gas hydrate fractions of 31-40% are required to explain the observed resistivity anomalies. In contrast, Takahe seep site is characterized by only a narrow channel (200 m) of moderately elevated resistivities (5 Ωm), which can be explained by gas hydrate fractions of ∼20%.

While seismic studies indicate the presence of narrow channels beneath the seep sites, further three-dimensional forward modeling studies are required to confirm if the CSEM data are consistent with these observations. These studies will also help to better understand the effect of three-dimensional structures on CSEM data.

Acknowledgments

We would like to thank the captain and crew of cruise SO214, Leg2 of RV Sonne. Funding by the German Federal Ministry for Education and Research (BMBF) under Grand No. 03G0214 is acknowledged.

References

Archie, G. (1942). The electrical resistivity log as an aid in determining some reservoir characteristics. *Transactions of the AIME*, *146*(01), 54-62.

Barnes, P. M., Lamarche, G., Bialas, J., Henrys, S., Pecher, I., Netzeband, G. L., et al. (2010). Tectonic and geological framework for gas hydrates and cold seeps on the Hikurangi subduction margin, New Zealand. *Marine Geology*, *272*(1–4), 26 - 48.

Bialas, J. (Ed.). (2011). *FS SONNE Fahrtbericht / Cruise Report SO214 NEMESYS : 09.03.-05.04.2011, Wellington - Wellington, 06.-22.04.2011 Wellington - Auckland* (Cruise Report No. 47). Kiel, Germany.

Bialas, J., Greinert, J., Linke, P., & Pfannkuche, O. (Eds.). (2007). *RV Sonne Fahrtbericht / Cruise Report SO191 - New Vents "Puaretanga Hou" : Wellington - Napier - Auckland, 11.01. - 23.03.2007* (Cruise Report No. 09). Kiel, Germany.

Davy, B., & Wood, R. (1994). Gravity and magnetic modelling of the Hikurangi Plateau. *Marine Geology*, *118*(1–2), 139 - 151.

Edwards, R. N., & Chave, A. D. (1986). A transient electric dipole-dipole method for mapping the conductivity of the sea floor. *Geophysics*, *51*(4), 984-987.

Greinert, J., Lewis, K., Bialas, J., Pecher, I., Rowden, A., Bowden, D., et al. (2010). Methane seepage along the Hikurangi Margin, New Zealand: Overview of studies in 2006 and 2007 and new evidence from visual, bathymetric and hydroacoustic investigations. *Marine Geology*, *272*(1–4), 6 - 25.

Hashin, Z., & Shtrikman, S. (1963). A variational approach to the theory of the elastic behaviour of multiphase materials. *Journal of the Mechanics and Physics of Solids*, *11*(2), 127 - 140.

Jackson, P., Smith, D., & Stanford, P. (1978). Resistivity-porosity-particle shape relationships for marine sands. *Geophysics*, *43*(6), 1250-1268.

Schwalenberg, K., Haeckel, M., Poort, J., & Jegen, M. (2010). Evaluation of gas hydrate deposits in an active seep area using marine controlled source electromagnetics: Results from Opouawe Bank, Hikurangi Margin, New Zealand. *Marine Geology*, *272*(1–4), 79 - 88.

Sparsity constrained magnetotelluric inversion

C. Nittinger and M. Becken

Institute of Geophysics, University of Münster

1 Introduction

The inversion of magnetotelluric (MT) data seeks to find a geologically plausible resistivity model which can explain measured magnetotelluric field data to within their errors. The resistivity models are most commonly discretized as block models with rectangular cells. Inversion schemes are designed to minimize an objective function dependent on the data residuals which are calculated from the forward response of an initial model and the difference to the observed data. The problem is non-unique and therefore a priori information is needed to obtain stable results. Invoking Occam's razor yields the simplest resistivity model that explains the data with a sufficient data fit. In this work we try to overcome the standard block model discretization of the subsurface and instead suggest to parametrize the model in a domain that supports a sparse model representation.
A sparse model representation means that the model is defined by a small number of non-zero coefficients based on a set of pre-known basis functions. The focus of this work is set to models represented by wavelet coefficients (Daubechies, 1992). Therefore, the regularization term of the objective function is modified. For a wavelet-parametrized model the inversion seeks the solution with the minimum number of coefficients needed to explain the data. Mathematically this is obtained by invoking a L1-norm regularization of the wavelet coefficients (Donoho, 2006), instead of the L2-norm. We apply an inversion approach to solve the magnetotelluric problem as a mixed L1-L2 norm problem using a scheme proposed by Borsic and Adler (2012) solving the nonlinear problem with a second order primal dual interior point method (PDIPM).
Such a sparsity promoting formulation of the magnetotelluric inversion problem could accelerate computations and reduce memory consumption of the inversion. The large variety of sparse representations may also improve the variety of resistivity models that can explain the data. Sparse model representations allow model appraisal methods to be used efficiently and a detailed further evaluation of the solution may be possible.

2 Wavelet representation

A wavelet describes a signal through a wavelet- and a scaling-function which are well localized in time/space on different scales. Such a representation of a signal/image allows a sparse representation, where local structures can be defined by a few number of wavelet coefficients. The wavelet functions of single coefficients are overlapping across the model space, therefore only indices and values of non-zero wavelet coefficients have to be stored.

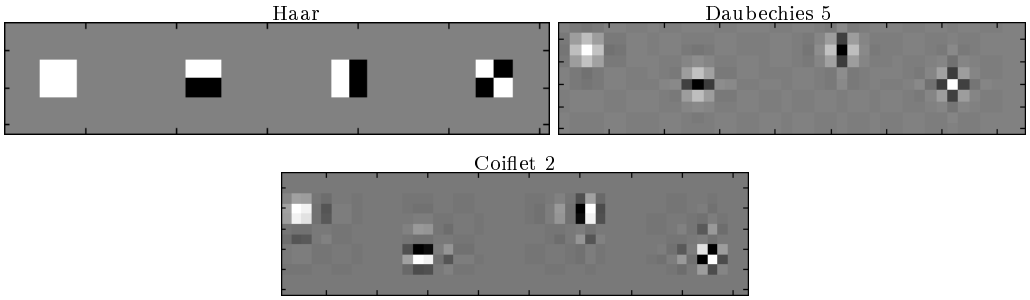

Figure 1: Image represented by single non-zero 2-D wavelet coefficients for the Haar, Coiflet 2 and Daubechies 5 wavelets. From left to right the picture shows the result of four coefficients which are (from left to right) the approximation coeff. as well as the horizontal, vertical and diagonal detail coefficients.

This renders wavelet functions a good choice for a sparse model representation. A large number of different wavelet families exists and they can be defined in 1-D and 2-D as well as in 3-D.
We perform a wavelet transform and decomposition within a multiresolution scheme (Mallat, 1999). A Multiresolution decomposition of the image allows to formulate the model in the wavelet domain with different scales j (level) and their translation k (localization). The formulation describes the image in terms of approximation coefficients related to the scaling function Φ and detail coefficients related to the wavelet function Ψ. The mathematical formulation of the decomposition yields

$$m(x) = \sum_{j}^{M} c_j \Phi_j(x) = \underbrace{\sum_{j} a_j \Phi_j(x)}_{\text{Approx. coeffs.}} + \underbrace{\sum_{j} \sum_{k} d_k^j \Psi_j, k(x)}_{\text{Detail coeffs.}} \quad . \tag{1}$$

To describe an image or in our case a 2-D resistivity model in the wavelet domain, 2-D versions of the wavelet functions are needed. This can be obtained by giving the wavelets additional directional characteristics. In the multiresolution analysis the wavelet coefficient representation consists of an approximation coefficient and additional horizontal, vertical and diagonal details on the desired levels. The approximation- and wavelet coefficients of the Haar, Daubechies and Coiflet wavelet for 2-D in the different directions for single coefficients are shown in Figure 1.
The graphical meaning of a multiresolution decomposition with the 2-D Haar wavelet for a single approximation coefficient is shown in Figure 2. A vertical wavelet coefficient supports a vertical variation on its scale-dependent support, as well as the horizontal and vertical coefficients describe their corresponding variations. In our transform scheme we use the wavelet transform as a linear operator represented by a decomposition matrix D and a reconstruction matrix R on a vector of the model resistivities.

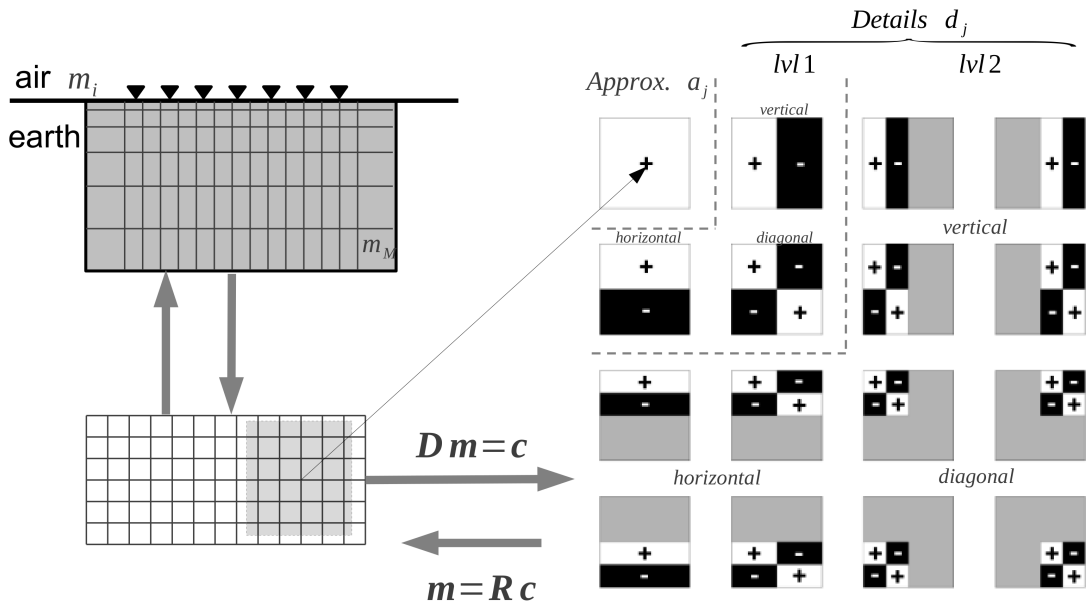

Figure 2: Transformation of the magnetotelluric model space – from grid used for the forward calculation – into the wavelet domain. The vector m represents the model parameters in the wavelet space and is transformed into the wavelet domain by $c = Dm$ and back by $m = Rc$. The right image shows the level 2 multiresolution decomposition with the Haar wavelet for a single approximation coefficient.

3 Inversion scheme

The inversion scheme aims at minimizing the objective function

$$\Phi(c) = ||W_e G(c) - W_e d^{obs}||_2 + \lambda ||L_c c||_1 \quad \rightarrow \min, \tag{2}$$

with respect to c to find the sparsest solution for c. The data is weighted by the data errors within the weighting matrix W_e. The regularization is represented by the sum of the absolute wavelet coefficients, which are weighted by L_c and the trade-off parameter λ. The minimization of the objective function with mixed L-2 and L-1 norms is a challenging numerical task. Due to the L-1 norm regularization the function is non-convex and non-differentiable at the origin.

It is possible to illustrate how the L-1 norm and L-2 norm regularized solutions for a linear line fit problem cause different sparse and non-sparse solutions (Loris et al., 2007). This is depicted in Figure 3 where a line is fitted in the L-1 norm to the L-1 ball or the L-2 ball in the L-2 norm. The line fit model can be described by two parameters, when the solution is regularized with the L-2 norm, both parameters yield non-zero values. If the L1-norm is applied and the line is fitted to the L-1 ball the solution yields one non-zero value and one zero-valued model parameter, but still the same line is reconstructed as with the L-2 regularization. This simple model shows how L1-norm regularization works in yielding a sparse solution and the same scheme can be used for higher dimensional problems.

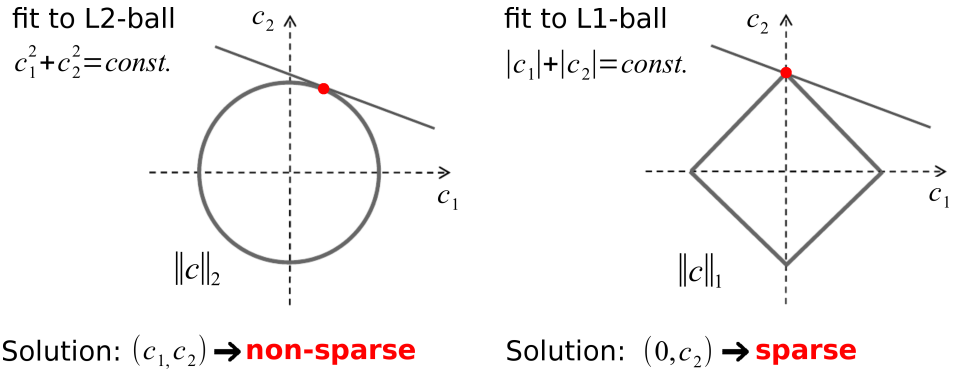

Figure 3: A line with two model parameters (c_1, c_2) is fitted with L2- (left) and L1-norm (right) regularization. In the L2 case the circular L2-ball is fitted to the line, resulting in a solution with two non-zero values. When the L1-ball is fitted to the line the solution constitutes only one non-zero value. Hence, the solution with the smallest L1-norm is sparser than L2-norm solution (Loris et al., 2007).

We apply a numerical scheme which is a second order primal-dual interior point method by Borsic and Adler (2012) which was proposed for mixed L1-L2-norm regularized inverse problems, but not explicitly for sparsity promoting problems. Roughly said, the approach makes use of a classical iterative newton scheme where the second derivative (Hessian) needs to be calculated. In the algorithm, the Jacobian has to be explicitly calculated during the forward computations. The used forward code from Lee et al. (2009) yields the Jacobian with respect to the block model parameters $J(m)$. The Jacobian with respect to the wavelet coefficients from the Jacobian in the block space domain is obtained from the chain-rule

$$\frac{\partial G(c)}{\partial c} = J(m) \cdot R. \tag{3}$$

The Jacobian in the wavelet domain can thus be expressed by a simple matrix multiplication of the wavelet reconstruction matrix R with the Jacobian in the model space.

4 Results on synthetic data

The test model is represented by two simple blocks, one conductive with $(1\,\Omega m)$ and one resistive $(1000\,\Omega m)$ block within a $50\,\Omega m$ background resistivity. The model is shown in Figure 4a. The data is affiliated with errors of 5 % on the apparent resistivities and 2 degrees on the phases. So far we only invert the E and B polarization impedances and not the vertical magnetic fields.
The inversion is started with a background model of $50\,\Omega m$. The model is defined on a grid which has a total number of 2340 blocks with 65 cells in horizontal direction and 36 cells in vertical direction. The grid spacing is uniform in horizontal direction in the inner region where the stations are located. Beyond the extent of the profile the horizontal grid sizes increase towards the boundaries. The vertical block size increases from a starting value of 50 m to the lower boundary of the model.
The wavelet basis in the calculated inversion model is represented by a bior2.4 wavelet in a level 5 multiresolution decomposition. The 2340 model parameters that have to be

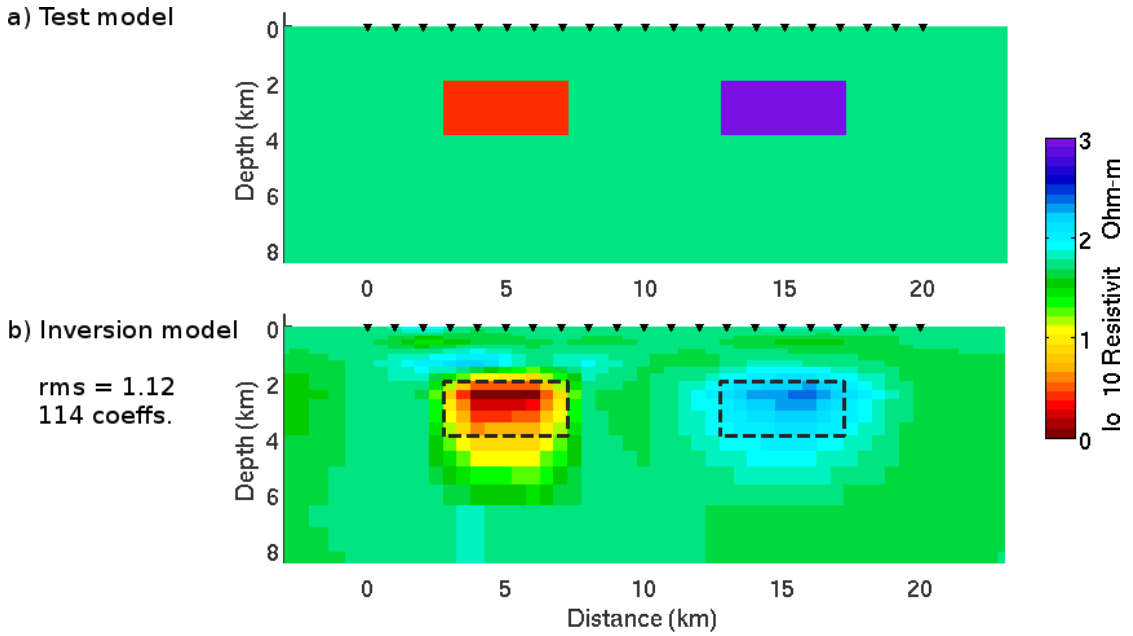

Figure 4: (a) Synthetic model with two block anomalies. The left conductive block has $1\,\Omega m$ and the right resistive block has $1000\,\Omega m$ within a $50\,\Omega m$ background resistivity. (b) Inversion result of the PDIPM algorithm from the test data of the two-block anomaly model. The inversion succeeds to find a smooth model with 114 non-zero coefficients after 14 iterations. The trade-off parameter λ was set to 0.05 and coefficients smaller than 0.001 were thresholded in every iteration. The misfit of the model constitutes 1.12.

estimated by the inversion transform into 4773 wavelet coefficients. The regularization parameter λ is found as the highest possible value where the algorithm succeeds to fit the data to the desired misfit. Therefore the final model is well explained by the data and as sparse as possible. For this test model, λ is found to give reasonable results with a value of 0.05.

The resulting inversion model is depicted in Figure 4b. After 12 iterations the inversion model reaches a root mean square (rms) error of 1.12 which is achieved by 114 non-zero wavelet coefficients. The observed and predicted data are shown in Figure 5a for three example stations. The inversion model is able to reproduce the two block anomalies in a smooth way but also shows small resistive artifacts on top of the conducting block.

Figure 5b shows the rms and the number of non-zero coefficients for each iteration. The inversion starts with all 4773 coefficients and a rms of 7.8. The number of coefficients reduces to 550 coefficients and the rms to 4.5 after the first iteration. In the following iterations the rms and the number of coefficients decrease further until the desired misfit is reached. The behavior of the inversion reflects that the algorithm, which tries to search model updates that point towards the direction of a sparse and fitting model. In every iteration the model updates fulfill this requirement such that the model becomes sparser during the computations.

a)

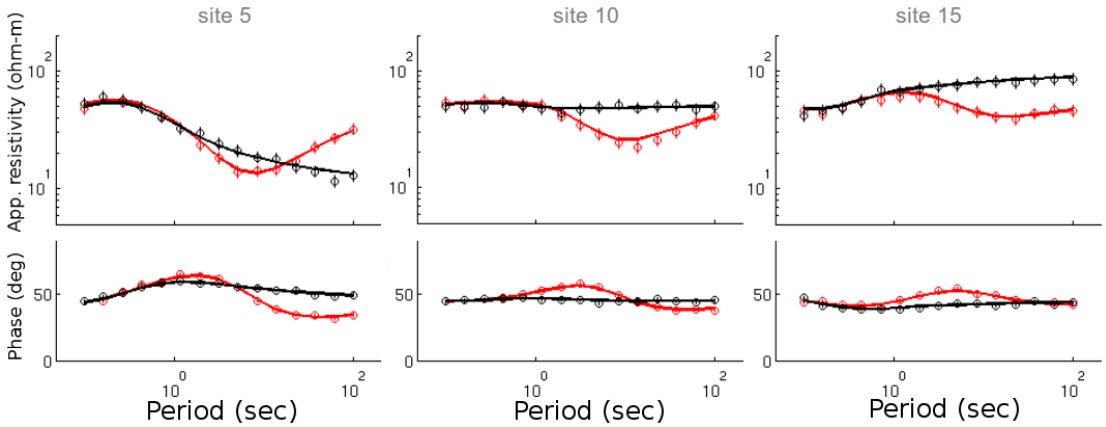

b)

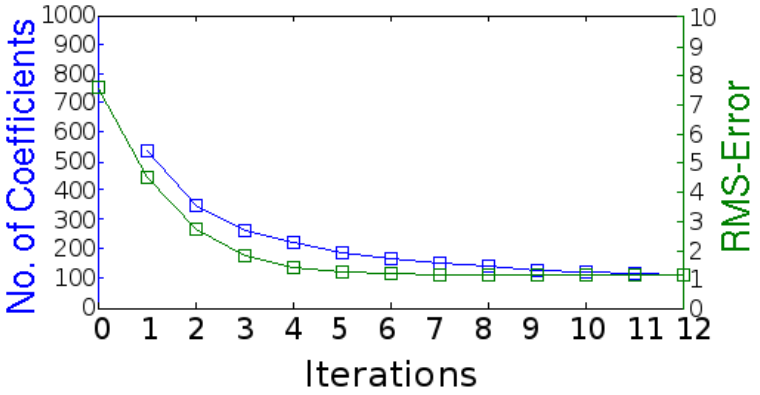

Figure 5: (a) Datafit for the model in Figure 4. The predicted data from the inversion model (straight line) fits well to the synthetic data points from the three shown test sites. (b) Number of non-zero coefficients (left vertical axis) and the rms error (right vertical axis) for each iteration (horizontal axis).

5 Conclusion

We showed that a L2-L1 norm minimization scheme in the wavelet domain is able to solve the magnetotelluric inverse problem. The convergence properties of the algorithm are good (cf. Figure 5b) and it finds a solution within a reasonable number of iterations for the simple two block model. Total computational times are dominated by the forward computations solved during the line search. The sparsity constraint of the inversion ensures that the model is as sparse as possible, but this can also be controlled and tightened by the choice of the trade-off parameter and the weighting of the model parameters.
The inversion of magnetotelluric data in a wavelet basis requires new regularization schemes that go beyond the usual smoothing. This can potentially generate resistivity models which are more strongly driven by the data and the inverse models may give a higher model resolution. In a next step this has to be evaluated in model appraisal schemes which may be much more efficient in the sparse domain, because only a few wavelet coefficients have to be evaluated. Ultimately the inversion scheme subsequently has to be applied to 3-D

models and real data. Wavelet transformations and functions are available in 3-D, hence the implementation could be possible in a suitable formulation which includes the forward modeling.

References

Borsic, A., & Adler, A. (2012). A primal–dual interior-point framework for using the l1 or l2 norm on the data and regularization terms of inverse problems. *Inverse Problems*, *28*(9), 095011.

Daubechies, I. (1992). *Ten lectures on wavelets*. Society for Industrial and Applied Mathematics (SIAM).

Donoho, D. L. (2006). Compressed sensing. *Information Theory, IEEE Transactions on*, *52*(4), 1289–1306.

Lee, S. K., Kim, H. J., Song, Y., & Lee, C.-K. (2009). Mt2dinvmatlab—a program in matlab and fortran for two-dimensional magnetotelluric inversion. *Computers & Geosciences*, *35*(8), 1722–1734.

Loris, I., Nolet, G., Daubechies, I., & Dahlen, F. (2007). Tomographic inversion using l1-norm regularization of wavelet coefficients. *Geophysical Journal International*, *170*(1), 359–370.

Mallat, S. (1999). *A wavelet tour of signal processing*. Academic press.

On sources of instrument motion in marine MT and how to deal with the resulting disturbances

Anne Neska[1] and Marion Jegen-Kulcsar[2]

[1]Institute of Geophysics PAS, ul. Ks. Janusza 64, 01-452 Warszawa, Poland. E-mail: anne@igf.edu.pl
[2]GEOMAR – Helmhotz Centre for Ocean Research Kiel, East Shore Campus, Wischhofstr. 1-3, D-24148 Kiel, Germany

Abstract

Many marine magnetotelluric (MT) datasets contain dominant, quasi-harmonic signals at a period of several seconds in the magnetic and (to a lesser degree) in the electric channels. In some cases these signals are strong enough to drive a standard processing into failure. Coherence with tilt records shows that these signals are generated by motion of the instrument. However, the source of this motion is controversial. It is unclear whether the surrounding water performs such oscillations that might be caused by microseisms, or if streaming water incites oscillations of the instrument.
This contribution contains a discussion resulting in a preference of the latter possibility.
Furthermore, the mechanism of electromagnetic noise generation due to that motion is explained, and possible noise-correction and processing strategies for disturbed data are presented. Data examples are from GEOMAR (Kiel) campaigns offshore Costa Rica and Namibia.

1. Introduction or
On some differences between onshore and offshore magnetotelluric data

Although this work focuses on just one specific problem of offshore MT data, the way of deployment and the special environment in marine measurements cause phenomena that are unheard of in onshore MT. Here we take the occasion to remind of some of them.

a) The coordinate system
Onshore MT measurements usually take place in the geomagnetic coordinate system. This requires a proper installation of the instruments: The magnetometer must be leveled, and both the magnetometer and the telluric lines have to be aligned to North (or East) by means of a compass. Offshore instruments are usually deployed free falling from the ship: After being dropped from the ship, they sink to the ground and as a consequence orientations cannot be controlled. Hence marine MT data are measured in a rather arbitrary coordinate system and additional steps to rotate them to usable coordinates are necessary before processing. The rotation process requires the information about three angles which are provided by the marine instruments: Two of them, describing the deviation from the true horizontal plane, are provided

by two inclinometers or tiltmeters. The third one controls the deviation from magnetic North and can be provided in different ways: If the magnetometer is a fluxgate instrument, the main magnetic field can be measured (which is superimposed on the magnetic variations that are needed for MT) and the North direction can be derived from it. Another possibility is to take it from a compass. If the MT measurement is combined with a controlled-source electromagnetic (CSEM) one, the North direction can be estimated by means of the transmitter signal (e.g. Mittet et al. 2007). Hence, additional data to the pure magnetic and electric ones have to be taken into account.

b) The coast effect

The coast effect known from onshore MT is based on the fact that data of stations situated close to the shore of a deep sea "perceive" the salty sea water as a good conductor. This emerges most clearly in the induction arrows: the real ones (in Wiese convention, Wiese 1962) point inland, away from the sea. A similar effect occurs in offshore stations situated close to the coast in the conductive sea water (Fig. 1): The land is visible in the data as a high-resistive structure, and real induction arrows point towards it. However, here the station is placed *beneath* a good conductor, and the resistive land is partly in an altitude *above* the station. This causes features in the data that are unusual from an onshore point of view: In the TE mode occur phases below 0 degree and the apparent resistivity rises with more than 45 degree (in an equidistant log-log plot) to a sharp maximum. The induction arrows increase and decrease rapidly over period and reach lengths as they rarely do onshore. For more details and explanation of this phenomenon, see Worzewski et al. (2012).

c) Noise generated by instrument's motion

Here a problem is outlined which is treated in detail in Neska et al. (2013). Figure 2 shows time series of a station offshore Costa Rica in ca. 3200 m depth that contain a dominant, quasi-harmonic signal with a period of 5.5 – 6 seconds. It is clear that this is not a usual MT source signal, since that period is too close to the dead band, and if such a signal came from above the atmosphere, it would be practically damped away by the conductive salt water layer. However, the strong correlation with the tilt channel (lowermost panel in Fig. 2) indicates that a rocking or swinging motion of the station produces such signals in the electric and magnetic channels. If they are strong, they can interfere with the MT signal even at much longer periods and hamper the data processing. Hence motion of the surrounding medium can cause problems in offshore data that are prevented onshore by burying the sensors in the soil. The noise is particularly large due to two reasons here: a) the instrumentation was of the first generation design, which turned out to be very sensitive to motion. Mechanical weak points responsible for this have been corrected for in the second generation instrumentation, b) a large number of instruments were placed on the steep continental slope causing a relatively weak coupling to the ground. Furthermore the continental slope is subjected to strong tidal currents coming from the open ocean. Although this type of problem has been significantly reduced by giving the GEOMAR stations more stability, we will consider it more closely in the following. Section 2 treats properties of motion-induced noise which has a relatively straight forward explanation, section 3 is an attempt to constrain the discussion on possible sources of the instrument's motion, and section 4 summarizes conclusions concerning the optimal processing approach for marine MT data affected by motion noise.

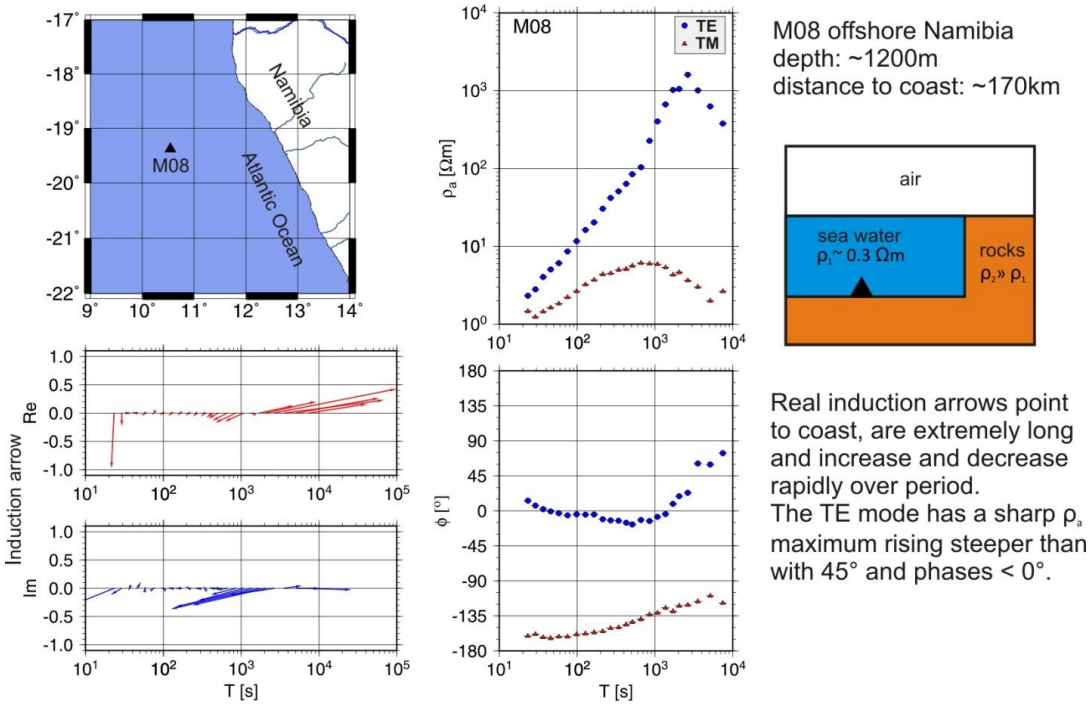

Fig. 1 Principle (sketch on the right-hand side) and exemplary data (sounding curves in the middle column, induction arrows on the left-hand side (bottom), site location on top) of the offshore coast effect

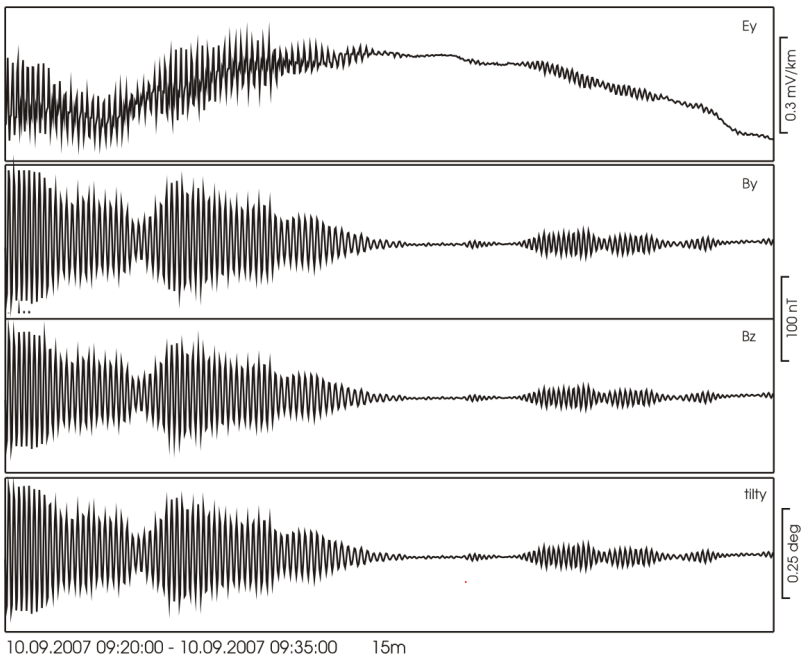

Fig. 2 Time series (instrument's coordinate system) of selected components of station m05 offshore Costa Rica.

2. Consequences of instrument's motion for magnetotelluric records

If an MT measurement is not performed by an instrument fixed to the solid Earth, but by a periodically tilting one, the consequences for both magnetic and electric channels are predictable. First, the static main magnetic field of the Earth will be measured in a periodically changing coordinate system which results in more or less dramatic, disturbing changes between the vertical magnetic component and the horizontal one parallel to the corresponding tiltmeter. This applies even to small tilt movements because the main field is larger than the MT source signals by more than two orders of magnitude. However, these tilt-generated magnetic changes are almost completely determined by the tilt records (the coherence between corresponding tilt and magnetic components is nearly 1 over the whole LMT period range), and this can be used to correct the magnetic records for the tilt-induced disturbances to a certain degree (Neska et al. 2013). Ibid. is pointed out that tilt-induced disturbances on electric channels are generated according to Faraday's law within the instrument, this means that fast tilt changes produce larger electric signals than slow ones. As a consequence, electric channels in the LMT-relevant period range (> 10 seconds) are practically free from motion noise, although it is visible for the dominant period (Fig. 2), and for its first harmonic it is even more pronounced for the electric than for the tilt spectra (Fig. 3). Moreover, the tilt-induced disturbances on electric channels can be predicted from tilt channels via the Lorentz expression

$$\underline{E} = \underline{v} \times \underline{B}$$

where $\underline{E}$ is the tilt-induced electric signal and $\underline{B}$ the static main magnetic field. The velocity $\underline{v}$ at the ends of the telluric tubes due to tilt motion can be calculated from the tilt angle records taking into account the tube length via differentiation with respect to time (Fig. 4).

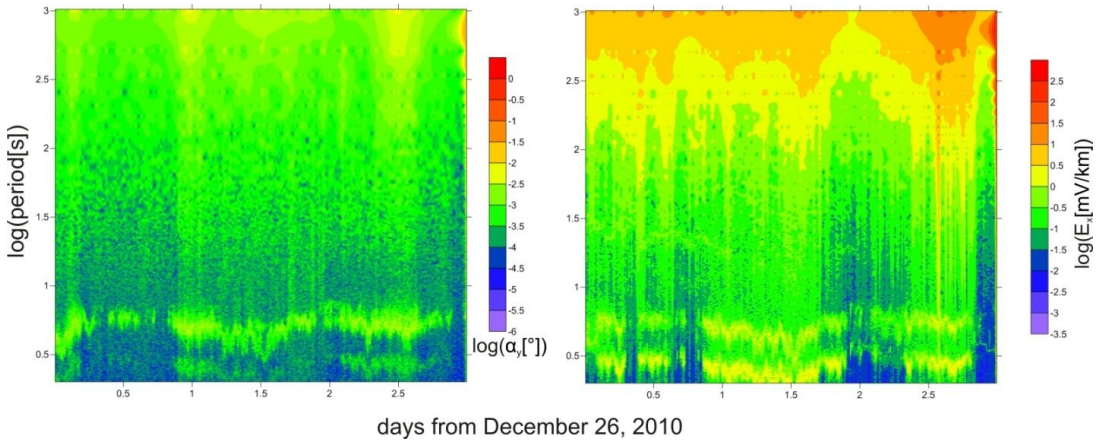

Fig. 3 Dynamic tilt (left-hand side) and electric field (right-hand side) spectra of site M16 offshore Namibia. The dominant period (log(6s) ≈0.8 on y axis) and its first harmonic (≈0.5 on y axis) are visible as horizontal signatures, the latter is more pronounced in the electric channel.

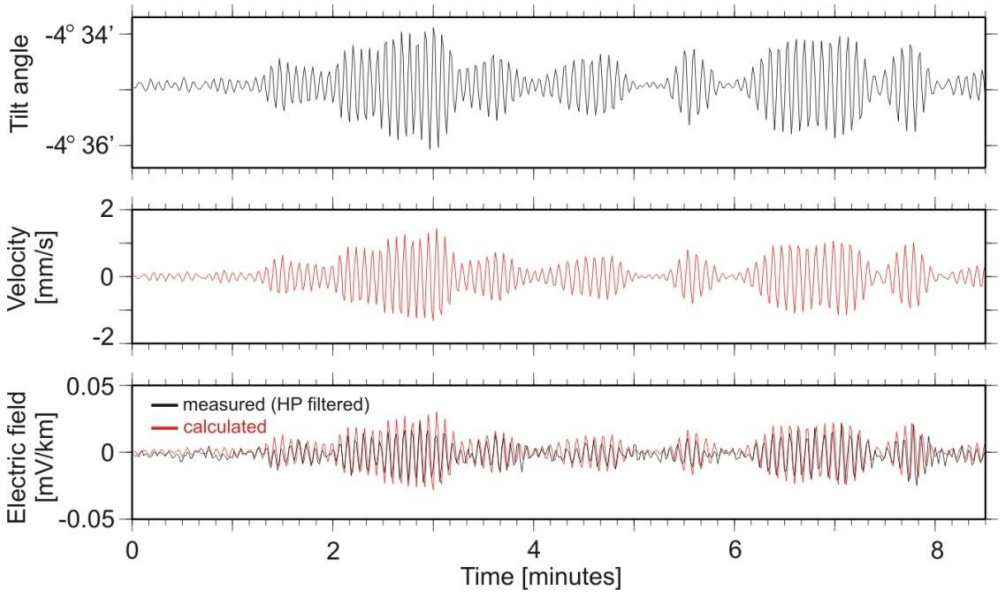

Fig. 4 The predicted electric signal (lower panel, red color) calculated from the tilt record (upper panel) via the velocity (middle panel) and the main magnetic field agrees well with the measured electric signal (after high-pass filtering to remove the large-amplitude natural MT signal, lower panel, black color). Data from site m04 offshore Costa Rica on September 22, 2007, start 08:54.

3. Constraints on the source mechanism of instrument's motion

It is obvious that the marine stations rock because they are forced by water motion. However, details on that water motion are not really known due to the fact that the sites are not accessible to direct observation during their work on the seafloor. On the other hand, from a multitude of marine observations, partly also from other geophysical methods, certain indirect conclusions on the source mechanism of tilt motion have been drawn. In this work we want to contribute to this discussion.

From experience with GEOMAR instruments we can say that the intensity of motion noise varies both between and within data sets and that there is evidence for a dependency on steep bathymetry (Neska et al. 2013), but often that noise is weak and does not pose a problem for further data processing. Nevertheless, it occurs in marine environments all over the world with a dominant period as mentioned above. This has been confirmed directly for data sets from the Pacific Ocean offshore Costa Rica, for the Atlantic Ocean offshore Namibia, for the Baltic Sea, and for the Mediterranean Sea.

The suspicion that the phenomenon of microseisms (Longuet-Higgins 1950) could influence marine electromagnetic measurements as well has been pointed out a long time ago (Cox et al. 1978). Microseisms is generated by meteorologic conditions like storms at the open ocean or by interaction of surface waves with coasts (Chevrot et al. 2007), and it is encountered in seismic data at similar frequencies as our motion noise (Kedar et al. 2008), hence it seems to be a possible explanation for the tilt motion. Microseisms between stations in the same region is strongly correlated (Bromirski 2001). Hence we check the coherence between tilt records of neighboring stations to test this hypothesis.

The coherence between tilt channels α_1 and α_2 of two stations is given by the formula

$$coh^2 = \frac{|\langle \alpha_1 \alpha_2^* \rangle|^2}{\langle \alpha_1 \alpha_1^* \rangle \langle \alpha_2 \alpha_2^* \rangle}$$

which is a function of frequency and where the asterisk * denotes the conjugate complex and brackets a stacking over a number of coefficients having the same frequency.

Acoustic waves in water have a propagation velocity of ca. 1500 m/s. Taking into account that the distance between neighboring stations considered here is about 20 km, the difference between arrival times at both stations can amount to somewhat more than a dozen seconds. This is much more than one would expect in an analog consideration of electromagnetic coherence and needs time windows of sufficient length during the calculation. The calculation has been done in a sort of cascade decimation with a start length of 4096 samples (= 4096 s). The results are displayed as dynamic spectral plots, where time dependence is shown along the x axis, period dependence along the y axis, and coherence (or amplitude, resp.) as color. The time resolution is (according to the basic time window length) one hour with a small overlap. Coherence values at periods > 100 s originating from this calculation are stacked only over a small number of coefficients (~10) which leads, unfortunately, to a "numerical" bias that is always directed upwards.

This operation has been applied to a pair of neighboring stations of the Costa Rica data set (Fig. 5) and of the Namibia data set (Fig. 6). From both perpendicular tilt channels of each station the ones have been selected which by incident are oriented roughly parallel (but the remaining three pairings have also been analyzed – with the same final result). The tilt motion is stronger for the Costa Rica example (note that the amplitude color scale is the same in both pictures) although streaming conditions and bathymetry at the Namibian Walvis Ridge are difficult, this reflects the enhanced stability of the new-generation GEOMAR instruments. The dominating frequency is visible in every amplitude plot as a horizontal structure sticking out from the background, and the latter is rising gently with period and varying over time. These time variations may appear roughly similar in both pairs of neighboring stations. However, the coherence plots for both pairs show one pervasive result and this is zero or values very close to zero. Tilt motion is not coherent between neighboring stations. Hence it cannot be connected to microseisms.

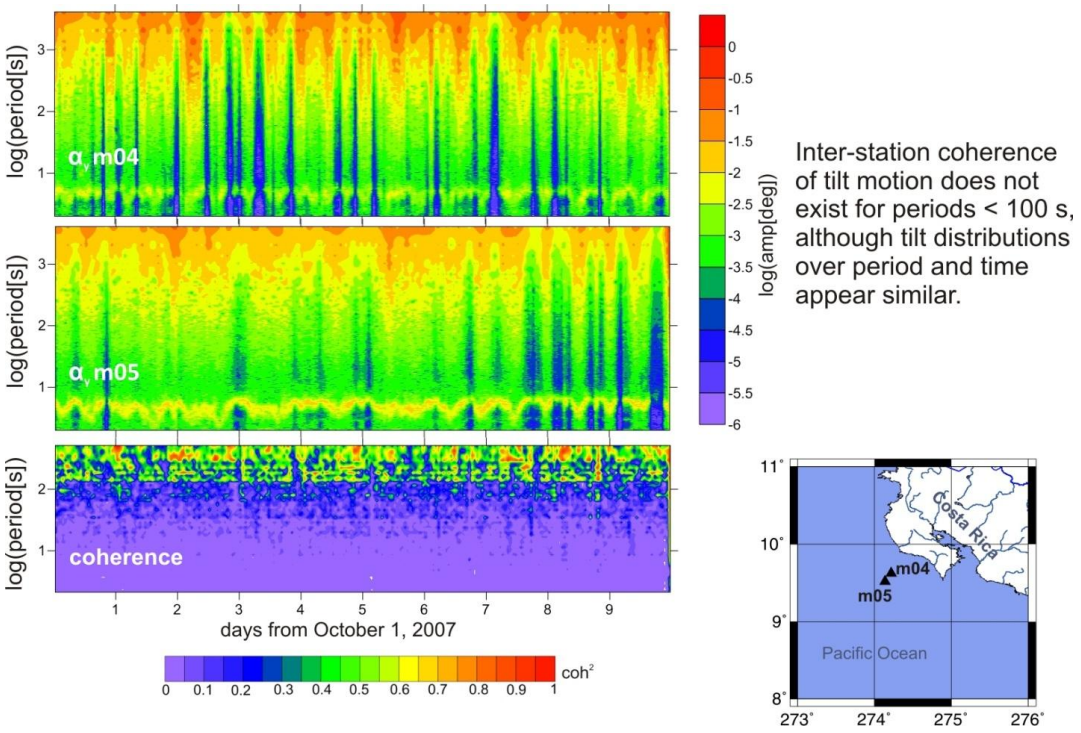

Fig. 5 Dynamic spectral power of tilt channels of stations m04 and m05 offshore Costa Rica (both upper panels) and coherence between them (lower panel). See text for interpretation.

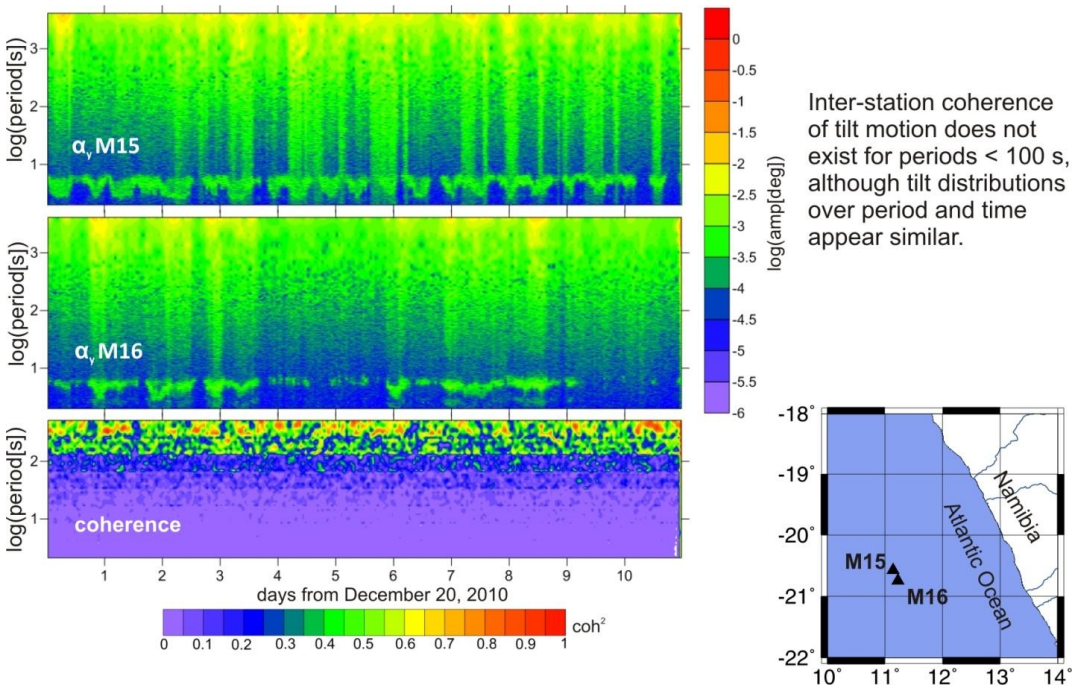

Fig. 6 Dynamic spectral power of tilt channels of stations M15 and M16 offshore Namibia (both upper panels) and coherence between them (lower panel). See text for interpretation.

However, there is evidence that the frequency of the instrument's motion depends on the device type: For the marine MT instruments of the Woods Hole Oceanographic Institution (WHOI), a dominant noise period of 4.5 s is reported (Lezaeta et al. 2005), which is significantly different from the GEOMAR one. Together with the first harmonic of our tilt frequency mentioned in section 2, this supports another idea of how the instrument's motion is generated. The dominant frequency of tilt motion and its harmonic(s) could be eigenfrequencies of the instruments that are excited by water motion, and it is not necessary to assume that the water motion is periodic or wave-like, but a simple streaming would be sufficient to explain the observed effects.

4. How to deal with the resulting disturbances

If the "signal packages" of tilt motion occur frequently and have large amplitudes as in Fig. 2, the motion noise on magnetic channels becomes so strong over the whole period range that a usual data processing can fail. This does not happen in many data sets nor in all stations of them, but occasionally (as for a part of the Costa Rica 2007 survey) strict manual selection of quiet time series fragments was necessary to obtain usable processing results (Worzewski 2011). In such cases it is advisable to correct the magnetic time series for the part induced by tilt motion before the processing. This is possible in two ways:

First, one can re-rotate every sample of the magnetic field vector into a fixed coordinate system by means of the corresponding tilt values (e.g., Nowożyński 2005). This works on the condition that the whole field vector including the static main field is known. Hence this method is limited to marine MT stations utilizing fluxgate magnetometers. Moreover, a careful calibration of the instrument's offsets (that are closely connected to the static field, but not relevant for field variations and therefore sometimes neglected in MT) is required for an effective performance of this method.

Second, a tilt-response correction can be carried out, which does not require the whole field vector. Here a transfer function is estimated between the tilt channels and the magnetic ones, that is used to reconstruct the tilt-induced part of the magnetic records, which, in turn, is subtracted from the original magnetic data. Both methods significantly improve the processing results of data affected by heavy motion noise (details in Neska et al. 2013).
If motion noise is present in a dataset, but not strong enough to justify an explicit correction for it, or if tilt records are unavailable, it is advantageous to apply a processing approach that takes the special distribution of motion noise into account. Many processing codes treat the horizontal magnetic channels by default as input channels during transfer function estimation, because they are usually less noisy than the electric ones in onshore MT. This would be an inopportune approach here, where electric channels (except for the shortest periods) are practically free of motion noise even where magnetic ones are strongly affected (cf. section 2). Here magnetic channels should not be used as input channels, neither in a single-site processing nor as reference channels in case of an application of the remote-reference technique (Gamble et al. 1979, note that a remote reference processing with offshore stations is allowed because motion and motion noise is not coherent between different sites as shown in section 3). Instead, one should either use electric channels as input and reference ones or apply a processing approach that is independent of such input/output schemes. Egbert's multiple-station processing (Egbert 1997) based on a Principal Component Analysis (PCA) can be recommended in this context, particularly because it has another advantage from a marine point of view: Its facility (or even need) to process data of many synchronous stations in one run fits to the fact that stations of marine arrays are both dropped and collected within a short time, hence their data are synchronous to a great extent. However, one should be cautious when estimating geomagnetic transfer functions with this method, because motion noise is highly coherent between the vertical and the horizontal magnetic components of a station (Fig. 2), and the PCA is sensitive to such complications.
Figure 7 shows which meaning the choice of an appropriate processing approach can have for the quality of a sounding curve.

5. Conclusions

Based on the datasets analyzed here, the hypothesis that microseisms are the source of instruments' motion in marine MT has to be regarded as improbable. Important arguments are first, that tilt motion is not coherent between neighboring stations as it is the case for wave fields connected to microseisms, and second, that the dominant frequency of tilt motion seems to depend on the device type. The latter favors rather an interpretation of the tilt motion patterns as an eigenfrequency of the instrument excited by an arbitrary water motion (e.g., streaming). However, these conclusions are drawn in a rather indirect way and further data may confirm or refute them.
The motion noise on the magnetic channels can either be reduced explicitly by means of a re-rotation or the tilt-response correction utilizing the tilt records, or its influence on transfer functions can be suppressed by applying processing approaches that do not use magnetic records as input channels.

Acknowledgements

The authors thank Sebastian Hölz and Lars Planert for sharing valuable information on microseisms.

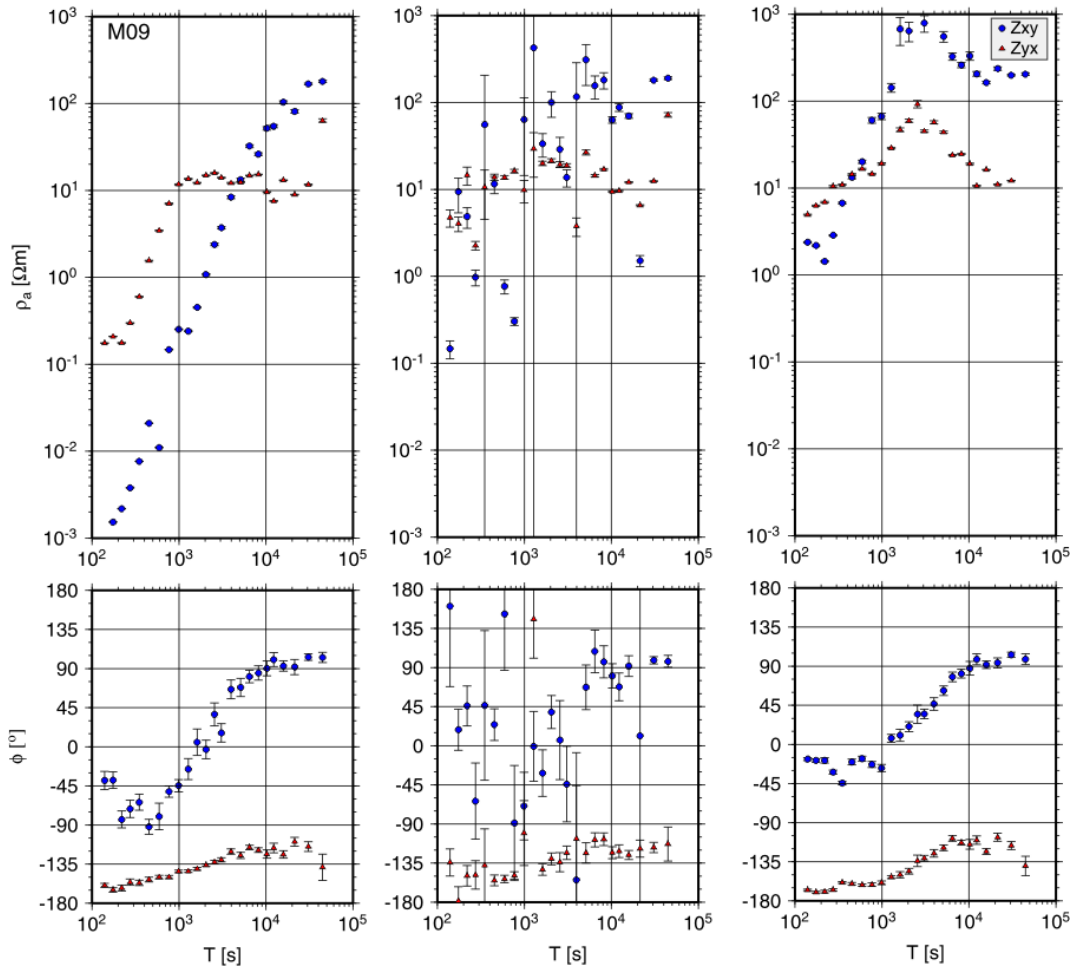

Fig. 7 Sounding curves of site M09 offshore Namibia rotated to geomagnetic coordinates. Left-hand side processed single-site after Egbert & Booker (1986) which leads to a heavy down-bias of ρ_a because of motion noise in the magnetic channels. Middle processed with the remote reference M15 and the same code which corrects the bias but leads to wild scattering due to magnetic motion noise in the reference. Right-hand side after multiple-station processing (Egbert 1997) of both sites which yields a reasonable, somewhat scattered result, cf. Fig. 1. Both stations are affected by moderate motion noise (cf. Fig. 6 for M15). Of course, including more stations significantly improves the multiple-station result, but here we want to draw attention on the fact that not only the amount of stations or data used matters, but also the method they are processed with.

References

Bromirski, P. D., 2001. Vibrations from the "Perfect Storm", *Geochem. Geophys. Geosyst.*, *2, 1030, doi:*10.1029/2000GC000119.

Chevrot,S., Sylvander,M., Benahmed,S., Ponsolles,C., Le fevre,J.M., and Paradis,D., 2007. Source locations of secondary microseisms in western Europe: Evidence for both coastal and pelagic sources, *J. Geophys. Res.*, **112**, B11301.

Cox, C., Kroll, N., Pistek, P., and Watson, K.,1978. Electromagnetic Fluctuations Induced by Wind Waves on the Deep-Sea Floor. *J. Geophys. Res.*, **83**, 431 – 441.

Egbert, G. D. and J. R. Booker, 1986. Robust estimation of geomagnetic transfer functions. *Geophysical Journal of the Royal Astronomical Society,* **87,** 173–194.

Egbert, G.D., 1997. Robust multiple-station magnetotelluric data processing, *Geophys. J. Int.*, **130,** 475–496.

Gamble, T.D., W.M. Goubau, and J. Clarke, 1979. Magnetotellurics with a remote reference. *Geophysics,* **44,** 53–68.

Kedar, S., M. Longuet-Higgins, F. Webb, N. Graham, R. Clayton, and C. Jones, 2008. The origin of deep ocean microseisms in the North Atlantic Ocean, *Proc. R. Soc. A,* **464 (2091)**, 777-793, doi:10.1098/rspa.2007.0277 1471-2946

Lezaeta, P., Chave, A. & Evans, R.L., 2005. Correction of shallow-water electromagnetic data for noise induced by instrument motion, *Geophysics,* **70(5),** G127–G133.

Longuet-Higgins,M.-S., 1950. A Theory of the Origin of Microseisms, *Phil. Trans. R. Soc. Lond. A,* **243 (857),** 1-35, doi:10.1098/rsta.1950.0012

Mittet, R., Aakervik, O. M., Jensen, H. R., Ellingsrud, S., & Stovas, A., 2007. On the orientation and absolute phase of marine CSEM receivers, *Geophysics,* **72(4),** F145–F155.

Neska, A., Nowożyński, K., Reda, J., Jegen-Kulcsar, M. 2013. Reducing motion noise in marine magnetotelluric measurements by means of tilt records. *Geophys. J. Int.*, **194**, 304 – 315.

Nowożyński, K., 2005. Tilt-Correction algorithm for Vector Magnetometers, *Publs. Inst. Geophys. Pol. Acad. Sc.*, **C-92(379),** 131–135.

Wiese, H., 1962. Geomagnetische Tiefentellurik Teil II: Die Streichrichtung der Untergrundstrukturen des elektrischen Widerstandes, erschlossen aus geomagnetischen Variationen, *Pure and Applied Geophysics,* **52 No. 1,** 83 – 103.

Worzewski, T., 2011. Marine magnetotellurics on a continental margin: imaging the hydration and dehydration cycle of the Costa Rican subduction zone, *PhD thesis*, Mathematisch-Naturwissenschaftliche Fakultät der Christian-Albrechts-Universität zu Kiel.

Worzewski, T., Jegen, M. & Swidinsky, A., 2012. Approximations for the 2-D coast effect on marine magnetotelluric data, *Geophys. J. Int.*, **189,** 357–368.

3D numerical modelling and 1D inversion and resolution analysis of time-domain marine controlled source electromagnetic data

Davood Moghadas[1], Martin Engels[1], Romina A. S. Gehrmann[2], and Katrin Schwalenberg[1]

[1]*Federal Institute for Geosciences and Natural Resources (BGR), B1.4 Marine Resource Exploration, Hannover, Germany*
[2]*School of Earth and Ocean Sciences, University of Victoria, Victoria, BC, Canada*

1 Introduction

The marine Controlled Source Electromagnetic (CSEM) method has been increasingly used for gas hydrate explorations and investigation of the marine subsurface. This technique is based on the diffusive propagation of electromagnetic (EM) signals emitted from a source dipole (Tx) on or close to the seafloor. The EM signal travels away from the source dipole through the conductive seawater where it is attenuated quickly, and through the more resistive seafloor sediments. It is recorded by one or more receivers located on the seafloor at some distance away from the Tx. The part of the signal passing through the seafloor arrives at the receivers first. The marine controlled source electromagnetic group at Federal Institute for Geosciences and Natural Resources (BGR) has developed a new, bottom-towed, time domain, multi-dipole CSEM system (Figure 1). The system consists of a bipolar electrical transmitting dipole located on the seafloor and electrical receiving dipoles at offsets between 100 m and 1000 m settled in-line with the source dipole. The system measures the horizontal component of the electric field (E_x).

The possibility to estimate accurately the seafloor properties from CSEM data is obstructed by the appropriateness of the inverse modeling technique to derive marine subsurface structures. Successful inversion is challenging, since the inverse problem should satisfy elemental well-posedness conditions. In the context of marine CSEM studies, several inversion scenarios are taken into account. OCCAM inversion assumes a smooth model and can be employed to have an initial estimation about the number of sub-seafloor layers. Marquardt inversion can also be used for marine CSEM applications. This method is more appropriate to resolve sharp boundaries. Nevertheless, the results are strongly dependent on the starting model, i.e. several initial models can produce different inversion outcomes.

Bathymetry effects on the marine CSEM response have been rarely reported in the geophysical literature. These effects can be simulated by numerical methods. Motivated by CSEM data collected in deep water offshore New Zealand and in shallow water in the

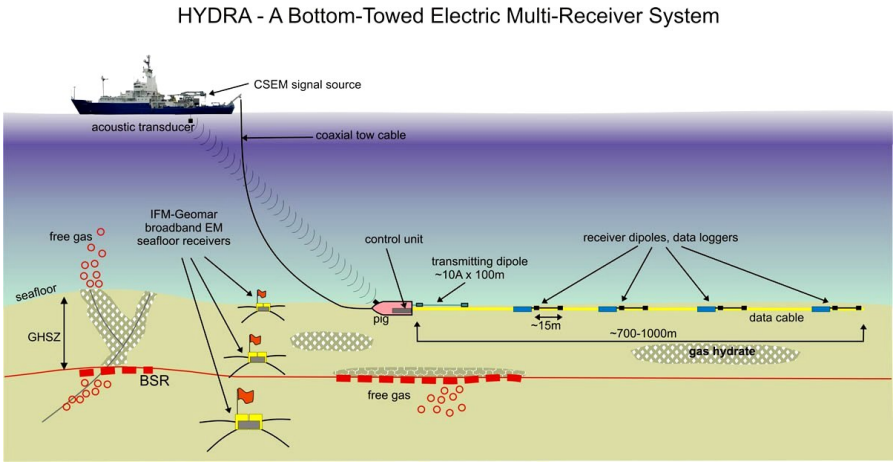

Figure 1: Set-up of the inline electric dipole-dipole system.

German North Sea, we study the effect of seafloor topography and sub-seafloor structure for both shallow and deep water environments. This study was carried out through systematic 3D forward modeling demonstrating to which extent topography is relevant, and should be included in the modeling process. These data sets were analyzed by 1D OCCAM- and Marquardt- type inversion strategies using the code by C. Scholl. Moreover, we compared the results of the OCCAM and Marquardt inversions with global-local optimization approaches to obtain sub-seafloor layering through numerical simulations. The global-local approaches correspond to the global multilevel coordinate search (MCS) algorithm (Huyer & Neumaier, 1999) combined sequentially with the classical Nelder-Mead simplex algorithm (NMS) (Lagarias et al., 1998).

2 Effect of topography

The sea floor topography can have great influences on the measured CSEM data. As a result, information about the extent of such influences can assist us for an accurate interpretation of the data. We simulated the sea floor topography using a 3D EM forward code of Zonghou Xiong. We considered four different scenarios including 1) a model without sea floor topography and sub-seafloor 3D structure, 2) a model without sea floor topography and with sub-seafloor 3D structure, 3) a model with sea floor topography and without sub-seafloor 3D structure, 4) a model with both sea floor topography and sub-seafloor 3D structure. The 3D structure was simulated considering a 3D block with $\rho = 50\ \Omega \times m$ in the sub-seafloor with background resistivity of $\rho = 1\ \Omega \times m$. The seafloor topography was simulated using a 3D block with 20 m height and resistivity of $\rho = 1\ \Omega \times m$. The numerical simulation was carried out considering both shallow (100 m) and deep (5000 m) water ($\rho = 0.3\ \Omega \times m$). The RMS error between the first scenario (E_x^1) and other scenarios (E_x^m) was calculated as follows:

$$RMSE_{1m} = 100 \times \sqrt{\frac{\sum(E_x^1 - E_x^m)^2}{\sum(E_x^1)^2}} \tag{1}$$

The results of simulations for shallow and deep water considering 1100 m offset are shown

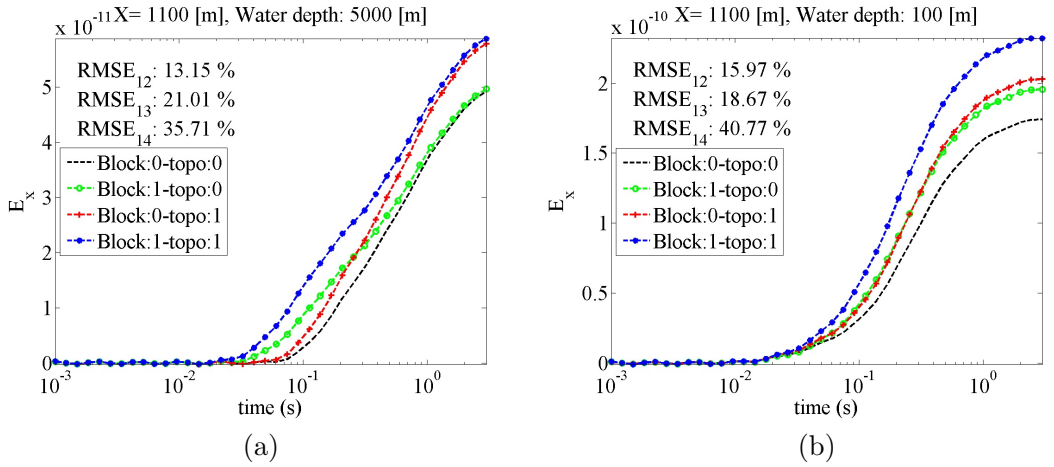

Figure 2: The results of simulations for shallow and deep water considering 1100 m offset.

in Figure 2. As can be seen, for shallow water, the air wave interferes to the results causing to obtain smoother data, i.e., the bumps originated from the sub-seafloor structure are not observed for data related to shallow water. Moreover, the RMS error between the first scenario and the second one (no topography) is lower than those between first and the other scenarios (see Fig. 2). Similar results (not shown here) were obtained for other offsets. Consequently, for interpretation of the marine CSEM data, the effect of topography should be taken into account.

3 Inversion scenarios

In order to investigate the robustness of several inversion algorithms to derive sub-seafloor structures, we performed 1D inversion using OCCAM, Marquardt and global-local approaches. In this respect, synthetic data were generated using a shallow water model with 200 m water depth ($\rho = 0.3\ \Omega \times m$) and a three layer sub-seafloor. In this example, the sub-seafloor layered medium consists of the two first layers with 100 m and 50 m thickness located over a homogenous half-spaces. The resistivity of the layers are $1\ \Omega \times m$, $20\ \Omega \times m$ and $1\ \Omega \times m$, respectively. In order to have simulations close to real case scenarios, we added Gaussian random noise of 2 percent to the electric field. The RMSE between measured (E_x^{meas}) and modeled (E_x^{mod}) data are calculated by

$$RMSE = \sqrt{\frac{1}{N}\sum\left(\frac{E_x^{meas} - E_x^{mod}}{\delta}\right)^2} \tag{2}$$

where ($\delta = \delta^{meas} \times E_x^{meas}$)/100 and δ^{meas} (%) is the measurement error. Figure 3 presents the synthetic data versus modeled values obtained using different inversion scenarios. For all offsets, the synthetic and modeled values presents very well agreements for both OCCAM and MCS-NMS inversion scenarios. In the case of Marquardt inversion, some discrepancies can be observed, in particular for larger offsets.

The final inversion results are illustrated in Figure 4. As expected, the OCCAM inversion suggests a three layer smoothed model. The global-local approach allows for accurate

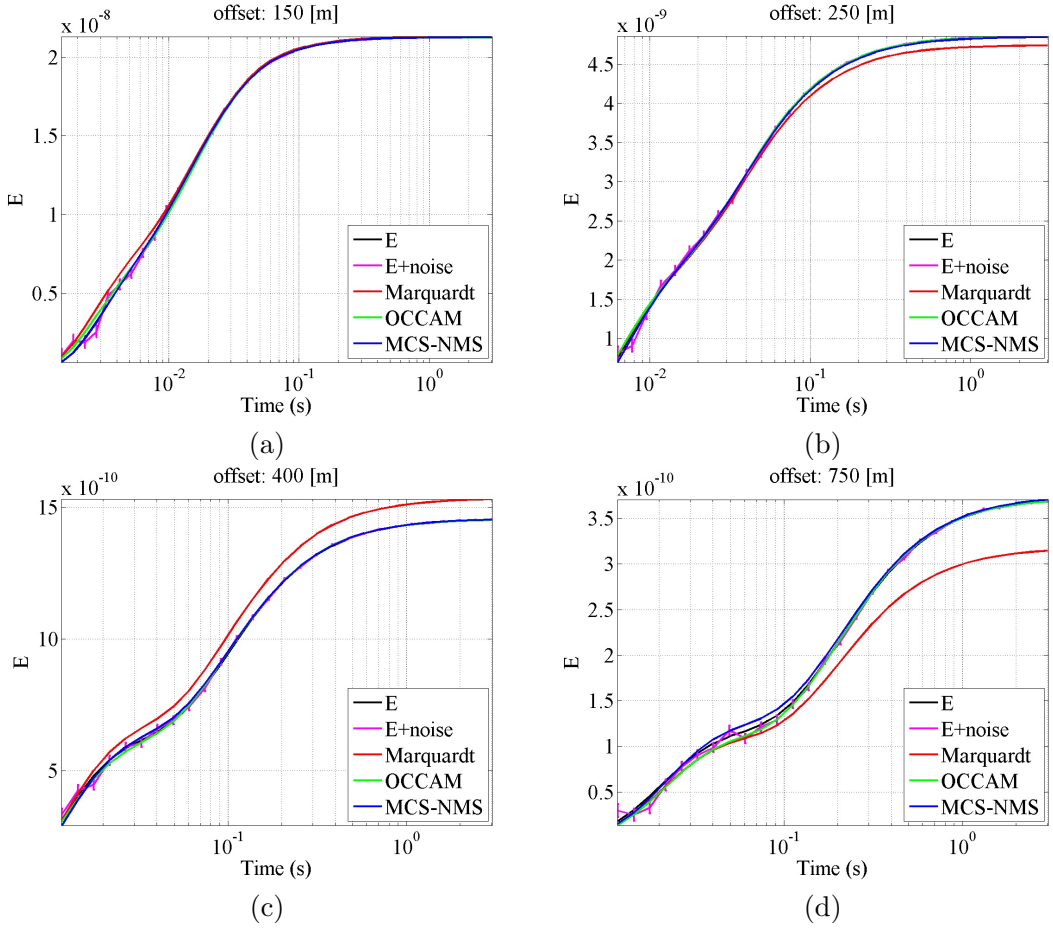

Figure 3: Synthetic and modeled marine CSEM data considering several inversion schemes.

retrieval of the sub-seafloor layering. Less satisfactory results obtained by Marquardt inversion which originates from the sensitivity of this approach to the starting model. Furthermore, the RMSE between synthetic and modeled data is also lower for MCS-NMS than those from Marquardt inversion.

4 Conclusions

We studied the effect of seafloor topography and sub-seafloor structure on marine CSEM data for both shallow and deep water environments. According to the results, the sea floor topography presents significant impact on the marine CSEM data. In addition, we compared the results of the OCCAM and Marquardt inversions with global-local optimization approaches to obtain sub-seafloor layering through numerical simulations. The results show that the MCS-NMS inversion appears to be promising to resolve sub-seafloor structures. The results are valid for 1D structures and for 2D or 3D cases a more complex inversion approach is required. Future work will focus on the inversion of marine CSEM data using MCS and Marquardt approaches in a sequential inversion scheme.

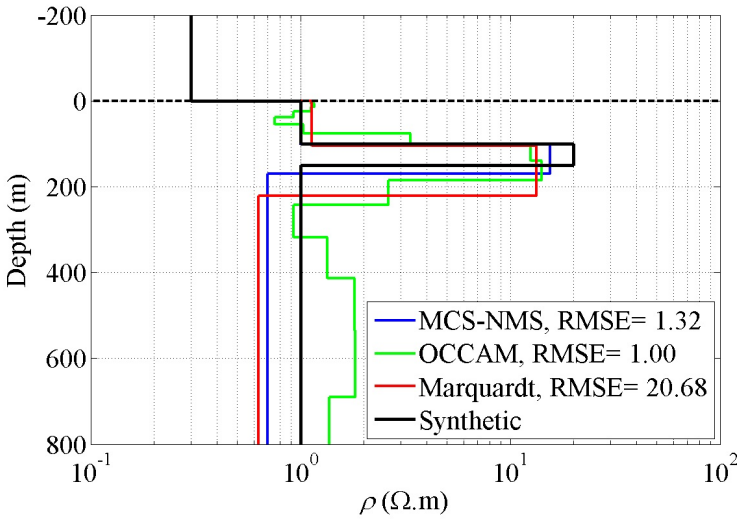

Figure 4: Inversely estimated sub-seafloor layers versus true values.

References

Huyer, W., & Neumaier, A. (1999). Global optimization by multilevel coordinate search. *Journal of Global Optimization*, *14*(4), 331-355.

Lagarias, J. C., Reeds, J. A., Wright, M. H., & Wright, P. E. (1998). Convergence properties of the Nelder-Mead simplex method in low dimensions. *Siam Journal on Optimization*, *9*(1), 112-147.

Impressed Current Cathodic Protection: A useful source for EM exploration?

Tobias Lindau[1] and Michael Becken[1]

[1]*Institut für Geophysik, Westfälische Wilhelms-Universität Münster*

1 Introduction

Many of the pipelines forming the dense system of water-, oil- and gas pipelines present in central Europe are protected against electrochemical corrosion by impressed current cathodic protection (ICCP) systems (Baeckmann et al. (1997), Ahmad (1999)). In normal operation mode an ICCP system injects a DC current into the pipeline in order to achieve protection. However, for occasional pipeline integrity tests the current is switched on- and off periodically, generating time-varying electrical currents and thereby inducing secondary electric- and magnetic fields in the surrounding earth (Bette & Vesper (2005), Grayver et al. (2014)). While to date these fields are considered to be unwanted cultural noise in electromagnetic exploration, this work aims at utilizing the fields generated by the switching of the ICCP current for determining the electrical resistivity of the subsurface. For this purpose we aim at performing electromagnetic field measurements as well as recordings of the injected pipeline current at the injection point. The measured data will be used to calculate transfer functions $\vec{T} = (T_x, T_y)$ describing the relationship between the measured electric fields $\vec{E} = (E_x, E_y)$ and the injected pipe current I:

$$\vec{E}(\vec{r}, \omega) = \vec{T}(\vec{r}, \omega) \cdot I(\omega) \tag{1}$$

For our study we investigate a pipeline segment in northern Germany and begin by determining the current distribution inside such an ICCP protected pipeline. We use the current distribution to create first models of the pipeline source and show first modelling results of the expected electric field distribution in vicinity to the pipeline. Subsequently we use our model to investigate the effect of conudctivity changes in the subsurface on the electric fields recorded at the surface.

2 Working Principle of ICCP Systems

As steel bodies exposed to environmental effects tend to be destroyed by corrosion, pipeline operators make great effort to prevent the destruction of their structures by such processes. While an insulating coating of a steel pipeline greatly reduces the damage caused by corrosion, protection is only achieved as long as the coating is intact. However, due to various factors, defects in the coating do occur along the pipe structure, causing the protection to fail at these locations. Therefore further protection against corrosion is necessary to add protection to the exposed areas of the pipeline as well (e.g. Kutz (2005)).

For this purpose *Cathodic Protection* systems are employed. Such systems are widely used not only for pipeline protection, but are also found in applications linked to the protection of ships hulls or water heaters (e.g. Kutz (2005)). The general idea of *Cathodic Protection* systems is to make the protected structure the cathode of an electrochemical cell. This is achieved by the addition of a suitable material that will act as the anode of the cell and which will be gradually destroyed in favor of the protection of the cathode (e.g. Baeckmann et al. (1997)). A schematic of a simple electrochemical cell, illustrating the principle, is given in Figure 1.

However, while this approach is well suited for smaller structures, it becomes less practical

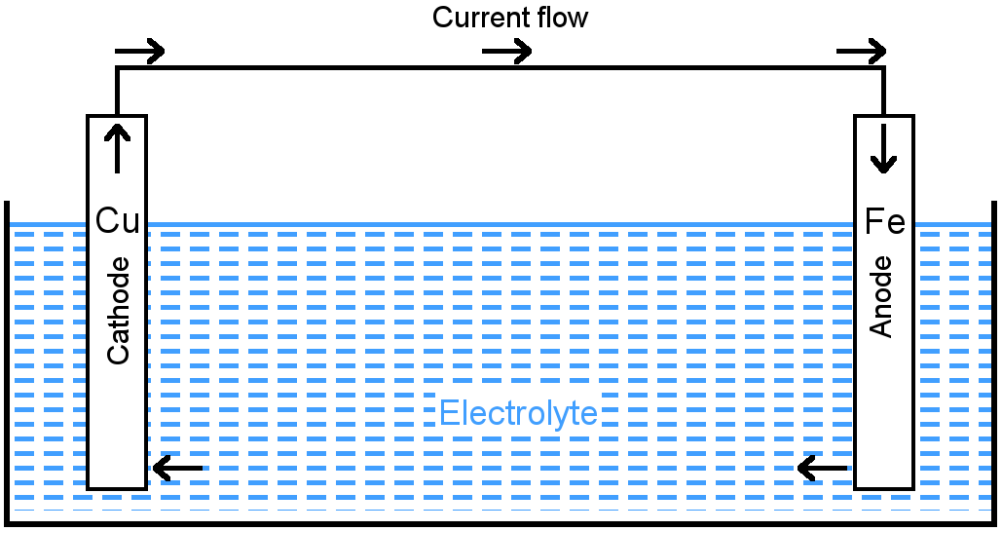

Figure 1: A simple electrochemical cell. Two metals of different electrochemical potential are placed in an electrolyte. Corrosion occurs at the anode, which has a higher energy level (i.e. lower electrochemical potential), whereas no corrosion occurs at the cathode with the lower energy level. Current is flowing through the electrical connection from the cathode to the anode and through the electrolyte from the anode to the cathode. In this example the cell consists of a copper cathode and an iron anode.

when the size of the protected structure becomes larger. Due to the increased amount of current that needs to be supplied by the galvanic anode, larger and more numerous anodes are required, rendering their usage uneconomical. Therefore another approach is pursued, in which a DC power source is added to the system. The power source supplies the additional current needed to protect the structure and which would otherwise have to be supplied by the galvanic anode alone, greatly reducing the anode requirements. Hence the name *Impressed Current Cathodic Protection* (e.g. Kutz (2005)). A schematic of such an ICCP system is shown in Figure 2. While in normal operation mode the current source injects a constant DC current, occasional pipeline integrity tests demand the current to be switched on- and off periodically (e.g. Bette & Vesper (2005)). This switching of the pipe current is automated and sychronized with DCF77 time. Usually a repeating switching pattern of 12 s on- and 3 s offtime is used. The switching of the current generates electromagnetic fields that vary with time and induce secondary electromagnetic fields in the surrounding subsurface. While this switching should be limited to the duration of such integrity surveys, experience has shown that the switching occurs more often. These fields can be measured and are usually considered to be electromagnetic noise. We, however, aim at utilizing these fields generated by the pipeline as sources for exploration purposes.

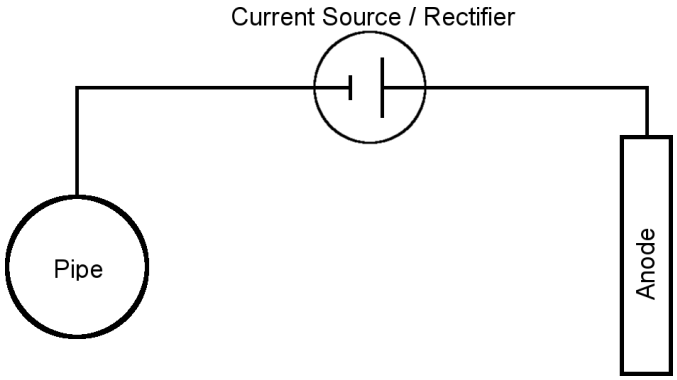

Figure 2: Principle of an ICCP system for pipelines. A DC current source is added to the elctrical connection of pipeline and anode to supply the necessary protection current.

3 Current Distribution

In order to be able to describe and understand the pipeline in terms of an EM source it is necessary to understand the current flow within the pipeline. While for the standard sources used in CSEM a uniform current flow is assumed, this assumption cannot be applied to pipeline sources. As coating defects occur along the pipeline, current flowing through the pipe and towards the anode will leak into the surrounding soil at various locations along the pipeline path. This leaking causes the current flow to decay towards the end, resulting in a non-uniform current flow within the pipeline. As the information about the current flow is not of primary interest for the pipeline operator but only the pipe potential relative to its surrounding (e.g. Bette & Vesper (2005)), there is no data avaiable and field measurements need to be performed in order to determine the current distribution.

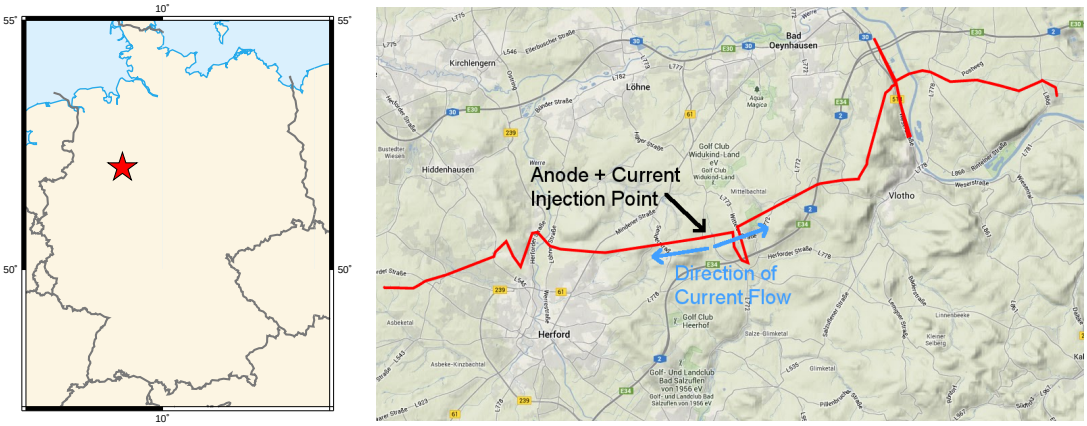

Figure 3: **Left:** Map of Germany with the location of the test segment marked by a star. **Right:** Map view of the area in which the pipeline is located with the approximate pipeline path and the locations of the current injection point and the anode drawn in. Source: maps.google.com

For our studies we chose a pipeline segment near Herford, Germany which is operated by the Westnetz GmbH (see Figure 3). It is approximately 30 km long and consists of a bitumen coated steel pipe with a diameter of 0.3 to 0.4 m. It is protected by a rectified

50 Hz current of 2.5 A. The anode and the current injection point are located in the approximate center of the pipeline segment, causing the current to split up in order to protect both branches of the pipe.
The current flow within the pipeline cannot be measured directly as it is buried and thereby cannot be accessed. To measure the current in the buried pipeline from the surface two measurement methods were applied. In a first approach the total magnetic fields along profiles crossing the pipeline perpendicularly were measured for active and inactive ICCP current. The difference in the total magnetic field was considered to be caused by the DC current flow withing the pipe as described by the law of Biot-Savart (e.g. Stratton (1941)). We then attempted to invert the gathered magnetic field data for the current strength, depth and additional parameters at the individual profile location. However, the data could be explained equally well by a number of parameter sets, making it impossible to make definite and unbiased statements about the current distribution. Subsequently the data was discarded.
The second measurement method also utilizes the magnetic fields generated by the current flow, but uses time variational magnetic field rather than the static magnetic field. Since the ICCP current consists of a rectified 50 Hz current, the DC current flowing in the pipe has a frequency of 100 Hz. The resulting magnetic field at this frequency is measured using two induction coils located in different heights above the pipeline, allowing to calculate the pipe depth as well as the current strength. The measurements were performed using a *RD400* pipeline detection tool supplied by Westnetz. The measurements took place at 47 locations located along the pipeline path. The results for the current from the measurement are shown in Figure 6.
The data shows the expected decay of current towards both ends of the pipeline. However, the maximum current amplitudes of both branches, directly at the injection point, do not add up to the expected injected current of 2.5 A. In order to evaluate the data measured by the *RD400* and check for possible corrections that may be needed to be applied to the data, calibration measurements were performed. For this purpose a cable was fed with a recitfied 50 Hz current similar to the pipes ICCP current.

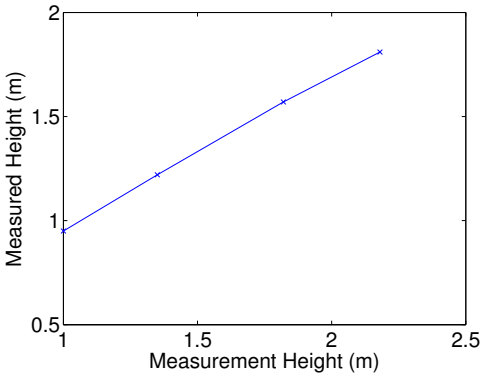

Figure 4: Results of the calibration measurements. Shown is the real- and the measured height for an injected current of 1 A

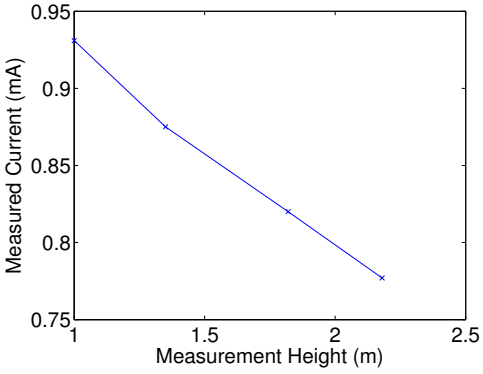

Figure 5: Results of the calibration measurements. Shown is the current that was measured at differents heights for an injected current of 1 A

The *RD400* was used to measure the current within the cable as well as the height above the cable for various combinations of measurement heights and current strengths. The data shows a strong dependence of the measured currents and heights from the distance to the cable (Figure 4 and 5). As the measured heights do not show dependence on the

injected current, a simple relationship between the measured height and real measurement height was derived and used to correct the measured currents depending on the measured height.
Assuming this relationship is valid for the pipeline data as well, the pipeline data was corrected using the same relationship. The resulting current distribution along the pipeline is depicted in Figure 6 along with the originally measured data. The peak values of both branches now add up to a value closer to the expected values of 2.5 A, indicating that the corrections give reasonable results. In general the current shows exponential decay away from the injection site and an exponential function is fitted to the data in order to be able to make statements about the current at locations where no measurements took place.

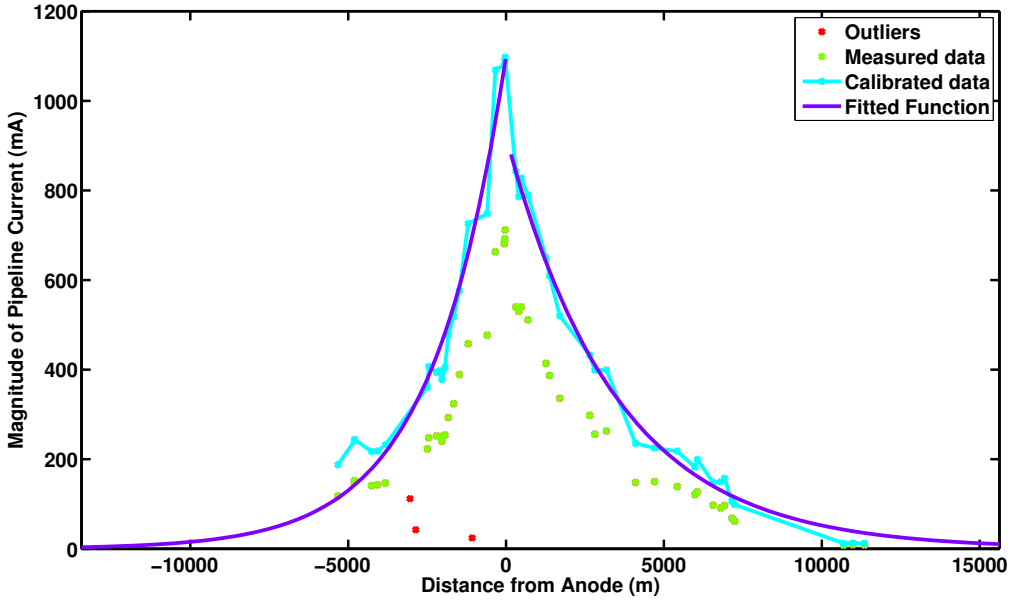

Figure 6: Data from the measurement of the pipe current using the RD400 pipeline detection tool. Shown is the originally measured data (red + green). The red datapoints are discarded as outliers. The data corrected by the function derived from the calibration measurements is shown in green. The purple line represents the function fitted to these points, describing the current distribution as it is used for our models.

4 Modelling Results

To get an impression of the electric fields generated by the pipeline, forward calculations were performed using the current distribution obtained from the calibrated data. The calculations were performed in 1D using the software EM1D which is capable of modelling the fields of various electric- and magnetic type sources for a layered resistivity distribution (Streich & Becken, 2011b). In our model the pipeline is represented by 101 finite wire sources to approximate the pipeline geometry and to incorporate the non-uniform current distribution (Streich & Becken, 2011a). The length of the individual wire sources does not exceed a length of 500 m. Each source is assigned a constant current value which is determined from the exponential function fitted to calibrated current data by calculating the mean current for the section of pipeline represented by the respective element.
Two resistivity distributions were considered: The first resistivity model consists of a

homogeneous half space of 7 Ωm resistivity, whereas the second model adds a 100 m thick conductive layer of 1 Ωm in 500 m depth to the homogeneous model. For the first model the resulting electric field components E_x and E_y at the surface are shown in Figure 7 for a evaluation frequency of 1 Hz.

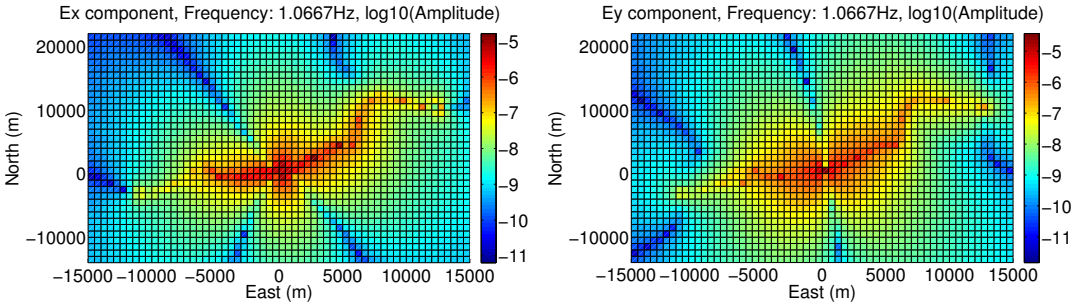

Figure 7: Shown are the electric field amplitudes at the surface resulting from the forward modeling at a frequency of 1 Hz for a homogeneous half space of 7 Ωm.
Left: Amplitude of E_x-component. **Right:** Amplitude of E_y-component.

The electric fields excited by the source are clearly visible and well within the measurable range. In addition, a comparison of the E_y amplitudes of both models, as shown in Figure 8, reveals a strong influence of the conductive layer on the electric fields amplitudes. This indicates sensitivity of the fields to conductivity changes in the subsurface in this depth.

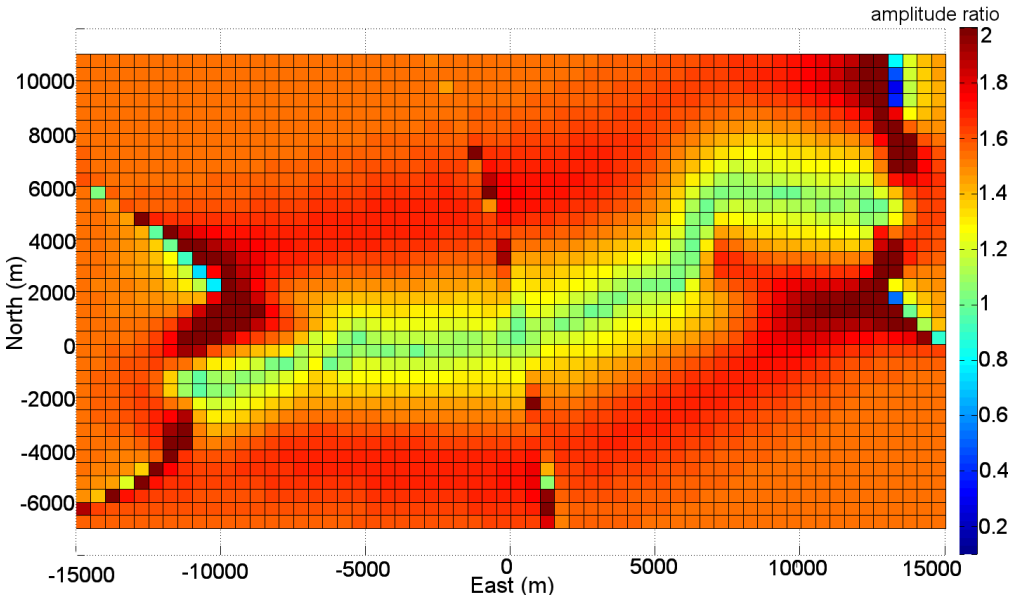

Figure 8: Comparison of the amplitude of E_y components from both models. Shown is the amplitude ratio given by $|E_{y,hom}|/|E_{y,cond}|$, where the subscript *hom* denotes the fields of homogeneous resistivity model and *cond* the values of the model with the conductive layer.

5 Conclusion

The current distribution within the pipeline can easily be determined by measurements with a pipeline detection tool similar to the RD400 device used in this study. The exponential current decay determined for the investigated pipeline segment confirms the expectation that the assumption of a uniform source current distribution is not applicable to pipeline sources.
Modelling of the pipeline source by using a number of finite wire sources and assuming a cascading source current yields resonable models for the electric fields generated by such a source. The electric field amplitudes of the model suggest that field measurements will be able to pick up the signals originating from such a source.
Field measurement, during which the electromagnetic fields and the injected current were recorded, have already been performed and are currently being analyzed. Signals originating in the switching of the pipelines ICCP current are clearly visible in the electric field data. Preliminary processing results give promising results and seem to be in good agreement with the models presented here. We plan, however, to perform additional field measurements along additional profiles to further map the electromagnetic field distribution.

References

Ahmad, Z. (1999). *Principles of corrosion engineering and corrosion control.* John Wiley & Sons Canada, Limited.

Baeckmann, W. von, Schwenk, W., & Prinz, W. (1997). *Handbook of cathodic corrosion protection.* Elsevier Science.

Bette, U., & Vesper, W. (2005). *Taschenbuch für den kathodischen korrosionsschutz.* Vulkan-Verlag.

Grayver, A., Streich, R., & Ritter, O. (2014). 3d inversion and resolution analysis of land-based csem data from the ketzin storage formation. *GEOPHYSICS*, *79*(2), E101-E114.

Kutz, M. (2005). *Handbook of environmental degradation of materials.* Elsevier Science.

Stratton, J. (1941). *Electromagnetic theory.* McGraw-Hill book Company, Incorporated.

Streich, R., & Becken, M. (2011a). Electromagnetic fields generated by finite-length wire sources: Comparison with point dipole solutions. *Geophysical Prospecting*, *59*(2), 361-374.

Streich, R., & Becken, M. (2011b). Sensitivity of controlled-source electromagnetic fields in planarly layered media. *Geophysical Journal International*, *187*(2), 705–728.

3-D reinterpretation of magnetotelluric data from the South American continental margin

Jonas Küster[1,2], Christine Kühn[1], and Heinrich Brasse[1]

[1]*Freie Universität Berlin, Fachrichtung Geophysik, Malteserstr. 74-100, 12249 Berlin, Germany*
[2]*email address: jon.kuester@gmx.de or jon.kuester@geophysik.fu-berlin.de*

1 Abstract

The Central Andean continental margin is characterized by subduction of the Nazca plate beneath the South American plate. This created the Altiplano-Puna high plateau in northern Chile, southwestern Bolivia and Peru and northwestern Argentina.

Magnetotelluric data were collected along two transects in the late 1990s. These data were previously analyzed by using 2-D inversion, neglecting several sites/regions with severe three-dimensional distortion. Here we describe efforts to employ 3-D modeling and inversion codes to include those problematic areas and achieve a more reliable conductivity image of the subsurface, from the coast to the high plateau between 19.9°S and 21.4°S.

Basically (and fortunately), we could confirm most of the results obtained earlier, particularly a vast high conductivity zone beneath the Altiplano, extending through the entire middle and lower crust and assumed to be caused primarily by partial melts. Furthermore our new inversions confirmed another elongated high conductivity zone associated with the Precordillera Fault System in the forearc and – contrary to common expectation – a resistive volcanic arc. However, we may now deduce a conductor close to the volcanic arc without being able to connect it with a specific edifice due to insufficient station coverage.

A great achievement is that we are now able to quantitatively explain phases above 90° of several MT stations in the Coastal Cordillera, with conductive near-surface structures extending from the Pacific Ocean and undulating around the sites. In contrast the deeper forearc close to the Pacific Ocean is electrically unexciting and resembles largely a homogeneous halfspace.

2 Introduction

Various scientific investigations throughout the last decades were carried out in the Central Volcanic Zone of the Andes in northern Chile, southwestern Bolivia and western Argentina. Here, a magmatic arc is linked to the subduction of the Nazca plate beneath the South American plate. The morphological appearance (Coastal Cordillera, Longitudinal Valley, Precordillera, Western Cordillera (WC), Eastern Cordillera) (Fig. 1) is evidence of this subduction-related development and the 200 km eastward arc-migration with the present-day volcanic arc in the WC (Scheuber et al., 2006). Furthermore tectonic uplift resulted

in today's Altiplano-Puna high plateau with an extreme crustal thickness of more than 70 km (Yuan et al., 2000).

Dehydration processes of the subducting slab produce ascending fluids that lead to melting of the mantle wedge and further rise into the crust. Those hydrothermal fluids and partial melts of volcanic systems are characterized by high electrical conductivity and therefore detectable by geophysical methods which are sensitive to conductivity, such as magnetotelluric (MT).

The long-period magnetotelluric data used here were collected in the late 1990s along two transects (19.9°S and 21.4°S) crossing the forearc, the Western Cordillera and the backarc (Altiplano high plateau). In previous studies data were interpreted based on 2-D models (Echternacht et al., 1997; Schwalenberg et al., 2002; Brasse et al., 2002; Brasse, 2011). Most of the data are compatible with a typical 2-D problem. Nevertheless, all previous studies left some questionable 3-D effects, in particular near the coast and on the Eastern Altiplano. The results introduced here, will give a reinterpretation based on new 3-D modeling and inversion of the areas shown in Fig. (1) by also adding some MT stations located between these two transects.

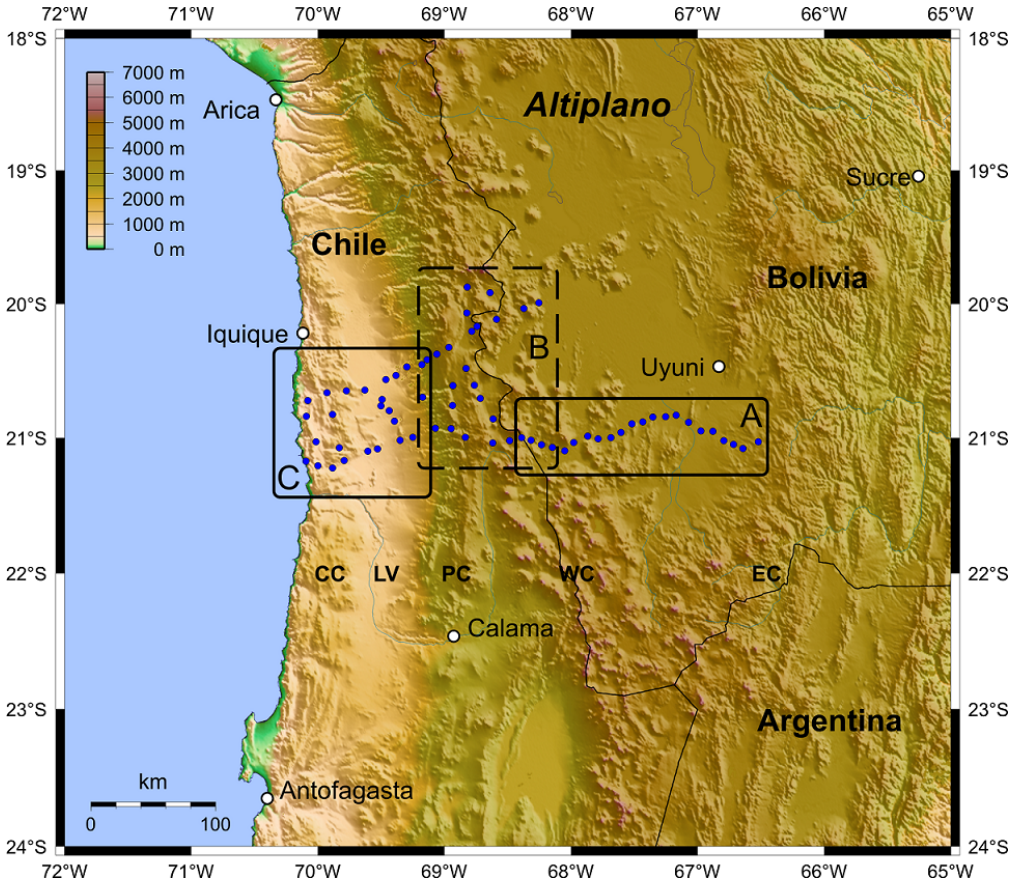

Figure 1: Map of the investigation area in northern Chile and southwestern Bolivia. Blue dots indicate the measured magnetotelluric (MT) sites. CC: Coastal Cordillera; LV: Longitudinal Valley; PC: Precordillera; WC: Western Cordillera; EC: Eastern Cordillera. A,B,C are areas for which the 3-D modeling was performed.

3 Previous studies and 3-D effects

The principal result from the 2-D modeling was a vast high conductivity zone (with a conductivity of 1 S/m) beneath the Altiplano at mid and lower crustal depth (ANCORP line at 21°S, area A). This conductivity anomaly in the backarc crust is thought to extend farther south into the Puna plateau (Díaz et al., 2012). Likewise a seismic low-velocity zone is connected to this anomalous feature (Yuan et al., 2000; Heit et al., 2014). Chmielowski et al. (1999) associated this zone with the Altiplano-Puna Magma body (APMB). Towards the north at 17°S this conductor vanishes and instead an anomaly is modeled in the upper mantle (Brasse and Eydam, 2008). These conductors are located about 100 km to the east of the recent volcanic arc, hinting at a further shifting of the magmatic system in the Central Andes. Nevertheless in the north (17°S) and in the south (23.5°S) a modest conductor (0.05-0.03 S/m) is detected beneath the arc (Brasse and Eydam, 2008; Díaz et al., 2012). In general the forearc is more resistive than the backarc region.

Especially in the Coastal Cordillera several MT stations display phases above 90°, indicating strong 3-D distortion (Brasse et al., 2002; Lezaeta, 2001). Additionally, real induction arrows show a more complex characteristic as would be expected as a result of the coast effect (i.e., pointing away from the ocean in Wiese convention).

On the Altiplano the MT-measurements also show deviations from a regional 2-D assumption. At longer periods the induction arrows on the Eastern Altiplano orientate along the Uyuni-Kenyani Fault Zone (Fig. 2), whereas at short periods the arrows are small and indicate a 1-D case. Fig. (2) shows the phase tensor ellipses and skew angle β for the period 3276 s computed after Caldwell et al. (2004). Rapid variation of the direction of the major axes with period and/or a high value for β demonstrate a 3-D case. For the Eastern Altiplano and two MT stations in the western Altiplano (*tar*, *mop*) the β values are close to or exceed 5°. Arbitrarily, we may assume a value below 5° as acceptable for a 2-D scenario (Díaz et al., 2012; Ingham, 2005). Therefore most of the Altiplano seems to be almost 3-D at a period of 3276 s (Fig. 2). Remarkably, the β values are small where induction arrows indicate a 3-D subsurface in the vicinity of the Uyuni-Kenyani Fault System. At smaller periods the β values indicate mainly a 2-D scenario; this agrees with the 2-D assumptions of previous studies.

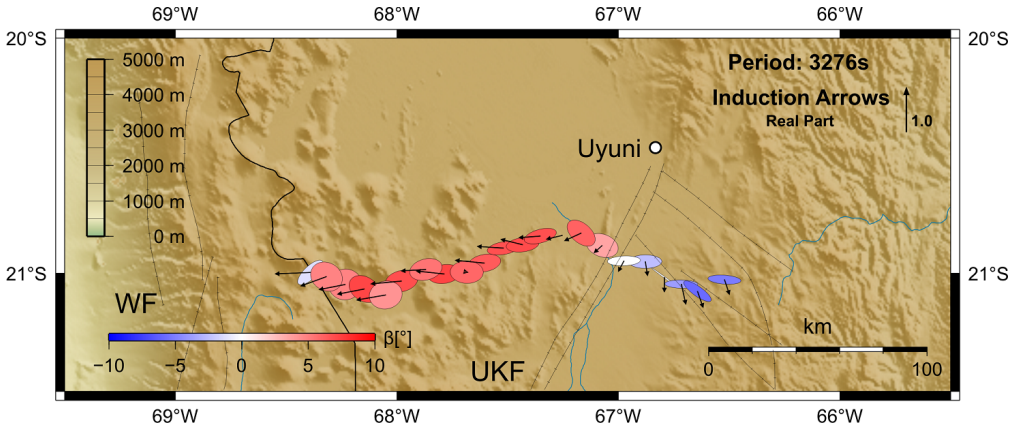

Figure 2: Altiplano region (area A) with induction vectors, phase tensor ellipses and skew angle β at 3276 s, which can be associated with mid crustal depths.

4 3-D inversion and results

In this work several 3-D inversions were performed for the depicted areas (Fig. 1) by applying the 3-D code of Siripunvaraporn et al. (2005). This program (WSINV3DMT) is an extension of the 2-D data space Occam's inversion (Siripunvaraporn and Egbert, 2000) and searches for the smoothest model to fit the data at a specified error floor (in this work 5%). This code inverts the eight components of the impedance tensor but does not take into account magnetic transfer functions.

Only every second period in the range 10-10000 s was used to increase the computational efficiency. Near the coast an ocean with a representative resistivity of 0.3 Ωm was added in the initial model, with a trench depth of nearly 8 km. The background resistivity of the initial model was set to 100 Ωm throughout with the exception of the forearc region (Fir. 1, area C), where we set a values of 1000 Ωm relying on previous studies. The largest depth of the models reach 650 to 800 km with increasing cell width (100 m x increasing factor 1.3) from top to bottom. As a measure for inversion quality we used the rms as well as the a visual control of data fitting.

4.1 Area A - Altiplano

The model results show well-conducting structures (Fig. 3, A1-A4) in the upper 2 km of the subsurface beneath the Altiplano. They can be linked to the young sedimentary fill of the Altiplano, containing highly saline fluids as obvious in the numerous salars with the Salar de Uyuni being the largest (Schwalenberg et al., 2002).

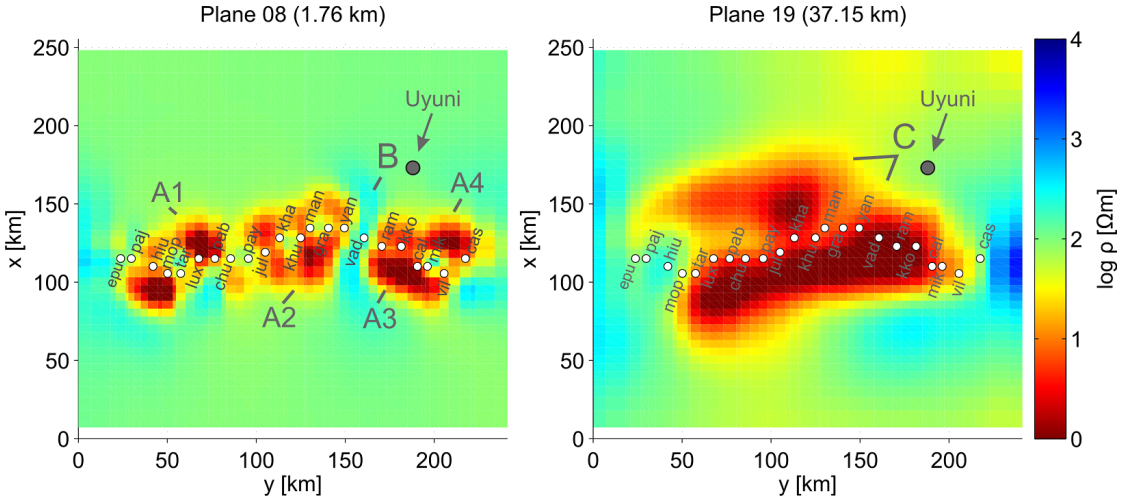

Figure 3: 3-D model (rms=1.76) of area A. Top view at a depth of 1.76 km (left) with sediments (A1-A4) and a resistive anomaly (B) correlative with morphological elevation, probably Uyuni-Kenyani Fault Zone as well as in a depth of 37.15 km (right) with the Altiplano Conductivity Anomaly (C).

A resistive structure (Fig. 3, B) cuts through the well-conducting patterns between station *ram* and *yan* in the Eastern Altiplano. It extends from 1.2 km to a depth of about 10 km. In previous 2-D models this structure did not appear so clearly and can be associated with an uplift of Paleozoic rocks along the Uyuni-Kenyani Fault Zone (UKFZ). Brasse et al. (2002) mentioned that the station *vad* was built on outcropping more compacted, and thus more resistive, Paleozoic sediments compared to the surrounding Quaternary

deposits. However, the UKFZ is not associated with an isolated and elongated conductive zone, neither at small nor large depths.

At depths of more than 20 km a huge conductivity anomaly (Fig. 3, C) is shown. This Altiplano Conductivity Anomaly (ACA) is comprehensively discussed in other scientific studies and can be associated with the northern extension of the APMB. The upper boundary at about depth of 20 km correlates with the so-called Andean Low Velocity Zone (ALVZ) in mid-crustal depth (15-20 km) proposed by Yuan et al. (2000).

The lower boundary of the ACA is poorly resolved. In accordance to Schwalenberg et al. (2002), a sensitivity study for the model in Fig. 3 indicates a minimum depth of about 50 km to 60 km, respectively. This was done by setting the low resistivities at depth to the background resistivity of 100 Ωm, check the model response and start inversion over. However, it is very conspicuous that the huge conductive structure is principally not positioned directly beneath the sites, but accumulates into two elongated bodies in the north and south. The reason for this remains for the time being. Probably by adding another transect the ACA could be seen as a continuous body, though it would be difficult to achieve due to inaccessibility of the surrounding areas. The N-S extent of the Altiplano conductor can be recognized in the northern part of the study area beneath the plateau as well but is limited there due to missing sites in the east.

Thus this huge conductor may cover the entire crust. The generally accepted assumption is a huge area of partially molten rocks together with saline fluids, i.e. an evolving pluton of enormous dimensions. Based on high-resolution gravity data del Potro et al. (2013) assume for an area more to south (21.5°S-23°S) a partially molten body that ascends diapirically through a strongly weakened crust up to the surface (Uturuncu volcano). For a deeper understanding of the ACA we refer to Schilling et al. (2006).

4.2 Area B - Precordillera and volcanic arc

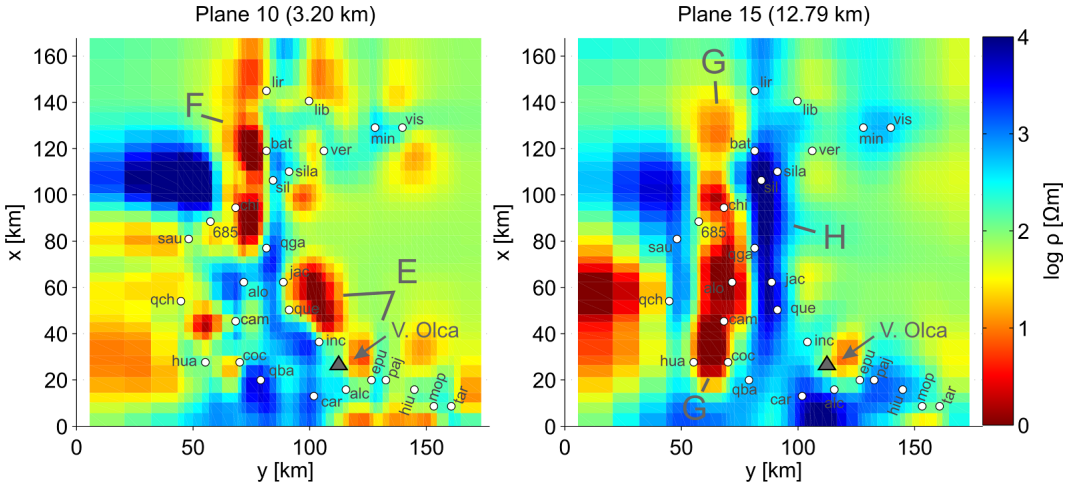

Figure 4: 3-D model (rms=1.79) of area B. Top view at a depth of 3.20 km (left) with conductive structure beneath volcanic arc (E) and Preandine Depression (F) as well as at a depth of 12.79 km (right) with highly conductive West Fissure (G) and resistive Western Cordillera (H).

As in previous 2-D modeling our 3-D models show the present volcanic arc as generally highly resistive (Fig. 4, H) throughout the entire study area between 19.9°S-21.4°S. Sur-

prisingly, a conductor (Fig. 4, E) can be detected now in the vicinity of the volcanic arc close to the stations *inc*, *que*, *jac*, and in the north of station *epu*. This structure becomes clearly visible at a depth of about 2 km and terminates between 5 and 7 km depth. Here fumarolic activity is reported at three potentially active centers, the Irruputuncu, the Olca and the Paruma volcanoes (González-Ferran, 1994).

In the Precordillera and western border of the Western Cordillera a conductive structure (Fig. 4, F) near the surface can be seen in the northern part of the model. Here, sediments of the Preandine Depression can be considered plausible. The good conductor along the Precordillera (Fig. 4, G) could be depicted here in its elongated shape the first time. In previous studies of Schwalenberg et al. (2002) and Echternacht et al. (1997) this enhanced conductivity could be seen along both transects. However, our models show the beginning of this conductor in a shallower depth of 12 km, whereas in earlier 2-D models the anomaly at 15 km depth and can be traced to a depth of 20 km. This conductor is correlated with the West Fissure (Precordillera Fault System) and serves probably as a conduit for aqueous fluids.

4.3 Area C - Forearc

The interpretation of the coastal MT sites is much more difficult. Data are affected by strong telluric distortion due to current channeling in an elongated conductor presumably connected to the Atacama Fault System. Earlier work assumed a narrow conductor, comparable to this Fault System but 2-D modeling (even with anisotropy) cannot explain the phases above 90° at several sites (Lezaeta, 2001; Beike, 2001). With the new 3-D modeling we were able to fit the anomalously high phases, and explain it with electrical currents flowing around the involved MT stations. The shallow conductivity distribution is very variable. Close to the coast these near-surface structures (Fig. 5, J1,J2) connect to the highly conductive ocean. J2 may run obliquely in SE direction but is interrupted by a modest resistor.

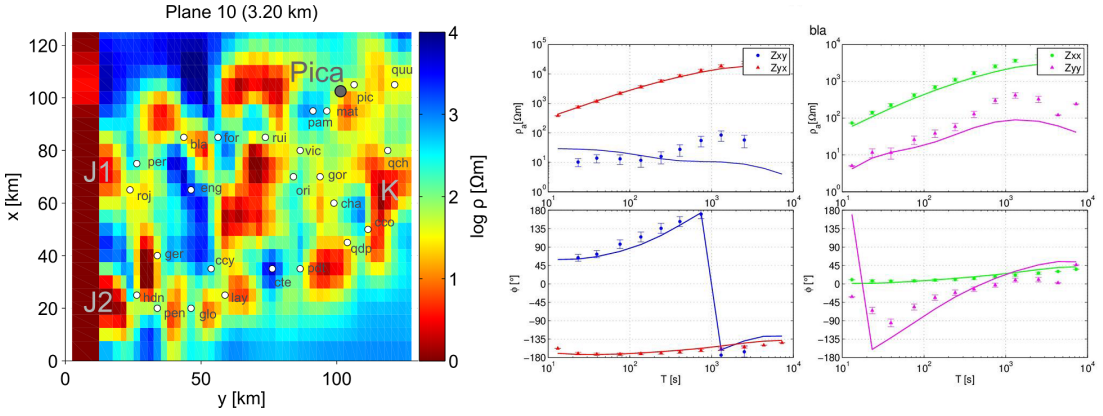

Figure 5: 3-D model (rms=2.75) of the forearc (area C). Top view at a depth of 3.20 km (left) with near-surface structures connecting to the ocean (J1, J2) and highly conductive anomalies in the Longitudinal Valley and near Chacarilla canyon (K). Right: Data fit for station *bla* including all four components of the impedance tensor with a good fit of phases above 90°. Note, however, that apparent resistivity of Z_{xy} is not well fitted.

The sediments of the Longitudinal Valley are well-conducting in the upper 1-3 km. At depths greater than 10 km a simple homogeneous, resistive halfspace occupies most of the forearc region beneath the Coastal Cordillera and is attributed to large assemblages of igneous rocks (Coastal Cordillera batholiths). MT station *qch*, located in the Chacarilla canyon in the foothills of the Precordillera (Fig. 5, K) is also characterized by phases exceeding 90°. One explanation could be the geology of this canyon, which is filled with higly conductive sediments in a resistive mountain environment.

5 Conclusion

The area between 19.9°S and 21.4°S was considered once again to gather new information based on 3-D modeling. Basically we could confirm most of the earlier results, particularly the large Altiplano Anomaly and the conductive Precordillera Fault System. Nevertheless we see now conductive zone near the volcanoes of the Western Cordillera along the ANCORP line. Furthermore we are now able to explain phases above 90° by meandering features in the Coastal and Precordillera. To correlate these conductive loops we would need a much denser station network, however.

Acknowledgment

Most of the plots in this manuscript have been prepared using Matlab routines developed by David Martens.

References

Beike, J. (2001), Studien zur anisotropen Leitfähigkeitsverteilung und ein Versuch zur Erklärung magnetotellurischer Übertragungsfunktionen in der Küstenkordillere Nordchiles, Diplomarbeit, FU Berlin

Brasse, H. (2011), Electromagnetic Images of the South and Central American Subduction Zones - In: The Earth's Magnetic Interior (eds. E. Petrovsky, E. Herrero-Bervera, T. Harinarayana and D. Ivers), IAGA Special Sopron Book Series 1, Springer, Berlin, 43-81

Brasse, H., Eydam, D. (1998), Electrical conductivity beneath the Bolivian Orocline and its relation to subduction processes at the South American continental margin, J. of Geophys. Res., Vol.113, B07109, doi:10.1029/2007JB005142

Brasse, H., Lezaeta, P., Rath, V., Schwalenberg, K., Soyer, W., Haak, V. (2002), The Bolivian Altiplano conductivity anomaly, J. Geophys. Res., Vol. 107, B5, 4-10

Caldwell, T., Bibby, H.M., Brown, C. (2004), The magnetotelluric phase tensor, Geophys. J. Int., 158, 457-469

Chmielowski, J., Zandt, G., Haberland, C. (1999), The Central Andean Altiplano-Puna Magma Body, Geophysical Research Letters, 26, 783-786

Díaz, D., Brasse, H., and Ticona, F. (2012), Conductivity distribution beneath Lascar volcano (Northern Chile) and the Puna, inferred from magnetotelluric data, J. Volc. Geotherm. Res., 217-218, doi:10.1016/j.jvolgeores.2011.12.007.

Echternacht, F., Tauber, S., Eisel, M., Brasse, H., Schwarz, G., Haak, V. (1997), Electromagnetic study of the active continental margin in northern Chile, Phys. Earth Planet. Inter., 102, 69-87

González-Ferran, O. (1994), Volcanes de Chile, Inst. Geográfico Militar, Santiago de Chile, 640 pp

Heit, B., Bianchi, M., Yuan, X., Kay, S., Sandvol, E., Kumar, P., Kind, R., Alonso, R., Brown, L., Comte, D. (2014), Structure of the crust and the lithosphere beneath the southern Puna plateau from teleseismic receiver functions, Earth Planet. Sci. Lett., 385, 1-11

Ingham, M. (2005), Deep electrical structure of the Central Volcanic Region and taupo Volcanic Zone, New Zealand, Earth Planets Space, 57, 591-603

Lezaeta, P. (2001), Distortion analysis and 3-D modeling of magnetotelluric data in the Southern Central Andes, PhD thesis, FU Berlin, 177 pp

del Potro, R., Diez, M., Blundy, J.D., Gottsmann, J.H, Camacho, A.G. (2013), Diapiric ascent of silicic magma beneath the Bolivian Altiplano, Geophys. Res. Lett., Vol.40, No.10, 2044-2048

Scheuber, E., Mertmann, D., Ege, H., Silva-González, P., Heubeck, C., Reutter, K.J., Jacobshagen, V. (2006), Exhumation and Basin Development Related to Formation of the Central Andean Plateau, 21°S, In: The Andes: Active Subduction Orogeny (eds: O. Oncken et al.), Frontiers in Earth Sciences, Springer, Berlin-Heidelberg, 285-302.

Schilling, F.R., Trumbull, R.B., Brasse, H., Haberland, C., Asch, G., Bruhn, D., Mai, K., Haak, V., Giese, P., Muoz, M., Ramelow, J., Rietbrock, A., Ricaldi, E., and Vietor, T. (2006), Partial Melting in the Central Andean Crust: A Review of Geophysical, Petrophysical, and Petrologic Evidence, In: The Andes: Active Subduction Orogeny (eds: O. Oncken et al.), Frontiers in Earth Sciences, Springer, Berlin-Heidelberg, 459-474.

Schwalenberg, K., Rath, V., Haak, V. (2002), Sensitivity studies applied to a 2-D resistivity model from the central Andes, Geophys. J. Int., 150, 673-686

Siripunvaraporn, W., Egbert, G. (2000), An efficient data-subspace inversion method for 2-D magnetotelluric data, Geophysics, 65, 791-803

Siripunvaraporn, W., Egbert, G., Lenbury, Y. (2005), Three-dimensional magnetotelluric inversion: data-space method., Phys. Earth Planet. Inter., 150, 3-14

Yuan, X., Sobolev, S.V., Kind, R., Oncken, O., Bock, G., Asch, G., Schurr, B., Gräber, F., Rudloff, A., Hanka, W., Wylegalla, K., Tibi, R., Haberland, C., Rietbrock, A., Giese, P., Wigger, P., Roewer, P., Zandt, G., Beck, S., Wallace, T., Pardo, M., Comte, D. (2000), Subduction and collision processes in the Central Andes constrained by converted seismic phases, Nature, 408, 958-961

Long-term variations of magnetotelluric transfer functions in northern Chile

Jaime Araya[1,2], Oliver Ritter[1,2], and Dirk Brändlein[1,2]

[1]*GFZ German Research Centre for Geosciences, Potsdam, Germany*
[2]*Freie Universität Berlin, Fachrichtung Geophysik, Berlin, Germany*

Summary

For monitoring the deep electrical conductivity structure of the Nazca-South America subduction zone, long-period magnetotelluric (MT) data are continuously collected at an array of 9 stations in northern Chile. This study presents a characterization of the temporal variations observed in MT transfer functions (TFs) after 5 years of measurements (2007-2012). MT impedances exhibit temporal variations, with variability patterns that depend on the period band and the tensor component considered. Daily estimations of TFs show variability ranges that are mainly related to systematic seasonal variations (which were interpreted as a source field effect by Brändlein *et al.*, 2012), and cultural noise. Some of these effects can be removed by examination of differences between monthly TFs obtained at similar seasons and using a processing interval of 30 days to calculate each TF estimate. Following this approach, off-diagonal impedance components show long-term (over 4 years) variability $\leq \pm 10\%$ in apparent resistivity and $\leq \pm 5^\circ$ in phase, for periods between 100 and 1000s.

1 Introduction

Integrated Plate Boundary Observatory Chile (IPOC) is a permanent array of geophysical stations to monitor the dynamic behavior of the active subduction zone in northern Chile (18 and 24°Lat S). This segment of the Chilean margin is now considered in the terminal stage of a seismic cycle, because it exhibits an anomalous long gap of large earthquakes since 1877 (Figure 1). Magnetotelluric (MT) data are collected at nine IPOC sites, for identifying possible changes in the deep electrical resistivity structure. Temporal variations in electrical resistivity could be caused by large scale fluid relocation related to major tectonic processes. For instance, changes observed in the seismic velocity structure after the 1995 Mw 8 Antofagasta earthquake were explained by deep fluid flow into the South American Plate (Husen and Kissling, 2001).

Previous analysis of IPOC MT data revealed systematic seasonal variations in the vertical magnetic transfer functions, which were correlated with changes in the electromagnetic source field (Brändlein *et al.*, 2012). Here, we present a characterization of the temporal variations observed in MT transfer functions (impedance, apparent resistivity and phase). For any monitoring purposes it is necessary to define a base line of the transfer functions (TF) variability, which should be considered in order to interpret changes of the subsurface electrical resistivity.

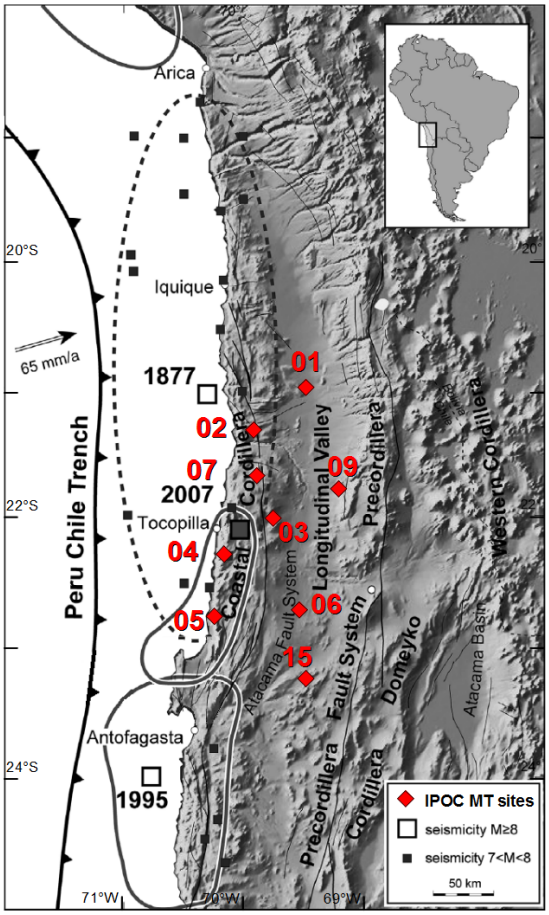

Figure 1: Map of northern Chile showing the IPOC MT array and the rupture areas of earthquakes with magnitude ≥8 since 1877 (modified from Victor *et al.*, 2011).

2 Data and Methodology

The MT IPOC array is distributed in an area of approx. 200 x 100 km, with an average separation of 50 km in between sites (Figure 1). At each site, the two orthogonal components of horizontal electric and magnetic fields and the vertical magnetic field are recorded. Magnetic field variations are measured using three component fluxgate magnetometers (Geomagnet), while electric fields are recorded with nonpolarizing Ag/AgCl electrodes (manufactured by the GFZ German Research Centre for Geosciences). The signals of all electromagnetic fields are continuously sampled at a rate of 20 Hz using Earth Data Logger system. The extremely dry conditions of northern Chile make electric field measurements very difficult, because usually electrolyte leaks and contact resistance are in the order of hundreds of kΩ. For this reason, electric field recordings are mostly unavailable between July 2007 and December 2010.

MT impedance (Z), apparent resistivity and impedance phase have been obtained using the EMERALD robust processing package (Ritter *et al.*, 1998; Weckmann *et al.*, 2005; Krings, 2007). We tried different processing intervals and data selection criteria, as well

single-site and remote reference processing, for testing the influence of a range of processing schemes on the TFs variability. To obtain statistically robust MT responses for periods >1000s on a daily basis requires time series longer than 3 consecutive days.

3 Results

The daily MT responses exhibit temporal variations, with variability patterns that depend on the impedance component and the period of the signal considered. Figure 2a shows the median apparent resistivity and phases of all daily TFs calculated for a consecutive recording of 2 years at site 01. As can be seen, scatter around the 2-years median value (error bars) is larger for TFs derived from the Zxy impedance (the smaller off-diagonal component which also exhibits a worse signal-to-noise ratio). TFs appear most stable (small error bars) for periods between 80 and 1000s. Particularly at long periods (>1000 s) variances can exceed 100% of the median value (Figure 2a and b).

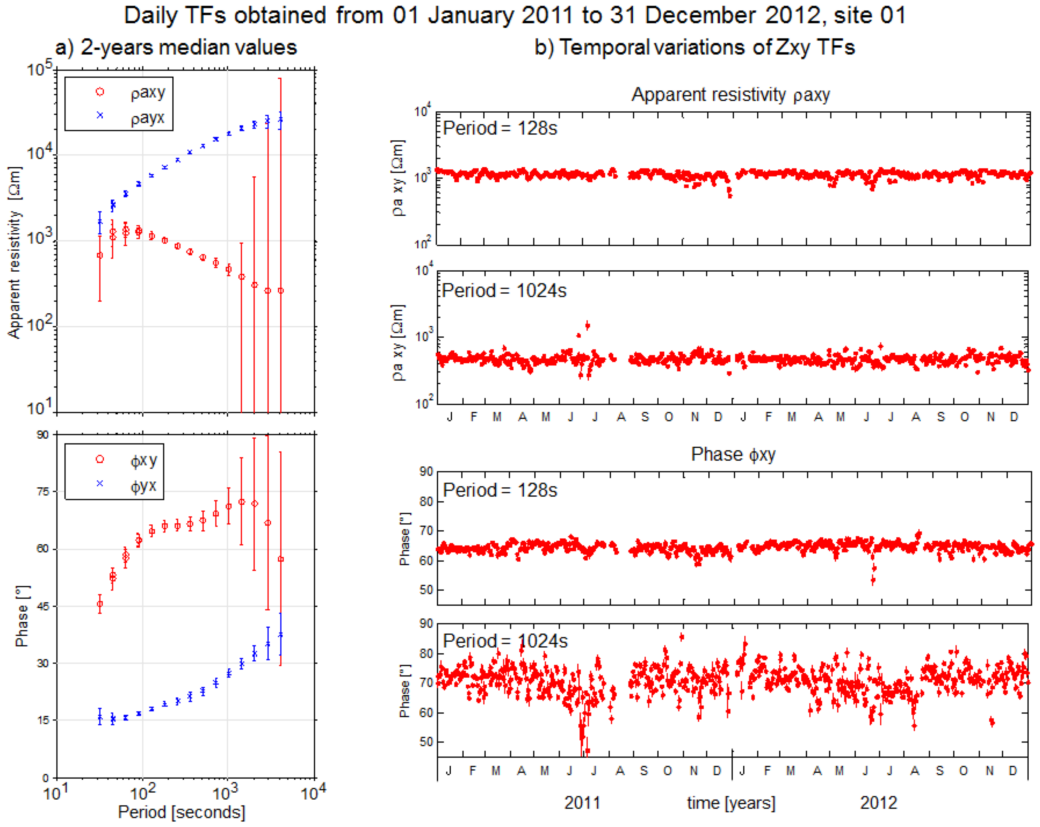

Figure 2: Daily apparent resistivity and phases from 01-January-2011 to 31-December-2012 for site 01: a) Median of all values (error bars represent one standard deviation of the population). b) Temporal variations of xy components, for periods 128 and 1024s (error bars represent the confidence interval of each daily TF). Note that the variability ranges in the Zxy components are larger than for the Zyx component, especially for periods > 1000s.

The observed TFs temporal variations show cyclic patterns with periodicities from 5 days to 1 year. The most obvious periodical signal are annual variations that peak around the June and December solstice, especially evident when the deviations of the daily estimates from the 2-year median is examined (for example, see daily temporal variations of phase in Figure 3). A similar pattern was observed for the vertical magnetic TFs, which was interpreted as a source field effect (Brändlein *et al.*, 2012). Other significant deviations from the median value appear to be randomly distributed, with durations of less than 10 days. As these patterns are not coherent across the array of stations, we suggest that most of these effects are caused by a combination of local noise sources and poor natural source activity.

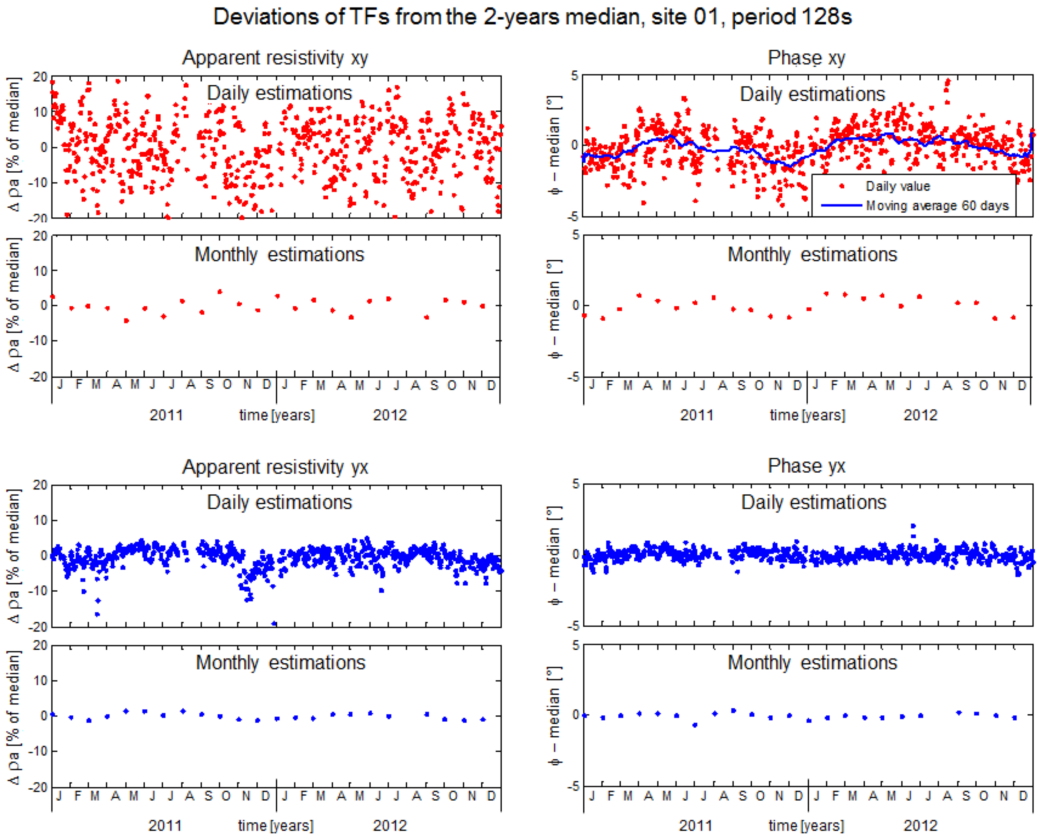

Figure 3: Comparison between daily and monthly TFs estimations presented as relative changes from the 2-years median, site 01, at a period of 128s. Deviations in apparent resistivity are expressed in terms of percentage of the 2-years median value. Note that daily temporal variations of phase show an annual periodical trend, with peaks around June and December.

To improve statistical properties of the TFs estimates, particularly for longer periods, we also calculated monthly averages. Figure 3 shows the TFs after processing 30-days intervals of the data in comparison with the daily values. As expected, this processing scheme results in more stable TFs. Now, we observe deviations from the median of less than $\pm 5\%$ in apparent resistivity and less than $\pm 5°$ in phase (Figure 3). To examine long term trends

and to reduce an influence of the seasonal variations, we compare TFs obtained at the same month (season).

Figure 4 shows that differences between May-2007 and May-2011 at sites 01 and 05, i.e. data recorded just prior to the November-2007 Mw7.7 Tocopilla earthquake and a long time afterwards. We generally observe differences $< \pm 10\%$ in apparent resistivity and $< \pm 5°$ in phase for the off-diagonal impedance components in a period band of 100-1000s, but without any clear trend. The Mw7.7 Tocopilla earthquake represents the largest seismic event registered since the MT array is working, and the epicenter was close to site 05. Unfortunately, the impedance estimates from months close to the Tocopilla seismic sequence could not be used, due to the bad quality of the electric fields measurements during that time (dried out electrodes).

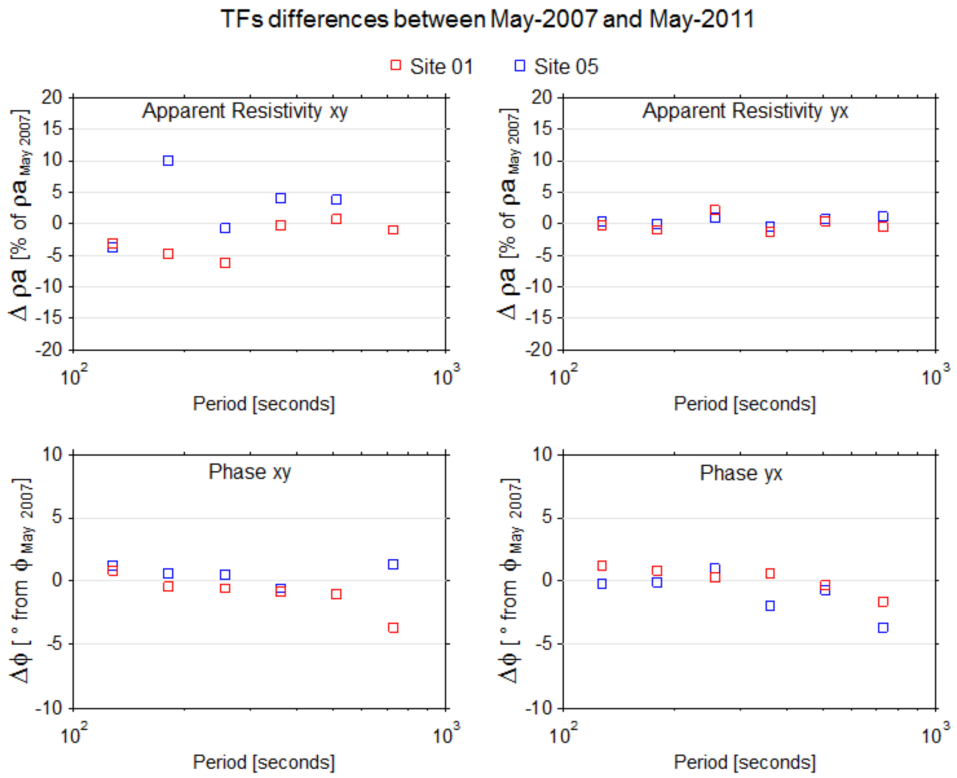

Figure 4: Comparison of deviations in the impedance estimates between May-2007 and May-2011 of sites 01 and 05. TFs were obtained using 1-month processing intervals. Site 05 is located close to the coast, inside the rupture area of the 14 November 2007 Mw7.7 Tocopilla earthquake, whereas site 01 is more than 100 km away from this region (see sites location and Tocopilla earthquake rupture area in Figure 1).

4 Conclusions

The IPOC MT data show that daily TFs exhibit temporal variations, with variability ranges that depend on the impedance component and period range considered. The variability is strongly influenced by seasonal variations which have been interpreted as a source effect (Brändlein *et al.*, 2012), and cultural noise in combination with varying natural activity. A more stable base line estimate of the impedance can be achieved with a processing interval of 30 days. Following this approach, off-diagonal impedance components show long-term (over 4 years) variability $< \pm 10\%$ in apparent resistivity and $< \pm 5^\circ$ in phase for periods between 100 and 1000s.

Aknowledgements

J. Araya gratefully acknowledges financial support from the German Academic Exchange Service (DAAD). The IPOC magnetotelluric instrumentation was partly provided by the GFZ Geophysical Instrument Pool Potsdam (GIPP). We wish to thank the discussions with people from the electromagnetic working groups of GFZ and Free University Berlin.

References

Brändlein, D., H. Lühr, and O. Ritter (2012), Direct penetration of the interplanetary electric field to low geomagnetic latitudes and its effect on magnetotelluric sounding, J. Geophys. Res., 117, A11314, doi:10.1029/2012JA018008.

Husen, S., and E. Kissling (2001), Postseismic fluid flow after the large subduction earthquake of Antofagasta, Chile, Geology, 29(9), 847-850.

Krings, T. (2007), The influence of robust statistics, remote reference, and horizontal magnetic transfer functions on data processing in magnetotellurics, Diploma thesis, Westfälische Wilhelms-Universität, Münster, Germany.

Ritter, O., A. Junge, and G. Dawes (1998), New equipment and processing for magnetotelluric remote reference observations, Geophys. J. Int., 132(3), 535-548, doi:10.1046/j.1365-246X.1998.00440.x.

Weckmann, U., A. Magunia, and O. Ritter (2005), Effective noise separation for magnetotelluric single site data processing using a frequency domain selection scheme, Geophys. J. Int., 161(3), 635-652, doi:10.1111/j.1365-246X.2005.02621.x.

Liste der Autoren